

PRECISION CALCULATIONS FOR HIGGS BOSON PHYSICS
AT THE LHC

FOUR-LOOP CORRECTIONS TO GLUON-FUSION PROCESSES AND HIGGS
BOSON PAIR-PRODUCTION AT NNLO

Zur Erlangung des akademischen Grades eines
DOKTORS DER NATURWISSENSCHAFTEN (Dr. rer. nat)

von der KIT-Fakultät für Physik
des Karlsruher Instituts für Technologie (KIT)

genehmigte

DISSERTATION

von

M.SC. FLORIAN HERREN

Tag der mündlichen Prüfung: 23.10.2020

Referent: Prof. Dr. Matthias Steinhauser

Korreferent: Prof. Dr. Kirill Melnikov



This document is licensed under a Creative Commons Attribution-ShareAlike 4.0 International License (CC BY-SA 4.0):
<https://creativecommons.org/licenses/by-sa/4.0/deed.en>

ABSTRACT

The search for the pair-production of the Higgs boson and the precise study of its properties are among the corner stones of the physics programme of the Large Hadron Collider and its High-Luminosity upgrade.

This thesis focuses on the evaluation of higher-order corrections to Higgs boson pair production: the effective two-Higgs boson–gluon coupling at four loops and next-to-next-to-leading order corrections to the total inclusive cross-section including finite top-quark mass effects.

In addition, finite top-quark mass effects in the Higgs boson–gluon vertex are studied at the four-loop order and four-loop corrections to the Higgs boson decay into photons are obtained.

CONTENTS

1	INTRODUCTION	1
I INTERACTIONS BETWEEN HIGGS BOSONS AND GLUONS		
2	THE EFFECTIVE COUPLING OF TWO HIGGS BOSONS TO GLUONS	9
2.1	Integrating out the top quark	9
2.1.1	The full theory	10
2.1.2	Effective Higgs boson–gluon couplings	11
2.2	Matching full and effective theories	12
2.2.1	Matching for C_H	12
2.2.2	Matching for C_{HH}	16
2.3	Computational setup	19
2.3.1	General setup	19
2.3.2	Building superdiagrams	21
2.4	C_{HH} to $\mathcal{O}(\alpha_s^4)$	23
3	TOP-QUARK–MASS EFFECTS IN THE HIGGS BOSON–GLUON FORM FACTOR AT FOUR LOOPS	25
3.1	Large mass expansion of the Higgs boson–gluon form factor	25
3.1.1	Structure of the computation	26
3.2	The infrared structure of the Higgs boson–gluon form factor	30
3.2.1	Expected infrared pole structure	31
3.2.2	Comparison with the explicit calculation	33
3.3	Results	33
3.3.1	Analytic results	34
3.3.2	Numerical impact of mass corrections	36
4	THE HIGGS BOSON DECAY INTO PHOTONS AT FOUR LOOPS	43
4.1	Computation of the four-loop corrections	43
4.2	Results	45
4.2.1	Analytic results	46
4.2.2	Numerical results	48
II HIGGS BOSON PAIR PRODUCTION		
5	APPLYING MULTI-LOOP TECHNIQUES TO PHASE SPACE INTEGRALS	53
5.1	Computing phase space integrals by reverse unitarity	55
5.1.1	Linear dependence among propagators	57
5.1.2	Minimization of integral families	60
5.2	LIMIT	62
5.2.1	Structure of the program	63

5.2.2	Application to Higgs boson pair production	70
5.2.3	Further applications	77
6	CONTRIBUTIONS WITH BOTH HIGGS BOSONS COUPLING TO DIFFERENT TOP-QUARK LOOPS AT NNLO	79
6.1	Contributions to the total cross-section	80
6.1.1	Real-radiative corrections	80
6.1.2	Computational setup for the real corrections	82
6.1.3	Virtual corrections to $gg \rightarrow HH$	84
6.1.4	Collinear counterterms	85
6.2	Computing the master integrals	87
6.2.1	Expansion around the production threshold	88
6.2.2	Exact computation by differential equations	90
6.3	Results	96
6.3.1	Partonic cross-sections	97
7	TOWARDS HIGGS BOSON PAIR PRODUCTION AT NNLO WITH FINITE TOP-QUARK-MASS EFFECTS	101
7.1	Double-real radiation	102
7.1.1	Four-gluon building blocks	103
7.1.2	Computing the four-particle cut master integrals	104
7.1.3	Results for the quark-quark initial state	109
7.2	Real-virtual contributions	110
7.2.1	Contributions with a third top-quark loop	113
7.2.2	Hard real-virtual corrections	114
7.2.3	Soft real-virtual corrections	115
7.2.4	Results for the quark-anti-quark initial state	118
7.3	Outlook	118
7.3.1	Completing the computation	118
7.3.2	Beyond the large mass expansion	120
8	CONCLUSION	123
III APPENDIX		
A	DEFINITIONS	127
A.1	Ghosts and gauge fixing	127
A.2	Renormalization of QCD	127
A.3	Decoupling constants	129
A.4	Colour factors	131
A.5	Projectors and tensors structures	132
A.6	Goncharov Polylogarithms	132
B	LARGE MASS EXPANSION	135
C	ADDITIONAL RESULTS	137
C.1	Effective coupling of a Higgs boson to quarks	137

c.2	Effective coupling of a Higgs boson to gluons	138
c.3	On-shell renormalization of gluons	141

BIBLIOGRAPHY 155

LIST OF FIGURES

Figure 1.1	Contributions to $gg \rightarrow H(g)$ involving the self-coupling	3
Figure 1.2	Leading order contributions to $gg \rightarrow HH$	3
Figure 2.1	$gg \rightarrow H$ contributions through three loops	14
Figure 2.2	Large mass expansion of three loop diagrams	15
Figure 2.3	Three contributions to Higgs boson pair-production in the EFT	17
Figure 2.4	Diagram contributing to 1PR and 1PI contribution in the EFT	17
Figure 2.5	General computational workflow	20
Figure 3.1	Large mass expansion at four-loop order	26
Figure 3.2	Bookkeeping system for tadpole reduction	30
Figure 3.3	μ -dependence of $\log F _{\text{finite}}$ renormalized in the on-shell scheme	38
Figure 3.4	μ -dependence of $\log F _{\text{finite}}$ renormalized in the $\overline{\text{MS}}$ scheme	39
Figure 3.5	ρ -dependence of $\log F$ renormalized in the on-shell scheme	40
Figure 3.6	ρ -dependence of $\log F _{\text{finite}}$ renormalized in the $\overline{\text{MS}}$ scheme	41
Figure 4.1	Leading order diagrams for $H \rightarrow \gamma\gamma$	44
Figure 4.2	Three-loop diagrams for $H \rightarrow \gamma\gamma$	44
Figure 4.3	Diagrams for $H \rightarrow \gamma\gamma$ with photons coupling to different quark loops	45
Figure 5.1	Sample diagrams of real-virtual and double-real corrections to Higgs boson pair-production	54
Figure 5.2	Forward-scattering diagrams for $gg \rightarrow HH$	57
Figure 5.3	Sample template family	71
Figure 5.4	Two-loop phase-space families	72
Figure 5.5	Three-loop real-virtual phase-space families	73
Figure 5.6	Planar double-real three-loop phase-space families 1	74
Figure 5.7	Planar double-real three-loop phase-space families 2	75
Figure 5.8	Non-planar double-real three-loop phase-space families	76
Figure 6.1	Diagrams with both Higgs bosons coupling to different quark loops	79
Figure 6.2	Large-mass expansion of a diagram with both Higgs bosons coupling to different quark loops	83
Figure 6.3	One-loop phase-space master integrals	87
Figure 6.4	Two-loop phase-space master integrals	87
Figure 6.5	Exact and expanded results for sample master integrals	96

Figure 6.6	Numerical results for partonic cross-sections	99
Figure 6.7	Convergence of the large mass expansion for the gluon-gluon channel	100
Figure 7.1	Quark-quark initial state diagrams	101
Figure 7.2	Four-loop building block diagrams	103
Figure 7.3	Double-real master integrals 1	105
Figure 7.4	Double-real master integrals 2	106
Figure 7.5	Master integral with the letter $x = -1/4$	107
Figure 7.6	Numerical results for quark-quark channels	111
Figure 7.7	Convergence of the large mass expansion for quark-quark channels	112
Figure 7.8	Sample real-virtual contributions	112
Figure 7.9	Large mass expansion of a real-virtual contribution with two top-quark loops	112
Figure 7.10	Large mass expansion of a real-virtual contribution with three top-quark loops	113
Figure 7.11	Diagram with a top-quark loop and two building blocks	114
Figure 7.12	Diagram leading to a two-quark–two-Higgs boson building block	115
Figure 7.13	Three-loop three-particle cut master integrals	116
Figure 7.14	Imaginary parts of real-virtual integrals	117
Figure 7.15	Numerical result for quark-anti-quark channel	119

LIST OF TABLES

Table 2.1	Number of Feynman diagrams and superdiagrams	20
-----------	--	----

ACRONYMS

$1PI$	one-particle irreducible
$1PR$	one-particle reducible
BSM	beyond the Standard Model
DE	differential equation
EFT	effective field theory

IBP	integration by parts
IR	infrared
GPL	Goncharov polylogarithm
HEFT	Higgs effective field theory
HL-LHC	high-luminosity extension of the Large Hadron Collider
LME	large mass expansion
LHC	Large Hadron Collider
LO	leading order
MI	master integral
$\overline{\text{MS}}$	modified minimal subtraction
NLO	next-to-leading order
NNLO	next-to-next-to-leading order
N ₃ LO	next-to-next-to-next-to-leading order
OS	on-shell
QCD	Quantum Chromodynamics
QED	Quantum Electrodynamics
QFT	quantum field theory
SM	Standard Model of elementary particle physics
UV	ultraviolet

INTRODUCTION

In 2012 the two general purpose experiments at the Large Hadron Collider ([LHC](#)), ATLAS and CMS, announced the discovery of a scalar boson with a mass of approximately 125 GeV [[1](#), [2](#)]. Since the Higgs boson's discovery, measurements of its properties in all production and decay channels accessible at the [LHC](#) have been carried out with all evidence pointing towards the particle being the long-sought Higgs boson of the Standard Model of elementary particle physics ([SM](#)) [[3–14](#)].

THE STATE OF THE ART: HIGGS BOSON PRODUCTION AND DECAY As the Brout-Englert-Higgs mechanism might not be realized in its minimal form, scrutinizing the properties of the Higgs boson might reveal the existence of new particles. In addition, it might shed light on unsolved problems in particle physics, such as the dominance of matter over anti-matter in the universe, neutrino masses or the existence of dark matter.

To this end, precise measurements of all production and decay channels accessible at the [LHC](#) are carried out by ATLAS and CMS. In the past years all four major production mechanisms have been established experimentally. In addition to the dominant gluon-fusion mechanism, also the production in vector-boson-fusion, associated production with a vector boson and recently even the production in association with a pair of top quarks have been observed. Furthermore, all major decay channels, the decays into third-generation fermions, τ -leptons and bottom quarks, pairs of W - or Z -bosons, as well as the loop-induced decay into photons have been observed. Recently, CMS even found evidence for the decay into two muons [[15](#)] indicating that the Higgs boson also couples to second-generation fermions. With the upcoming high-luminosity extension of the Large Hadron Collider ([HL-LHC](#)) program, the statistical uncertainties on all of the above processes will decrease, allowing for percent-level measurements.

To fully exploit the experimental precision, equally precise theoretical predictions need to be available. Generally, predictions at next-to-next-to-leading order ([NNLO](#)) or even next-to-next-to-next-to-leading order ([N₃LO](#)) are required to accomplish this task. Computations of corrections at this order are extremely challenging, but in recent years all of the aforementioned production channels except the associated production with a pair of top quarks have become available at [NNLO](#). For a recent summary see e.g. [[16](#)]. The inclusive total cross-section for the production of a Higgs boson in gluon-fusion is even known at [N₃LO](#) [[17](#), [18](#)] in the limit of an infinitely heavy top quark.

THE SCALAR POTENTIAL Despite the successes of the Higgs programme at the [LHC](#), the nature of the scalar potential remains elusive. In the unbroken phase of the [SM](#), it takes the form

$$V(\Phi) = -\mu^2 \Phi^\dagger \Phi + \lambda (\Phi^\dagger \Phi)^2, \quad (1.1)$$

where $\mu^2 > 0$, $\lambda > 0$ and Φ is a doublet under $SU(2)_L$ with weak hypercharge $Y = 1^1$. The minimum of $V(\Phi)$ is located at

$$\Phi_0 = \frac{1}{\sqrt{2}} \begin{pmatrix} 0 \\ v \end{pmatrix}, \quad \text{where } v = \sqrt{\frac{\mu^2}{\lambda}}. \quad (1.2)$$

This minimum breaks the gauge symmetry of the [SM](#) from $SU(3)_c \times SU(2)_L \times U(1)_Y$ to $SU(3)_c \times U(1)_Q$ leading to masses for the W - and Z -bosons and all fermions except neutrinos. The vacuum expectation value v is related to Fermi's constant by

$$v = \frac{1}{\sqrt{\sqrt{2}G_F}} \approx 246.22 \text{ GeV}. \quad (1.3)$$

Expanding the scalar potential around its minimum yields the potential for the physical Higgs boson field H

$$V(H) = \frac{m_H^2}{2} H^2 + v\lambda H^3 + \frac{\lambda}{4} H^4. \quad (1.4)$$

The mass of the Higgs boson is related to the parameters of the unbroken phase by

$$m_H^2 = 2\mu^2. \quad (1.5)$$

As a consequence, the self-coupling λ is given by

$$\lambda = \frac{v^2}{\mu^2} = \frac{2v^2}{m_H^2} \approx 0.13 \quad (1.6)$$

and thus the cubic and quartic terms in Eq. (1.4) are fixed within the [SM](#).

In many Beyond the Standard Model ([BSM](#)) theories, the cubic and quartic coupling are not directly related to m_H and v , but also receive other contributions. As a consequence, a precise measurement of the cubic and quartic Higgs boson interaction strength can either severely constrain [BSM](#) theories or, in case a deviation from the [SM](#) expectation is found, hint towards [BSM](#) phenomena.

ACCESSING THE CUBIC SELF-COUPLING INDIRECTLY The cubic self-coupling can be constrained by comparing precise measurements of the different Higgs boson production and decay channels with precise theoretical predictions. Higher-order corrections, such

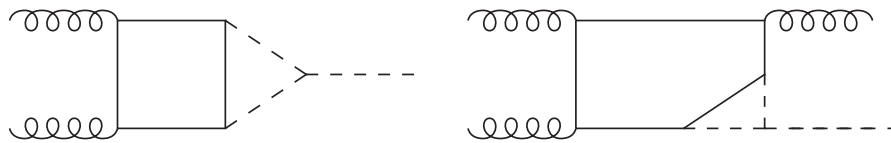


Figure 1.1: Higher-order contributions to Higgs boson production in gluon-fusion involving the cubic Higgs boson self-coupling. Dashed, solid and curly lines denote Higgs bosons, top quarks and gluons, respectively.

as the ones depicted in Fig. 1.1, involve the cubic self-coupling and are sensitive to modifications of it. Based on the results presented in Ref. [19], the cubic self-coupling is constrained within the range of -4.7 and 12.6 times the SM value [20] under the assumption that no other Higgs boson couplings deviate from their SM value. Since in BSM theories this is not the case in general, the constraint that can be obtained crucially depends on assumptions about deviations in other Higgs boson couplings. To overcome this issue, differential distributions of processes involving Higgs bosons have to be taken into account in the future.

HIGGS BOSON PAIR-PRODUCTION A direct way to access the cubic Higgs boson coupling is the process of Higgs boson pair-production. As in the case of single Higgs boson production, gluon-fusion is the dominant production channel. Sample diagrams at leading order (LO) can be found in Fig. 1.2, where only the diagram on the right involves the cubic Higgs boson coupling. The two contributions interfere negatively with each



Figure 1.2: The two LO contributions to Higgs boson pair-production in gluon-fusion. Only the diagram on the right involves the cubic Higgs boson self-coupling.

other, leading to a significant reduction of the production cross-section in the SM. Taking both contributions into account, the total Higgs boson pair production cross-section is approximately three orders of magnitude smaller than the single Higgs boson production cross-section. As a consequence, Higgs boson pair-production has not been observed to date and current measurements allow the cubic self-coupling to lie between -5.0 and 12 times the SM value [21], which is comparable to the aforementioned constraint obtained by measurements of processes with a single Higgs boson. Significant improvements will be made with the HL-LHC and the significance of the observation might reach 4.0σ [22]. This corresponds to upper and lower bounds of the cubic self-coupling of 0.1 and 2.3

¹ Here, $Q = T_{3L} + Y/2$ with Q being the electric charge and T_{3L} the third Pauli matrix.

times the SM value, respectively. This is comparable to the constraint that can be obtained by measuring processes involving a single Higgs boson [20]. Combining both ways to access the cubic self-coupling will provide an even stronger constraint.

Proposed future proton-proton colliders such as the hadron option of the *future circular collider* are expected to reach a sensitivity on λ of up to 5% [22].

On the theoretical side, computing higher-order corrections to Higgs boson pair-production involves the challenge of evaluating four-point functions with an internal massive particle. As a consequence the computation of exact next-to-leading order (NLO) corrections was achieved only recently by employing numerical methods [23–25]. Before exact NLO results became available, approximation methods were used. Two prominent examples are the expansion in a large top-quark mass [26] and the combination of the exact LO corrections with the exact real-radiation contributions and the virtual corrections in the limit $M_t \rightarrow \infty$ [27]. Both methods have been extended to NNLO [28, 29] where they supersede predictions based on the infinitely heavy top-quark limit [30]. N₃LO corrections in the limit of an infinitely heavy top quark also became available recently [31, 32].

IMPROVING THE CURRENT PREDICTIONS The remainder of this thesis is divided into two parts. In the first part, we discuss computations based on the large mass expansion (LME) at four-loop order. We start with the computation of the effective coupling of two Higgs bosons to gluons [33] in chapter 2, which served as an important ingredient in the recent N₃LO computation of the Higgs boson pair-production cross-section [31, 32]. In chapter 3, we perform a LME of the Higgs boson–gluon vertex at four loops [34] as a first step towards including finite top-quark mass effects at N₃LO to the production of a single Higgs boson. We conclude the first part by computing the N₃LO corrections to the Higgs boson decay into photons.

In the second part of this work we focus on the process of Higgs boson pair-production and compute real-radiation contributions at NNLO in the limit $s \ll 4M_t^2$. In order to process the phase-space integrals arising in this context efficiently, we introduce the versatile program LIMIT in chapter 5 and highlight its other applications. As the first step towards the full real-radiation contributions including top-quark mass suppressed terms, we consider the subset of contributions where both Higgs bosons couple to different top-quark loops. We expand this subset through $\mathcal{O}(1/M_t^8)$ [35] and combine them with the corresponding virtual corrections, as described in chapter 6. In chapter 7 we discuss the remaining contributions and outline the full calculation, which is still work in progress.

Appendices A and B of this thesis introduce several concepts relevant to the aforementioned computations. Using the methods outlined in chapter 2 we computed further quantities to four-loop order. They can be found in appendix C.

FURTHER RESULTS OBTAINED DURING THESE DOCTORAL STUDIES As the aforementioned topics are all centered around the phenomenology of the Higgs boson, we refrain from discussing further results that were obtained in the course of these doctoral studies. These additional results do not fit with the other topics discussed in this thesis, as they are centered around the computation of higher-order beta functions in the [SM](#) and beyond.

As a major result, we obtained the four-loop gauge coupling beta functions in the full [SM](#) [36]. Previous attempts to compute the top-quark Yukawa coupling contribution to the beta function of the strong gauge coupling at this order were plagued by ambiguities related to the treatment of γ_5 in dimensional regularization [37, 38]. We extended the novel approach introduced in Ref. [39], relating the ambiguous contributions to certain terms of the three-loop Yukawa coupling beta functions, to the full [SM](#) and combined it with an explicit four-loop computation of all remaining contributions.

Part I

INTERACTIONS BETWEEN HIGGS BOSONS AND GLUONS

In this part we compute two quantities at four-loop order, relevant to the production and decay of Higgs bosons: the effective coupling of two Higgs bosons to gluons and corrections to the Higgs boson–gluon vertex for a finite top quark mass.

As by-products we also obtain the $N_3\text{LO}$ corrections to the Higgs decay rate into photons, as well as several decoupling and renormalization constants at four loops. The latter are presented in Sec. [C](#).

Since the top quark is the heaviest particle of the SM with a mass of 172.76 GeV [40], its coupling to the Higgs boson is larger than for all other particles of the SM. For many phenomenological applications it is a sufficiently good approximation to consider the top-quark mass to be much larger than all energy scales involved in the process under consideration. This has several advantages, the most obvious being that the top quark does not appear as a dynamical degree of freedom. This is advantageous for calculating higher-order corrections to the production of one or two Higgs bosons in gluon fusion where loops involving top quarks get replaced by Higgs boson–gluon couplings in the effective theory. As a consequence one has to deal with one scale and one loop less in such calculations.

In this chapter we compute the effective coupling of two Higgs bosons to gluons in a diagrammatic approach through four loops, following [33]. This effective coupling enters cross-section predictions for Higgs boson pair-production at N₃LO. In the course of this computation we also encounter the effective coupling of one Higgs boson to gluons, which we compute in a diagrammatic approach.

STRUCTURE OF THE CHAPTER We introduce the effective Lagrangian governing interactions between Higgs bosons and gluons in Sec. 2.1 and derive relations for extracting the effective couplings from amplitudes in the full theory in Sec. 2.2. In Sec. 2.3 we introduce the computational setup used for evaluating the necessary amplitudes. We present the result for the effective coupling of two Higgs bosons to gluons in Sec. 2.4 and compare it to a relation between the effective coupling and the decoupling constant ζ_{α_s} .

Furthermore, in App. C we provide the on-shell wave-function renormalization constant for gluons through four loops, higher order terms in the dimensional regulator for the effective Higgs boson–gluon coupling C_H , as well as the effective coupling C_2 of a Higgs boson to light quarks expressed through $SU(N)$ colour factors. These results have been obtained in the course of the computations of Ref. [33], but not explicitly given there.

2.1 INTEGRATING OUT THE TOP QUARK

In the following we discuss Quantum Chromodynamics (QCD), which is the full theory in the context of this chapter, only briefly. A more detailed discussion of several technical aspects can be found in App. A. We then introduce the effective theory with its effective Higgs boson–gluon couplings, commonly called Higgs effective field theory (HEFT) [41].

2.1.1 The full theory

The Lagrangian density describing QCD with a massive top quark t and $n_l = 5$ massless quarks q_i at the classical level is given by ¹

$$\mathcal{L}_{\text{QCD}}^{(n_f)} = -\frac{1}{4} G^{a,\mu\nu} G_{\mu\nu}^a + \sum_f^{n_l} \bar{q}_f i \not{D} q_f + \bar{t} (i \not{D} - M_t) t . \quad (2.1)$$

Here, $n_f = n_l + 1$ is the number of active quark flavours, M_t is the mass of the top quark and the field strength tensor $G_{\mu\nu}^a$ is related to the gluon field G_μ^a by

$$G_{\mu\nu}^a = \partial_\mu G_\nu^a - \partial_\nu G_\mu^a + g_s f^{abc} G_\mu^b G_\nu^c , \quad (2.2)$$

where the f^{abc} are the structure constants of $SU(3)$ and g_s is related to the strong coupling constant α_s by

$$\alpha_s = \frac{g_s^2}{4\pi} . \quad (2.3)$$

The covariant derivative is given by

$$D_\mu = \partial_\mu - i g_s G_\mu^a T^a , \quad (2.4)$$

where the T^a are the generators of the fundamental representation of $SU(3)$.

The kinetic term of the Higgs boson H and its self-interactions are given by

$$\mathcal{L}_H = \frac{1}{2} (\partial^\mu H) (\partial_\mu H) - \frac{1}{2} m_H^2 H^2 - v \lambda H^3 - \frac{\lambda}{4} H^4 , \quad (2.5)$$

where m_H is the mass of the Higgs boson, v its vacuum expectation value and λ the quartic coupling. It couples to the top quark via

$$\mathcal{L}_{\text{Yukawa}} = -\frac{M_t}{v} \bar{t} t H . \quad (2.6)$$

Several modifications to the above discussion need to be made for a correct description at the quantum level. Fields and parameters in Eqs. (2.1) to (2.6) need to be replaced by so-called *bare* quantities and a gauge fixing term and ghost fields need to be added. Since they are not relevant for the qualitative understanding of the following, we refrain from explicitly discussing them here but refer to Sec. A.1 and Sec. A.2.

¹ The definitions in this section can be found in most quantum field theory (QFT) textbooks. Here, we follow the conventions of [42].

2.1.2 Effective Higgs boson–gluon couplings

All fields and parameters in the previous section are defined in the full theory with n_f quark flavours. In the following, they will carry a label to make this explicit. By integrating out the top quark one obtains an effective Lagrangian \mathcal{L}_{eff} , given by

$$\mathcal{L}_{\text{eff}} = \mathcal{L}_{\text{QCD}}^{(n_l)} \left(G^{(n_l)}, q_f^{(n_l)}, \alpha_s^{(n_l)} \right) + \mathcal{L}_H(H, m_H, \lambda, v) + \mathcal{L}_{\mathcal{O}}, \quad (2.7)$$

where $\mathcal{L}_{\text{QCD}}^{(n_l)}$ is the QCD Lagrangian in Eq. (2.1) without the top quark. Furthermore, $G^{(n_f)}, q_f^{(n_f)}$ and $\alpha_s^{(n_f)}$ are replaced by effective n_l -flavour versions. The relations between fields and parameters in the full and effective theories are encoded in the so-called decoupling constants, introduced in Sec. A.3. The Higgs boson Lagrangian \mathcal{L}_H , as well as its parameters and the Higgs field remain as in Eq. (2.5), since we do not consider electroweak corrections.

EFFECTIVE INTERACTIONS The effective Lagrangian $\mathcal{L}_{\mathcal{O}}$ contains an infinite set of effective operators built from quark, gluon and Higgs fields. In the following we will only focus on the effective coupling of one or two Higgs bosons to gluons at $\mathcal{O}(1/v)$, thus the infinite set is restricted to just

$$\mathcal{L}_{\mathcal{O}} \supset -\frac{H}{v} C_H^0 \mathcal{O}_1^0 + \frac{1}{2} \left(\frac{H}{v} \right)^2 C_{HH}^0 \mathcal{O}_1^0, \quad (2.8)$$

where the operator \mathcal{O}_1^0 gives rise to interactions involving two to four gluons and is constructed from gluon field-strength tensors:

$$\mathcal{O}_1^0 = \frac{1}{4} (G^0)^{a,\mu\nu} (G^0)_{\mu\nu}^a. \quad (2.9)$$

All radiative contributions of the top quark are encoded in the two Wilson coefficients C_H^0 and C_{HH}^0 . These coefficients govern the interaction strength between Higgs bosons and gluons in the limit $M_t \rightarrow \infty$.

For $X \in \{H, HH\}$ the renormalized operators and Wilson coefficients can be obtained by

$$C_X^0 \mathcal{O}_1^0 = \frac{C_X^0}{Z_{\mathcal{O}_1}} Z_{\mathcal{O}_1} \mathcal{O}_1^0 = C_X \mathcal{O}_1, \quad (2.10)$$

where the renormalization constant $Z_{\mathcal{O}_1}$ is related to the QCD beta function through all orders in perturbation theory [43]:

$$Z_{\mathcal{O}_1} = \frac{\epsilon}{\epsilon - \beta \left(\alpha_s^{(n_l)} \right)}. \quad (2.11)$$

LOW-ENERGY THEOREMS The Wilson coefficient C_H was computed at two loops almost forty years ago [41, 44]. Three loop results have been obtained by direct calculation of the Higgs boson–gluon vertex [45], as well as by relating C_H to ζ_{α_s} , the decoupling constant of α_s , via a so-called low-energy theorem [46]:

$$C_H = -\frac{M_t}{\zeta_{\alpha_s}} \frac{\partial}{\partial M_t} \zeta_{\alpha_s}. \quad (2.12)$$

The derivation of this relation is non-trivial and requires the introduction of further operators that do not contribute to physical matrix elements. In Ref. [46] this low-energy theorem was combined with the QCD beta function and quark mass anomalous dimension to obtain C_H at four loops. Similarly, with the five loop mass anomalous dimension and beta function available, the five loop result has been derived [47–49].

C_{HH} has been obtained at three loops only recently [50]. At one and two loops it coincides with C_H but starts to differ at three loops. In contrast to C_H , no low-energy theorem existed until recently a relation between the decoupling constant of α_s and C_{HH} was obtained [51]:

$$C_{HH} = \frac{M_t^2}{\zeta_{\alpha_s}} \frac{\partial^2}{\partial M_t^2} \zeta_{\alpha_s} - 2 \left(\frac{M_t}{\zeta_{\alpha_s}} \frac{\partial}{\partial M_t} \zeta_{\alpha_s} \right)^2. \quad (2.13)$$

In analogy to C_H , five-loop results can be obtained by combining Eq. (2.13) with the five-loop mass anomalous dimension and beta function.

2.2 MATCHING FULL AND EFFECTIVE THEORIES

To compute the Wilson coefficients we need to compare observables or amplitudes in a kinematical limit where the full and the effective theories are both valid. In the case at hand we are only interested in operators that are not suppressed by inverse powers of the top-quark mass, thus we choose the infinitely heavy top quark limit. Furthermore, we have to work with on-shell gluons and both gluon momenta unequal to avoid contributions from unphysical operators appearing in \mathcal{L}_O . In the following, we will derive matching formulae, relating C_H and C_{HH} to amplitudes in the full theory.

2.2.1 Matching for C_H

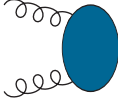
THE AMPLITUDE The simplest amplitude involving gluons and the Higgs boson is the amplitude for Higgs boson production in gluon-fusion. This amplitude has a rather simple structure, given by

$$= \delta^{ab} \epsilon_1^\mu \epsilon_2^\nu A_{\mu\nu}(p_1, p_2, M_t^2), \quad (2.14)$$

where the ϵ_i and p_i are the polarization vectors and momenta of the two gluons. The amplitude $A_{\mu\nu}$ can be decomposed into three terms:

$$A^{\mu\nu}(p_1, p_2, M_t^2) = g^{\mu\nu} A_1(p_1, p_2, M_t^2) + p_2^\mu p_1^\nu A_2(p_1, p_2, M_t^2) + \epsilon^{\mu\nu\rho\sigma} p_{1,\rho} p_{2,\sigma} A_3(p_1, p_2, M_t^2). \quad (2.15)$$

Any other combination of the external momenta does not contribute, since the gluon polarization vectors are transversal and thus $\epsilon_i^\mu p_{i,\mu} = 0$. The third term in Eq. (2.15) does not contribute, since the Higgs boson is a scalar particle and perturbative QCD is a parity conserving theory. Eq. (2.15) can be further simplified employing gauge invariance, $p_1^\mu A_{\mu\nu} = p_2^\nu A_{\mu\nu} = 0$. As a consequence $A_1 = -A_2(p_1 p_2)$, leading to



$$= \delta^{ab} ((\epsilon_1 \cdot \epsilon_2)(p_1 \cdot p_2) - (\epsilon_1 \cdot p_2)(\epsilon_2 \cdot p_1)) \mathcal{A}(s, M_t^2), \quad (2.16)$$

where $s = (p_1 \cdot p_2)/2$. The above discussion only depends on the external particles, hence Eq. (2.14) is valid for the full theory as well as the effective one. To obtain C_H we need to compute $\mathcal{A}(s, M_t^2)$ in both theories, taking the limit $M_t \rightarrow \infty$.

EFFECTIVE THEORY In the effective theory the amplitude is independent of M_t and, at LO, is simply given by C_H/v . Higher-order corrections lead to single scale three-point integrals with trivial dependence on s and can be written as ²

$$\mathcal{A}_{\text{eff}}(s, M_t^2) = Z_{\mathcal{O}_1} \frac{C_H}{v} \left(1 + \sum_l \left(\frac{\alpha_s^{(n_l)}}{\pi} \right)^l \left(\frac{\mu^2}{-s} \right)^{l\epsilon} \mathcal{A}_{\text{eff},l} \right). \quad (2.17)$$

Here, we renormalized the strong coupling constant in the modified minimal subtraction ($\overline{\text{MS}}$) scheme with n_l active flavours

$$\alpha_s^0 = \mu^{2\epsilon} Z_{\alpha_s}(\alpha_s^{(n_l)}, n_l) \alpha_s^{(n_l)}, \quad (2.18)$$

where the renormalization constant Z_{α_s} is known through five loops [52–55]. The $\mathcal{A}_{\text{eff},l}$ still contain ultraviolet (UV) divergences which are cancelled by $Z_{\mathcal{O}_1}$ as well as infrared (IR) divergences which remain. Since all quarks in the effective theory are massless, the on-shell (OS) wavefunction renormalization constant of the gluons is simply 1. Sample diagrams contributing to $\mathcal{A}_{\text{eff},l}$ are shown in Fig. 2.1.

² The s dependence can be derived by rescaling loop and external momenta by $p \rightarrow \sqrt{s}\tilde{p}$. Each loop integration measures scales as $\sqrt{s}^{-2\epsilon} = s^{-\epsilon}$ and the resulting integrals do not depend on any kinematic scale.

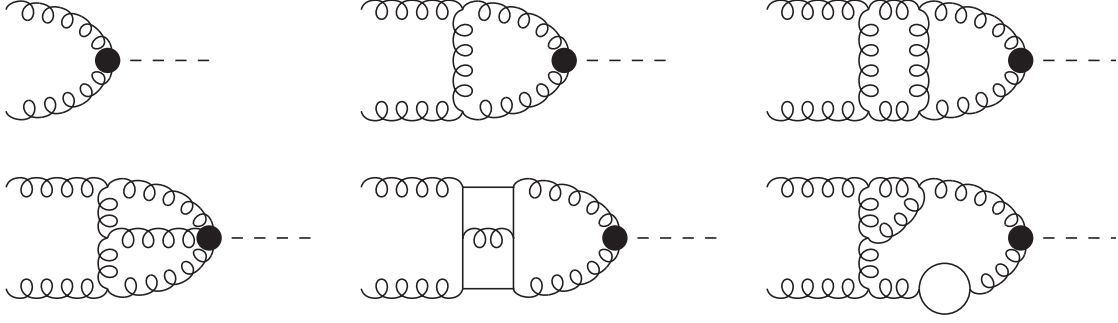


Figure 2.1: Sample diagrams contributing to \mathcal{A}_{eff} through three loops. The black dot denotes the effective Higgs boson–gluon coupling. Straight, dashed and curly lines denote light quarks, Higgs bosons and gluons respectively.

FULL THEORY To compute the amplitude in the full theory while taking the limit $M_t \rightarrow \infty$, we perform an asymptotic expansion [56] in the large mass, also called **LME**. The **LME** simplifies loop integrals by splitting each loop integral into a *hard* region, in which the respective loop momentum scales like M_t , and a *soft* region, where the loop momentum scales like the external momenta and the Higgs boson mass. In each region we can perform a Taylor expansion in the soft scales, simplifying the calculation tremendously. Loop momenta flowing through massive lines are always hard, since for a soft loop momentum the Taylor expansion would lead to vanishing integrals. The method of *expansion by subgraph* allows one to perform the separation algorithmically at the level of Feynman diagrams. Each diagram is decomposed into a sum of hard subgraphs, which have to be Taylor expanded in all of their external momenta and then re-inserted into their respective co-subgraphs. The procedure is illustrated in Fig. 2.2³.

By applying the **LME** and taking the limit $M_t \rightarrow \infty$ we can write the full amplitude as

$$\mathcal{A}_{\text{full}}(s, M_t^2) = Z_3^{\text{OS}} \sum_l \sum_k^{l-1} \left(\frac{\alpha_s^{(n_f)}}{\pi} \right)^l \left(\frac{\mu^2}{M_t^2} \right)^{(l-k)\epsilon} \left(\frac{\mu^2}{-s} \right)^{k\epsilon} \mathcal{A}_{\text{full},l}^{(l-k,k)}, \quad (2.19)$$

where Z_3^{OS} is the **OS** gluon wavefunction renormalization constant given in Sec. C.3. The $\mathcal{A}_{\text{full},l}^{(l-k,k)}$ denote l -loop amplitudes with k soft-scaling loop momenta and $l - k$ hard-scaling ones. At one loop there only is a hard contribution, thus

$$C_H = v \left(\frac{\mu^2}{M_t^2} \right)^\epsilon \frac{\alpha_s^{(n_f)}}{\pi} \mathcal{A}_{\text{full},1}^{(1,0)}. \quad (2.20)$$

The prefactor v cancels against a factor of $1/v$ in the full theory amplitude which originates from the top-quark Yukawa coupling. Starting from two loops, also soft contributions appear, which come with a prefactor of $M_t^{-2\epsilon} s^{-\epsilon}$ and thus scale exactly like

³ Examples of the **LME** at four loop order can be found in Fig. 3.1 in the next chapter.

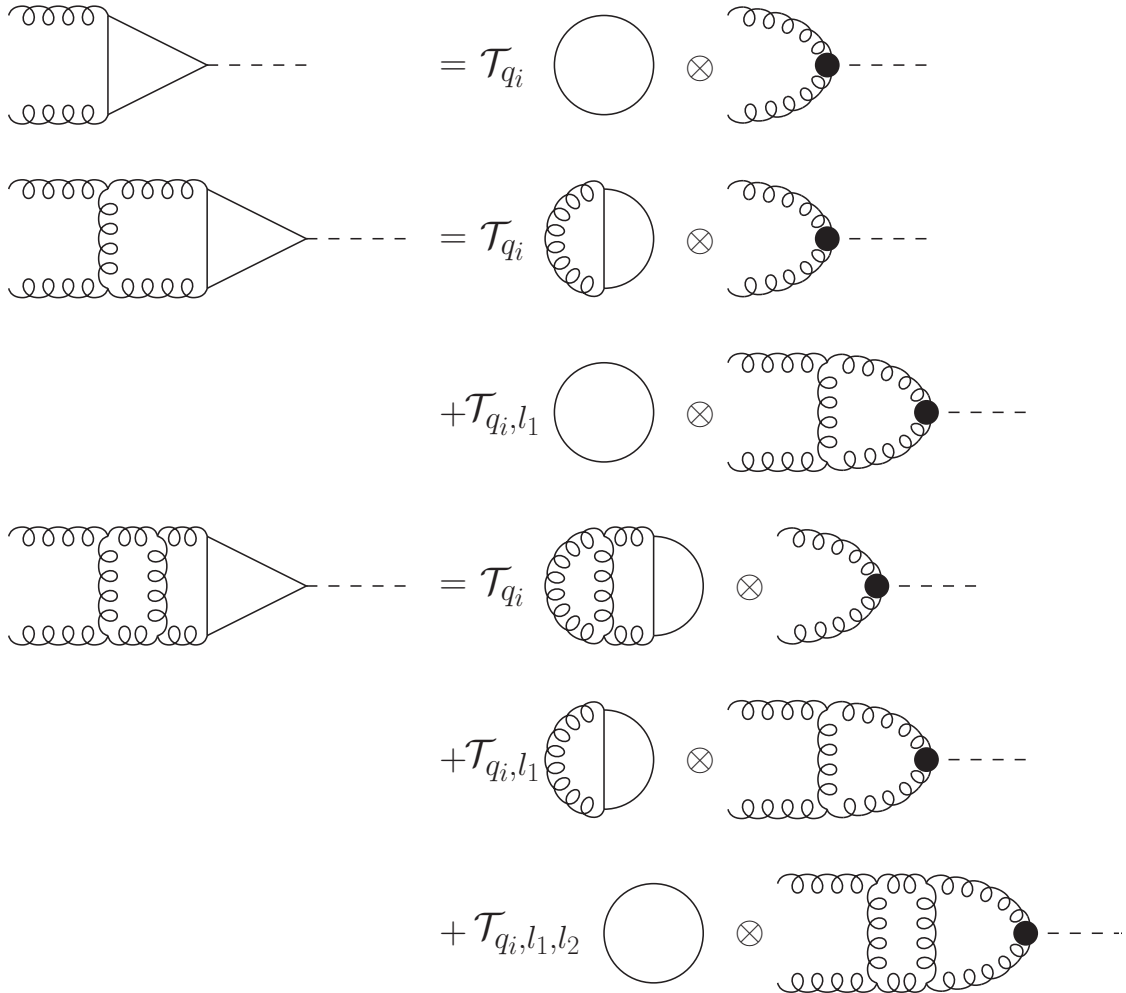


Figure 2.2: Expansion by subgraph of sample diagrams contributing to $\mathcal{A}_{\text{full}}$ through three loops. \mathcal{T} denotes Taylor expansion w.r.t. momenta and the hard subgraphs are re-inserted in the co-subgraphs in the vertex denoted by the black dot. Straight, dashed and curly lines denote top quarks, Higgs bosons and gluons respectively.

the LO Wilson coefficient C_H combined with the one-loop corrections in the effective field theory (EFT). Indeed, these two contributions are equal and thus cancel when comparing \mathcal{A}_{eff} with $\mathcal{A}_{\text{full}}$. To make this cancellation explicit, we renormalize α_s and the top-quark mass in the $\overline{\text{MS}}$ scheme:

$$\alpha_s^0 = \mu^{2\epsilon} Z_{\alpha_s} \left(\alpha_s^{(n_f)}, n_f \right) \alpha_s^{(n_f)}, \quad (2.21)$$

$$M_t^0 = Z_m \left(\alpha_s^{(n_f)}, n_f \right) M_t, \quad (2.22)$$

where the renormalization constant Z_m is known through five loops [57–59]. Similarly at higher orders the various soft contributions are equal to the higher-order corrections in the EFT, when taking the different renormalization constants into account and translating $\alpha_s^{(n_f)}$ to $\alpha_s^{(n_l)}$. As a consequence, no higher-order corrections in the EFT and no soft contributions in the full theory need to be considered for computing C_H . An intuitive, pictorial way of arriving at this conclusion is given by the method of expansion by subgraph: each co-subgraph corresponds to a diagram in the EFT, while each hard subgraph corresponds to contributions to C_H . Since we do not need to consider soft contributions in the full theory we can naively Taylor expand each integrand in the external momenta.

MATCHING BOTH THEORIES By combining Eq. (2.17) with Eq. (2.19) we thus obtain the matching relation

$$Z_{\mathcal{O}_1} \frac{C_H}{v} = Z_3^{\text{OS}} \sum_l \left(\frac{\alpha_s^{(n_f)}}{\pi} \right)^l \left(\frac{\mu^2}{M_t^2} \right)^{l\epsilon} \mathcal{A}_{\text{full},l}^{(l,0)}. \quad (2.23)$$

The integrals appearing in $\mathcal{A}_{\text{full},l}^{(l,0)}$ are single-scale vacuum integrals only depending on M_t , so-called *tadpole* integrals.

2.2.2 Matching for C_{HH}

STRUCTURE Deriving the matching relation for C_{HH} proceeds in a similar way as in the case of C_H . Thus, we only have to take tree-level contributions in the EFT, as well as hard contributions in the full theory into account. However, in contrast to the case of C_H more than one contribution in the EFT has to be taken into account. The first contribution, $\mathcal{A}_{\text{eff},1\text{PI}}$, is one-particle irreducible (1PI) and involves the coupling of two Higgs bosons to gluons and thus the Wilson coefficient C_{HH} . The other two contributions are one-particle reducible (1PR) and either involve a gluon propagator or a Higgs boson propagator. The first of the 1PR contributions, $\mathcal{A}_{\text{eff},1\text{PR},\lambda=0}$, is proportional to C_H^2 , while the second one, $\mathcal{A}_{\text{eff},1\text{PR},\lambda \neq 0}$, involves the trilinear Higgs boson self coupling λ and thus is proportional to $C_H \lambda$. The three different contributions are shown in Fig. 2.3.

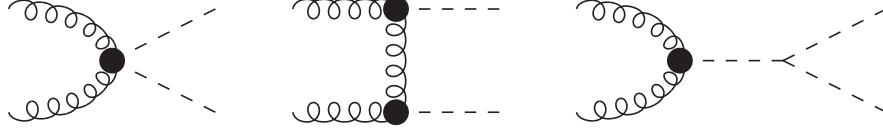


Figure 2.3: The three different contributions to the Higgs boson pair-production amplitude in the EFT. The first one involves the sought-after two-Higgs boson–gluon coupling C_{HH} , while the other two involve C_H .

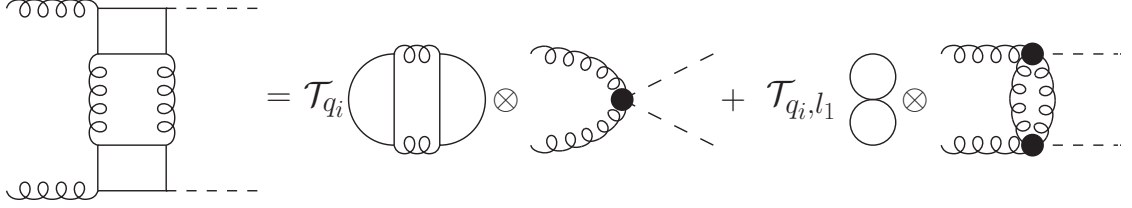


Figure 2.4: Three-loop diagram contributing to, both, C_{HH} and C_H^2 .

CONTRIBUTIONS WITH A TRILINEAR COUPLING Naively one might expect that we only have to compute the hard part of the $\mathbf{1PI}$ amplitude $\mathcal{A}_{\text{full},\mathbf{1PI},l}^{(l,0)}$ in the full theory and can neglect all $\mathbf{1PR}$ contributions. This is only true for diagrams involving the Higgs boson self coupling, since in pure QCD they always match the corresponding EFT diagrams. Thus the required calculation is exactly the same as in the previous section, except for the Higgs propagator and the trilinear coupling, which do not affect the loop integration, leading to

$$Z_{\mathcal{O}_1} \frac{C_H}{v} \frac{\lambda}{s - m_H^2} = Z_3^{\text{OS}} \sum_l \left(\frac{\alpha_s^{(n_f)}}{\pi} \right)^l M_t^{-2l\epsilon} \mathcal{A}_{\text{full},\mathbf{1PR},\lambda \neq 0,l}^{(l,0)}. \quad (2.24)$$

CONTRIBUTIONS WITHOUT A TRILINEAR COUPLING The second $\mathbf{1PR}$ contribution only contributes from two loops, where it exactly matches the EFT diagram proportional to C_H^2 . From three loops, the distinction between $\mathbf{1PI}$ and $\mathbf{1PR}$ contributions is not straightforward, as can be seen from the diagram in Fig. 2.4. The hard part of this diagram clearly contributes to the $\mathbf{1PI}$ contribution in the EFT, while the soft part is captured by a one-loop correction to the $\mathbf{1PR}$ contribution. As a consequence, we need to keep both contributions for the computation of C_{HH} , since otherwise we would be left with UV divergences.

RENORMALIZATION OF AN OPERATOR PRODUCT One further complication, first pointed out in Ref. [60]⁴, arises from the appearance of the product of two operators \mathcal{O}_1 in the **1PR** contribution. Naively, one would renormalize this product by

$$[\mathcal{O}_1 \mathcal{O}_1] = Z_{\mathcal{O}_1}^2 [\mathcal{O}_1^0 \mathcal{O}_1^0] . \quad (2.25)$$

However, in Ref. [60] it was shown, with a similar derivation as for the case of only one operator \mathcal{O}_1 [43], that an additional term, linear in \mathcal{O}_1 has to be taken into account:

$$[\mathcal{O}_1 \mathcal{O}_1] = Z_{\mathcal{O}_1}^2 [\mathcal{O}_1^0 \mathcal{O}_1^0] + Z_{11}^L \mathcal{O}_1^0 . \quad (2.26)$$

The renormalization constant Z_{11}^L can be related to the **QCD** beta function [60]

$$Z_{11}^L = \frac{1}{\epsilon} \left(1 - \frac{\beta_{\alpha_s}}{\epsilon} \right)^{-2} \alpha_s^2 \frac{\partial}{\partial \alpha_s} \left(\frac{\beta_{\alpha_s}}{\alpha_s} \right) \quad (2.27)$$

$$= -\frac{\alpha_s^2}{(4\pi^2)^2} \frac{\beta_1}{\epsilon} + \mathcal{O}(\alpha_s^3) , \quad (2.28)$$

where β_1 is the two-loop contribution to the **QCD** beta function. Thus, starting from four loops in the full theory and $\mathcal{O}(\alpha_s^2 C_H^2)$ in the **EFT**, this non-trivial renormalization contribution has to be taken into account.

MATCHING FORMULA Applying Eq. (2.26) to our computation leads us to the final matching formula for C_{HH} :

$$\begin{aligned} & \left(Z_{\mathcal{O}_1} \frac{C_{HH}}{v} + Z_{11}^L \frac{C_H^2}{v^2} \right) \mathcal{A}_{\text{eff,1PI}} + Z_{\mathcal{O}_1}^2 \frac{C_H^2}{v^2} \mathcal{A}_{\text{eff,1PR},\lambda=0} \\ & = Z_3^{\text{OS}} \sum_l \left(\frac{\alpha_s^{(n_f)}}{\pi} \right)^l M_t^{-2l\epsilon} \left(\mathcal{A}_{\text{full,1PI},l}^{(l,0)} + \mathcal{A}_{\text{full,1PR},\lambda=0,l}^{(l,0)} \right) . \end{aligned} \quad (2.29)$$

As C_H is known to four-loop order, we can insert the corresponding expression and solve for C_{HH} . Let us emphasize again, that the additional contribution due to the renormalization of the operator product only starts to contribute at four loops. As a consequence, the three loop results for C_{HH} computed in Ref. [50] are not affected.

One more comment concerning the evaluation of the relevant amplitudes is in order. While it would be tempting to take one of the external momenta to be equal to 0 to simplify the evaluation, this would lead to additional complications in the matching procedure. With all external momenta on-shell and different from each other, only \mathcal{O}_1 contributes, but for unphysical choices, three additional operators, discussed in Ref. [43], would contribute. As a consequence, they also would affect the renormalization of the

⁴ While the topic studied in Ref. [60] was not directly connected to Higgs boson pair-production, the author noticed that this issue also will arise here.

operator product and an extension of Eq. (2.26) would be required. However, keeping all momenta different from 0 leads to an additional tensor structure, discussed in Sec. A.5. Thus, we need to apply the projector in Eq. (A.20) which correctly projects on the tensor structure of interest. After applying the projector and performing Lorentz and Dirac algebra, as well as the integrations, we can simplify the resulting expressions by expanding around $q_3 \approx 0$, as no divergences in the limit $q_3 \rightarrow 0$ occur. The second tensor structure does not contribute to C_{HH} , since it vanishes in the limit $M_t \rightarrow \infty$.

2.3 CALCULATIONAL SETUP

To evaluate the hard parts of the relevant amplitudes through four loops tens of thousands of Feynman diagrams need to be calculated. Each of these diagrams leads to multiple Feynman integrals and thus hundreds of thousands of integrals need to be computed. This situation calls for an efficient and highly automatized computational setup that can handle diagram generation, algebraic manipulations and the reduction of the number of integrals to a small set. An overview of the general workflow is depicted in Fig. 2.5. In the following we will discuss the general structure of the computation, as well as its key element: the use of superdiagrams.

2.3.1 General setup

GENERATING DIAGRAMS We start by generating all relevant Feynman diagrams with the program QGRAF [61]. In the next step Feynman rules are inserted by q2e and the diagrams are mapped onto underlying graph topologies by exp [62, 63]. Using the FORM [64] package COLOR [65] we compute the colour factors of each diagram, which are then expressed in terms of the quadratic Casimir invariants and symmetric tensors of $SU(N)$. The individual diagrams are then grouped together into so-called *superdiagrams*, which will be discussed in Sec. 2.3.2. One exception is the Green's function involving two Higgs bosons and two gluons. Since multiple independent tadpole integrals appear in each `1PR` diagram, they are not grouped together but computed individually. The `1PI` contributions are treated as for all other Green's functions. The number of diagrams and superdiagrams contributing to the individual Green's functions at the relevant loop orders can be found in Tbl. 2.1. Albeit modifications to suit the task at hand are necessary, most of the steps are also relevant for chapters 3, 6 and 7

COMPUTING DIAGRAMS The superdiagrams are processed using FORM, which projects onto the tensor structure of interest, and performs Lorentz and Dirac algebra. In the next step the external momenta are nullified and all Feynman integrals are rewritten in terms of scalar functions, which only depend on the heavy quark mass. The scalar integrals are then reduced to a set of so-called master integrals (MIs) using integration by parts (IBP) relations [66, 67]. For one- to three-loop tadpole integrals this is performed by

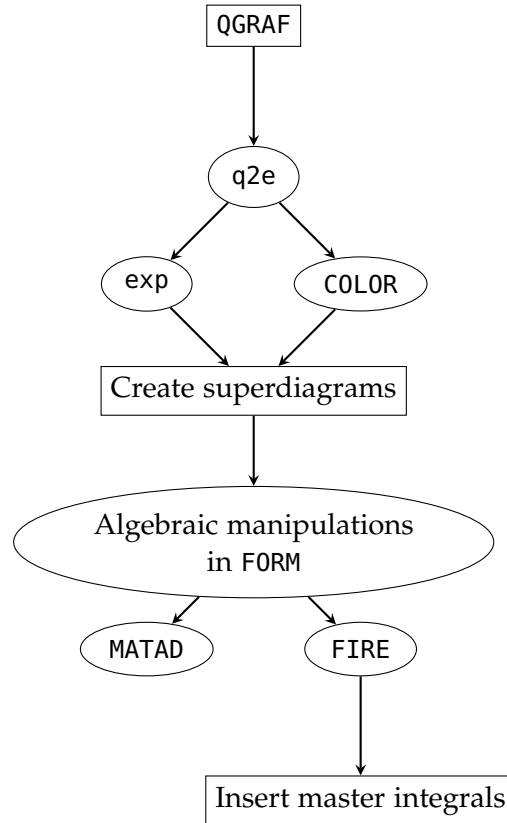


Figure 2.5: General workflow of the computation. Steps in ellipses are performed in parallel for the individual diagrams, superdiagrams or integral topologies.

Green's function	1-loop		2-loop		3-loop		4-loop	
ggh	2	1	23	3	657	23	23251	112
$gghh$ $_{1PI}$	6	1	99	3	3192	23	124149	112
$gghh$ $_{1PR}$	0	-	8	-	216	-	7200	-
$c\bar{c}$	0	0	1	1	25	6	765	27
$q\bar{q}$	0	0	1	1	25	6	765	27
$g\bar{g}$	1	1	7	3	189	23	6245	112
$c\bar{c}g$	0	0	5	1	228	9	10118	74

Table 2.1: Number of Feynman diagrams and superdiagrams contributing to the relevant Green's functions. At each loop order the first column shows the number of regular diagrams and the second one the number of superdiagrams. We also list the number of diagrams contributing to the amplitudes relevant to the computation of decoupling constants, discussed in App. C.

the program MATAD [68], while at four loops the implementation of Laporta's algorithm [69] in the program FIRE [70] is used together with symmetries provided by LiteRed [71, 72]. The final step is the insertion of the four loop master integrals, which are known to sufficiently high order in ϵ [73–76].

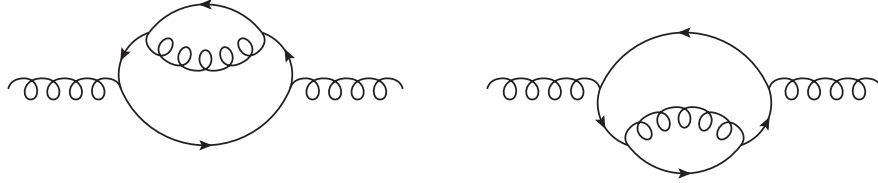
2.3.2 Building superdiagrams

A crucial element in the organization of our computational setup is the use of superdiagrams. They are the sum of individual Feynman diagrams with similar properties, such as colour factors and underlying graph topology.

ADVANTAGES The most obvious advantage of this approach is the case of diagrams cancelling exactly or becoming identical up to a prefactor at some stage during the calculation. In the latter case, all manipulations after this step only take as much computing resources as in the case of a single diagram. Generally, this happens after applying projecting operators and expanding in the external momentum, as demonstrated in the following example.

Example 1 (Superdiagrams)

In the computation of the two gluon amplitude the following two diagrams share the same colour factor and underlying topology:



In Feynman gauge their Dirac structure is given by

$$D_1 \propto \int \frac{d^D l}{(2\pi)^D} \frac{\text{Tr}(\gamma^\mu(m_Q - \not{p}_1)\gamma^\rho(m_Q - \not{p}_2)\gamma_\rho(m_Q - \not{p}_1)\gamma^\nu(m_Q - \not{p}_3))}{(m_Q^2 - p_1^2)^2 (m_Q^2 - p_2^2) (m_Q^2 - p_3^2) p_4^2},$$

$$D_2 \propto \int \frac{d^D l}{(2\pi)^D} \frac{\text{Tr}(\gamma^\mu(m_Q - \not{p}_3)\gamma^\nu(m_Q - \not{p}_1)\gamma^\rho(m_Q - \not{p}_2)\gamma_\rho(m_Q - \not{p}_1))}{(m_Q^2 - p_1^2)^2 (m_Q^2 - p_2^2) (m_Q^2 - p_3^2) p_4^2},$$

where the line momenta are given by

$$p_1 = l_1, \quad p_2 = l_1 - l_2, \quad p_3 = l_1 + q, \quad p_4 = l_2.$$

After applying the projector (A.18) and expanding in the external momentum q , both diagrams simplify to

$$D \propto \int \frac{d^D l}{(2\pi)^D} q^2 \frac{\text{Tr}(\gamma^\mu(m_Q - \not{p}_1)\gamma^\rho(m_Q - \not{p}_2)\gamma_\rho(m_Q - \not{p}_1)\gamma_\mu(m_Q - \not{p}_1))}{(m_Q^2 - p_1^2)^3 (m_Q^2 - p_2^2) p_4^2} \\ + \int \frac{d^D l}{(2\pi)^D} \frac{\text{Tr}(q(m_Q - \not{p}_1)\gamma^\rho(m_Q - \not{p}_2)\gamma_\rho(m_Q - \not{p}_1)q(m_Q - \not{p}_1))}{(m_Q^2 - p_1^2)^3 (m_Q^2 - p_2^2) p_4^2}$$

In the superdiagram approach, this simplification already occurs in a very early stage of the computation. Thus, the computation time is only slightly longer than for computing one of two diagrams alone, leading to a reduction of total computation time by roughly 50%.

While this example is rather simple, analogous cases appear at the three- and four-loop level, where the impact of these simplifications is much larger. Another possible simplification is connected to the gauge parameter ζ . Individual Feynman diagrams might contain higher powers of ζ than the final result, however in the superdiagram approach ζ already cancels in intermediate steps.

There are further advantages of more technical nature to superdiagrams. The most simple one being the reduction of batch scheduling overhead. The number of superdiagrams is several orders of magnitude smaller than the number of diagrams, see e. g. Tbl. 2.1, and thus the batch system has to deal with a few, longer running, jobs instead of many short jobs. This also reduces network usage, since fewer input expressions are read and less result files are written.

Furthermore, FORM is optimized to manipulate a large number of terms with each instruction and capable of efficiently using multiple cores on a computing node. Hence, applying the same manipulation to all diagrams in a superdiagram at once is more efficient on a multi-core machine than subsequently processing batches of diagrams in parallel on the same machine. In the task at hand and other calculations such as the four-loop beta functions in the full SM [36], computing a single diagram typically only requires a few Megabytes of memory. Thus most of the memory of a computing node is unused, if diagrams are processed by single core jobs in parallel. Superdiagrams on the other hand, allow to make use of the available memory and thus make far better use of available computing resources.

Generally, the advantages of superdiagrams are more pronounced at higher loop orders. While for the computation of the $1PI$ $ggHH$ amplitude at three loops 3192 diagrams get grouped into 23 superdiagrams, at four loops 124149 diagrams get grouped into 112 superdiagrams. Thus, while the number of diagrams grows by a factor of 39, the number of superdiagrams only grows by a factor of five when going from three to four loops in this case. The picture is similar for all other Green's functions considered in this chapter.

CAVEATS However, there is one drawback to this approach. In situations with a large number of diagrams, such as the amplitude involving two gluons and two Higgs bosons, individual superdiagrams might contain too many terms to fit into the memory of one machine. Thus they have to be split up and the cancellation at intermediate stages is partially lost. In our current setup a maximum number of diagrams contributing to a superdiagram can be specified and if this limit is reached, all further diagrams will be added up in an additional superdiagram.

As simplifications and cancellations generally do not occur between all diagrams with the same underlying topology and colour factor, but subsets thereof, a possible solution to this problem would be to group diagrams not only by topology and colour factor, but also by the number of fermion, ghost or gluon propagators.

2.4 C_{HH} TO $\mathcal{O}(\alpha_s^4)$

We are now in the position to present our result for the four-loop Wilson coefficient C_{HH} . The results for C_H , as well as the decoupling constants through four loops can be found in App. C.

Some comments regarding the correctness of our results are in order. Our result is free of the gauge parameter ζ in the sum of $\mathbf{1PI}$ and $\mathbf{1PR}$ contributions. In addition, taking into account the nontrivial renormalization of the product of two insertions of \mathcal{O}_1 , as discussed in Eq. (2.26), leads to a finite result.

Furthermore, we computed the $\mathbf{1PR}$ contributions in two different ways yielding the same result: by directly evaluating all contributing diagrams, as well as by constructing them out of the Higgs boson-two-gluon-vertex with an off-shell gluon [77]. Finally, we find agreement with the known three-loop result [50].

Our result for C_{HH} can be cast into the form

$$C_{HH} = -\frac{2}{3}T_F \sum_i C_{HH}^{(i)} \left(\frac{\alpha_s^{(n_i)}}{\pi} \right)^i \quad (2.30)$$

where

$$C_{HH}^{(1)} = 1, \quad (2.31)$$

$$C_{HH}^{(2)} = \frac{5}{4}C_A - \frac{3}{4}C_F, \quad (2.32)$$

$$C_{HH}^{(3)} = \frac{1567}{576}C_A^2 - \frac{83}{24}C_A C_F + \frac{27}{32}C_F^2 + n_l T_F \left[-\frac{47}{144}C_A + \frac{11}{16}C_F \right] \\ + \left[-\frac{11}{16}C_A^2 + \frac{7}{16}C_A C_F + \frac{1}{2}n_l T_F C_F \right] \ln \left(\frac{\mu^2}{M_t^2} \right), \quad (2.33)$$

$$C_{HH}^{(4)} = \left(\frac{253537}{41472} - \frac{1567}{3072}\zeta_3 \right) C_A^3 + \left(-\frac{161687}{6912} + \frac{5105}{512}\zeta_3 \right) C_A^2 C_F$$

$$\begin{aligned}
& + \left(-\frac{4615}{1152} + \frac{1}{384}\zeta_3 \right) C_A^2 T_F + \left(\frac{4943}{384} - \frac{407}{128}\zeta_3 \right) C_A C_F^2 \\
& + \left(\frac{10969}{1728} - \frac{115}{64}\zeta_3 \right) C_A C_F T_F + \left(\frac{31}{216} - \frac{7}{64}\zeta_3 \right) C_A T_F^2 - \frac{471}{128} C_F^3 \\
& + \left(-\frac{23}{12} + \frac{13}{32}\zeta_3 \right) C_F^2 T_F + \left(\frac{161}{432} - \frac{7}{32}\zeta_3 \right) C_F T_F^2 + \left(-\frac{2}{3} + \frac{13}{2}\zeta_3 \right) \frac{d_A^{abcd} d_F^{abcd}}{N_A T_F} \\
& + \left(\frac{11}{12} - 2\zeta_3 \right) \frac{d_F^{abcd} d_F^{abcd}}{N_A T_F} + n_l T_F \left[\left(-\frac{16381}{10368} - \frac{51}{256}\zeta_3 \right) C_A^2 \right. \\
& + \left(\frac{17525}{2592} - \frac{1145}{384}\zeta_3 \right) C_A C_F + \left(\frac{29}{54} - \frac{7}{64}\zeta_3 \right) C_A T_F + \left(-\frac{577}{288} + \frac{127}{96}\zeta_3 \right) C_F^2 \\
& + \left. \left(\frac{47}{144} - \frac{7}{32}\zeta_3 \right) C_F T_F + \left(\frac{11}{6} - 4\zeta_3 \right) \frac{d_F^{abcd} d_F^{abcd}}{N_A T_F^2} \right] + n_t^2 T_F^2 \left[\frac{19}{2592} C_A - \frac{533}{1296} C_F \right] \\
& + \left[\frac{3841}{1152} C_A^3 - \frac{913}{144} C_A^2 C_F - \frac{391}{576} C_A^2 T_F + \frac{99}{64} C_A C_F^2 + \frac{55}{72} C_A C_F T_F + n_l T_F \left(-\frac{223}{288} C_A^2 \right. \right. \\
& + \left. \left. \frac{77}{18} C_A C_F + \frac{5}{144} C_A T_F - \frac{5}{8} C_F^2 - \frac{11}{18} C_F T_F \right) + n_t^2 T_F^2 \left(\frac{5}{144} C_A - \frac{11}{18} C_F \right) \right] \ln \left(\frac{\mu^2}{M_t^2} \right) \\
& + \left[\frac{77}{192} C_A^3 - \frac{121}{192} C_A^2 C_F + n_l T_F \left(-\frac{7}{48} C_A^2 + \frac{11}{6} C_A C_F \right) - \frac{1}{6} n_t^2 C_F T_F^2 \right] \ln^2 \left(\frac{\mu^2}{M_t^2} \right).
\end{aligned} \tag{2.34}$$

Here, M_t is the $\overline{\text{OS}}$ renormalized top-quark mass and

$$\zeta_n = \sum_{i=1}^{\infty} \frac{1}{i^n} \tag{2.35}$$

is the Riemann Zeta function. The numerical values for the $SU(N)$ colour factors are given in Sec. A.4. Expressions for C_{HH} in terms of the $\overline{\text{MS}}$ renormalized top-quark mass or $\alpha_s^{(n_f)}$ are given in Ref. [33].

The result presented in Eq. (2.34) is in agreement with the prediction of the low-energy theorem given in Eq. (2.13), thus confirming this relation through four loops. Under the assumption that Eq. (2.13) also holds for higher orders, $C_{HH}^{(5)}$ can be constructed with the help of the five-loop QCD beta function and mass anomalous dimension. As the proper renormalization of operator products in the matching procedure has been taken care of, we do not expect that further modifications to the Eq. (2.29) are necessary and, as a consequence, that Eq. (2.13) is indeed valid also for higher orders. The five-loop expressions can be found in the ancillary files of [33].

TOP-QUARK-MASS EFFECTS IN THE HIGGS BOSON-GLUON FORM FACTOR AT FOUR LOOPS

Virtual corrections to the Higgs boson–gluon form factor are an important building block for predictions of the Higgs boson production cross-section in gluon fusion. In contrast to the previous chapter, we are interested in contributions beyond the infinitely heavy top quark approximation. While exact analytic results for the form factor are available through two loops [78–80], at three loops contributions with a closed light quark loop [81], as well as the leading-colour contributions [82] became available analytically only recently. To this end, two approaches to address the top-quark-mass dependence at three loops are studied in the literature. First, a LME of the form factor [83, 84] was performed, providing an analytic approximation in the phenomenologically interesting kinematic regime for the production of a single Higgs boson. Furthermore, these results were combined with a LME of the real radiation contribution [85–87]. The second approach is based on numerical techniques, which allow one to describe the full mass dependence. One numerical approach studied in the literature combines the results of the aforementioned LME, including terms through $\mathcal{O}(1/M_t^{14})$ [88] with an expansion of the form factor around the top-quark threshold using Padé approximants [89]. The second approach performs an IBP reduction of the form factor, evaluating all MIs numerically [90]. At four loops however, only the infinitely heavy top quark approximation exists.

In this chapter we will, based on [34], provide the first ingredient for calculations of the Higgs boson production cross-section in gluon fusion at N₃LO beyond the infinitely heavy top quark limit: the four-loop virtual corrections to the Higgs boson–gluon form factor.

STRUCTURE OF THE CHAPTER In Sec. 3.1 we introduce the technical setup of the calculation, followed by the discussion of the expected IR pole structure of the form factor in Sec. 3.2. We present analytic results and discuss the numerical impact of higher-order terms in the LME in Sec. 3.3.

3.1 LARGE MASS EXPANSION OF THE HIGGS BOSON-GLUON FORM FACTOR

The computation of the Higgs boson–gluon form factor follows similar steps as the computation of C_H , described in Sec. 2.2.1. However, we are now also interested in soft contributions and terms suppressed by $1/M_t$. To this end, we can not naively Taylor expand all integrands, but have to perform a full LME of the amplitude. In the following,

we will describe the computation while focusing on the differences w.r.t. Sec. 2.2.1. Furthermore, we will assemble the leading order term in the top-quark-mass expansion in the EFT where the top quark has been integrated out.

3.1.1 Structure of the computation

GENERATING DIAGRAMS We generate all contributing diagrams and process them as described in Sec. 2.3 with the difference that exp performs an asymptotic expansion in the top-quark mass instead of a naive Taylor expansion. As a consequence, we obtain one or more subdiagrams for each original diagram, including the information about the scaling of the loop momenta. Examples of the diagrammatic LME through three loops are shown in Fig. 2.2 and four-loop examples are shown in Fig. 3.1.

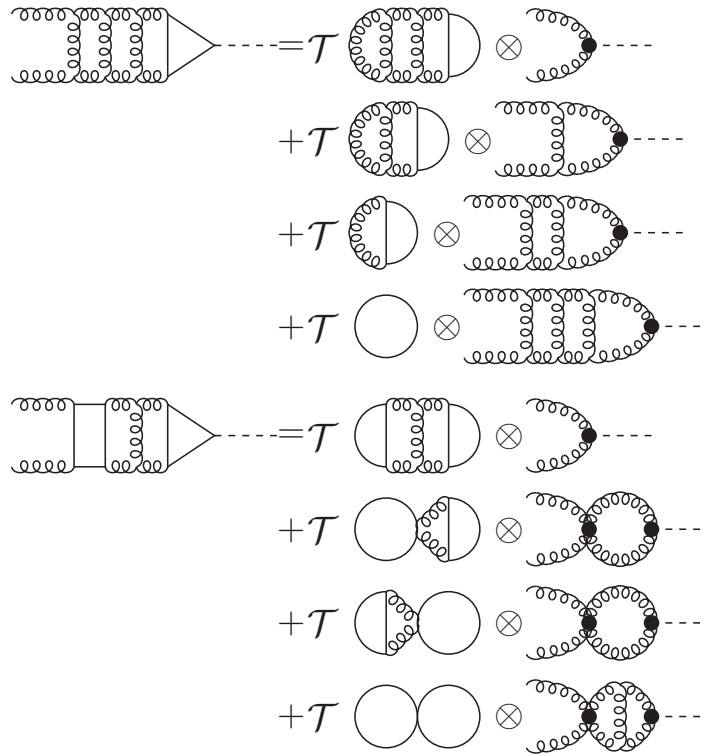


Figure 3.1: Expansion by subgraph of sample diagrams contributing to the form factor at four loops. \mathcal{T} denotes a Taylor expansion in the momenta and the hard subgraphs are re-inserted into the co-subgraphs in the vertices, denoted by the black dots. Straight, dashed and curly lines denote top quarks, Higgs bosons and gluons, respectively.

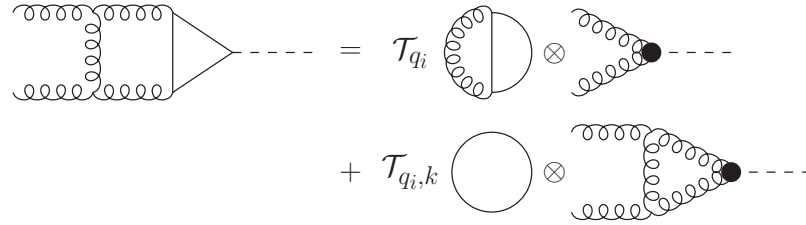
DIFFERENCES W.R.T. THE PREVIOUS CHAPTER In contrast to the computation of the Wilson coefficients, we can not simply build superdiagrams, since diagrams with

the same colour factor might lead to different subdiagrams with different momentum assignments. We would need to construct the superdiagrams out of the subdiagrams instead, which is more complex since a subdiagram might involve up to four different loop integrals. While technically possible, we proceed without creating superdiagrams. Computing each subdiagram individually was sufficiently fast in this case. Each subdiagram is processed by FORM. The main differences w.r.t. the computation of the Wilson coefficients are the deeper expansion depth in terms of M_t , increasing the number of terms in each diagram, and the massless three-point integrals appearing.

TENSOR REDUCTION As a consequence of the expansion tensor integrals need to be evaluated¹, as shown in the following example.

Example 2 (LME leading to tensor integrals)

Let us consider the following two-loop diagram, where also the soft region contributes in the LME:



After projecting onto the scalar form factor and performing the numerator algebra, we are left with scalar integrals $I(\rho)$ where $\rho = s/M_t^2$. As shown in the figure above, the LME splits these integrals into two-loop tadpole integrals and the product of one-loop tadpole and massless three-point integrals:

$$I(\rho) \rightarrow \sum_j \rho^j \int_{k,l} \frac{P_j(q_i \cdot k, q_i \cdot l)}{(k^2)^{a_j} ((k-l)^2 - M_t^2)^{b_j} (l^2 - M_t^2)^{c_j}} + \sum_j \rho^j \int_k \frac{1}{(k^2)^{a_j} ((k+q_1)^2)^{b_j} ((k-q_2)^2)^{b_j}} \int_l \frac{Q_j(q_i \cdot l, k \cdot l)}{(l^2 - M_t^2)^{d_j}}.$$

Here, the indices a_j to d_j are, possibly negative, integers which depend on the expansion depth. The numerator polynomials P_j and Q_j generally depend on scalar products between the loop momenta and momenta which do not arise in propagators of the respective integrals. As a consequence, for the two-loop tadpole integral in the first line, we need to perform a tensor reduction. For the integrals in the second line, we could either perform the tensor reduction for the one-loop three-point function or for the one-loop tadpole.

¹ This is already the case in the computations of chapter 2. However, the efficient treatment of tensor integrals is more relevant when considering higher order terms in the LME.

Since, in general, tensor integrals are rather cumbersome to evaluate, we perform a so-called *tensor reduction* of the integrand. The method is based on the fact that the result of the loop integration can only be a function of the external momenta present in the denominators and numerators, as well as two Lorentz covariant tensors: the metric $g_{\mu\nu}$ as well as the totally antisymmetric tensor $\epsilon_{\mu\nu\rho\sigma}$. Since QCD is parity invariant, the latter can not occur.

In the case at hand, it is advantageous to perform the tensor reduction for the tadpole integrals for two reasons. Firstly, since no external momenta are present in their denominators, the tensor structure can only be composed out of metric tensors and thus only tensors with even rank contribute. Secondly, since the tensor reduction needs to be performed for the tadpole integrals in the fully hard subgraph anyway, the routines can simply be used for all other subgraphs too.

TENSOR REDUCTION FOR TADPOLE INTEGRALS At one-loop order, a closed formula for tensor-tadpole integrals with arbitrary rank is known [56]. For two-loop tadpole integrals an algorithm for arbitrary tensor rank is known [91] and implemented in MATAD [68]. At the three- and four-loop order, we derive relations reducing tensors through rank eight using the program of [92]. This program derives relations by constructing projectors onto the different tensor structures at each rank, which are then used to decompose generic tensors. An explicit example for rank two and rank four tensors is given below.

Example 3 (*Tensor reduction*)

As a warm up exercise, consider a rank two tensor tadpole integral $I^{\mu\nu}$, which can be written as

$$I^{\mu\nu} = I g^{\mu\nu} .$$

To relate $I^{\mu\nu}$ to I we contract both sides of the equation with the metric tensor, obtaining

$$g_{\mu\nu} I^{\mu\nu} = dI .$$

Thus, to obtain I we have to apply the projector $P_{\mu\nu} = g_{\mu\nu}/D$ to the integrand.

Now, consider the rank four tensor tadpole integral $I^{\mu\nu\rho\sigma}$. This integral can be decomposed into three terms

$$I^{\mu\nu\rho\sigma} = I_1 T^{\mu\nu\rho\sigma} + I_2 T^{\mu\rho\nu\sigma} + I_3 T^{\mu\sigma\nu\rho} ,$$

where $T^{\alpha\beta\gamma\delta} = g^{\alpha\beta} g^{\gamma\delta}$. To relate the I_i to the original tensor integral, we contract both sides of the equations with the three different versions of T :

$$T_{\mu\nu\rho\sigma} I^{\mu\nu\rho\sigma} = D^2 I_1 + D (I_2 + I_3) ,$$

$$T_{\mu\rho\nu\sigma} I^{\mu\nu\rho\sigma} = D^2 I_2 + D (I_1 + I_3) ,$$

$$T_{\mu\sigma\nu\rho} I^{\mu\nu\rho\sigma} = D^2 I_3 + D (I_1 + I_2) .$$

This linear system of equations can be solved leading to the three projection operators

$$\begin{aligned}
 P_{1,\mu\nu\rho\sigma} &= \frac{1}{D(D-1)(D+2)} \left((D+1)T_{\mu\nu\rho\sigma} - T_{\mu\rho\nu\sigma} - T_{\mu\sigma\nu\rho} \right) , \\
 P_{2,\mu\nu\rho\sigma} &= \frac{1}{D(D-1)(D+2)} \left(-T_{\mu\nu\rho\sigma} + (D+1)T_{\mu\rho\nu\sigma} - T_{\mu\sigma\nu\rho} \right) , \\
 P_{3,\mu\nu\rho\sigma} &= \frac{1}{D(D-1)(D+2)} \left(-T_{\mu\nu\rho\sigma} - T_{\mu\rho\nu\sigma} + (D+1)T_{\mu\sigma\nu\rho} \right) ,
 \end{aligned}$$

with $P_{i,\mu\nu\rho\sigma}I^{\mu\nu\rho\sigma} = I_i$.

SCALAR INTEGRALS After the tensor reduction, we are left with scalar tadpole integrals up to four loops and massless three point integrals up to three loops. While some diagrams, for example the second diagram in Fig. 3.1, also yield massless two-point integrals, they can be simply treated as three-point integrals, with one denominator power equal to zero.

APPLICATION OF IBP TABLES Due to the deeper expansion in $1/M_t$, each diagram yields more tadpole integrals, as well as tadpole integrals with higher denominator powers, compared to the calculation of C_H and C_{HH} . As a consequence, each diagram requires a significant amount of storage space, posing a non-negligible challenge². To reduce the required disk space, as well as the algebraic complexity arising when summing up all diagrams and inserting the **IBP** reduction tables, we do not perform the **LME** up to $\mathcal{O}(1/M_t^4)$ directly. Instead, we compute the $\mathcal{O}(M_t^0)$ contribution first and perform the reduction of the required integrals. We then compute the expansion through $\mathcal{O}(1/M_t^2)$ but already apply the **IBP** tables which we generated for the $\mathcal{O}(M_t^0)$ contribution at the level of each subdiagram. Thus, each subdiagram is already smaller than it would have been, had we not have inserted the already existing tables. In the next step, we perform the reduction for the missing integrals only and add them to our tables. The same procedure is repeated at $\mathcal{O}(1/M_t^4)$. In total more than 40 million three- and four-loop tadpole integrals are reduced.

BOOKKEEPING OF INTEGRALS To perform the **IBP** reduction without re-reducing already known integrals, we implement a simple but powerful bookkeeping system, depicted in Fig. 3.2. In a first step, the list of required integrals is compared with the list of already reduced integrals to determine which integrals are actually unknown. The next step is the reduction of the unknown integrals using **FIRE**, followed by converting the output of **FIRE** to fill statements for **FORM** tablebases. Next, the new integrals are appended to the list of known integrals and the fill statements are added to a file

² Even after applying the optimization described here, all diagrams together require more than one Terabyte of storage space.

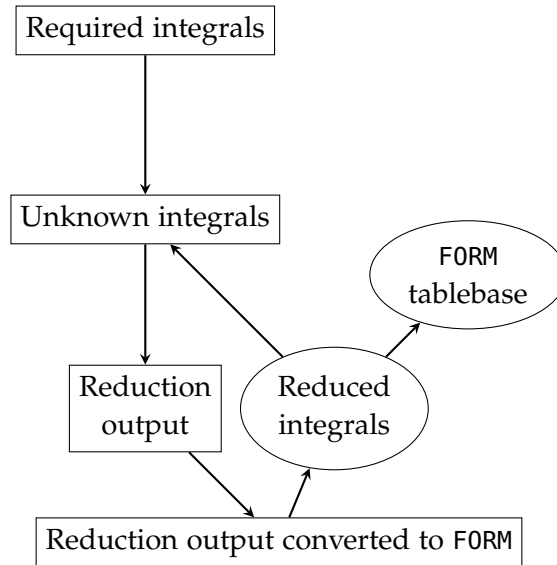


Figure 3.2: Bookkeeping system for tadpole reduction. Only the list of known integrals and their reduction tables are stored in the end.

containing all of them. The final step is building a FORM tablebase from the generated fill statements. Bookkeeping is done for each three- and four-loop tadpole integral family independently, allowing us to speed up the computation by processing all families in parallel. The largest table generated for the computation at $\mathcal{O}(1/M_t^4)$ contains more than eleven million entries. During its generation a previously unknown bug in FORM was uncovered and subsequently fixed. All MIs are known at sufficiently high orders in ϵ [73–76].

MASSLESS THREE-POINT FUNCTIONS The massless three-point functions through three loops are also reduced to MIs with FIRE. In total, three million three-loop three-point integrals appear through $\mathcal{O}(1/M_t^4)$ with, in contrast to the tadpole integrals, lower denominator powers, but higher numerator powers. All master integrals are known, to sufficiently high order in the ϵ -expansion [93–97].

3.2 THE INFRARED STRUCTURE OF THE HIGGS BOSON-GLUON FORM FACTOR

The resulting expression for the form factor $\mathcal{A}(s, M_t^2)$ still contains UV, as well as IR singularities. We can remove the UV singularities by renormalizing the strong coupling constant using Eq. (2.21), the top-quark mass using Eq. (2.22), as well as the external gluon fields by multiplying the form factor with Z_3^{OS} . Note that, Z_3^{OS} also contains finite terms and we thus need higher-order terms in its ϵ expansion. These terms have been

computed in the course of the computations described in chapter 2 and we provide them in Sec. C.3.

In the following we investigate the IR pole structure of the form factor. To this end we discuss the expectation for the form of the IR poles in Sec. 3.2.1. Next, in Sec. 3.2.2 we compare the expectation to our explicit calculation.

3.2.1 Expected infrared pole structure

In Quantum Electrodynamics (QED) the infrared pole structure is determined by the emission of soft photons and can be obtained at higher-orders by exponentiating the LO contribution [98]. For amplitudes in QCD the situation is more complicated, as also collinear singularities appear and soft gluon emissions receive higher-order loop corrections [99, 100]. Still, in Refs. [101, 102] an all-order formula describing the IR singularities of amplitudes in QCD was conjectured. In the following we briefly discuss this conjecture and apply it to the Higgs boson–gluon form factor.

GENERAL STRUCTURE OF THE IR DIVERGENCES In Refs.[101, 102] the IR singularities of an n -parton amplitude in QCD were related to the anomalous dimension matrix of n -jet operators in soft-collinear effective theory and thus related to their UV singularities. Following [101, 102] we introduce a renormalization constant, which we call Z_{IR} , subtracting all IR poles from an amplitude \mathcal{M} :

$$\widetilde{\mathcal{M}} = Z_{\text{IR}}^{-1} \mathcal{M} . \quad (3.1)$$

Here $\widetilde{\mathcal{M}}$ is finite in the limit $\epsilon \rightarrow 0$.

The key conjecture of [101, 102] is that the anomalous dimension Γ , related to Z_{IR} by

$$\Gamma(\{p\}, \mu) = -Z_{\text{IR}}^{-1}(\epsilon, \{p\}, \mu) \frac{d}{d\mu} Z_{\text{IR}}(\epsilon, \{p\}, \mu) , \quad (3.2)$$

is given by

$$\Gamma(\{p\}, \mu) = \sum_{(i,j)} \frac{\mathbb{T}_i \cdot \mathbb{T}_j}{2} \gamma^{\text{cusp}} \ln \frac{\mu^2}{-s_{ij}} + \sum_i^n \gamma^i . \quad (3.3)$$

Here $\{p\}$ denotes the set of all parton momenta with $s_{ij} = 2\sigma_{ij}p_i p_j + i0$ and $\sigma_{ij} = 1$ for both momenta in- or outgoing and -1 for one ingoing and one outgoing momentum. The (i, j) are all distinct pairs of partons, \mathbb{T}_i is the $SU(N)$ colour generator for the respective parton i , γ^{cusp} is the cusp soft anomalous dimension and γ^i is the collinear anomalous dimension of parton i . In Refs. [101, 102] it is conjectured that Eq. (3.3) holds to all loop orders and any number of external partons. For the case of two partons at three loops Eq. (3.3) is proven to be valid.

Specifying Eq. (3.3) to the case of the Higgs boson-gluon form factor yields

$$\Gamma^{ggH}(p_1, p_2, \mu) = -C_A \gamma^{\text{cusp}} \ln \frac{\mu^2}{-s} + 2\gamma^g. \quad (3.4)$$

The relation between Γ and Z_{IR} in Eq. (3.2) can be inverted, resulting in

$$Z_{\text{IR}} = \exp \left[- \int_0^{\alpha_s} \frac{d\alpha}{\beta(\alpha, \epsilon)} \left(\Gamma(\alpha) + \frac{\partial \Gamma(\alpha)}{\partial \ln \mu} \int_{\alpha_s}^{\alpha} \frac{d\alpha'}{\beta(\alpha', \epsilon)} \right) \right], \quad (3.5)$$

thus exponentiating all IR singularities. Note, that $\beta_{\alpha_s}(\alpha_s, \epsilon) = \beta(\alpha_s) - 2\epsilon\alpha_s$ where $\beta(\alpha_s)$ denotes the regular four-dimensional QCD beta function.

EXPLICIT FORM OF THE INFRARED COUNTERTERM The expression for Z_{IR} for the Higgs boson-gluon form factor in the infinitely heavy top quark limit is explicitly given in Ref. [95]. Taking the logarithm we obtain

$$\begin{aligned} \log Z_{\text{IR}} = & \left(\frac{\alpha_s^{(n_l)}}{4\pi} \right) \left[- \frac{C_A \gamma_0^{\text{cusp}}}{2\epsilon^2} + \frac{\gamma_0^g}{\epsilon} \right] \\ & + \left(\frac{\alpha_s^{(n_l)}}{4\pi} \right)^2 \left[\frac{3C_A \beta_0 \gamma_0^{\text{cusp}}}{8\epsilon^3} - \frac{1}{2\epsilon^2} \left(\beta_0 \gamma_0^g + \frac{C_A \gamma_1^{\text{cusp}}}{4} \right) + \frac{\gamma_1^g}{2\epsilon} \right] \\ & + \left(\frac{\alpha_s^{(n_l)}}{4\pi} \right)^3 \left[- \frac{11C_A \beta_0^2 \gamma_0^{\text{cusp}}}{36\epsilon^4} + \frac{1}{3\epsilon^3} \left(\frac{5C_A \beta_0 \gamma_1^{\text{cusp}}}{12} + \beta_0^2 \gamma_0^g + \frac{2C_A \beta_1 \gamma_0^{\text{cusp}}}{3} \right) \right. \\ & \left. - \frac{1}{3\epsilon^2} \left(\beta_0 \gamma_1^g + \frac{C_A \gamma_2^{\text{cusp}}}{6} + \beta_1 \gamma_0^g \right) + \frac{\gamma_2^g}{3\epsilon} \right]. \end{aligned} \quad (3.6)$$

Here β_l , γ_l^{cusp} , γ_l^g are the $(l-1)$ -loop terms of the QCD beta function, the cusp soft anomalous dimension and the gluon collinear anomalous dimension, respectively. Both anomalous dimensions are known up to three loops [102, 103]. They are given by

$$\begin{aligned} \gamma_0^{\text{cusp}} &= 4, \\ \gamma_1^{\text{cusp}} &= C_A \left(\frac{268}{9} - \frac{4}{3}\pi^2 \right) - \frac{40}{9}n_l, \\ \gamma_2^{\text{cusp}} &= C_A^2 \left(\frac{490}{3} - \frac{536}{27}\pi^2 + \frac{44}{45}\pi^4 + \frac{88}{3}\zeta_3 \right) + C_A n_l \left(-\frac{836}{27} + \frac{80}{27}\pi^2 - \frac{112}{3}\zeta_3 \right) \\ & \quad + C_F n_l \left(-\frac{110}{3} + 32\zeta_3 \right) - \frac{16}{27}n_l^2 \end{aligned} \quad (3.7)$$

and

$$\gamma_0^g = -\frac{11}{3}C_A + \frac{2}{3}n_l,$$

$$\begin{aligned}
\gamma_1^g &= C_A^2 \left(-\frac{692}{27} + \frac{11}{18}\pi^2 + 2\zeta_3 \right) + C_A n_l \left(\frac{128}{27} - \frac{1}{9}\pi^2 \right) + 2C_F n_l, \\
\gamma_2^g &= C_A^3 \left(-\frac{97186}{729} + \frac{6109}{486}\pi^2 - \frac{319}{270}\pi^4 + \frac{122}{3}\zeta_3 - \frac{20}{9}\pi^2\zeta_3 - 16\zeta_5 \right) \\
&\quad + C_A^2 n_l \left(\frac{30715}{1458} - \frac{599}{243}\pi^2 + \frac{41}{135}\pi^4 + \frac{356}{27}\zeta_3 \right) + C_A C_F n_l \left(\frac{1217}{27} - \frac{1}{3}\pi^2 - \frac{4}{45}\pi^4 - \frac{152}{9}\zeta_3 \right) \\
&\quad - C_F^2 n_l + C_A n_l^2 \left(-\frac{269}{1458} + \frac{10}{81}\pi^2 - \frac{56}{27}\zeta_3 \right) - \frac{11}{9}C_F n_l^2. \tag{3.8}
\end{aligned}$$

While the highest pole of the l -loop contribution to $\log Z_{\text{IR}}$ is of $\mathcal{O}(\epsilon^{-l-1})$ the highest pole of Z_{IR} is of $\mathcal{O}(\epsilon^{-2l})$.

3.2.2 Comparison with the explicit calculation

In the following we normalize the form factor to 1 at leading order in α_s

$$F = \frac{\mathcal{A}(s, M_t^2)}{\mathcal{A}^{(1)}(s, M_t^2)} \approx 1 + \mathcal{O}(\alpha_s), \tag{3.9}$$

where $\mathcal{A}^{(1)}(s, M_t^2)$ is the one-loop contribution to the Higgs boson–gluon form factor. Note that we also expand $\mathcal{A}^{(1)}(s, M_t^2)$ in $1/M_t$. In the following F plays the role of \mathcal{M} in Sec. 3.2.

Taking the limit $M_t \rightarrow \infty$ we observe that, as expected, the two-, three- and four-loop contributions of F start at $\mathcal{O}(\epsilon^{-2})$, $\mathcal{O}(\epsilon^{-4})$ and $\mathcal{O}(\epsilon^{-6})$, respectively. This is in agreement with the expectation in Sec. 3.2, as in the infinitely heavy mass limit all top-quark contributions are encapsulated in C_H , and we thus deal with one-, two- and three-loop effective diagrams. When taking the logarithm of F we find that the IR poles are indeed given by Eq. (3.6).

The higher-order contributions in the LME of F at two-, three- and four-loop order start at $\mathcal{O}(\epsilon^0)$, $\mathcal{O}(\epsilon^{-2})$ and $\mathcal{O}(\epsilon^{-4})$, respectively. As the discussion in Refs. [101, 102] does only rely on the external particles present, these poles should be products of lower order terms of F and Z_{IR} in Eq. (3.1) and thus should not be present in $\log F$. Taking the logarithm indeed shows that the poles of $\log F$ are free from higher-order terms in the LME and, as a consequence, in agreement with the conjecture of [101, 102].

3.3 RESULTS

Having discussed the calculational details and the infrared pole structure of the result, we are now in the position to present analytic results for the top-quark–mass suppressed terms of the Higgs boson–gluon form factor. Our result passes several checks. Through three loops we agree with the results available in the literature [83, 84, 88]. Furthermore,

we project on the two terms in Eq. (2.16) individually and find full agreement between both results.

COMPARISON TO THE EFFECTIVE FIELD THEORY RESULT As discussed in Sec. 2.2.1 the form factor is given by Eq. (2.17) in the EFT. In contrast to Sec. 2.2.1 however, we are now interested in all contributions to $\mathcal{A}_{\text{eff}}(s, M_t^2)$ and thus we also need the higher-order contributions $\mathcal{A}_{\text{eff},l}$ in the EFT through three loops. We can extract the contributions in the EFT in terms of $\alpha_s^{(n_l)}$ from [93, 95]. Here, the renormalization of \mathcal{O}_1 is already included and thus we only need to combine the results with the Wilson coefficient C_H through four loops. Note that, as in the case of Z_3^{OS} , we need to include higher-order ϵ terms in C_H . They can be found in Sec. C.1.

By replacing $\alpha_s^{(n_f)} = \zeta_{\alpha_s}^{-1} \alpha_s^{(n_l)}$ in the leading term in the LME we find agreement with the EFT result. When expressed in terms of $\alpha_s^{(n_l)}$, the dependence on the top-quark mass is fully determined by logarithms of the renormalization scale over the top-quark mass stemming from C_H .

In the following we present the analytic result for the finite part of $\log F$ in Sec. 3.3.1 and discuss the numerical impact of top-quark-mass corrections in Sec. 3.3.2.

3.3.1 Analytic results

In the following we write

$$\log F = \log F|_{\text{poles}} + \log F|_{\text{finite}}, \quad (3.10)$$

where $\log F|_{\text{poles}} = -\log Z_{\text{IR}}$ as given in Eq. (3.6). We provide the result for $\log F|_{\text{finite}}$ with the top-quark mass renormalized in the OS scheme, $N_c = 3$ and $\mu = M_t$. Note that in order to convert from the $\overline{\text{MS}}$ renormalized mass to the OS renormalized mass, higher-order ϵ terms in the conversion relation are needed, which we take from Ref. [104]. The finite part of $\log F$ is given by

$$\begin{aligned} \log F|_{\text{finite}} = & \left(\frac{\alpha_s^{(n_l)}}{\pi} \right) \left[\frac{11}{4} + \frac{3}{4} \zeta_2 - \frac{3}{4} l_{tH}^2 + \frac{17}{135} \rho + \frac{3553}{226800} \rho^2 \right] \\ & + \left(\frac{\alpha_s^{(n_l)}}{\pi} \right)^2 \left[\frac{6793}{288} + \frac{201}{32} \zeta_2 - \frac{143}{16} \zeta_3 + l_{tH} \left(-\frac{5}{3} + \frac{33}{8} \zeta_2 + \frac{9}{8} \zeta_3 \right) + l_{tH}^2 \left(-\frac{67}{16} \right. \right. \\ & \left. \left. + \frac{9}{8} \zeta_2 \right) - \frac{11}{16} l_{tH}^3 + \rho \left(-\frac{49160591}{2488320} + \frac{7}{30} \zeta_2 + \frac{7}{90} \zeta_2 a_1 + \frac{1909181}{110592} \zeta_3 - \frac{1}{16} l_{tH} \right) \right. \\ & \left. + \rho^2 \left(-\frac{340842656767}{78033715200} + \frac{857}{25200} \zeta_2 + \frac{857}{75600} \zeta_2 a_1 + \frac{267179777}{70778880} \zeta_3 + \frac{1663}{403200} l_{tH} \right) \right] \end{aligned}$$

$$\begin{aligned}
& + n_l \left[-\frac{3239}{864} - \frac{5}{16} \zeta_2 + \left(-\frac{19}{36} - \frac{1}{4} \zeta_2 \right) l_{tH} + \frac{5}{24} l_{tH}^2 + \frac{1}{24} l_{tH}^3 + \rho \left(\frac{14563}{97200} \right. \right. \\
& \left. \left. - \frac{7}{180} \zeta_2 + \frac{1441}{51840} l_{tH} \right) + \rho^2 \left(\frac{4565713}{571536000} - \frac{857}{151200} \zeta_2 - \frac{7}{24} \zeta_3 + \frac{80231}{43545600} l_{tH} \right) \right] \\
& + \left(\frac{\alpha_s^{(n_l)}}{\pi} \right)^3 \left[\frac{48557965}{124416} + \frac{165289}{3456} \zeta_2 - \frac{515171}{3072} \zeta_3 - \frac{2477}{128} \zeta_4 - \frac{693}{32} \zeta_2 \zeta_3 - \frac{39}{8} \zeta_3^2 \right. \\
& + \frac{3333}{32} \zeta_5 - \frac{193}{8} \zeta_6 + l_{tH} \left(\frac{373975}{3456} + \frac{3415}{48} \zeta_2 - 32 \zeta_3 - \frac{2871}{64} \zeta_4 - \frac{45}{8} \zeta_2 \zeta_3 - \frac{27}{4} \zeta_5 \right) \\
& + l_{tH}^2 \left(-\frac{8375}{384} + \frac{765}{32} \zeta_2 - \frac{297}{32} \zeta_4 \right) + l_{tH}^3 \left(-\frac{445}{48} + \frac{33}{16} \zeta_2 \right) - \frac{121}{128} l_{tH}^4 \\
& + \rho \left(-\frac{259223248932251}{1448500838400} + \frac{9307759}{777600} \zeta_2 - \frac{1307}{540} \zeta_2 a_1 + \frac{450431988509}{26824089600} \zeta_3 \right. \\
& - \frac{11392069483}{1149603840} a_1^4 + \frac{11310106987}{191600640} a_1^2 \zeta_2 - \frac{11392069483}{47900160} a_4 + \frac{195119667535}{613122048} \zeta_4 \\
& + \frac{718337}{9979200} a_1^5 - \frac{718337}{997920} a_1^3 \zeta_2 + \frac{46111267}{2661120} a_1 \zeta_4 - \frac{10073}{4320} \zeta_2 \zeta_3 - \frac{718337}{83160} a_5 \\
& \left. - \frac{3254515597}{31933440} \zeta_5 - \frac{39053}{46080} l_{tH} - \frac{1}{32} l_{tH}^2 \right) + \rho^2 \left(-\frac{6315352135895222062373}{33406832776052736000} \right. \\
& + \frac{4678810931}{2612736000} \zeta_2 - \frac{30433}{90720} a_1 \zeta_2 + \frac{28040615442439394953}{117837152649216000} \zeta_3 \\
& + \frac{5434377893299}{4782351974400} a_1^4 - \frac{783438973429}{113865523200} a_1^2 \zeta_2 + \frac{5434377893299}{199264665600} a_4 \\
& - \frac{195021650114479}{2550587719680} \zeta_4 + \frac{46902913}{202176000} a_1^5 - \frac{46902913}{20217600} a_1^3 \zeta_2 - \frac{8632107859}{377395200} a_1 \zeta_4 \\
& \left. - \frac{1233223}{3628800} \zeta_2 \zeta_3 - \frac{46902913}{1684800} a_5 + \frac{49563452909}{4528742400} \zeta_5 + \frac{5087874569}{73156608000} l_{tH} + \frac{9311}{1612800} l_{tH}^2 \right) \\
& + n_l \left[-\frac{18092863}{186624} - \frac{4775}{5184} \zeta_2 + \frac{214255}{41472} \zeta_3 + \frac{269}{288} \zeta_4 + \frac{13}{48} \zeta_2 \zeta_3 + \frac{931}{144} \zeta_5 \right. \\
& + l_{tH} \left(-\frac{77873}{2592} - \frac{119}{18} \zeta_2 + \frac{313}{144} \zeta_3 + \frac{107}{32} \zeta_4 \right) + l_{tH}^2 \left(\frac{281}{576} - 2 \zeta_2 + \frac{5}{8} \zeta_3 \right) \\
& + l_{tH}^3 \left(\frac{301}{288} - \frac{1}{8} \zeta_2 \right) + \frac{11}{96} l_{tH}^4 + \rho \left(\frac{33522117079}{13436928000} - \frac{2143291}{1866240} \zeta_2 - \frac{77}{810} a_1 \zeta_2 \right. \\
& \left. - \frac{127474675}{7962624} \zeta_3 - \frac{841}{165888} a_1^4 + \frac{7789}{138240} a_1^2 \zeta_2 - \frac{841}{6912} a_4 + \frac{17870813}{1105920} \zeta_4 \right)
\end{aligned}$$

$$\begin{aligned}
& + \frac{13719599}{27993600} l_{tH} + \frac{135427}{3732480} l_{tH}^2 \Big) + \rho^2 \left(\frac{55089024397554433}{8849023303680000} - \frac{269760917}{1567641600} \zeta_2 \right. \\
& - \frac{9427}{680400} a_1 \zeta_2 - \frac{4434255669689}{535088332800} \zeta_3 - \frac{82337}{191102976} a_1^4 + \frac{35470607}{5573836800} a_1^2 \zeta_2 \\
& \left. - \frac{82337}{7962624} a_4 + \frac{154381746143}{44590694400} \zeta_4 + \frac{2587551899}{82301184000} l_{tH} + \frac{4941929}{3135283200} l_{tH}^2 \right) \Big] \\
& + n_l^2 \left[\frac{109031}{34992} - \frac{11}{432} \zeta_2 + \frac{17}{162} \zeta_3 - \frac{1}{864} \zeta_4 + l_{tH} \left(\frac{19673}{15552} + \frac{5}{36} \zeta_2 \right) \right. \\
& + l_{tH}^2 \left(\frac{41}{432} + \frac{1}{24} \zeta_2 \right) - \frac{5}{216} l_{tH}^3 - \frac{1}{288} l_{tH}^4 + \rho \left(- \frac{16171327}{186624000} + \frac{10177}{311040} \zeta_2 \right. \\
& \left. - \frac{11}{17280} \zeta_3 - \frac{21037}{466560} l_{tH} - \frac{1441}{311040} l_{tH}^2 \right) + \rho^2 \left(- \frac{96024044047}{23044331520000} \right. \\
& \left. \left. + \frac{1149767}{261273600} \zeta_2 - \frac{137}{2903040} \zeta_3 - \frac{137329}{48988800} l_{tH} - \frac{80231}{261273600} l_{tH}^2 \right) \right] \Big] . \quad (3.11)
\end{aligned}$$

Here, $\rho = m_H^2/M_t^2$, $l_{tH} = \log(M_t^2/m_H^2) + i\pi$, ζ_n is the Riemann Zeta function as defined in Eq. (2.35) and $a_n = \text{Li}_n(1/2)$. Note that $a_1 = \ln 2$. Results for F and $\log F$ expressed in terms of $SU(N)$ colour factors and for arbitrary μ can be found in the ancillary files of [34].

3.3.2 Numerical impact of mass corrections

We are now in the position to discuss the numerical impact of the mass suppressed terms of the Higgs boson-gluon form factor. Since, in contrast to the form factor itself, only the finite part of $\log F$ contains mass suppressed terms, we discuss $\log F|_{\text{finite}}$ in the following.

NUMERICAL INPUT QUANTITIES In the following we study the impact of the mass suppressed terms for the top-quark mass renormalized in the $\overline{\text{OS}}$ scheme as well as the $\overline{\text{MS}}$ scheme. Furthermore, we will investigate the size of the corrections for several different renormalization scales. To this end, we use the program (C)RunDec version 3 [105] to convert the top-quark mass between $\overline{\text{OS}}$ and $\overline{\text{MS}}$ scheme, as well as to evaluate the $\overline{\text{MS}}$ renormalized mass at different renormalization scales. For the numerical evaluation of Eq. (3.11) we use the default values in (C)RunDec:

$$m_H = 125.09 \text{ GeV} , \quad M_t = 173.21 \text{ GeV} , \quad \alpha_s^{(5)}(M_Z) = 0.1181 , \quad (3.12)$$

where $M_Z = 91.1876 \text{ GeV}$.

In a first step, we compute $\alpha_s^{(6)}(M_t)$ employing the five-loop QCD beta function [52–55] and the four-loop decoupling constant of the strong coupling [33, 47, 48]. With M_t and $\alpha_s^{(6)}(M_t)$ available, we can compute the scale-invariant top-quark mass using the four-loop $\overline{\text{MS}}$ -OS relation [104]. As a result, we obtain

$$\alpha_s^{(6)}(M_t) = 0.107732, \quad m_t(m_t) = 163.382 \text{ GeV}. \quad (3.13)$$

The scale-invariant top-quark mass, together with the five-loop quark mass anomalous dimension [57–59], can be used to obtain m_t at any renormalization scale μ .

RENORMALIZATION SCALE DEPENDENCE: OS SCHEME First, we consider $\log F|_{\text{finite}}$ with the top-quark mass renormalized in the OS scheme and $\mu = M_t$. Through four loops the real part of $\log F|_{\text{finite}}$ is given by

$$\begin{aligned} \text{Re}(\log F)|_{\text{OS}, \mu=M_t} &= \left(\frac{\alpha_s^{(n_l)}}{\pi}\right) \left(11.0681|_{\rho^0} + 0.065677|_{\rho^1} + 0.004261|_{\rho^2}\right) \\ &+ \left(\frac{\alpha_s^{(n_l)}}{\pi}\right)^2 \left(22.6025|_{\rho^0} + 1.01519|_{\rho^1} + 0.0654393|_{\rho^2}\right) \\ &+ \left(\frac{\alpha_s^{(n_l)}}{\pi}\right)^3 \left(-73.0929|_{\rho^0} + 7.6059|_{\rho^1} + 0.694711|_{\rho^2}\right). \end{aligned} \quad (3.14)$$

The expansion in ρ converges rapidly. While at two and three loops the $\mathcal{O}(\rho^1)$ contributions are less than 5% of the leading term, at four loops the $\mathcal{O}(\rho^1)$ contributions are more than 10% of the leading term, indicating that the impact of higher-order corrections in the LME of the form factor is larger for higher loop orders. However, even at four loops, the $\mathcal{O}(\rho^2)$ are less than 1% of the leading contribution.

For different values of the renormalization scale, the relative impact of the higher-order corrections in the LME changes considerably. In Fig. 3.3 we show the dependence of the four-loop contribution to $\log F|_{\text{finite}}$, renormalized in the OS scheme, as a function of μ for the expansion through $\mathcal{O}(\rho^0)$, $\mathcal{O}(\rho^1)$ and $\mathcal{O}(\rho^2)$ respectively. The relative size of the higher-order ρ corrections rapidly increases for $\mu > M_t$ and decreases for smaller values of μ . However, even for the commonly chosen renormalization scale $\mu = m_H/\sqrt{2}$ the mass corrections do not become smaller than 3%. Below $\mu = 200 \text{ GeV}$, the relative size of ρ^2 contributions w.r.t. those of ρ^1 do not exceed 2.5% as can be seen in the lower panel of Fig. 3.3. Thus the ρ^1 contribution has, depending on the chosen renormalization scale, an impact of $\mathcal{O}(10\%)$, the ρ^2 contribution stabilizes the convergence of the LME.

RENORMALIZATION SCALE DEPENDENCE: $\overline{\text{MS}}$ SCHEME Taking $\mu = m_t(m_t)$ and using the $\overline{\text{MS}}$ renormalized top-quark mass we obtain

$$\text{Re}(\log F)|_{\overline{\text{MS}}, \mu=m_t} = \left(\frac{\alpha_s^{(n_l)}}{\pi}\right) \left(11.1719|_{\rho^0} - 0.017369|_{\rho^1} - 0.002407|_{\rho^2}\right)$$

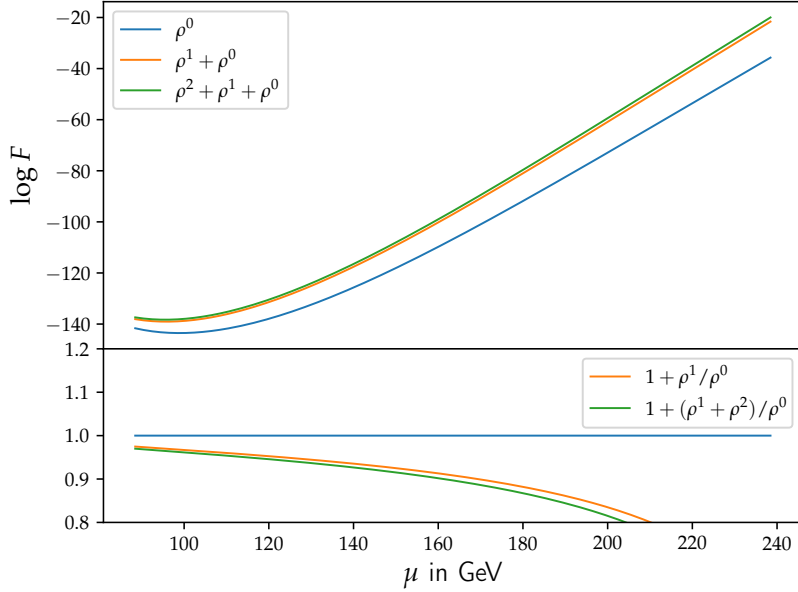


Figure 3.3: Four-loop contribution of the real part of $\log F|_{\text{finite}}$ renormalized in the OS scheme as a function of μ . The impact of higher-order $1/M_t$ corrections grows with increasing μ . The upper panel shows the four-loop contribution including different order in the LME. In the lower panel, the ratios between the result including the ρ^1 term and the leading order, as well as between the result including both, the ρ^1 and ρ^2 term and the leading order are shown.

$$\begin{aligned}
 & + \left(\frac{\alpha_s^{(n_l)}}{\pi} \right)^2 \left(20.976|_{\rho^0} + 0.557998|_{\rho^1} + 0.0312618|_{\rho^2} \right) \\
 & + \left(\frac{\alpha_s^{(n_l)}}{\pi} \right)^3 \left(-90.2709|_{\rho^0} + 1.31135|_{\rho^1} + 0.158557|_{\rho^2} \right) . \quad (3.15)
 \end{aligned}$$

As in the OS case, the convergence of the ρ expansion is very good. At all considered loop orders, the $\mathcal{O}(\rho^2)$ are approximately an order of magnitude smaller than the $\mathcal{O}(\rho^1)$ contributions. Contrary to the OS case however, the four loop $\mathcal{O}(\rho^1)$ contributions only amount to 1.5% of the leading order contribution, while the three-loop $\mathcal{O}(\rho^1)$ contributions amount to 2.6% of the leading term. In both cases, the LME of the imaginary part of $\log F|_{\text{finite}}$ converges faster than the real part.

The case of $\log F|_{\text{finite}}$ with the top-quark mass renormalized in the $\overline{\text{MS}}$ scheme is shown in Fig. 3.4. Overall, the convergence of the LME is better than in the OS case and more stable w.r.t. to changes of μ . For $m_H < \mu < 200$ GeV the relative impact of

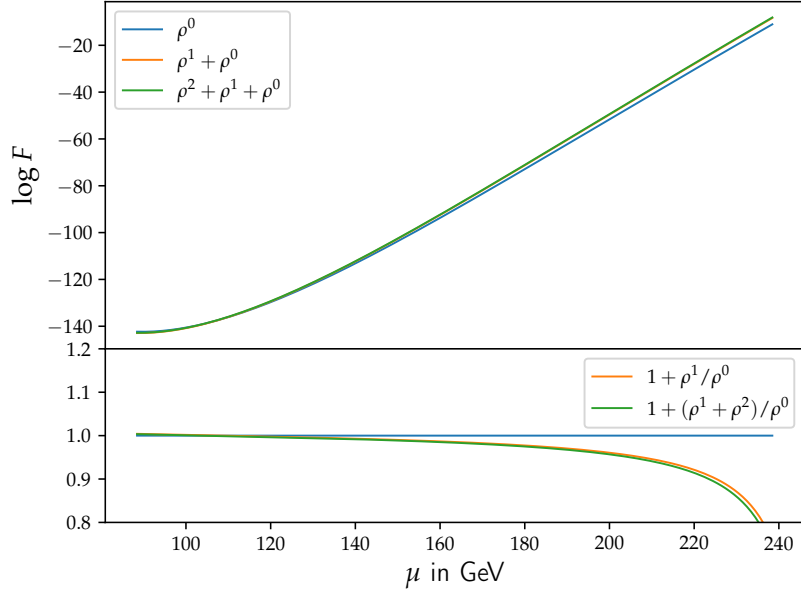


Figure 3.4: Four-loop contribution of the real part of $\log F|_{\text{finite}}$ renormalized in the $\overline{\text{MS}}$ scheme as a function of μ . The convergence of the LME is better than for the OS case.

the ρ^1 contribution does not exceed 4% w.r.t. to the leading term. Furthermore, the ρ^2 contribution remains below 0.5% throughout the whole range.

ρ DEPENDENCE: OS SCHEME For the on-shell production of a single SM Higgs boson the center-of-mass energy is $\sqrt{s} = m_H$, however there are processes where the Higgs boson–gluon form factor enters at higher center-of-mass energies. Examples are:

- processes with an off-shell Higgs boson propagator, such as Higgs boson or Z-boson pair-production,
- production of BSM scalar particles with masses larger than m_H .

It is thus instructive to study up to which value in ρ our expansion shows a convergent behaviour.

In Fig. 3.5 we fix $\mu = M_t$ and vary ρ . The value for on-shell Higgs boson production is indicated by the vertical red line. Around $\sqrt{\rho} \approx 0.5$ the real part of $\log F|_{\text{finite}}$ crosses zero and thus the relative size of higher-order corrections in the LME diverges. For $\sqrt{\rho} \approx 1.04$ which corresponds to the threshold for Z-boson pair production, the relative size of the ρ^1 contribution amounts to 12.5% and the ρ^2 contributions are as big as 2.5% w.r.t. those of ρ^1 . Going to values such as $\sqrt{\rho} \approx 1.44$, corresponding to the threshold for Higgs boson pair production, increases the relative sizes to 15.5% and 4.5% respectively.

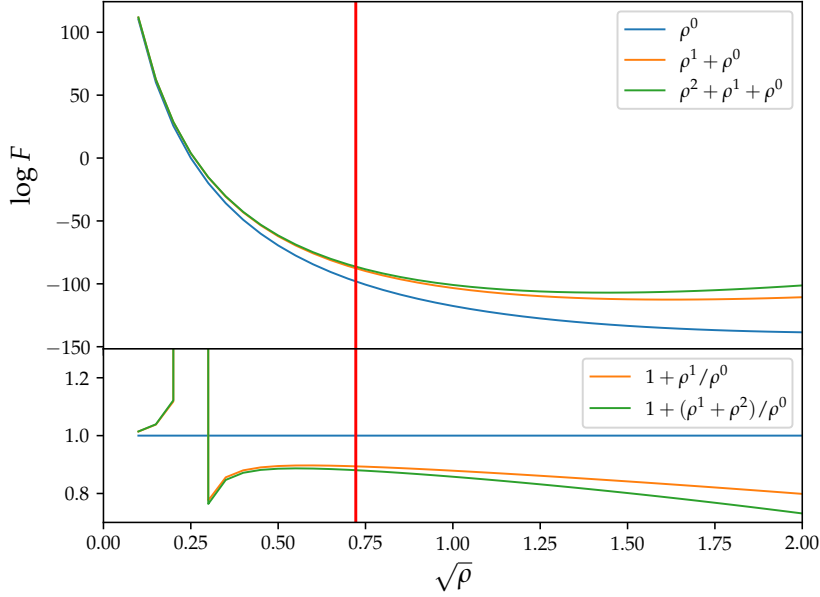


Figure 3.5: Four-loop contribution of the real part of $\log F$ renormalized in the OS scheme with $\mu = M_t$ as a function of $\sqrt{\rho}$. The red line indicates the value for on-shell Higgs boson production.

ρ DEPENDENCE: $\overline{\text{MS}}$ SCHEME As in the case of the μ -dependence, higher-order corrections in the LME with the top-quark mass renormalized in the $\overline{\text{MS}}$ scheme are less sensitive to variations of ρ than for the OS scheme. In Fig. 3.6 we show the four-loop contribution to the real part of $\log F|_{\text{finite}}$ with $\mu = m_t$. For $\sqrt{\rho} \approx 1.1$, corresponding to the Z-Boson pair production threshold, the mass corrections are below 2% and 0.5% respectively. At the Higgs boson pair production threshold, $\sqrt{\rho} \approx 1.53$, the corrections grow to 3% and 1.5% respectively.

SUMMARY In summary, the LME of the Higgs boson-gluon form factor through $\mathcal{O}(1/M_t^2)$ is sufficiently precise for the description of on-shell Higgs boson production in gluon fusion, as well as the decay of a Higgs boson into gluons. Even for applications with an off-shell Higgs boson, such as Z-boson or Higgs boson pair production near the production threshold, the $\mathcal{O}(1/M_t^4)$ contributions are below 5% and thus the LME shows a good convergence in the region where it is valid. Overall, the $\overline{\text{MS}}$ scheme for the top-quark mass shows better convergence behaviour than the OS scheme.

Note, that our discussion is purely based on the logarithm of the form factor, which by itself is not directly linked to physical observables. To assess the real impact of higher-order terms in the LME , we would need to combine the form factor with real

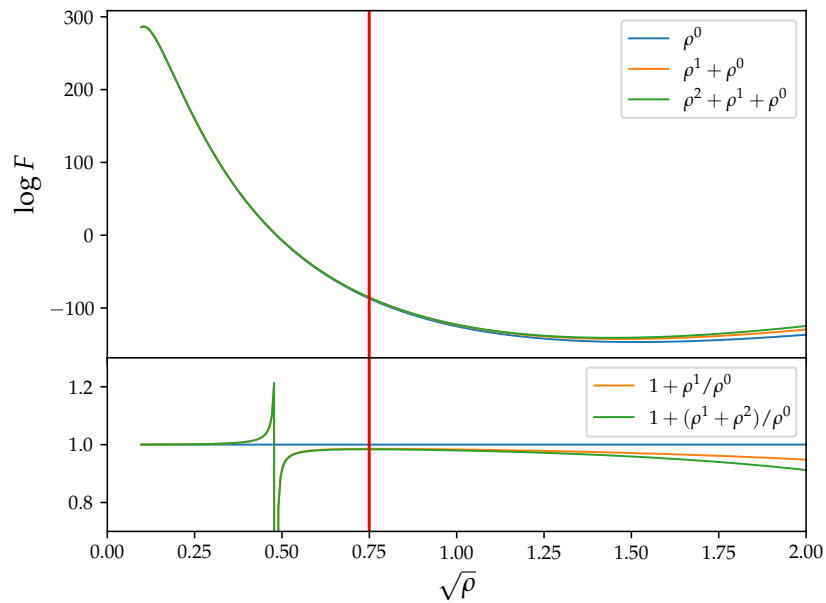


Figure 3.6: Four-loop contribution of the real part of $\log F|_{\text{finite}}$ renormalized in the $\overline{\text{MS}}$ scheme with $\mu = m_t$ as a function of $\sqrt{\rho}$. The red line indicates the value for on-shell Higgs boson production.

radiative corrections to the process under consideration. This however, is beyond the scope of this work.

THE HIGGS BOSON DECAY INTO PHOTONS AT FOUR LOOPS

In this chapter, we investigate a process which shares similarities with the Higgs boson–gluon form factor, but can be directly linked to a physical quantity: the QCD correction to the Higgs boson–photon form factor. Despite the small branching fraction of 0.23% [40], the decay into photons played a crucial role in the discovery of the Higgs boson [1, 2]. Due to the excellent mass resolution, it is one of the most precise channels for Higgs boson mass measurements, see e.g. [106].

THEORETICAL STATUS Numerical [107] and analytical NLO QCD [78, 80, 108] are available. NNLO QCD corrections have been computed in the LME in [109], where only contributions with photons coupling to top-quark loops have been considered, and in Ref. [110], where also the contributions with photons coupling to massless quark loops have been taken into account. Recently, also numerical results with the full quark mass dependence have become available [111].

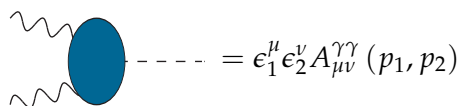
Furthermore, NLO electroweak corrections are known in a combination of LME and exact results [112, 113], as well as fully numerical [114, 115].

WHAT WE CAN LEARN AT N₃LO While the NNLO QCD corrections are probably sufficient for phenomenological applications, the N₃LO corrections we present in the following allow the assessment of the impact of top-quark mass suppressed terms at N₃LO for a physical quantity. In addition to the convergence of the LME it is instructive to study the convergence of the perturbative series in α_s itself. As the perturbative series is expected to behave like an asymptotic series [116], higher order corrections should start diverging starting from some order. Not many observables are known at N₃LO or higher, especially including finite quark mass effects. As a consequence investigating the convergence of higher-order corrections to the Higgs boson decay into photons is of interest in its own right.

In Sec. 4.1 we briefly describe the computation of the N₃LO corrections and in Sec. 4.2 we discuss the results.

4.1 COMPUTATION OF THE FOUR-LOOP CORRECTIONS

The Higgs boson–photon form factor can be rewritten as



$$\text{Diagram} = \epsilon_1^\mu \epsilon_2^\nu A_{\mu\nu}^{\gamma\gamma}(p_1, p_2)$$

$$= ((\epsilon_1 \cdot \epsilon_2)(p_1 \cdot p_2) - (\epsilon_1 \cdot p_2)(\epsilon_2 \cdot p_1)) \mathcal{A}^{\gamma\gamma}(s) , \tag{4.1}$$

in analogy to Eq. (2.16). The scalar form factor $\mathcal{A}^{\gamma\gamma}(s)$ is directly related to the decay rate Γ of the Higgs boson into photons

$$\Gamma_{h \rightarrow \gamma\gamma} = \frac{M_h^3}{64\pi^3} |\mathcal{A}^{\gamma\gamma}(M_h^2)|^2 \tag{4.2}$$

and, when only considering QCD corrections¹, can be decomposed into diagrams with W-boson loops, as well as top-quark loops

$$\mathcal{A}^{\gamma\gamma} = \mathcal{A}_W^{\gamma\gamma} + \mathcal{A}_t^{\gamma\gamma} . \tag{4.3}$$

Sample one-loop diagrams are shown in Fig. 4.1.

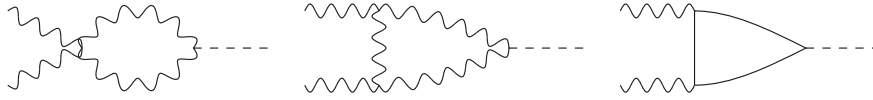


Figure 4.1: Leading order Feynman diagrams contributing to the Higgs boson–photon form factor. External wavy lines represent photons, internal wavy lines W-bosons, solid lines fermions and dashed lines Higgs bosons.

DIFFERENCES W.R.T. THE HIGGS BOSON–GLUON CASE The computation of the four-loop corrections to the Higgs boson–photon form factor proceeds in the same way as for the case of external gluons as described in Sec. 3.1.1. In general, the computation is less involved than in the gluonic case, since photons do not directly couple to gluons and thus fewer Feynman diagrams contribute to the form factor. Furthermore, at one- and two-loop order, only fully hard subgraphs contribute. As a consequence, the form factor is real through two loops.

ADDITIONAL QUARK LOOPS Starting from three loops also diagrams where the photons do not couple to the same quark loop as the Higgs boson, such as the second diagram in Fig. 4.2, appear. This second quark loop can be either a top-quark loop

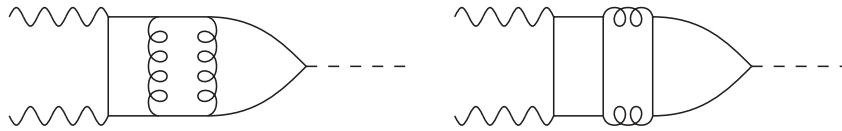


Figure 4.2: Three-loop diagrams contributing to the form factor. In the second diagram, the quark loop coupling to the photons can be massless.

and thus massive, or a light quark loop. For the light quark case, we have to take into

¹ Here we neglect the Yukawa couplings of all quarks except the top quark.

account the differing electric charges of up- and down-type quarks. At three loops the first diagram in Fig. 4.3 also appears, involving a top-quark loop with one photon and the Higgs boson coupling to it and a second, possibly massless, quark loop to which the second photon couples to. Diagrams of this type involve fermion loops with an odd

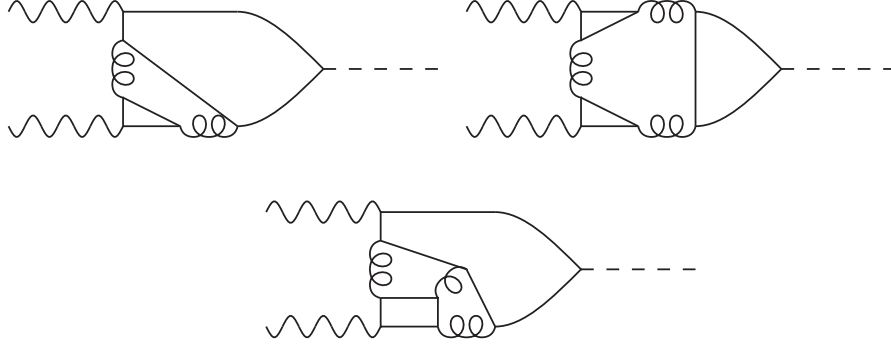


Figure 4.3: The two Feynman diagrams in the first line vanish due to Furry's theorem. The diagram in the second line leads to a non-vanishing contribution.

number of gauge bosons attached to it. Due to charge conservation, the sum of such diagrams, involving at most two gluons, add up to zero according to Furry's theorem [117]. At four loops, diagrams with an even number of attached gauge bosons, such as the one in the second line of Fig. 4.3, appear. These diagrams lead to a non-zero contribution and, in case the second quark loop is massless, terms proportional to the electric charge of the top quark multiplied by the sum of light quark charges. The second diagram in the first line of Fig. 4.3 with each external particle coupling to a different quark loop add up to zero following Furry's theorem.

4.2 RESULTS

We are now in the position to discuss the results obtained for the Higgs boson–photon form factor at four loops. To this end we decompose $\mathcal{A}_t^{\gamma\gamma}$ into four different contributions:

$$\mathcal{A}_t^{\gamma\gamma} = \tilde{\mathcal{A}}_t^{\gamma\gamma} \left(e_t^2 A_t^\dagger + e_t^2 A_t^{\square,t} + \sum_q e_q^2 A_t^1 + e_t \sum_q e_q A_t^{\square,l} \right). \quad (4.4)$$

Here $e_t = 2/3$ is the electric charge of the top quark, e_q are the charges of the light quarks and the sum over q runs over all five massless quark flavours. The quark charges sum up to

$$\sum_q e_q = \frac{1}{3} \quad \text{and} \quad \sum_q e_q^2 = \frac{11}{9}. \quad (4.5)$$

The overall factor is given by

$$\tilde{\mathcal{A}}_t^{\gamma\gamma} = \frac{2\alpha}{3\pi} N_c \sqrt{\sqrt{2}G_F}, \quad (4.6)$$

where $N_c = 3$, α is the fine-structure constant and G_F is Fermi's constant. Furthermore, A_t^t denotes the contributions where both photons couple to the same top-quark loop and A_t^l denote contributions where both photons couple to the same massless quark loop. Finally the contributions arising at the four-loop level with only one photon coupling to a different loop than the Higgs boson and the second photon, such as the one in the second row of Fig. 4.3, are denoted as $A_t^{\square,t/1}$.

4.2.1 Analytic results

CHECKS We perform several checks of the result. First, through three loops, we find agreement with [109, 110]. At four loops, the leading terms of A_t^t and $A_t^{\square,t}$ in the LME are known [118] with which we find agreement. As in the case of the Higgs boson–gluon form factor, we project on both terms of the tensor structure in Eq. (4.1) individually, obtaining the same result. Finally, we explicitly check the cancellation of diagrams with both photons and the Higgs boson coupling to different quark loops.

ANALYTIC RESULTS For the four terms in Eq. (4.4) we obtain

$$\begin{aligned} A_t^t &= 1 + \frac{7}{120}\rho + \frac{1}{168}\rho^2 \\ &+ \left(\frac{\alpha_s^{(5)}}{\pi}\right) \left[-1 + \frac{61}{270}\rho + \frac{554}{14175}\rho^2 \right] \\ &+ \left(\frac{\alpha_s^{(5)}}{\pi}\right)^2 \left[-\frac{7}{6} + \rho \left(-\frac{4904561}{622080} + \frac{7}{180}\zeta_2 + \frac{7}{90}a_1\zeta_2 + \frac{206951}{27648}\zeta_3 \right) \right. \\ &\left. + \rho^2 \left(-\frac{14134687057}{10450944000} + \frac{1}{126}\zeta_2 + \frac{1}{63}a_1\zeta_2 + \frac{18180533}{13271040}\zeta_3 + \frac{1}{360}l_{tH} \right) \right] \\ &+ \left(\frac{\alpha_s^{(5)}}{\pi}\right)^3 \left[-\frac{7229}{288} + \frac{2195}{96}\zeta_3 + \rho \left(-\frac{1662825322699}{51732172800} + \frac{2800187}{388800}\zeta_2 - \frac{895}{324}a_1\zeta_2 \right. \right. \\ &\left. \left. + \frac{62283356969}{1277337600}\zeta_3 - \frac{90069911}{26127360}a_1^4 + \frac{88771607}{4354560}a_1^2\zeta_2 - \frac{90069911}{1088640}a_4 + \frac{1475256743}{34836480}\zeta_4 \right. \right. \\ &\left. \left. - \frac{46}{2835}a_1^5 + \frac{92}{567}a_1^3\zeta_2 + \frac{19133}{1512}a_1\zeta_4 - \frac{10073}{4320}\zeta_2\zeta_3 + \frac{368}{189}a_5 - \frac{839243}{18144}\zeta_5 \right) \right] \\ &+ \rho^2 \left(-\frac{159076957488068267}{4842131374080000} + \frac{2029217}{1360800}\zeta_2 - \frac{44311}{85050}a_1\zeta_2 + \frac{712744062504367}{23911759872000}\zeta_3 \right) \end{aligned}$$

$$\begin{aligned}
& - \frac{914726935901}{512394854400} a_1^4 + \frac{6366714842507}{597793996800} a_1^2 \zeta_2 - \frac{914726935901}{21349785600} a_4 \\
& + \frac{106092752802611}{4782351974400} \zeta_4 + \frac{32309}{277992} a_1^5 - \frac{161545}{138996} a_1^3 \zeta_2 - \frac{5014747}{370656} a_1 \zeta_4 \\
& - \left. \frac{1439}{3024} \zeta_2 \zeta_3 - \frac{161545}{11583} a_5 + \frac{10527619}{1482624} \zeta_5 + \frac{1963}{29160} l_{tH} + \frac{23}{4320} l_{tH}^2 \right) \Bigg], \quad (4.7)
\end{aligned}$$

$$\begin{aligned}
A_t^{\square,t} &= \left(\frac{\alpha_s^{(5)}}{\pi} \right)^3 \left[\frac{55}{216} - \frac{5}{9} \zeta_3 + \rho \left(\frac{24226021}{114960384} - \frac{59351603}{76640256} \zeta_3 - \frac{151}{2592} a_1^4 + \frac{151}{432} a_1^2 \zeta_2 \right. \right. \\
& - \left. \frac{151}{108} a_4 + \frac{7445}{6912} \zeta_4 \right) + \rho^2 \left(\frac{1234082295799}{20085878292480} + \frac{5991575341}{165315870720} \zeta_3 \right. \\
& \left. \left. + \frac{1010393}{557383680} a_1^4 - \frac{1010393}{92897280} a_1^2 \zeta_2 + \frac{1010393}{23224320} a_4 - \frac{16542457}{148635648} \zeta_4 \right) \right], \quad (4.8)
\end{aligned}$$

$$\begin{aligned}
A_t^1 &= \left(\frac{\alpha_s^{(5)}}{\pi} \right)^2 \left[-\frac{13}{12} + \frac{2}{3} \zeta_3 - \frac{1}{6} l_{tH} + \rho \left(-\frac{3493}{194400} + \frac{7}{180} \zeta_3 - \frac{19}{6480} l_{tH} \right) \right. \\
& \left. \rho^2 \left(-\frac{3953}{6350400} + \frac{1}{252} \zeta_3 + \frac{1}{60480} l_{tH} \right) \right] \\
& + \left(\frac{\alpha_s^{(5)}}{\pi} \right)^3 \left[-\frac{10337}{648} + \frac{115}{216} \zeta_2 + \frac{27}{2} \zeta_3 + \frac{23}{108} \zeta_4 - \frac{25}{9} \zeta_5 + l_{tH} \left(-\frac{167}{36} + \frac{23}{9} \zeta_3 \right) \right. \\
& - \frac{23}{72} l_{tH}^2 + \rho \left(-\frac{19038301}{26244000} + \frac{9973}{233280} \zeta_2 + \frac{424577}{622080} \zeta_3 + \frac{161}{12960} \zeta_4 - \frac{35}{216} \zeta_5 \right. \\
& \left. + l_{tH} \left(-\frac{1887643}{6998400} + \frac{161}{1080} \zeta_3 \right) - \frac{4193}{233280} l_{tH}^2 \right) + \rho^2 \left(\frac{328389003179}{512096256000} + \frac{42667}{8709120} \zeta_2 \right. \\
& - \frac{352361479}{696729600} \zeta_3 + \frac{23}{18144} \zeta_4 - \frac{25}{1512} \zeta_5 + l_{tH} \left(-\frac{132673099}{5486745600} + \frac{23}{1512} \zeta_3 \right) \\
& \left. \left. - \frac{31351}{17418240} l_{tH}^2 \right) \right], \quad (4.9)
\end{aligned}$$

as well as

$$\begin{aligned}
A_t^{\square,1} &= \left(\frac{\alpha_s^{(5)}}{\pi} \right)^3 \left[\frac{55}{108} - \frac{10}{9} \zeta_3 + \rho \left(\frac{3545}{10368} + \frac{245}{648} \zeta_3 - \frac{85}{108} \zeta_4 \right) \right. \\
& \left. + \rho^2 \left(\frac{9222149}{100776960} + \frac{2129}{15552} \zeta_3 - \frac{3137}{12960} \zeta_4 \right) \right]. \quad (4.10)
\end{aligned}$$

Here the top-quark mass is renormalized in the $\overline{\text{OS}}$ scheme, $\mu = M_t$ and $n_l = 5$. Note that both $A_t^{\square,t}$ and $A_t^{\square,l}$, contain $l_{tH} = \log(M_t^2/m_H^2) + i\pi$ and thus have an imaginary part, whereas $A_t^{\square,t}$ and $A_t^{\square,l}$ are real at four loops. The massless cut of the contributing diagrams vanishes, since the only external scale involved in the box-type contribution is an on-shell photon momentum.

4.2.2 Numerical results

In the following we discuss the impact of the N_3LO corrections on $\Gamma_{h \rightarrow \gamma\gamma}$ as well as the convergence of the LME at four loops. To this end, we expand $\Gamma_{h \rightarrow \gamma\gamma}$ in $\alpha_s^{(n_l)}$ making use of the fact that the one- and two-loop contributions are real:

$$\begin{aligned} \Gamma_{h \rightarrow \gamma\gamma} = \frac{M_h^3}{64\pi} & \left((\mathcal{A}_{\text{LO}}^{\gamma\gamma})^2 + 2 \frac{\alpha_s^{(n_l)}}{\pi} \mathcal{A}_{\text{LO}}^{\gamma\gamma} \mathcal{A}_{t,\text{NLO}}^{\gamma\gamma} \right. \\ & + \left(\frac{\alpha_s^{(n_l)}}{\pi} \right)^2 \left((\mathcal{A}_{t,\text{NLO}}^{\gamma\gamma})^2 + 2 \mathcal{A}_{\text{LO}}^{\gamma\gamma} \text{Re}(\mathcal{A}_{t,\text{NNLO}}^{\gamma\gamma}) \right) \\ & \left. + \left(\frac{\alpha_s^{(n_l)}}{\pi} \right)^3 \left(2 \mathcal{A}_{t,\text{NLO}}^{\gamma\gamma} \text{Re}(\mathcal{A}_{t,\text{NNLO}}^{\gamma\gamma}) + 2 \mathcal{A}_{\text{LO}}^{\gamma\gamma} \text{Re}(\mathcal{A}_{t,\text{N}_3\text{LO}}^{\gamma\gamma}) \right) \right). \quad (4.11) \end{aligned}$$

Here we only take QCD corrections to $\mathcal{A}_t^{\gamma\gamma}$ into account. The exact expression for the LO amplitude defined in Eq. (4.3) is taken from [110]. For the numerical evaluation we use the values as in Eq. (3.12), as well as [40]

$$\alpha = 1/137.036, \quad G_F = 1.1663787 \times 10^{-5} \text{ GeV}^{-2}, \quad M_W = 80.379 \text{ GeV}, \quad (4.12)$$

where M_W is the W-Boson mass. For the Higgs boson decay rate into photons at N_3LO with the top-quark mass renormalized in the $\overline{\text{MS}}$ scheme and $\mu = M_h$ we obtain

$$\Gamma_{h \rightarrow \gamma\gamma} \times 10^6 \text{ GeV} = 9.11767 + 0.16423 + 0.00697 - 0.000199 = 9.28867. \quad (4.13)$$

Clearly, the N_3LO corrections are too small to have any phenomenological impact. The N_3LO contribution can be decomposed into

$$\begin{aligned} \Gamma_{h \rightarrow \gamma\gamma}|_{\text{N}_3\text{LO}} \times 10^9 \text{ GeV} = & 0.05608|_{\text{NLO} \times \text{NNLO}} - 1.72666|_t + 1.27532|_l \\ & + 0.09738|_{\square,t} + 0.09914|_{\square,l}, \quad (4.14) \end{aligned}$$

where the subscripts of the last four terms refer to the four terms in Eq. (4.4). It is worth noting, that there is a large cancellation between the N_3LO contribution to A_t^\dagger and all other terms. Compared to the approximation in Ref. [118], where only contributions where both photons couple to top quark loops are taken into account, our result for the

four-loop corrections is an order of magnitude smaller. Adopting the OS scheme for the top-quark mass leads to

$$\Gamma_{h \rightarrow \gamma\gamma} \times 10^6 \text{ GeV} = 9.12998 + 0.15635 + 0.00300 - 0.00107 = 9.2883 \quad (4.15)$$

and

$$\begin{aligned} \Gamma_{h \rightarrow \gamma\gamma}|_{\text{N3LO}} \times 10^9 \text{ GeV} &= 0.01995|_{\text{NLO} \times \text{NNLO}} - 2.3858|_t + 1.10544|_l \\ &+ 0.0973|_{\square,t} + 0.09894|_{\square,l}, \end{aligned} \quad (4.16)$$

showing the same convergence and cancellation patterns as for the top-quark mass renormalized in the $\overline{\text{MS}}$ scheme.

For the top-quark mass renormalized in the $\overline{\text{MS}}$ scheme, the N₃LO contribution to $\Gamma_{h \rightarrow \gamma\gamma}$ shows a different convergence pattern as $\log F$, w.r.t. higher-order terms in the ρ expansion. The three terms contribute as

$$\Gamma_{h \rightarrow \gamma\gamma}|_{\text{N3LO}} \times 10^{10} \text{ GeV} = -3.72262|_{\rho^0} + 1.75822|_{\rho^1} - 0.02468|_{\rho^2} \quad (4.17)$$

and thus the next-to-leading term in the expansion is half as big as the leading one but opposite in sign. However, as in the case of $\log F$, the ρ^2 contribution is smaller than 1%, signaling a good convergence.

As in the case of $\log F$ the convergence for the top-quark mass renormalized in the OS scheme is not as good as when renormalized in the $\overline{\text{MS}}$ scheme. The N₃LO contributions renormalized in the OS scheme are given by

$$\Gamma_{h \rightarrow \gamma\gamma}|_{\text{N3LO}} \times 10^{10} \text{ GeV} = 0.936|_{\rho^0} - 10.004|_{\rho^1} - 1.585|_{\rho^2}. \quad (4.18)$$

In this case, the ρ^1 contribution is an order of magnitude larger than the leading term and has a different sign. The ρ^2 contribution is still 50% larger than the leading term. A similar behaviour can be observed at NNLO, where the ρ^2 and the ρ^1 contributions are of similar size and have an opposite sign w.r.t the ρ^0 term [110].

As a consequence, we would need to compute more terms in the ρ expansion to have a stable prediction for the size of the N₃LO contributions with the top-quark mass renormalized in the OS scheme. The major bottleneck for computing more terms in the ρ expansion is the tensor reduction. As the tensor rank of the involved tadpole integrals increases with the expansion depth, we need to implement reduction routines for tensors of rank ten to compute the ρ^3 contribution. While this is, in principle, possible, for the program of [92] to generate the relevant rules, we would need to split the tensors by the number of equal loop-momenta. This means, we would derive separate rules for, e.g., tensors composed of ten equal loop momenta and tensors composed of five copies of two different loop momenta, and so on, making it a rather daunting task.

CONCLUSION The N_3LO corrections to the Higgs decay into photons amount to $\mathcal{O}(10^{-5})$ times the LO contribution when the top-quark mass is renormalized in the \overline{MS} scheme and is more than an order of magnitude smaller than the $NNLO$ corrections. Thus there is no sign of divergence of the asymptotic series at N_3LO . Individual contributions amount to $\mathcal{O}(10^{-4})$ times the LO contribution, however they cancel largely against each other. While the ρ^1 amounts to $\mathcal{O}(50\%)$ of the ρ^0 term, the LME shows a good perturbative behaviour and the ρ^2 term is clearly negligible.

With the top-quark mass renormalized in the OS scheme, the N_3LO contributions amount to $\mathcal{O}(10^{-4})$ times the LO contribution. As the ρ^2 contribution is larger than the ρ^0 contribution however, higher-order terms in the LME would be required for a stable answer.

In both renormalization schemes, top-quark-mass corrections seem to have a bigger impact than for $\log F$ in the previous chapter. In both quantities however, the suppressed mass terms have a larger impact in the OS scheme than in the \overline{MS} scheme.

A final comment regarding possible IR divergences is in order. As the three-point integrals entering A_t^1 contain soft singularities, one might expect them to not be finite. On the other hand, since the external photons are not carrying colour charge Eq. (3.3) implies that there are no IR divergences. Our explicit calculation shows that there are indeed no IR divergences.

Part II

HIGGS BOSON PAIR PRODUCTION

A prime objective of the [HL-LHC](#) and also of future hadron colliders is the study of Higgs boson pair production. This process enables a direct measurement of the trilinear Higgs boson self-coupling and thus a direct probe of electroweak symmetry breaking.

The dominant channel for the production of a pair of Higgs bosons is gluon fusion and thus, as in the case of single Higgs boson production, higher order [QCD](#) corrections are necessary to make reliable predictions and unveil possible deviations from the [SM](#) expectations.

To this end, we compute the inclusive Higgs boson pair-production cross-section at [NNLO](#) in the [LME](#), improving upon existing results in the literature. In particular, we compute the real radiative contributions beyond the limit of an infinitely heavy top quark using the method of reverse unitarity.

APPLYING MULTI-LOOP TECHNIQUES TO PHASE SPACE INTEGRALS

To obtain the fully inclusive hadronic cross-section for $pp \rightarrow HH + X$ we need to compute the individual inclusive partonic cross-sections for the different initial states contributing at **NNLO** in **QCD**. The various contributions at **NNLO** can be split into the following subsets:

- Double-virtual corrections: three-loop amplitudes contributing to the partonic process $gg \rightarrow HH$. They are known at $\mathcal{O}(1/M_t^8)$ in the **LME** [88].
- Real-virtual corrections: two-loop amplitudes contributing to the partonic processes $gg \rightarrow gHH$, $qg \rightarrow qHH$ and $q\bar{q} \rightarrow gHH$. Example diagrams are shown in the first row of Fig. 5.1.
- Double-real corrections: one-loop amplitudes contributing to the partonic processes $gg \rightarrow ggHH$, $gg \rightarrow q\bar{q}HH$, $qg \rightarrow qgHH$, $q\bar{q} \rightarrow ggHH$, $q\bar{q} \rightarrow q\bar{q}HH$, $qq \rightarrow qqHH$ and $qq' \rightarrow qq'HH$. Example diagrams are shown in the second and third row of Fig. 5.1.

The real-virtual corrections can further be split into contributions with both Higgs bosons coupling to different top-quark loops and contributions with both Higgs bosons coupling to the same loop. We discuss the former set of corrections in chapter 6 and the remaining real-virtual, as well as all double-real contributions, in chapter 7.

GOAL The goal of this chapter is to discuss the application of techniques developed for multi-loop integrals to phase-space integrals, arising in the computation of the contributions of the real-virtual and double-real amplitudes to the total cross-section.

In the following we employ the **EFT** introduced in Chap. 2, as the mass-suppressed terms in the **LME**, which are discussed in chapters 6 and 7, only change the numerator structure of the involved integrals which does not matter for the present discussion. Furthermore, we focus on the two-gluon initial state, since it exhibits all relevant features.

THE INCLUSIVE CROSS-SECTION The inclusive partonic cross-section for the two-gluon initial state can be written as

$$\begin{aligned} \sigma_{gg \rightarrow HH+X} = & \frac{1}{2s} \int d\text{PS}_2 |\mathcal{A}_{gg \rightarrow HH}|^2 + \frac{1}{2s} \int d\text{PS}_3 |\mathcal{A}_{gg \rightarrow HHg}|^2 \\ & + \frac{1}{2s} \sum_{x=gg, q\bar{q}} \int d\text{PS}_4 |\mathcal{A}_{gg \rightarrow HHx}|^2, \end{aligned} \quad (5.1)$$

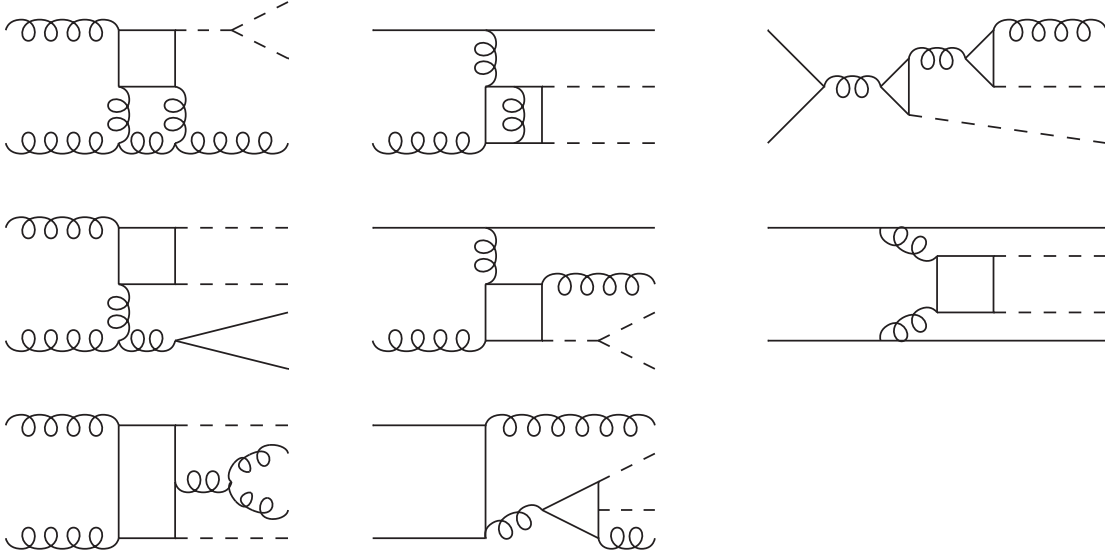


Figure 5.1: Sample diagrams of real-virtual and double-real corrections. The last diagram in the first row belongs to the subset discussed in chapter 6. All others are discussed in chapter 7.

where averaging over the initial state gluon polarization and colours as well as summation over the final state particle polarization and colours is implied. The D -dimensional phase-space integration measures are given by

$$d\text{PS}_i = (2\pi)^D \prod_{j=3}^{i+2} \frac{d^{D-1}p_j}{(2\pi)^{D-1}} \frac{1}{2E_j} \delta^{(D)} \left(q_1 + q_2 - \sum_{k=3}^{i+2} p_k \right). \quad (5.2)$$

Here, q_1 and q_2 are the momenta of the ingoing gluons with $q_i^2 = 0$ and $2q_1 \cdot q_2 = s$, p_3 and p_4 are the momenta of the Higgs bosons with $p_{3/4}^2 = m_H^2$, while the other p_i are massless. The D -dimensional delta function $\delta^{(D)}$ ensures total energy and momentum conservation. The $(D-1)$ -dimensional integrations are over the spatial components of the four vectors.

By rewriting

$$\begin{aligned} \frac{1}{2E_j} &= \int dp_{j,0} \frac{1}{2E_j} \delta(p_{j,0} - E_j) = \int dp_{j,0} \theta(p_{j,0}) \delta(p_j^2 - m_j^2) \\ &\equiv \int dp_{j,0} \delta^{(+)}(p_j^2 - m_j^2) \end{aligned} \quad (5.3)$$

Eq. (5.2) becomes

$$d\text{PS}_i = (2\pi)^{(1-i)D+i} \prod_{j=3}^{i+2} \left(d^D p_j \right) \delta^{(+)}(p_j^2 - m_j^2) \delta^{(D)} \left(q_1 + q_2 - \sum_{k=3}^{i+2} p_k \right), \quad (5.4)$$

where $m_4 = m_5 = 0$. Thus we are left with the evaluation of i -fold D -dimensional integrals of the squared amplitudes. These integrals seem to have a completely different structure than the loop integrals arising in the previous chapter. In Sec. 5.1 we, however, show that they can be treated using similar methods and in Sec. 5.2 we introduce a program capable of simplifying calculations involving phase-space integrals.

5.1 COMPUTING PHASE SPACE INTEGRALS BY REVERSE UNITARITY

To apply the tools developed in the context of loop integrals to the problem at hand, we need to relate Eq. (5.4) to a form in which methods like [IBP](#) reduction can be directly applied. An example of such a relation is the optical theorem, relating the total inclusive cross-section of two particles with momenta p_i to the imaginary part of the forward-scattering amplitude of the two particles:

$$\sigma_{p_1, p_2 \rightarrow X} = \frac{1}{s} \text{Im} (\mathcal{A}_{p_1 p_2 \rightarrow p_1 p_2}) . \quad (5.5)$$

Thus the sum of all phase-space integrals arising in the computation of $\sigma_{p_1, p_2 \rightarrow X}$ can be rewritten as the imaginary part of a loop integral.

REVERSE UNITARITY Since we are only interested in contributions coming from the production of a pair of Higgs bosons and massless partons, we need a way to select these contributions. To this end, we follow the so-called method of *reverse unitarity* introduced in the context of the production of a single Higgs boson at [NNLO](#) [119]. First, we perform one of the phase-space integrations and resolve the energy-momentum conserving delta function:

$$\begin{aligned} d\text{PS}_i &= (2\pi)^{(1-n)D+n} \prod_{j=3}^{i+1} (d^D p_j) \delta^{(+)}(p_j^2 - m_j^2) \\ &\quad \times \delta^{(+)} \left(\left(q_1 + q_2 - \sum_{k=3}^{i+1} p_k \right)^2 - m_{i+2}^2 \right) . \end{aligned} \quad (5.6)$$

In the next step, we replace each remaining delta function by a *cut* propagator

$$2\pi i \delta^{(+)}(p^2 - m^2) \rightarrow \frac{1}{p^2 - m^2 + i0} - \frac{1}{p^2 - m^2 - i0} \equiv \frac{1}{[p^2 - m^2]_c} . \quad (5.7)$$

For the application of methods based on [IBP](#) relations, these can be treated as regular propagators with one exception. In case the power of a cut propagator becomes zero or negative, the integral vanishes and we can discard it. Powers greater than one are treated as in the case of regular loop integrals, however in this case we can not directly apply Eq. (5.7) to re-write them as phase-space integrals again. As a consequence, we choose our [MIs](#) to not have cut propagators raised to higher powers.

APPLICATION TO HIGGS BOSON PAIR-PRODUCTION The method thus turns phase-space integrals for n final states into $(n - 1)$ -loop integrals. The procedure is illustrated in the following example:

Example 4 (NLO real radiation correction to $gg \rightarrow HH$)

Let us consider the following contribution to $|\mathcal{A}_{gg \rightarrow HHg}|^2$:

$$\left| \begin{array}{c} \text{---} \text{---} \text{---} \text{---} \text{---} \text{---} \\ | \quad \bullet \quad | \\ \text{---} \text{---} \text{---} \text{---} \text{---} \text{---} \\ | \quad \bullet \quad | \\ \text{---} \text{---} \text{---} \text{---} \text{---} \text{---} \end{array} \right|^2 \subset |\mathcal{A}_{gg \rightarrow HHg}|^2 .$$

The phase-space integral for this contribution is, after integrating over the final-state gluon momentum, given by

$$\begin{aligned} & \int d\text{PS}_3 \left| \begin{array}{c} \text{---} \text{---} \text{---} \text{---} \text{---} \text{---} \\ | \quad \bullet \quad | \\ \text{---} \text{---} \text{---} \text{---} \text{---} \text{---} \\ | \quad \bullet \quad | \\ \text{---} \text{---} \text{---} \text{---} \text{---} \text{---} \end{array} \right|^2 \\ &= (2\pi)^{3-2D} \int d^D p_3 d^D p_4 \frac{\delta^{(+)}(p_3^2 - m_H^2) \delta^{(+)}(p_4^2 - m_H^2) \delta^{(+)}(p_5^2)}{(q_1 - p_3 - p_4)^4} [\dots] , \end{aligned}$$

where the numerator structures have been omitted and $p_5 = q_1 + q_2 - p_3 - p_4$. Applying Eq. (5.7) leads to

$$\begin{aligned} & \int d\text{PS}_3 \left| \begin{array}{c} \text{---} \text{---} \text{---} \text{---} \text{---} \text{---} \\ | \quad \bullet \quad | \\ \text{---} \text{---} \text{---} \text{---} \text{---} \text{---} \\ | \quad \bullet \quad | \\ \text{---} \text{---} \text{---} \text{---} \text{---} \text{---} \end{array} \right|^2 \\ &= \int \frac{d^D p_3 d^D p_4 (2\pi)^{3-2D} [\dots]}{[(p_4^2 - m_H^2)]_c [(p_3^2 - m_H^2)]_c [(q_1 + q_2 - p_3 - p_4)^2]_c (q_1 - p_3 - p_4)^4} \\ &= \begin{array}{c} \text{---} \text{---} \text{---} \text{---} \text{---} \text{---} \\ | \quad \bullet \quad | \\ \text{---} \text{---} \text{---} \text{---} \text{---} \text{---} \\ | \quad \bullet \quad | \\ \text{---} \text{---} \text{---} \text{---} \text{---} \text{---} \end{array} , \end{aligned}$$

where the blue dashed line denotes the cut. The resulting integral can be treated as a normal loop integral and reduced to master integrals.

As a consequence of Eq. (5.7), Eq. (5.1) turns into

$$\sigma_{gg \rightarrow HH+X} \propto \widetilde{\text{Disc}}(\mathcal{A}_{gg \rightarrow gg}) , \quad (5.8)$$

where $\widetilde{\text{Disc}}$ denotes the discontinuity associated with the two Higgs boson threshold, indicating that exactly two cut Higgs bosons and possibly cut massless parton propagators are present. Example diagrams contributing to $\widetilde{\text{Disc}}(\mathcal{A}_{gg \rightarrow gg})$ in the EFT are shown in Fig. 5.2.

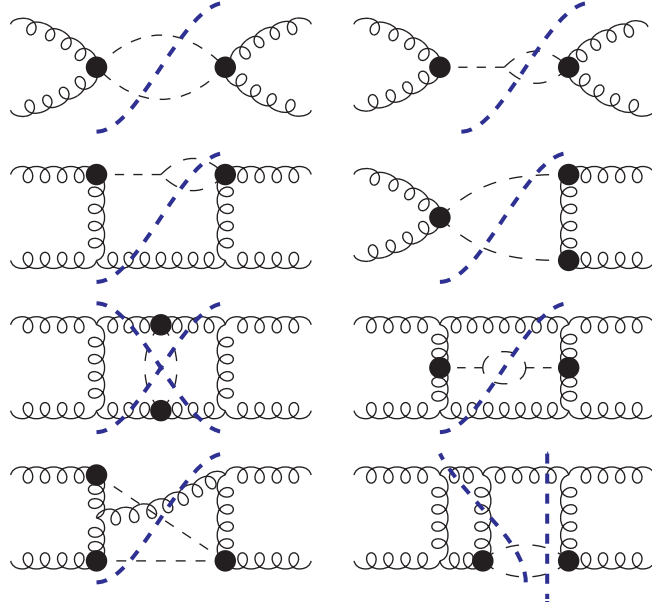


Figure 5.2: Forward-scattering diagrams for $\sigma_{gg \rightarrow HH+X}$. The first row contains LO, the second row NLO and the other rows NNLO diagrams. Some diagrams have multiple possible cuts.

GENERATING DIAGRAMS To generate and evaluate the diagrams contributing to $\sigma_{gg \rightarrow HH+X}$ we can now resort to the tools used in the previous chapters. We generate all diagrams contributing to the relevant forward-scattering amplitude using QGRAF [61] and select only those diagrams with a valid cut, following the algorithm presented in Ref. [120, 121]. In the next step we use q2e to insert Feynman rules and use exp [62, 63] to map onto integral families. Since exp can not handle forward-scattering kinematics, we need to define proper four-point integral families with three independent external momenta, q_1 , q_2 and q_3 . Then, we use FORM [64] to perform algebraic manipulations and identify the momentum q_3 with $-q_2$. Thus, we turn the four-point families into forward-scattering families. However, before performing an IBP reduction and evaluating the MIs, we first need to resolve two issues arising in the context of reverse unitarity: linearly dependent propagators and the minimization of integral families. These two topics are discussed in Sec. 5.1.1 and Sec. 5.1.2.

5.1.1 Linear dependence among propagators

As a result of applying the method of reverse unitarity, many of the forward-scattering Feynman integral families contain linearly dependent denominators. Since, in the context of IBP reduction, it is crucial to have a linearly independent set of denominators to uniquely express scalar products between loop momenta and external momenta, we

thus have to find and eliminate such linear dependencies by partial fractioning. The procedures described in this section are loosely based on the methods discussed in Ref. [121].

FINDING LINEAR DEPENDENCIES To this end, we start with a four point integral family used by exp and set $q_3 = -q_2$ in the definition of its propagators and irreducible scalar products ¹. In the following we choose all irreducible scalar products to be of the same form as propagators, i.e. to be squared linear combinations of momenta, and refer to them as *numerators*. Next, we derive a $n \times m$ dimensional matrix M_{sp} , relating the vector of denominators $\vec{D} = (D_1, \dots, D_n)$ with the vector containing all m possible scalar products $\vec{s} = (l_i \cdot l_j, l_i \cdot q_j)$ by:

$$\vec{D} = M_{\text{sp}} \vec{s} + \mathcal{O}(m_H, s) , \quad (5.9)$$

where terms involving the Higgs boson mass or s are neglected. The terms of $\mathcal{O}(m_H, s)$ can be easily reconstructed, as briefly discussed at the end of example 5.

If $\text{Rank}(M_{\text{sp}}) = r \leq n$, then there are $n - r$ independent linear relations among the D_i . To find these relations, we construct the augmented matrix $N_{\text{sp}} = (M_{\text{sp}} | \mathbb{1}_{n \times n})$ allowing us to write Eq. (5.9) as

$$0 = N_{\text{sp}} \begin{pmatrix} \vec{s} \\ \vec{D} \end{pmatrix} . \quad (5.10)$$

By performing Gaussian elimination on N_{sp} we cast it into upper reduced row echelon form. As a consequence, its last $n - r$ rows only contain entries for the denominators, thus revealing linear relations among them up to terms involving s and m_H , which can be easily restored.

An explicit example is given in the following:

Example 5 (Linear dependence at NLO)

Let us consider the following contribution to $|\mathcal{A}_{gg \rightarrow HHg}|^2$:

$$2\text{Re} \left(\text{Diagram 1} \times \left(\text{Diagram 2} \right)^* \right) \subset |\mathcal{A}_{gg \rightarrow HHg}|^2 .$$

Using the method of reverse unitarity, the phase-space integral can be written as

$$\int d\text{PS}_3 \, 2\text{Re} \left(\text{Diagram 1} \times \left(\text{Diagram 2} \right)^* \right) = \int \frac{d^D p_3 d^D p_4 (2\pi)^{3-2D} [\dots]}{[D_1]_c [D_2]_c [D_3]_c D_4 D_5 D_6} .$$

The six propagators appearing in the integral are given by

$$D_1 = p_3^2 - m_H^2 , \quad D_2 = p_4^2 - m_H^2 , \quad D_3 = (q_1 + q_2 - p_3 - p_4)^2 ,$$

¹ Note, that the described procedure also works for incomplete sets of denominators.

$$D_4 = (q_1 - p_3 - p_4)^2, \quad D_5 = (q_2 - p_3 - p_4)^2, \quad D_6 = (p_3 + p_4)^2 - m_H^2$$

and are not linearly independent.

The matrix relating the denominators and scalar products is given by

$$\vec{D} = \begin{pmatrix} 1 & 0 & 0 & 0 & 0 & 0 & 0 \\ 0 & 1 & 0 & 0 & 0 & 0 & 0 \\ 1 & 1 & 2 & -2 & -2 & -2 & -2 \\ 1 & 1 & 2 & -2 & -2 & 0 & 0 \\ 1 & 1 & 2 & 0 & 0 & -2 & -2 \\ 1 & 1 & 2 & 0 & 0 & 0 & 0 \end{pmatrix} \vec{s},$$

where $\vec{s} = (p_3^2, p_4^2, p_3 \cdot p_4, p_3 \cdot q_1, p_4 \cdot q_1, p_3 \cdot q_2, p_4 \cdot q_2)$. Its rank is 5 and thus we have one linear relation among the D_i .

To find it, we construct $N_{\text{sp}} = (M_{\text{sp}} | \mathbb{1}_{6 \times 6})$ and perform Gaussian elimination. The last row of the manipulated N_{sp} yields

$$0 = D_3 - D_4 - D_5 + D_6.$$

Setting

$$x = D_3 - D_4 - D_5 + D_6.$$

and inserting the definitions of the D_i gives $x = s - m_H^2$.

ELIMINATING LINEAR DEPENDENCIES In the next step, we need to eliminate the linear dependencies. They are of the form

$$x = \sum_{i \in I} c_i D_i, \tag{5.11}$$

where the c_i are rational numbers and x is either 0 or a linear combination of s and m_H^2 . The set I denotes the indices involved in the linear relation. We have to consider two distinct cases: $x = 0$ and $x \neq 0$.

In the case that $x \neq 0$ we can divide both sides of Eq. (5.11) by x and all the D_i . We thus arrive at the partial fractioning relation

$$\frac{1}{\prod_{i \in I} D_i} = \frac{1}{x} \sum_{i \in I} \frac{c_i}{\prod_{j \in I \setminus \{i\}} D_j}. \tag{5.12}$$

By employing Eq. (5.12) we can express every integral involving all denominators present in the linear relation as a sum of integrals with one denominator fewer. In case a linear relation involves one or more cut denominators, one or more of the integrals resulting

from applying the partial fractioning relation will vanish. In the following we continue the previous example by employing this method.

Example 6 (Linear dependence at NLO, continued)

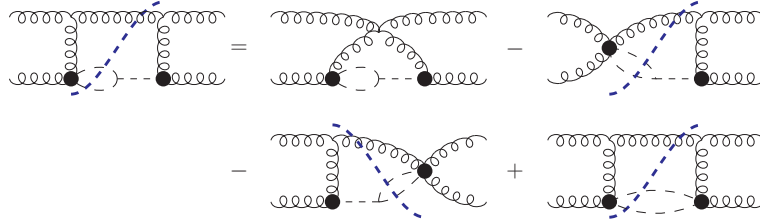
The linear relation among denominators in the previous example is given by

$$s - m_H^2 = D_3 - D_4 - D_5 + D_6 .$$

Hence, we can divide by all denominators and obtain

$$\frac{1}{D_3 D_4 D_5 D_6} = \frac{1}{s - m_H^2} \left(\frac{1}{D_4 D_5 D_6} - \frac{1}{D_3 D_5 D_6} - \frac{1}{D_3 D_4 D_6} + \frac{1}{D_3 D_4 D_5} \right) .$$

Representing the integrals involved in a pictorial way, this equation becomes



Note that the momentum q_1 enters all diagrams through the lower-left line and leaves it through the upper-right one. The first diagram on the right-hand side can be discarded, since it does not have a valid cut. The other three diagrams only have linearly independent propagators.

The case $x = 0$ requires more care. In this case Eq. (5.11) can be re-written as

$$0 = \sum_{i \in I} \frac{c_i}{\prod_{j \in I \setminus \{i\}} D_j} , \quad (5.13)$$

showing that, in contrast to the case of $x \neq 0$, there is no unique way of eliminating the linear dependence. A choice has to be taken of which combination of denominators to eliminate.

The implementation in a program of the described procedure and its applications are discussed in Sec. 5.2.

5.1.2 Minimization of integral families

As a result of partial fractioning, we are left with a large set of possibly equivalent, incomplete integral families. We thus introduce additional propagators appearing only as numerators to complete each family. Furthermore, it is advantageous to minimize the set of families to a minimal set before performing IBP reduction and other manipulations.

FINDING EQUIVALENT FAMILIES To identify equivalent integral families, we follow the method outlined in Ref. [120] with minor modifications. First we compute the two graph polynomials U and F for the top-level sector of each family. In the next step, we form the Lee-Pomeransky Polynomial $G = F + U$ [122] and canonically order the variables by employing the algorithm described in Ref. [120]. Next, we compare the canonically ordered polynomials G of all families and search for identical ones. Thus, we are left with sets of identical integral families.

Finally, we identify shifts of the loop momenta to map all members of a set of identical families onto one representative family. I.e. for the loop momenta l_i of an n -loop family we need to find a shift

$$l_i \rightarrow \tilde{l}_i = \sum_{j=1}^n c_{ij} l_j + \sum_{j=1}^2 d_{ij} q_j \quad (5.14)$$

such that all denominators match a denominator of the representative family. The c_{ij} and d_{ij} can, in principle, be arbitrary rational numbers. In the cases considered in this work, they are either 1, -1 or 0. This task is simplified by the presence of cut denominator factors which drastically reduce the possible momentum shifts, since each cut denominator has to map onto another cut denominator. Massive factors furthermore need to map onto massive factors. Thus, we first constrain the c_{ij} and d_{ij} by demanding that denominators which are both cut and massive map onto cut and massive denominators. Then we further constrain them by demanding massless cut denominators mapping onto massless cut denominators, followed by uncut massive denominators mapping onto uncut massive ones. Finally, if some freedom remains, we deal with massless uncut denominators. Once all momenta have been fixed, the remaining factors are checked for compatibility of the transformation.

EXTERNAL MOMENTUM SYMMETRIES Not all families with the same canonically ordered polynomials can be mapped onto each other by this procedure, however. The reason for this is symmetry transformations of the external momenta, i.e. transformations which leave all kinematic invariants appearing in the problem unchanged. In the case at hand, the only invariant is $s = 2q_1 \cdot q_2$ and thus transformations such as

$$(q_1, q_2) \rightarrow (-q_1, -q_2), \quad (q_1, q_2) \rightarrow (q_2, q_1), \quad (q_1, q_2) \rightarrow (-q_2, -q_1) \quad (5.15)$$

leave s unchanged. Thus, we can find a valid mapping by first applying a symmetry transformation of the external momenta followed by the search for a loop momentum shift.

Example 7 (Minimization at NLO)

One such example is given by the second and the third family on the right-hand side of the partial fractioning relation of the previous example. Neglecting numerators, their denominators are given by

$$D_1 = p_3^2 - m_H^2, \quad D_2 = p_4^2 - m_H^2, \quad D_3 = (q_1 + q_2 - p_3 - p_4)^2,$$

$$\begin{aligned}
D_4 &= (q_1 - p_3 - p_4)^2, \quad D_5 = (p_3 + p_4)^2 - m_H^2 \\
\tilde{D}_1 &= \tilde{p}_3^2 - m_H^2, \quad \tilde{D}_2 = \tilde{p}_4^2 - m_H^2, \quad \tilde{D}_3 = (q_1 + q_2 - \tilde{p}_3 - \tilde{p}_4)^2, \\
\tilde{D}_4 &= (q_2 - \tilde{p}_3 - \tilde{p}_4)^2, \quad \tilde{D}_5 = (\tilde{p}_3 + \tilde{p}_4)^2 - m_H^2.
\end{aligned}$$

Here the D_i belong to the first and the \tilde{D}_i to the second family. The denominators with $i \in \{1, 2, 3\}$ are cut. The requirement of the cut, massive denominators being equal fixes all d_{ij} to vanish. Combining this with the requirement for the massless, cut denominator leaves two solutions:

1. $\tilde{p}_3 = p_3$ and $\tilde{p}_4 = p_4$
2. $\tilde{p}_3 = p_4$ and $\tilde{p}_4 = p_3$

Both solutions are compatible with $\tilde{D}_5 = D_5$ but do not lead to $\tilde{D}_4 = D_4$. This situation is resolved by first applying the transformation $(q_1, q_2) \rightarrow (q_2, q_1)$ to the \tilde{D}_i . This leads to $\tilde{D}_4 = (q_1 - \tilde{p}_3 - \tilde{p}_4)^2$ while all other denominator factors remain the same. Thus, both possible solutions for the \tilde{p}_i are valid shifts in this case and we can pick either of them.

Having identified a valid momentum shift for a family, we now can re-write all numerators. First we apply the relevant symmetry transformation, as well as momentum shift to them and then re-express the terms as linear combination of denominators and numerators of the representative family.

As a result of the above procedure, we arrive at a small set of integral families. However, this might not yet be a minimal set. It is possible that some families have more numerators than others, as a consequence of the involved linear relations. In this case, these families might be embeddable into the families with fewer numerators. To this end, try to identify the top-level sector of families with more numerators with subsectors of families with a lower amount of numerators. Thus we can find mappings to identify families with subsectors of other families.

As in the case of finding linear relations and partial fractioning, this procedure has been implemented in the program described in Sec. 5.2.

5.2 LIMIT

In this section we discuss the implementation of the methods discussed in Sec. 5.1 in the Mathematica package LIMIT (Linearly Independent and MInimal Topologies). First, we briefly describe its structure in Sec. 5.2.1, followed by an in-depth example focusing on Higgs boson pair production in Sec. 5.2.2. We conclude by presenting applications of LIMIT to different problems.

5.2.1 *Structure of the program*

The program package is divided into two independent modules. The first deals with partial fraction decomposition and the second with the minimization of families.

PARTIAL FRACTION DECOMPOSITION The first module is centered around the function `ProcessTopology` which performs all operations described in Sec. 5.1.1 in an automated manner.

INPUT It takes the following eight arguments:

1. `orig`: list of denominators of the original family.
2. `name`: name of the original family, used in the code generation only.
3. `cut`: list of cuts that should be taken into account. Each of them has to be a list with the same length as `orig`, where a 0 indicates an uncut propagator and a 1 a cut one.
4. `int`: list of internal (loop) momenta.
5. `ext`: list of external momenta.
6. `mass`: list of masses of internal lines.
7. `kinrep`: list of replacements for products of external momenta.
8. `numerators`: list of numbers indicating denominators only appearing as numerators. Each entry is a position of a denominator in the `orig` list.

WORKFLOW To find the linear relations, the function `ProcessTopology` now performs the following steps:

1. Form all possible scalar products between momenta in `int` and `ext`.
2. Compute M_{sp} using the propagators in `orig` following Eq. (5.9).
3. Following Eq. (5.10) construct N_{sp} and apply the built-in Mathematica function `RowReduce`, resulting in linear relations among denominators.
4. Restore the masses and external invariants involved in the linear relations.

Instead of directly eliminating linear dependencies by deriving partial fractioning relations of the form Eq. (5.12), two more intermediate steps are applied first:

5. Pick all linear relations which involve at least one numerator and solve them for one of those numerators.

6. Select linear relations relating exactly two denominators and no masses or external invariants. These directly map one denominator onto another one.

These two steps reduce the set of linear relations for which partial fractioning relations of the form Eq. (5.12) need to be derived. In both steps FORM code is generated that applies the relations found in each step to scalar integrals of the form $\text{name}(n_1, \dots, n_x)$ where x is the number of elements of `orig` and the n_x are the powers of the individual denominators in `orig`.

Finally, for one of the remaining linear relations the partial fractioning relation, as well as replacement rules for cases where some of the denominators arise with negative powers, are derived and FORM code is generated. The way denominators with negative powers are treated is based on [120, 121]. In the case of $x = 0$ discussed in Sec. 5.1.1, solve the linear relation to eliminate cut propagators if possible, as this reduces the number of generated terms. If none of the involved propagators is cut, we simply eliminate the lexicographically highest propagator.

Since only one of the remaining linear relations is eliminated, the resulting families might still be linearly dependent. Instead of also eliminating these linear dependencies in the same step the output of `ProcessTopology` might need to be processed by `ProcessTopology` again. While this requires several calls of `ProcessTopology` on the user side, it keeps the involved `Mathematica` code simple and the generated FORM code transparent, due to its iterative nature.

OUTPUT The output of `ProcessTopology` is a list with the following entries:

1. `names`: list of names of the resulting families, based on the original name of the input family.
2. `props`: list of denominators of the resulting families.
3. `cuts`: list of cuts of the resulting families.
4. `numerators`: list of numerators of the resulting families.
5. `form`: FORM code string with all replacement rules.
6. `done`: 0 in case one or more of the resulting families is still linearly dependent, 1 otherwise.

Both cuts and numerators are in the same format as for the input.

After performing partial fractioning the function `DeleteZeroTopos` can discard all families from the returned list which do not possess a valid cut. To this end, the output of `ProcessTopology` as well as the input cut are passed to `DeleteZeroTopos`, which then checks if the cuts of the output families contain the same number of cut line as the input ones. In case none of the cuts agree with the input cut, the family is discarded and a FORM statement which nullifies the family is appended to the code string.

As an example consider the family of example 6:

Example 8 (Application of LIMIT I)

To demonstrate the partial fractioning module of LIMIT we take the integral family defined by the denominators in example 6 as an input and add three more numerators

$$D_7 = (q_1 - p_3)^2, D_8 = (q_2 - p_4)^2, D_9 = (q_2 - p_3)^2.$$

To perform partial fractioning we load LIMIT and define the input as

```
Get["LIMIT.m"];
props = {p3^2 - mh2, p4^2 - mh2, (q1 + q2 - p3 - p4)^2,
  (q1 - p3 - p4)^2, (q2 - p3 - p4)^2, (p3 + p4)^2 - mh2,
  (q1 - p3)^2, (q2 - p4)^2, (q2 - p3)^2};
cuts= {{1, 1, 1, 0, 0, 0, 0, 0, 0}};
nums = {7, 8, 9};
loopmom = {p3, p4};
externalmom = {q1, q2};
masses = {mh2};
kinrep = {q1^2 -> 0, q2^2 -> 0, q1*q2 -> s/2};
```

Here, mh2 is m_H^2 . Finally we call ProcessTopology by

```
ret = ProcessTopology[props, "examplefam", cutorig,
  loopmom, externalmom, masses, kinrep, nums];
```

LIMIT finds two linear relations:

$$0 = s + D_1 + D_2 - D_3 + D_4 + 2D_5 - 2D_6 - D_8 - D_9,$$

$$0 = s - m_H^2 - D_3 + D_4 + D_5 - D_6.$$

The first relation involves two numerators and thus is solved to generate the replacement rule

$$D_9 \rightarrow s + D_1 + D_2 - D_3 + D_4 + 2D_5 - 2D_6 - D_8.$$

The FORM code generated in this case reads

```
repeat id
examplefam(n1?,n2?,n3?,n4?,n5?,n6?,n7?,n8?,n9?neg_) =
  (-1)*(examplefam(n1,n2,n3-1,n4,n5,n6,n7,n8,n9+1)) +
  (-1)*(examplefam(n1,n2,n3,n4,n5,n6,n7,n8-1,n9+1)) +
  (2)*(examplefam(n1,n2,n3,n4,n5-1,n6,n7,n8,n9+1)) +
  (-2)*(examplefam(n1,n2,n3,n4,n5,n6-1,n7,n8,n9+1)) +
  examplefam(n1-1,n2,n3,n4,n5,n6,n7,n8,n9+1) +
  examplefam(n1,n2-1,n3,n4,n5,n6,n7,n8,n9+1) +
  examplefam(n1,n2,n3,n4-1,n5,n6,n7,n8,n9+1) +
  (s)*(examplefam(n1,n2,n3,n4,n5,n6,n7,n8,n9+1));
```

In the next step the second relation is transformed to partial fraction integrals involving the denominators D_3 through D_6 by

```
repeat id
examplefamno0(n1?, n2?, n3?pos_, n4?pos_, n5?pos_, n6?pos_, n7?, n8?) =
  (-Den(mh2 - s)*examplefamno0(n1, n2, n3-1, n4, n5, n6, n7, n8)) +
  (Den(mh2 - s)*examplefamno0(n1, n2, n3, n4-1, n5, n6, n7, n8)) +
  (Den(mh2 - s)*examplefamno0(n1, n2, n3, n4, n5-1, n6, n7, n8)) +
  (-Den(mh2 - s)*examplefamno0(n1, n2, n3, n4, n5, n6-1, n7, n8));
id examplefamno0(n1?, n2?, 0, n4?, n5?, n6?, n7?, n8?) =
  examplefamno0p1(n1, n2, 0, n4, n5, n6, n7, n8);
id examplefamno0(n1?, n2?, n3?, 0, n5?, n6?, n7?, n8?) =
  examplefamno0p2(n1, n2, n3, 0, n5, n6, n7, n8);
id examplefamno0(n1?, n2?, n3?, n4?, 0, n6?, n7?, n8?) =
  examplefamno0p3(n1, n2, n3, n4, 0, n6, n7, n8);
id examplefamno0(n1?, n2?, n3?, n4?, n5?, 0, n7?, n8?) =
  examplefamno0p4(n1, n2, n3, n4, n5, 0, n7, n8);
```

Thus we are left with the four families shown in example 6.

MINIMIZATION The second module uses the Mathematica package LiteRed [71, 72] to perform the minimization of the integral families.

GENERATING INPUT FOR LITERED To this end, the function GenerateLiteRedData generates all information relevant to find mappings between families with LiteRed. Its arguments are

1. fam: list with the following four entries:
 - a) name: string with the name of the family.
 - b) propagators: list of propagators in LiteRed format, i.e. with scalar products denoted by sp.
 - c) cut: list of cut propagators. Note that in contrast to the partial fractioning, LiteRed can only handle one cut per family.
 - d) numerators: list of positions of numerators in Propagators.
2. loopmoms: list of loop momenta.
3. dir: string with the directory name to hold all files.
4. sym: external momenta symmetries. If omitted, built-in LiteRed routines are used to search for them instead.

FINDING EQUIVALENT FAMILIES After calling `GenerateLiteRedData` for all families under consideration, the function `GroupTopologiesBySignature` can compute the canonically ordered Lee-Pomeransky polynomial G for the top-level sectors and group the families by them. The input should be a list of all fam lists passed to `GenerateLiteRedData`. Its output takes the form

```
{{signature, topsectors, numerators}, ... }
```

where `signature` is an internal identifier for the polynomial G of each set of equivalent families, `topsectors` is a list containing the top-level sector of each family in the group in `LiteRed` notation and `numerators` is the number of numerators.

MAPPING EQUIVALENT FAMILIES Based on this output, the function `MapTopoGroups` takes a group of equivalent families and calls the `LiteRed` function `FindExtSymmetries` to map all families onto one representative family. The second argument of `MapTopoGroups` is a list of symmetry relations between external momenta, such as the ones in Eq. (5.15). Its output takes the form

```
{{signature, NameOfFirstEntry, NumberOfNumerators},  
 {signature, UnmappedFamilies, NumberOfNumerators}}
```

and an example is shown in example 9. Here `NameOfFirstEntry` is the name of the representative family, `NumberOfNumerators` is the number of numerators and `UnmappedFamilies` is a list of all families which have the same signature as the representative family, but could not be mapped onto it by `FindExtSymmetries`. There are two possible reasons for `UnmappedFamilies` not being an empty list. Firstly, in most cases, an external momentum symmetry is missing. The second problem might arise when dealing with cut propagators. In this case safety measures in `FindExtSymmetries` are active, such that no possibly wrong mappings are done. This also excludes some correct mappings and thus some families might remain unmapped. In this case, `MapTopoGroups` can be called again, with the families in `UnmappedFamilies` as an input.

EMBEDDING FAMILIES Should we only deal with families with the same number of numerators, we could now generate FORM code for all mappings. In the case that there are some families with more numerators than others, we can try to embed them into the families with fewer numerators. To this end, we group the representative families for each signature by the number of numerators by calling `SortMappedTopos` with the list of all mapped groups as input. The output takes the form

```
{{NumberOfNumerators, Names}, ... }
```

where `Names` is the list of names of the representative families with the same number of numerators. The output now can be passed to `EmbedMappedTopos` which tries to embed the families with more numerators into the ones with fewer numerators.

GENERATING CODE Finally, after mapping all families onto a minimal set, FORM code applying all mappings can be generated. For this purpose we provide several functions converting LiteRed rules to FORM identification statements, each of them returning a string for including the generated files:

- `ReturnZeroFORM[fams_, dir_]`: writes out rules for nullifying vanishing integrals in the families `fams` into the directory `dir`.
- `ReturnSymFORM[fams_, dir_, dirzero_]`: writes out rules for mapping integrals in equivalent sectors in each of the families in `fams` to minimize the number of integrals before mapping. `dir` is the output directory and `dirzero` is the directory where the rules generated by `ReturnZeroFORM` can be found.
- `ReturnMappingFORM[group_, dir_]`: writes out rules for mapping integrals from families with the same signature into a representative family. `group` should be an output group of `MapTopoGroups` and `dir` is the directory to hold the FORM statements.
- `ReturnSymandEmbedFORM[embeddedfams_, dir_, dirsym_, dirzero_]`: writes out rules for symmetrizing and embedding the representative families with more numerators into families with fewer numerators. The rules generated by `ReturnSymFORM` and `ReturnZeroFORM` need to be in `dirsym` and `dirzero`, respectively.

In the following we display the use of the minimization module on the example of the families resulting from example 8

Example 9 (Application of LIMIT II)

In the first step, we load LIMIT which subsequently loads LiteRed and define the momenta and variables appearing in the problem:

```
Get["LIMIT.m"];
SetDim[d];
Declare[{p3, p4, q1, q2}, Vector, {s, mh2}, Number];
sp[q1, q1] = 0;
sp[q2, q2] = 0;
sp[q1, q2] = s/2;
```

In the next step, we define two further integral families which do not appear in example 8:

```
{{"T1", {sp[p3, p3], sp[p4, p4], sp[p3 + q1, p3 + q1],
  sp[p4 + q1, p4 + q1], -mh2 + sp[p3 + q1 + q2, p3 + q1 + q2],
  -mh2 + sp[p4 + q1 + q2, p4 + q1 + q2],
  -mh2 + sp[p3 - p4, p3 - p4]}},
{0, 1, 0, 0, 1, 0, 1}, {}},
{"L2", {sp[p3 + q1, p3 + q1],
```

```

sp[p4 + q1, p4 + q1], -mh2 + sp[p4 + q1 + q2, p4 + q1 + q2],
sp[p4 + q2, p4 + q2], sp[p3 + q2, p3 + q2],
sp[p3, p3], -mh2 + sp[p3 - p4, p3 - p4]],
{0, 0, 1, 0, 0, 1, 1}, {}}}

```

They can be depicted as



where solid lines are massive with mass m_H and dashed lines are massless. The momentum q_1 enters and leaves via the lines with the arrows. In the next step we add the new and old families together in one list `fams` and run all necessary LiteRed commands by

```
GenerateLiteRedData[#, {p3, p4}, "LR"] & /@ fams;
```

Now, we compute the signatures of each family and group them:

```
uniquefams = GroupTopologiesBySignature[fams];
```

The result is stored in `uniquefams` and given by

```

{{20216085449316752538415658696276286202,
  {js[T1, 1, 1, 1, 1, 1, 1, 1]}, 0},
 {118632354605253600004828853610037442495,
  {js[L2, 1, 1, 1, 1, 1, 1, 1]}, 0},
 {297847790944173985318275321513850848248,
  {js[examplefamno0p2no0, 1, 1, 1, 1, 1, 0, 0],
   js[examplefamno0p3no0, 1, 1, 1, 1, 1, 0, 0]}, 2},
 {224975629750526536673378408099951220967,
  {js[examplefamno0p4no0, 1, 1, 1, 1, 1, 0, 0]}, 2}}

```

showing that two of the three non-vanishing families of example 8 are actually equivalent. They can be mapped onto each other by

```

mappedfams =
  MapTopoGroups[#, {{q1 -> q1, q2 -> q2}, {q1 -> q2, q2 -> q1},
    {q1 -> -q1, q2 -> -q2}, {q1 -> -q2, q2 -> -q1}}] &
  /@ uniquefams;

```

Here the list containing the external momentum mappings contains all symmetries of Eq. (5.15). As a result, `examplefamno0p3no0` is mapped onto `examplefamno0p2no0`. In the next step, we discard the empty information about unmapped families:

```
cleanedfams = First[Drop[Transpose[mappedfams], -1]];
```

The output is given by

```
{20216085449316752538415658696276286202, T1, 0},
{118632354605253600004828853610037442495, L2, 0},
{297847790944173985318275321513850848248, examplefamno0p2no0, 2},
{224975629750526536673378408099951220967, examplefamno0p4no0, 2}}
```

Next, we try to embed the two remaining families with two numerators into the two families without numerators that we added above:

```
sortedfams = SortMappedTopos[cleanedfams];
finalfams = EmbedMappedTopos[sortedfams,
  {{q1 -> q1, q2 -> q2}, {q1 -> q2, q2 -> q1},
  {q1 -> -q1, q2 -> -q2}, {q1 -> -q2, q2 -> -q1}}];
```

As a consequence, examplefamno0p2no0 is embedded into T1 and examplefamno0p4no0 into L2. The final output reads

```
{{0, {{20216085449316752538415658696276286202, T1, 0},
      {118632354605253600004828853610037442495, L2, 0}}},
 {2, {}}}
```

indicating, that there are no families with two numerators are left.

5.2.2 Application to Higgs boson pair production

In the following we discuss the application of LIMIT to the process of Higgs boson pair production. There are three different sets of forward-scattering integral families with one or more cuts which appear during the calculation:

- Two-loop families with one or two three-particle cuts that appear in the real corrections at [NLO](#) and real-virtual corrections involving three top-quark loops at [NNLO](#).
- Three-loop families with a three particle cut, appearing in the remaining real-virtual corrections at [NNLO](#).
- Three-loop families with one or two four-particle cuts contributing to the double real emission corrections at [NNLO](#).

For each of these sets of integral families LIMIT is applied to the four-point families required for exp to map all diagrams.

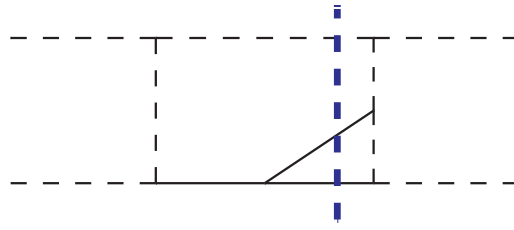


Figure 5.3: Sample template integral family. Solid lines denote Higgs bosons and dashed lines massless particles. The blue dashed lines indicate the cut.

GENERATING FOUR-POINT FAMILIES To generate all four-point families for exp, first a set of *template* families are chosen, such as the one depicted in Fig. 5.3. These families have four external momenta r_1, r_2, r_3 and r_4 . The template momenta enter the family in an anti-clockwise manner, starting from the upper left leg. In the next step, the template momenta are replaced by permutations of the momenta used by exp: q_1, q_2, q_3 and $q_4 = -q_3 - q_2 - q_1$. Only permutations which exchange $q_1 \leftrightarrow q_2, q_3 \leftrightarrow q_4$, or $q_1, q_2 \leftrightarrow q_3, q_4$ are needed and thus we are left with eight versions of each template family.

TWO-LOOP PHASE-SPACE FAMILIES The real corrections at NLO and the subset of real-virtual corrections at NNLO with either three effective Higgs boson–gluon vertices and LO Wilson coefficients, as discussed in chapter 6, or two effective vertices with one LO and one NLO Wilson coefficient, as discussed in Sec. 7.2.2, each lead to two-loop phase space integral families with three-particle cuts.

The required template families are depicted in the leftmost column of Fig. 5.4. Note that eight copies are required only for the first template family. The second template family is symmetric under $r_1, r_2 \leftrightarrow r_3, r_4$ and thus only four copies of it are needed. Similarly, the last family is symmetric under $r_1 \leftrightarrow r_2$. Thus, 16 families are required in total. After specifying forward-scattering kinematics by setting $q_3 = -q_2$ and partial fractioning, the eight families resulting from the first template family are mapped onto the three temporary families depicted in the middle column. Each of them has six lines and one numerator. In the next step, the four copies of each of the other two template families are minimized, resulting in the families T_1, T_2 and X_1 in the rightmost column. Finally the three temporary families can be embedded into the families T_1 and T_2 , as well as the family L_2 . Thus, LIMIT maps the 16 original families on four final forward-scattering families. Note, that the families with two cuts are split into two distinct families in intermediate steps, so that LiteRed can process them, and merged again in the end.

THREE-LOOP PHASE SPACE FAMILIES, THREE-PARTICLE CUTS The remaining real-virtual corrections at NNLO with two effective vertices and LO Wilson coefficients lead to

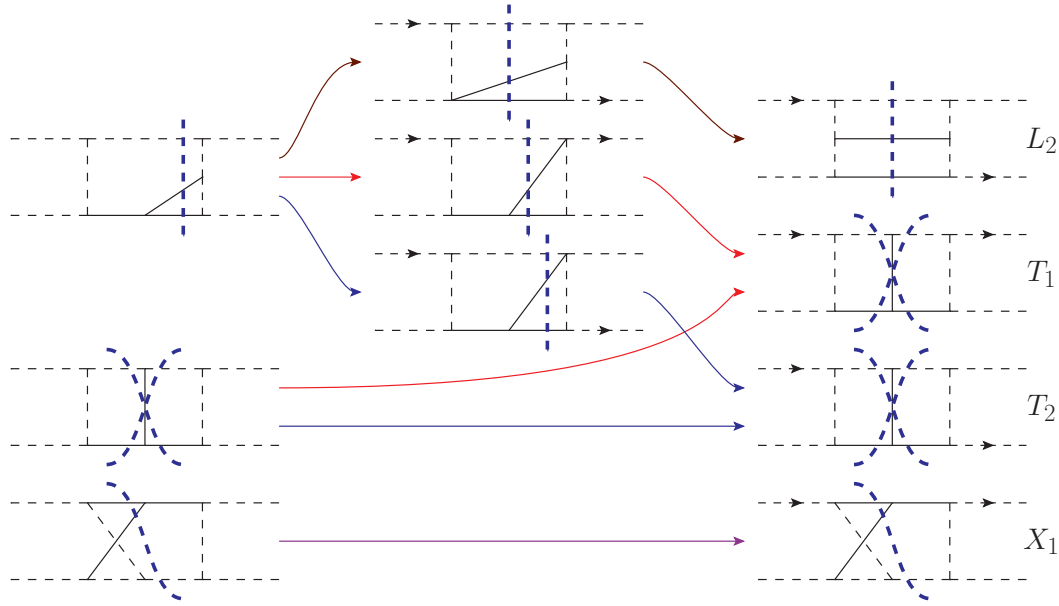


Figure 5.4: Integral families relevant for the two-loop phase-space contributions at **NLO** and **NNLO**. Arrows on external lines indicate where q_1 enters or leaves the integral. The lines follow the conventions of Fig. 5.3.

three-loop integrals with three-particle cuts. In contrast to the previous case, we deal with families involving one actual loop integration. All relevant template families are depicted in the leftmost column of Fig. 5.5. While the first three template families yield eight actual integral families each, the fourth one is symmetric under $r_1 \leftrightarrow r_2$ and thus only yields four. In total, the four template families lead to 28 actual families. The partial fractioning of the second and third group of families leads to three new families with eight instead of nine lines. Two of each of them can be embedded into the two families $T_{3pt,1}$ and $T_{3pt,2}$ resulting from the minimization of the first group of template families. We keep the remaining two families with eight lines as they are and do not add extra lines. As in the case of the two-loop families all non-planar four-point families map onto one non-planar forward scattering family.

THREE-LOOP PHASE SPACE FAMILIES, FOUR-PARTICLE CUTS The integral families with four-particle cuts can be divided into three subsets. Two of them contain planar families and the third one non-planar ones.

The first planar subset contains four template families, depicted in Fig. 5.6. The second template family is symmetric under $r_1, r_2 \leftrightarrow r_3, r_4$ and thus leads to only four distinct four-point families. Overall, there are 28 four-point families resulting from this subset of template families. Partial fractioning of the template families generates eight families with one line fewer, of which seven are embedded into the families P_1 , P_2 and P_3 . The

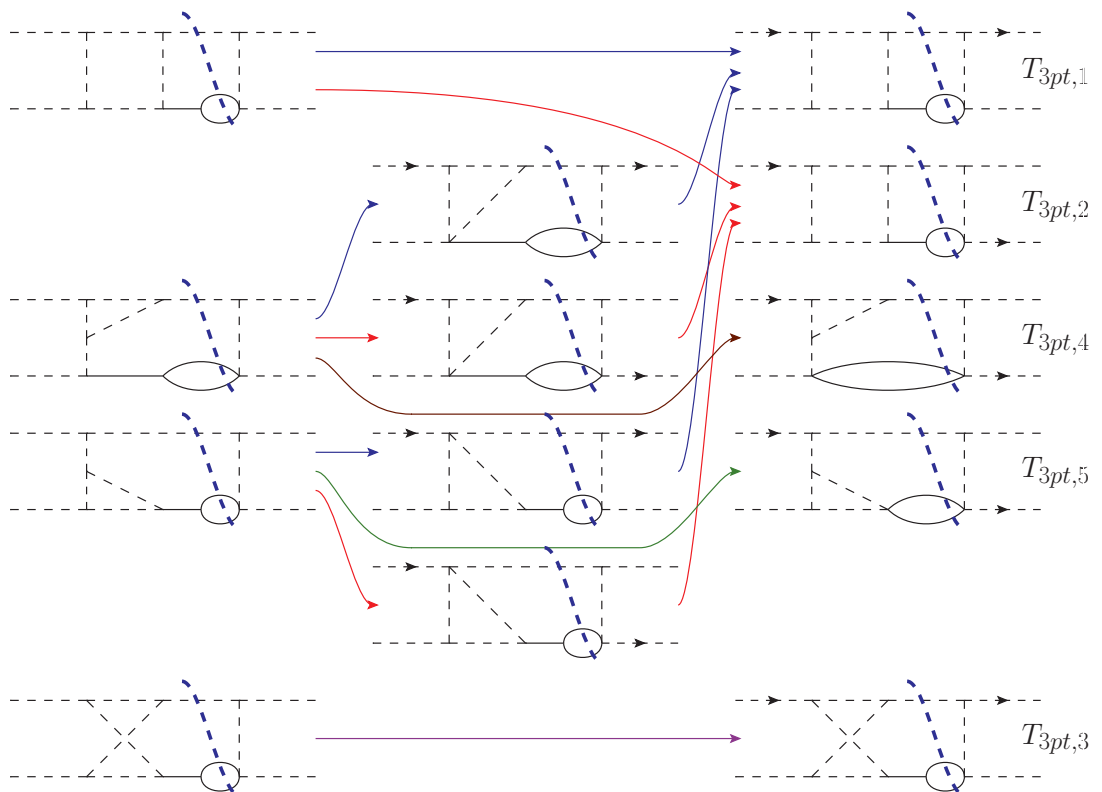


Figure 5.5: Integral families relevant for the three-loop real-virtual phase-space contributions at NNLO. The lines follow the conventions of Fig. 5.3.

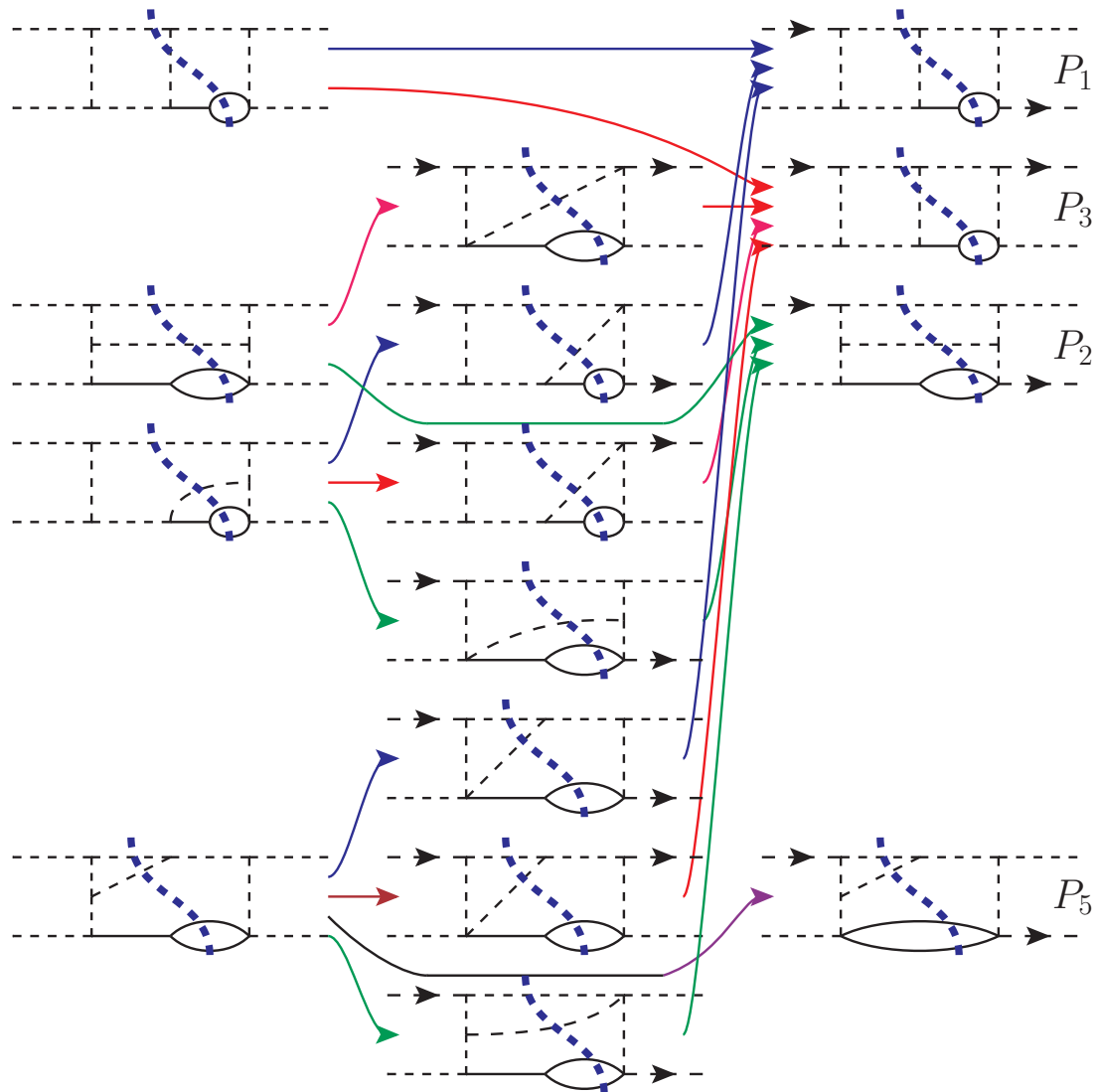


Figure 5.6: Subset of the planar, three-loop real-real phase-space contributions at NNLO. The lines follow the conventions of Fig. 5.3.

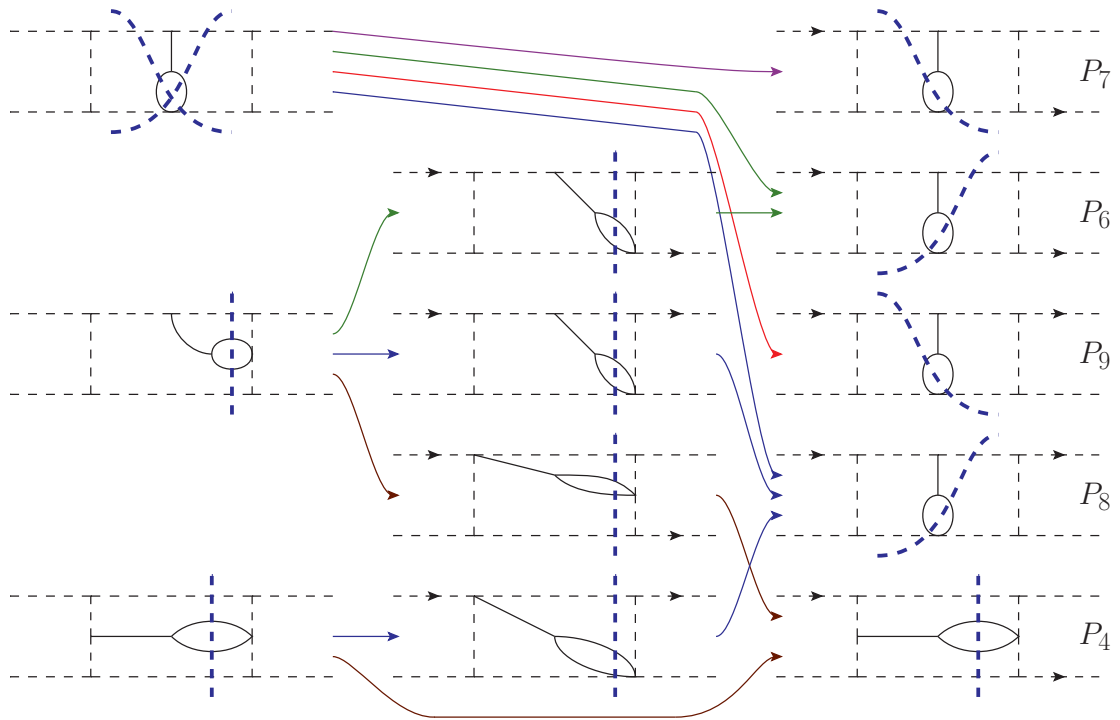


Figure 5.7: Second subset of the planar, three-loop real-real phase-space contributions at NNLO. The lines follow the conventions of Fig. 5.3.

one remaining eight-line family can not be embedded into any of the other families and thus is chosen as one of the final forward-scattering families.

We start off with three template families in the second set of planar families, depicted in Fig. 5.7. The first two template families are symmetric under $r_1, r_2 \leftrightarrow r_3, r_4$ and $r_1, r_3 \leftrightarrow r_2, r_4$, thus leading to two four-point families each. In total, there are 12 four-point families resulting from this set of template families. For LIMIT to perform the minimization using LiteRed, we need to split up the families resulting from the first template family, since they have two valid four-particle cuts. Thus, in the end we are left with four final families resulting from the first template family. Partial fractioning leads to four temporary families with one line fewer that can be embedded into the final forward-scattering families. Furthermore, the last of the template families leads to the final family P_4 .

Finally we have the four non-planar template families depicted in the first column of Fig. 5.8. The first two of them are symmetric under $r_1 \leftrightarrow r_2$ and $r_1, r_2 \leftrightarrow r_3, r_4$ respectively, thus leading to four four-point families each. The other two possess no external momentum symmetries and we are thus left with 24 non-planar four-point families. Partial fractioning leads to two temporary families which can be embedded into the final five non-planar forward-scattering families.

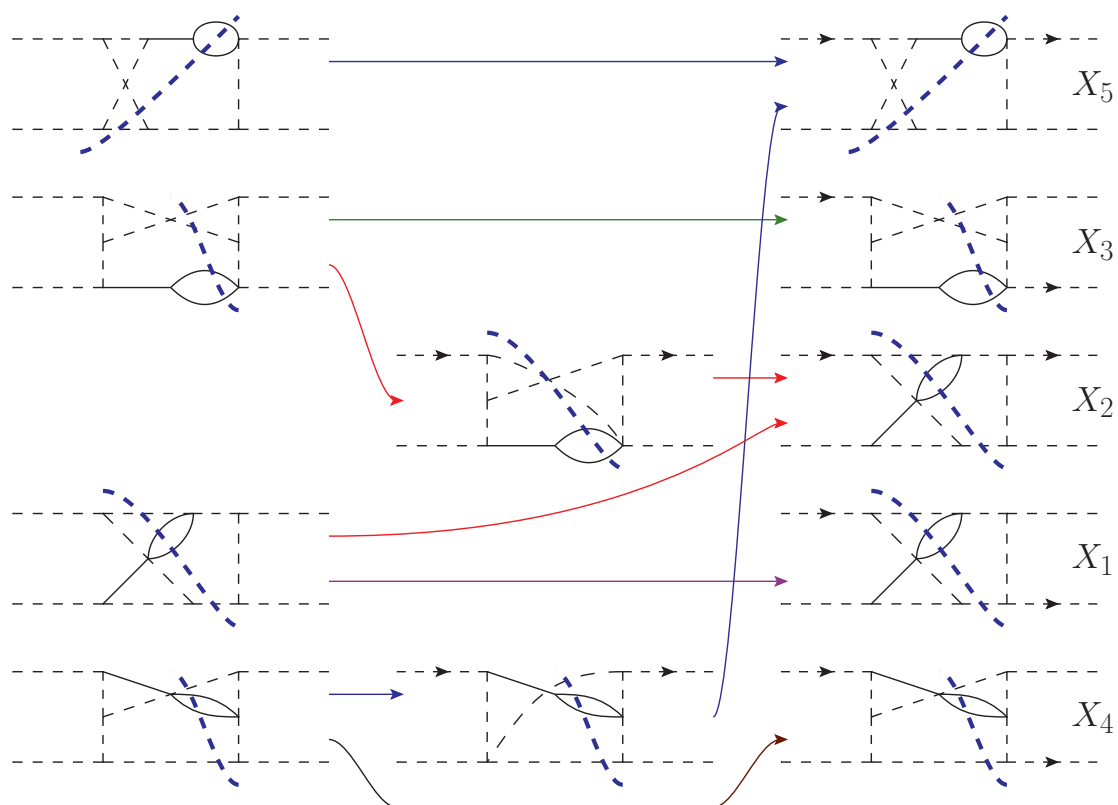


Figure 5.8: Non-planar, three-loop real-real phase-space contributions at NNLO. The lines follow the conventions of Fig. 5.3.

SUMMARY The application of LIMIT to all integral families contributing to the real corrections for Higgs boson pair production at NLO and NNLO provides us with FORM code to perform all mappings described and depicted above. In total, LIMIT maps 16 two-loop four-point families onto four forward-scattering families, 28 three-loop, three-particle cut families onto five forward-scattering families, as well as 64 three-loop, four-particle cut families onto nine forward-scattering families.

5.2.3 Further applications

In this section we briefly discuss the application of LIMIT to other problems requiring the partial fractioning of integral families: matching coefficients for non-relativistic QCD and the relation between the $\overline{\text{MS}}$ renormalized quark mass and the kinetic quark mass.

MATCHING COEFFICIENTS FOR NON-RELATIVISTIC QCD In Ref. [123], two-loop matching coefficients between QCD and non-relativistic QCD of four-fermion operators are computed. These operators are relevant e.g., for top-quark pair production close to threshold in electron-positron collisions. To compute higher order corrections to these operators, the scattering amplitude of a massive quark and its anti-quark needs to be computed in the limit where both of them have the same momentum p and are on-shell: $p^2 = m^2$. This kinematic setup can be obtained from the forward-scattering kinematics relevant for phase-space integrals by also setting $q_1 = q_2 = p$. Furthermore, no cuts are involved. Thus, the application of LIMIT is straightforward.

KINETIC MASS In Ref. [124] the relation between the kinetic quark mass, which is commonly used to study semi-leptonic B -meson decays, and the $\overline{\text{MS}}$ renormalized quark mass is computed through three loops. In this problem, forward-scattering amplitudes of a heavy quark with mass m , as well as momentum p , and an external current with momentum q need to be computed. Here, $p^2 = m^2$ and $(p + q)^2 = s$. To simplify the computation, a threshold expansion [56, 125] is performed and each loop momentum either scales as m (hard) or as y/m (ultra-soft), where $y = m^2 - s$. Only the purely ultra-soft region is relevant and the expansion in y leads to linearly dependent integral families. At three loops, performing partial fractioning of the 510 linearly dependent families contributing to the purely ultra-soft region leads to 2650 linearly independent families. Subsequently minimizing the linearly independent families leads to 14 three-loop families in the purely ultra-soft region.

CONTRIBUTIONS WITH BOTH HIGGS BOSONS COUPLING TO DIFFERENT TOP-QUARK LOOPS AT NNLO

Having established a powerful and flexible tool-chain for handling phase-space integrals within the context of reverse unitarity in chapter 5, we are now in the position to compute the partonic cross-sections contributing to the pair-production of Higgs bosons at NNLO. In this chapter, we will focus on the interference contributions of amplitudes where both Higgs bosons couple to different top-quark loops with amplitudes where both Higgs bosons couple to the same top-quark loop as computed in Ref. [35]. Sample contributions for the gluon-initiated channel at NLO and NNLO are shown in Fig. 6.1.

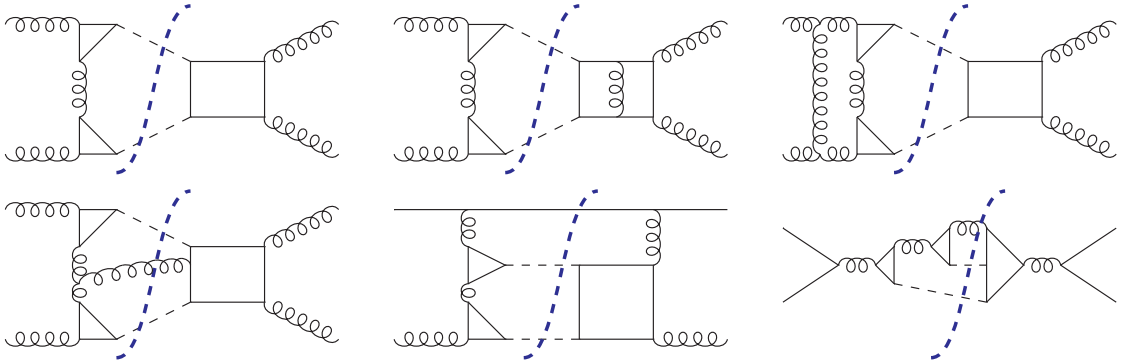


Figure 6.1: Contributions under consideration. Diagrams in the first row show NLO, as well as double-virtual NNLO contributions. The diagrams in the second row are real-radiative contributions.

The main objective of this chapter is the computation of the real-radiative contributions, i.e. diagrams like in the second row of Fig. 6.1, in the LME. To this end we introduce so-called *building blocks* to perform the LME of the cut five-loop forward-scattering diagrams in an efficient manner. Furthermore, the use of reverse unitarity allows us to apply IBP reduction to the phase-space integrals, reducing them to a small set of MIs, which we need to evaluate. These MIs are then computed as an expansion around the production threshold $\delta \approx 0$ with

$$\delta = 1 - 4x \quad \text{with} \quad x = \frac{m_H^2}{s}, \quad (6.1)$$

as well as exact in x .

The real-radiative contributions then have to be combined with virtual contributions, i.e. diagrams such as the ones in the first row of Fig. 6.1, and collinear counterterms to cancel soft and collinear divergences, respectively.

STRUCTURE OF THE CHAPTER We discuss the individual steps for the computations of the real-virtual contributions under consideration in Sec. 6.1. The computation of the phase-space master integrals is presented in Sec. 6.2. Finally we present analytical and numerical results for the different partonic channels in Sec. 6.3.

6.1 CONTRIBUTIONS TO THE TOTAL CROSS-SECTION

The subset with both Higgs bosons coupling to different top-quark loops arises first at NLO. We can write their contribution to the total partonic cross-section for Higgs boson pair production as

$$\sigma_{ij \rightarrow HH+X}(s, \rho)|_{n_h^3} = \frac{\alpha_s^{(5)}(\mu)}{\pi} \delta_{ig} \delta_{jg} \sigma_{gg}^{(1), m_h^3}(s, \rho) + \left(\frac{\alpha_s^{(5)}(\mu)}{\pi} \right)^2 \sigma_{ij}^{(2), m_h^3}(s, \rho). \quad (6.2)$$

Here $\rho = m_H^2/M_t^2$ with the top-quark mass M_t renormalized in the OS scheme and $ij \in \{gg, qg, \bar{q}g, q\bar{q}\}$ denote the partonic sub-channels. Note, that since $\sigma_{ij}^{(0), m_h^3}$ is absent, $\sigma_{gg}^{(1), m_h^3}$ effectively acts as a LO contribution.

In the following we introduce the different partonic channels in Sec. 6.1.1 and discuss the computational setup in Sec. 6.1.2. Furthermore, we briefly discuss the virtual corrections entering the gluon-gluon initial state at NNLO in Sec. 6.1.3, as well as the counterterms dealing with collinear singularities in Sec. 6.1.4.

6.1.1 Real-radiative corrections

To obtain the various contributions to $\sigma_{ij}^{(2), m_h^3}$, as well as $\sigma_{gg}^{(1), m_h^3}$, we need to average over the possible colour and helicity states of the initial-state partons. For each initial-state gluon we get a prefactor of

$$a_g = \frac{1}{N_A(2-2\epsilon)}, \quad (6.3)$$

while for each initial-state quark we get

$$a_q = \frac{1}{2N_c}. \quad (6.4)$$

The flux factor is given by $1/(2s)$.

Since in the final state we always have two identical Higgs bosons we need to introduce a factor of 1/2. This factor is, however, implicitly accounted for by the symmetry factor of the forward-scattering Feynman diagrams we consider.

THE GLUON-GLUON INITIAL STATE In order to simplify the treatment of external gluons and handle the propagators of cut gluons on the same footing as regular gluon propagators we use

$$\sum_{\lambda} \epsilon_{\mu}^{(\lambda)*}(q_1) \epsilon_{\nu}^{(\lambda)}(q_2) \rightarrow -g_{\mu\nu} \quad (6.5)$$

as sum over polarizations. Since this choice of the polarization sum is not physical, we also need to compute forward-scattering amplitudes with ghosts as external particles and consider cuts involving ghosts.

At **NLO** the ghost channels do not contribute to the subset with both Higgs bosons coupling to different top-quark loops. We can therefore write this contribution as

$$\sigma_{gg}^{(1),m_h^3} = \frac{a_g^2}{2s} \widetilde{\text{Disc}} \left(\mathcal{A}_{gg \rightarrow gg}^{(1),m_h^3} \right). \quad (6.6)$$

$\widetilde{\text{Disc}}$ denotes the contributions to the discontinuity of \mathcal{A} stemming from cuts involving two Higgs bosons and possibly massless partons, but no cuts involving top quarks or only one Higgs boson. In the case of $\sigma_{gg}^{(1),m_h^3}$ only one cut with exactly two Higgs bosons contributes.

At **NNLO** we need to take into account all possible ghost forward-scattering amplitudes and subtract their contributions from the gluon-gluon forward scattering amplitude obtained with the polarization sum in Eq. (6.5). As a consequence, $\sigma_{gg}^{(2),m_h^3}$ is given by

$$\begin{aligned} \sigma_{gg}^{(2),m_h^3} = \frac{a_g^2}{2s} & \left[\widetilde{\text{Disc}} \left(\mathcal{A}_{gg \rightarrow gg}^{(2),m_h^3} \right) - \widetilde{\text{Disc}} \left(\mathcal{A}_{gc \rightarrow gc}^{(2),m_h^3} \right) - \widetilde{\text{Disc}} \left(\mathcal{A}_{cg \rightarrow cg}^{(2),m_h^3} \right) \right. \\ & \left. - \widetilde{\text{Disc}} \left(\mathcal{A}_{g\bar{c} \rightarrow g\bar{c}}^{(2),m_h^3} \right) - \widetilde{\text{Disc}} \left(\mathcal{A}_{\bar{c}g \rightarrow \bar{c}g}^{(2),m_h^3} \right) - \widetilde{\text{Disc}} \left(\mathcal{A}_{c\bar{c} \rightarrow c\bar{c}}^{(2),m_h^3} \right) - \widetilde{\text{Disc}} \left(\mathcal{A}_{\bar{c}c \rightarrow \bar{c}c}^{(2),m_h^3} \right) \right]. \end{aligned} \quad (6.7)$$

Note, that the averaging factor for ghosts is identical to the one for gluons and the amplitudes $\mathcal{A}_{cc \rightarrow cc}^{(2)}$ and $\mathcal{A}_{\bar{c}\bar{c} \rightarrow \bar{c}\bar{c}}^{(2)}$ only contribute to the subset under consideration from **N₃LO**. All contributions with one external gluon and one external ghost or anti-ghost are equal, since the amplitudes are invariant w.r.t. $q_1 \leftrightarrow q_2$ and relative signs between ghosts and anti-ghosts cancel. Similarly, $\mathcal{A}_{c\bar{c} \rightarrow c\bar{c}} = \mathcal{A}_{\bar{c}c \rightarrow \bar{c}c}$.

Since we integrate over the full phase-space of the final-state particles, the real-radiative contributions contain **IR** singularities stemming from the region of phase-space where the massless final-state parton is soft, i.e. its energy is vanishing, or collinear to an initial-state parton. As a consequence, the real-radiative contributions have explicit poles in ϵ . The soft singularities lead to $1/\epsilon^2$ poles, whereas the collinear singularity leads to contributions starting at $1/\epsilon$. Soft singularities cancel against soft singularities present

in the virtual corrections. To cancel the collinear singularity we need to introduce a so-called *collinear counterterm*.

In the following we split $\sigma_{gg}^{(2),n_h^3}$ into three pieces:

$$\sigma_{gg}^{(2),n_h^3} = \sigma_{gg,\text{virt}}^{(2),n_h^3} + \sigma_{gg,\text{real}}^{(2),n_h^3} + \sigma_{gg,\text{coll}}^{(2),n_h^3} . \quad (6.8)$$

The computation of the real-radiative corrections $\sigma_{gg,\text{real}}^{(2),n_h^3}$ are discussed in Sec. 6.1.2, the virtual corrections $\sigma_{gg,\text{virt}}^{(2),n_h^3}$ are briefly discussed in Sec. 6.1.3 and the collinear counterterm $\sigma_{gg,\text{coll}}^{(2),n_h^3}$ is introduced in Sec. 6.1.4.

THE QUARK-GLUON INITIAL STATE Contributions to the subset under consideration with a quark or anti-quark, as well as a gluon in the initial state first arise at NNLO. Due to Eq. (6.5) we would also need to consider forward-scattering amplitudes with ghosts and quarks in the initial state. However, these do not contribute to the subset with both Higgs bosons coupling to different top-quark loops at this order. As a consequence,

$$\sigma_{qg}^{(2),n_h^3} = \sigma_{\bar{q}g}^{(2),n_h^3} = \frac{a_g a_q}{2s} \widetilde{\text{Disc}} \left(\mathcal{A}_{qg \rightarrow qg}^{(2),n_h^3} \right) . \quad (6.9)$$

While there are no virtual corrections we need to take into account for the quark-gluon channel, it has collinear singularities and thus we need to take into account a collinear counterterm $\sigma_{qg,\text{coll}}^{(2),n_h^3}$ as in the case of the gluon-gluon channel.

THE QUARK-ANTI-QUARK INITIAL STATE The third channel contributing to the subset with both Higgs bosons coupling to different top-quark loops is the quark-anti-quark channel. Its partonic cross-section is given by

$$\sigma_{q\bar{q}}^{(2),n_h^3} = \frac{a_q^2}{2s} \widetilde{\text{Disc}} \left(\mathcal{A}_{q\bar{q} \rightarrow q\bar{q}}^{(2),n_h^3} \right) \quad (6.10)$$

and neither receives contributions from virtual corrections nor has collinear divergences.

6.1.2 Computational setup for the real corrections

To compute the various partonic channels we need to consider five-loop forward-scattering diagrams such as the one in Fig. 6.2. Directly applying the LME to five-loop diagrams is very challenging since the LME leads to a large number of terms for each of them.

BUILDING BLOCKS To simplify this computation we introduce so-called *building blocks* following [126]. First, we observe that the LME of all 1PI one-loop amplitudes with two or three off-shell gluons and one or two Higgs bosons is local, i.e. polynomial in the

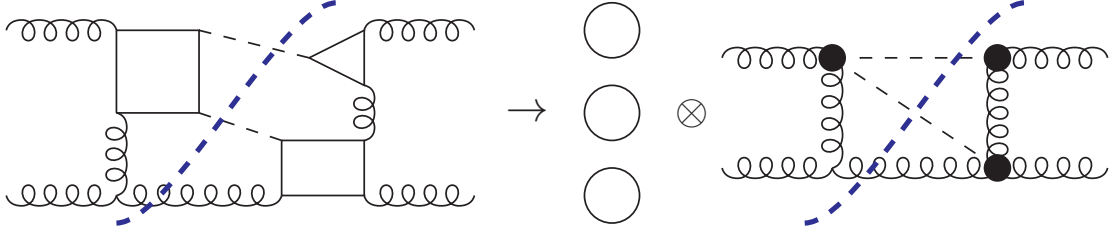


Figure 6.2: Sample contribution to the subset under consideration at NNLO. The hard subgraph leads to three one-loop tadpole integrals and a two-loop phase space integral.

external momenta, since the co-subgraphs are tree-level graphs. As a consequence we can write the LME of the Higgs boson–two-gluon vertex as

$$\begin{aligned}
 \text{Diagram} &= \frac{\alpha_s^{(6)}(\mu^2)}{v\pi} \left(\frac{\mu^2}{M_t^2}\right)^\epsilon T_F \delta^{ab} \sum_{ij} \rho^i c_{ij}(\epsilon) T_{ij}^{\mu\nu}(q_1, q_2) \\
 &= \frac{\alpha_s^{(6)}(\mu^2)}{v\pi} \left(\frac{\mu^2}{M_t^2}\right)^\epsilon T_F \delta^{ab} \left(c_{01} g^{\mu\nu}(q_1 \cdot q_2) + c_{02} q_1^\nu q_2^\mu \right. \\
 &\quad \left. + \rho \left[c_{11} q_1^\nu q_2^\mu (q_1 \cdot q_2) + c_{12} q_1^\nu q_2^\mu (q_1^2 + q_2^2) + c_{13} q_1^\mu q_2^\nu (q_1 \cdot q_2) + c_{14} g^{\mu\nu} q_1^2 q_2^2 \right. \right. \\
 &\quad \left. \left. + c_{15} g^{\mu\nu} (q_1 \cdot q_2) (q_1^2 + q_2^2) + c_{16} (q_1^2 q_2^\mu q_2^\nu + q_2^2 q_1^\mu q_1^\nu) + c_{17} g^{\mu\nu} (q_1 \cdot q_2)^2 \right] + \mathcal{O}(\rho^2) \right).
 \end{aligned} \tag{6.11}$$

Here v is the Higgs vacuum expectation value and the momenta q_1 and q_2 are taken to off-shell, since in the actual forward-scattering diagram they might correspond to a loop-momentum. At LO in the LME the coefficients are given by $c_{01} = -c_{02} = -8/3\Gamma(1 + \epsilon)$, leading to the well known result for C_H . At higher orders the coefficients are rational functions in ϵ , while the tensors T_{ij} are polynomial in the external momenta. For the cases with three gluons or two Higgs bosons the results take a similar form. We expand each of the building blocks through ρ^4 .

As a consequence, we can precompute the LME of the four relevant off-shell amplitudes and use them as a set of *effective vertices* to generate forward-scattering diagrams. This means, that, instead of five-loop diagrams, we deal with two-loop forward-scattering diagrams which resemble diagrams in the EFT introduced in chapter 2. Hence, the phase-space integral families introduced in chapter 5 are sufficient for describing the phase-space integrals appearing in the LME.

Not only does the use of building blocks reduce the number of loops, it also makes cancellations of terms in the ρ -expansion with negative powers, that appear in individual diagrams, but vanish in their sum, explicit at the level of each building block, thus reducing the total number of terms. Furthermore, the number of diagrams is greatly

reduced. As an example consider the diagram in Fig. 6.2. Once we account for all possible inequivalent ways to attach gluons to the top-quark boxes and take into account the different directions of the fermion line, we are left with 288 diagrams contributing to the same effective diagram.

SETUP Having established an efficient way to handle the forward-scattering diagrams relevant to the subset under consideration, we are now in the position to compute them. To this end, we generate one-¹ and two-loop four-point diagrams using QGRAF [61] and select diagrams with a valid cut and non-vanishing colour factor using additional scripts. The selected diagrams are then processed by q2e [62, 63] which inserts placeholders for the building blocks for the various Higgs boson–gluon vertices and mapped onto the permutations of the template families described in Sec. 5.2.2 by exp [62, 63]. The one-loop tensor tadpole integrals appearing in the computation of the building blocks are evaluated using MATAD [68]. In the next step, the output of exp is processed by FORM [64] and the colour factors are computed by color [65].

As a result, we are left with expressions for the amplitude in terms of four-point integrals depending on q_1 , q_2 and q_3 . Next, we specify forward-scattering kinematics by setting $q_3 = -q_2$ and perform the partial fractioning of the linearly dependent integrals with the FORM code provided by LIMIT. We then discard all resulting linearly independent integrals with negative powers of at least one cut propagator and map the remaining integrals on the minimal set of families found by LIMIT. Graphical representations for the two-loop families can be found in the rightmost column of Fig. 5.4.

The integrals in the resulting families are then reduced to a set of two MIs at one loop and 16 MIs at two loops using FIRE5 [70]. We discuss the computation of the MIs in Sec. 6.2.

6.1.3 Virtual corrections to $gg \rightarrow HH$

The double-virtual amplitudes $\mathcal{A}_{gg \rightarrow HH}^{\text{virt}}$ for Higgs boson pair production are known at NNLO in the LME through ρ^4 [28, 88]. To compute $\sigma_{gg, \text{virt}}^{(2), m_h^3}$ we compute the square of the absolute value of $\mathcal{A}_{gg \rightarrow HH}^{\text{virt}}$ and select all contributions with three closed top-quark loops. These contributions also contain diagrams where both Higgs bosons couple to the same top-quark loop. However, these contributions do not have soft divergences at NNLO so we can safely add them. As they are already included here, we do include them in the subset discussed in chapter 7. In the next step, we need to perform the two-particle phase-space integration

$$\sigma_{gg, \text{virt}}^{(2), m_h^3} = \frac{1}{2s} \left(\frac{1}{N_A(2 - 2\epsilon)} \right)^2 \int d\text{PS}_2 \left| \mathcal{A}_{gg \rightarrow HH}^{\text{virt}} \right|_{m_h^3}^2, \quad (6.12)$$

¹ We also recompute $\sigma_{gg}^{(1), m_h^3}$.

where $d\text{PS}_2$ is defined in Eq. (5.2). All angular integrals but the integral over the angle between one final-state Higgs boson and an initial-state gluon can be performed, since the squared virtual amplitude depends on the Mandelstam variable t and thus has a non-trivial dependence on this angle. The remaining angular integral can be re-written as an integral over t [126]:

$$\sigma_{gg,\text{virt}}^{(2),m_h^3} \propto \int_{t_-}^{t_+} dt \left| \mathcal{A}_{gg \rightarrow HH}^{\text{virt}} \right|_{m_h^3}^2. \quad (6.13)$$

The integration boundaries t_{\pm} are given by

$$t_{\pm} = -\frac{s}{4} \left(1 + \delta \mp 2\sqrt{\delta} \right). \quad (6.14)$$

Substituting

$$t = -\frac{s}{4} \left(1 + \delta + 2\sqrt{\delta} (1 - 2\xi) \right) \quad (6.15)$$

transforms the integration interval to $\xi \in [0, 1]$ and allows one to perform a systematic expansion in δ of the integrals involved. The remaining integrands are rational functions and logarithms in ξ , allowing for a straight-forward evaluation.

6.1.4 Collinear counterterms

DEFINITION The collinear counterterms for the gluon-gluon and quark-gluon channels can be obtained by convoluting the *effective* LO contribution $\sigma_{gg}^{(1),m_h^3}$ with the one-loop gluon or quark splitting functions². These splitting functions can be found, e.g. in Refs. [128, 129] and are given by

$$P_{ij}(z) = \frac{\alpha_s^{(5)}(\mu)}{\pi} P_{ij}^{(0)} + \mathcal{O}(\alpha_s^2), \quad (6.16)$$

$$P_{gg}^{(0)}(z) = C_A \left(\left[\frac{1}{1-z} \right]_+ - 2 + \frac{1}{z} + z - z^2 \right) + \beta_0 \delta(1-z), \quad (6.17)$$

$$P_{gq}^{(0)}(z) = C_F \left(\frac{1}{z} - 1 + \frac{z}{2} \right), \quad (6.18)$$

where β_0 is the one-loop term of the QCD beta function and the plus distribution is defined by

$$\int_0^1 dz \left[\frac{1}{1-z} \right]_+ f(z) = \int_0^1 dz \frac{f(z) - f(1)}{1-z} \quad (6.19)$$

for a function $f(z)$ which has at most a logarithmic singularity for $z \rightarrow 1$.

² See [119, 127] for the case of a single Higgs boson.

The two collinear counterterms are given by

$$\begin{aligned}\sigma_{gg,\text{coll}}^{(2),m_h^3} &= \frac{2}{\epsilon} \left(\frac{\mu^2}{\mu_f^2} \right)^\epsilon \int_0^1 dy dz \theta(1/4 - z) \delta(x - yz) P_{gg}^{(0)}(z) \sigma_{gg}^{(1),m_h^3}(y) \\ &= \frac{2}{\epsilon} \left(\frac{\mu^2}{\mu_f^2} \right)^\epsilon \int_{1-\delta}^1 dz P_{gg}^{(0)}(z) \sigma_{gg}^{(1),m_h^3}(x/z) ,\end{aligned}\quad (6.20)$$

$$\begin{aligned}\sigma_{qg,\text{coll}}^{(2),m_h^3} &= \frac{1}{\epsilon} \left(\frac{\mu^2}{\mu_f^2} \right)^\epsilon \int_0^1 dy dz \theta(1/4 - z) \delta(x - yz) P_{qg}^{(0)}(z) \sigma_{gg}^{(1),m_h^3}(y) \\ &= \frac{1}{\epsilon} \left(\frac{\mu^2}{\mu_f^2} \right)^\epsilon \int_{1-\delta}^1 dz P_{gq}^{(0)}(z) \sigma_{gg}^{(1),m_h^3}(x/z) ,\end{aligned}\quad (6.21)$$

where μ is the renormalization scale, μ_f the factorization scale and the factor of 2 in the gluon-gluon counterterm comes from the two ways to convolute $P_{gg}^{(0)}$ with the effective LO cross-section. The lower boundary of the remaining integration is set by the θ -function and corresponds to the Higgs boson pair-production threshold $s = 4m_H^2$, below which the cross-section vanishes.

INTEGRATION To perform the integration involving the plus distribution we re-write

$$\begin{aligned}\int_{1-\delta}^1 dz \left[\frac{1}{1-z} \right]_+ \sigma_{gg}^{(1),m_h^3}(x/z) &= \int_0^1 dz \left[\frac{1}{1-z} \right]_+ \sigma_{gg}^{(1),m_h^3}(x/z) \\ &\quad - \int_0^{1-\delta} dz \left[\frac{1}{1-z} \right]_+ \sigma_{gg}^{(1),m_h^3}(x/z) .\end{aligned}\quad (6.22)$$

Next, we apply Eq. (6.19) to the first integral on the right-hand side of the above equation. Since the plus distribution regulates divergences in the limit $z \rightarrow 1$, which is not part of the integration interval of the second integral, we can treat the plus distribution as a regular function. As a consequence we obtain

$$\begin{aligned}\int_{1-\delta}^1 dz \left[\frac{1}{1-z} \right]_+ \sigma_{gg}^{(1),m_h^3}(x/z) &= \int_0^1 dz \frac{\sigma_{gg}^{(1),m_h^3}(x/z) - \sigma_{gg}^{(1),m_h^3}(x)}{1-z} - \int_0^{1-\delta} dz \frac{\sigma_{gg}^{(1),m_h^3}(x/z)}{1-z} \\ &= \int_{1-\delta}^1 dz \frac{\sigma_{gg}^{(1),m_h^3}(x/z) - \sigma_{gg}^{(1),m_h^3}(x)}{1-z} - \int_0^{1-\delta} dz \frac{\sigma_{gg}^{(1),m_h^3}(x)}{1-z} \\ &= \int_{1-\delta}^1 dz \frac{\sigma_{gg}^{(1),m_h^3}(x/z) - \sigma_{gg}^{(1),m_h^3}(x)}{1-z} + \sigma_{gg}^{(1),m_h^3}(x) \ln(\delta) .\end{aligned}\quad (6.23)$$

The remaining integral can now be computed by substituting $z = 1 - \delta(1 - \mu)$ [26] and expanding in δ . Integrals over terms regular in the limit $z \rightarrow 1$ can be computed by simply performing the aforementioned substitution and expansion, whereas the integration involving the delta distribution is trivial.

Infinite series representations for the two counterterms are given in Ref. [35] and results through $\delta^{199/2}$ can be found in the ancillary files.

6.2 COMPUTING THE MASTER INTEGRALS

The IBP reduction leads to two one-loop two-particle cut MIs, depicted in Fig. 6.3, and 16 two-loop three-particle cut MIs, depicted in Fig. 6.4. Both one-loop MIs have been computed in an expansion around $\delta \approx 0$ in Ref. [26]. Out of the 16 two-loop MIs I_1, I_2 and

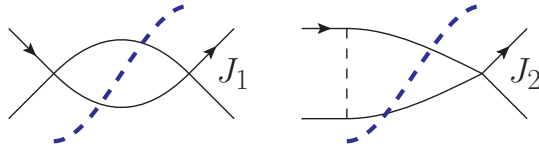


Figure 6.3: One-loop MIs contributing to $\sigma_{gg}^{(1),m_h^3}$. The momentum q_1 enters and leaves the diagrams through the external lines with an arrow. Dashed and solid lines depict massless and massive lines, respectively.

I_7 contribute to the NLO cross-section and have been computed in an expansion around $\delta \approx 0$ in Ref. [26]. The remaining integrals have not been considered in the literature, to the best of our knowledge. In the following, we discuss the computation of all 18 MIs.

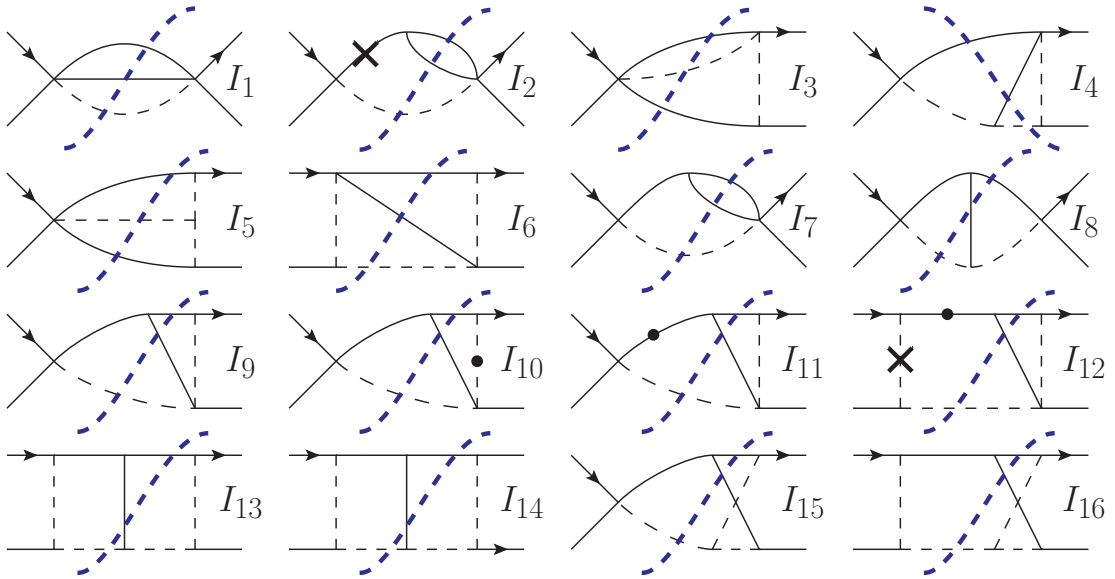


Figure 6.4: Two-loop MIs to the real radiative contributions with both Higgs bosons coupling to different top-quark loops. Dots on lines denote squared propagators, whereas crosses on lines denote propagators raised to a negative power.

In Sec. 6.2.1 we compute each MI in an expansion for $\delta \approx 0$ by direct integration of the

final-state phase-space. Some of the results obtained in this section serve as boundary conditions for the exact computation by means of differential equation in Sec. 6.2.2.

6.2.1 Expansion around the production threshold

SETUP To compute the 16 two-loop three-particle cut $\overline{\text{MIs}}^3$ in an expansion around the Higgs boson pair-production threshold, we express them as phase-space integrals

$$\begin{aligned} I_i &= C^{2\epsilon} \int d\text{PS}_3 \mathcal{Q}_i \\ &= C^{2\epsilon} \int \prod_{i=3}^5 \mathcal{D}p_i (2\pi)^D \delta^{(D)}(q_1 + q_2 - p_3 - p_4 - p_5) \mathcal{Q}_i . \end{aligned} \quad (6.24)$$

Here, the pre-factor C is chosen to account for $\overline{\text{MS}}$ subtraction:

$$C = \frac{e^{\gamma_E} \mu^2}{4\pi} . \quad (6.25)$$

The momenta p_3 and p_4 are the momenta of the two final-state Higgs bosons and the respective integration measures can be written as

$$\mathcal{D}p_{3/4} = \frac{p_{3/4}^{D-2} dp_{3/4} d\Omega_{D-1}^{(3/4)}}{2E_{3/4} (2\pi)^{D-1}} , \quad (6.26)$$

whereas p_5 is the momentum of the massless final-state parton and the respective integration measure is given by

$$\mathcal{D}p_5 = \frac{p_5^{D-3} dp_5 d\Omega_{D-1}^{(5)}}{2 (2\pi)^{D-1}} . \quad (6.27)$$

We express the D -dimensional angular integration measure $d\Omega_{D-1}^{(j)}$ as [130]

$$\int d\Omega_{D-1}^{(j)} = \frac{2\pi^{\frac{D-3}{2}}}{\Gamma(\frac{D-3}{2})} \int_{-1}^1 (1 - \cos^2 \theta_j)^{\frac{D-4}{2}} d \cos \theta_j \int_{-1}^1 (1 - \cos^2 \phi_j)^{\frac{D-5}{2}} d \cos \phi_j . \quad (6.28)$$

Each of the \mathcal{Q}_i is composed out of the uncut propagators of the I_i . As an example

$$\mathcal{Q}_1 = 1 , \quad \mathcal{Q}_2 = m_H^2 - (p_3 + p_4)^2 , \quad \mathcal{Q}_3 = \frac{-1}{(q_2 - p_4)^2} , \quad (6.29)$$

while the other 13 \mathcal{Q}_i can be found in Ref. [35].

³ The two one-loop integrals J_1 and J_2 can be computed along the same lines.

SIMPLIFYING AND EXPANDING THE INTEGRALS We are now in the position to perform the integrations over angles and momenta. First, we integrate over p_4 by exploiting the δ distribution:

$$\begin{aligned} & \int \mathcal{D}p_3 \mathcal{D}p_4 \mathcal{D}p_5 (2\pi)^D \delta^{(D)}(q_1 + q_2 - p_3 - p_4 - p_5) \mathcal{Q}_i \\ &= \int \mathcal{D}p_3 \mathcal{D}p_5 \frac{\pi}{E_4} \delta(\sqrt{s} - E_3 - E_4 - |\vec{p}_5|) \mathcal{Q}_i. \end{aligned} \quad (6.30)$$

Thus, we express the spatial components of p_4 as $\vec{p}_4 = -\vec{p}_3 - \vec{p}_5$. The four remaining D -dimensional momenta can be written as

$$q_1 = \frac{\sqrt{s}}{2} \begin{pmatrix} 1 \\ 0 \\ \vdots \\ 0 \\ 1 \end{pmatrix}, \quad q_2 = \frac{\sqrt{s}}{2} \begin{pmatrix} 1 \\ 0 \\ \vdots \\ 0 \\ -1 \end{pmatrix}, \quad p_3 = \begin{pmatrix} E_3 \\ \vdots \\ \vdots \\ k \sin \theta_3 \cos \phi_3 \\ k \cos \theta_3 \end{pmatrix}, \quad p_5 = \begin{pmatrix} l \\ 0 \\ \vdots \\ l \sin \theta_5 \\ l \cos \theta_5 \end{pmatrix}. \quad (6.31)$$

With this parametrization of the momenta, Eq. (6.30) becomes

$$\begin{aligned} I_i &= \frac{C^{2\epsilon}}{4(2\pi)^{2D-3}} \int \frac{k^{D-2} dk d\Omega_{D-1}^{(3)} l^{D-3} dl d\Omega_{D-1}^{(5)}}{E_3 E_4} \\ &\quad \times \delta\left(\sqrt{s} - \sqrt{m_H^2 + k^2} - \sqrt{m_H^2 + k^2 + 2kl \cos \gamma + l^2} - l\right) \mathcal{Q}_i, \end{aligned} \quad (6.32)$$

where $\cos \gamma = \cos \theta_3 \cos \theta_5 + \cos \phi_3 \sin \theta_3 \sin \theta_5$.

The l -integration can now be performed by exploiting the remaining δ distribution and we obtain

$$I_i = \frac{C^{2\epsilon}}{4(2\pi)^{2D-3}} \int dk \int \frac{k^{D-3} l^{D-3} \mathcal{Q}_i d\Omega_{D-1}^{(3)} d\Omega_{D-1}^{(5)}}{\sqrt{m_H^2 + k^2} \left(l + k \cos \gamma + \sqrt{m_H^2 + k^2 + 2kl \cos \gamma + l^2} \right)} \Big|_{l=l_\delta}, \quad (6.33)$$

where l_δ is the value of l for which the argument of the δ distribution vanishes. It is given by

$$l_\delta = \frac{\sqrt{s} \left[-2k^2 - 2m^2 + k \cos \gamma \left(\sqrt{s} - 2\sqrt{k^2 + m^2} \right) - \sqrt{s} \sqrt{k^2 + m^2} + s \right]}{2 \left[s + 2\sqrt{sk} \cos \gamma - m^2 + k^2 (\cos^2 \gamma - 1) \right]} \quad (6.34)$$

Up to this point no expansion has been performed. The remaining integrations in Eq. (6.33) depend on the exact form of the \mathcal{Q}_i and are in general too complicated to be

performed without any approximation. To perform an expansion around $\delta \approx 0$ we first notice that the upper boundary of the k -integration is determined by the value of k for which E_3 is maximal. The energy E_3 is maximal when both Higgs bosons are produced back-to-back and given by $\sqrt{s}/2$. Exploiting energy momentum conservation we thus find $k \leq \sqrt{s\delta}/2$.

As a result we substitute $k \rightarrow \xi\sqrt{s\delta}/2$ and expand the integrand in δ . The ξ -integration and the remaining angular integrals are now straightforward, since the resulting integrand is polynomial in ξ , $\cos\theta_3$, $\cos\theta_5$ and $\cos\phi_3$. As an example, the leading term in the δ expansion of the first two integrals is given by

$$\begin{aligned} I_1 &= \mathcal{N}^2 s \left[\frac{2^{2(3\epsilon-4)} \pi^{2\epsilon-\frac{5}{2}} \Gamma(1-\epsilon)}{\Gamma(\frac{7}{2}-3\epsilon)} \delta^{\frac{5}{2}-3\epsilon} + \mathcal{O}\left(\delta^{\frac{7}{2}}\right) \right], \\ I_2 &= -\mathcal{N}^2 s^2 \left[\frac{3 \cdot 2^{2(3\epsilon-4)} \pi^{2\epsilon-\frac{5}{2}} \Gamma(1-\epsilon)}{\Gamma(\frac{7}{2}-3\epsilon)} \delta^{\frac{5}{2}-3\epsilon} + \mathcal{O}\left(\delta^{\frac{7}{2}}\right) \right], \end{aligned} \quad (6.35)$$

where

$$\mathcal{N} = \left(\frac{e^{\gamma_E} \mu^2}{4\pi s} \right)^\epsilon. \quad (6.36)$$

The remaining 14 integrals can be found in Ref. [35]. As the number of terms in the integrand at higher orders in δ quickly grows we resort to a more efficient approach in Sec. 6.2.2.

6.2.2 Exact computation by differential equations

CANONICAL BASIS OF MASTER INTEGRALS To compute the two one-loop and the 16 two-loop integrals exactly in δ , we employ the method of differential equations [131–133]. In a first step, we take the derivative of the MIs w.r.t. to x . The result of taking the derivative is a linear combination of Feynman integrals. These can be reduced to MIs again and we obtain a closed set of differential equations (DEs) of the form

$$\partial_x \vec{I} = M(x, \epsilon) \vec{I}. \quad (6.37)$$

Here, M is rational in x and ϵ and takes a lower block-triangular form. Furthermore, in our case $\vec{I} = (J_1, J_2)$ or $\vec{I} = (I_1, \dots, I_{16})$.

While Eq. (6.37) can be solved with various different methods, we are aiming at finding a new basis of MIs, a so-called *canonical* basis \vec{J} [134], in which the DEs take the form

$$\partial_x \vec{J} = \epsilon \sum_i \frac{\tilde{M}^{(i)}}{x-x_i} \vec{J} \equiv \epsilon \mathcal{M}(x) \vec{J}. \quad (6.38)$$

The formal solution of Eq. (6.38) is given by

$$\vec{J}(x) = U(x, x_0, \epsilon) \vec{J}(x_0), \quad (6.39)$$

where the evolution operator U is defined as

$$\begin{aligned} U(x, x_0, \epsilon) &= \mathcal{P} \exp \left(\epsilon \int dx \mathcal{M}(x) \right) \\ &\approx 1 + \epsilon \int_{x_0}^x dy \mathcal{M}(y) + \epsilon^2 \int_{x_0}^x dy \int_{x_0}^y dz \mathcal{M}(y) \mathcal{M}(z) + \mathcal{O}(\epsilon^3). \end{aligned} \quad (6.40)$$

Thus, the MIs can be computed to any order in ϵ in terms of iterated integrals if a canonical basis \vec{J} is found and suitable boundary conditions $\vec{J}(x_0)$ are known. In our case, the δ -expanded MIs can serve as boundary conditions. In the following we discuss the procedure of finding a canonical basis. The class of functions arising from the iterated integrations in Eq. (6.40), the so-called Goncharov polylogarithms (GPLs), are discussed in Sec. A.6.

REDUCING THE SYSTEM TO FUCHSIAN FORM A change of the basis of MIs can be written as a, in general x - and ϵ -dependent, transformation matrix T :

$$\vec{I} = T(x, \epsilon) \vec{J}. \quad (6.41)$$

Under such a basis change, the matrix M transforms as:

$$\tilde{M} = T^{-1} M T - T^{-1} \partial_x T. \quad (6.42)$$

An algorithm for finding a rational transformation T , such that the system of DEs is in normal Fuchsian form, i.e. only has simple poles in x , has been introduced in Ref. [135]. We apply its implementation in the program EPSILON⁴⁵ [137] to arrive at

$$\partial_x \vec{J} = \sum_i \frac{M^{(i)}(\epsilon)}{x - x_i} \vec{J}. \quad (6.43)$$

The residues $M^{(i)}$ only depend on ϵ . In our case the letters x_i are given by

$$x_i \in \{0, 1/4, 1, r_1 = e^{i\pi/3}, r_2 = e^{-i\pi/3}, -1/3\}. \quad (6.44)$$

The first three letters correspond to the kinematic limits $s \rightarrow \infty$, $s \rightarrow 4m_H^2$ and $s \rightarrow m_H$, respectively. In the DEs for I_1 through I_6 as well as the one-loop MIs only the first two letters appear. In the DE of I_7 also $x_3 = 1$ appears, which is due to the uncut massive line. In the DEs for I_8 through I_{14} , in addition to the first three letters, also the fourth and fifth letter are present, whereas the last letter only appears in the DEs of the non-planar MIs I_{15} and I_{16} .

⁴ The example in the manual is sufficiently detailed for our case.

⁵ We re-derived the canonical basis using LIBRA [136] as a test for its use in chapter 7.

NORMALIZING THE EIGENVALUES Next, we want to find a transformation relating the basis \vec{J} for which the system of DEs is in normal Fuchsian form to the canonical basis $\vec{\mathcal{J}}$. To this end, we observe that for a matrix which is proportional to ϵ , all its eigenvalues need to be proportional to ϵ . In our case, the eigenvalues take the form $a + b\epsilon$ where b is an integer and a is either integer or half-integer. Thus, to find a canonical basis, we need to find transformations nullifying the non- ϵ -dependent part of the eigenvalues of all residues.

Due to the block-triangular structure of the DEs, we only need to focus on the eigenvalues of the blocks along the diagonals of the residues. In Ref. [135] a second algorithm is discussed which constructs so-called *balance transformations*. These transformations take the form

$$\mathcal{B}(x_i, x_j) = \tilde{\mathbb{P}} + \frac{x - x_i}{x - x_j} \mathbb{P}, \tag{6.45}$$

where \mathbb{P} depends on ϵ and projects onto the subspace of the eigenvalues under consideration, $\mathbb{P}^2 = \mathbb{P}$ and $\tilde{\mathbb{P}} = \mathbb{1} - \mathbb{P}$. The projection operator \mathbb{P} is constructed based on the diagonal block under consideration. Applying such a balance transformation lowers the eigenvalue of $M^{(i)}$ by 1 and raises the one of $M^{(j)}$ by 1. By successively applying balance transformations all eigenvalues of the residues of the DEs can be either brought to the form $\tilde{b}\epsilon$ or $\pm\frac{1}{2} + \tilde{b}\epsilon$.

An explicit example is given in the following.

Example 10 (Normalizing eigenvalues)

Consider the following system of two DEs:

$$M = \begin{pmatrix} \frac{6-7\epsilon}{x-1} - \frac{\epsilon}{x} & -\frac{6(\epsilon-1)}{x-1} \\ -\frac{\epsilon-2}{6x} + \frac{7\epsilon-6}{2(x-1)} & \frac{3(\epsilon-1)}{x-1} - \frac{2\epsilon}{x} \end{pmatrix}.$$

It has three singular points: $x = 0$, $x = 1$ and $x = \infty$. The eigenvalues of the corresponding residues are given by

$$M^{(0)} : -\epsilon, -2\epsilon,$$

$$M^{(1)} : 0, 3 - 4\epsilon,$$

$$M^{(\infty)} : -2 + 4\epsilon, -1 + 3\epsilon.$$

To lower the second eigenvalue of $M^{(1)}$ and raise the first eigenvalue of $M^{(\infty)}$ by one, we need to compute the left eigenvector v of $M^{(1)}$ and the right eigenvector u of $M^{(\infty)}$ to the corresponding eigenvalues. They are given by

$$v = \left(\frac{7\epsilon - 6}{6\epsilon - 6}, 1 \right) \quad \text{and} \quad u = \begin{pmatrix} -\frac{3}{2} \\ 1 \end{pmatrix}.$$

As $v^\dagger \cdot u = (2 - 3\epsilon)/(4\epsilon - 4) \neq 0$, we can construct a balance transformation. To this end we can construct the projector $\mathbb{P} = uv^\dagger/(v^\dagger \cdot u)$ and thus the balance transformation reads

$$\mathcal{B}(1, \infty) = \frac{1}{(3\epsilon - 2)} \begin{pmatrix} -4(\epsilon - 1) & -6(\epsilon - 1) \\ \frac{2}{3}(7\epsilon - 6) & 7\epsilon - 6 \end{pmatrix} + \frac{(x - 1)}{3\epsilon - 2} \begin{pmatrix} 7\epsilon - 6 & 6(\epsilon - 1) \\ -\frac{2}{3}(7\epsilon - 6) & -4(\epsilon - 1) \end{pmatrix}$$

CHANGING THE VARIABLE To also reduce the eigenvalues of the form $\pm \frac{1}{2} + \tilde{b}\epsilon$ to be proportional to ϵ we need a different kind of transformation. So far, all basis changes T have been rational functions of x . One way of rendering half-integer eigenvalues fully integer would be to allow square roots of the form $\sqrt{x - x_i}$ in the transformations. This however, would introduce square roots in addition to the simple poles in x in Eq. (6.38) and as a consequence, the iterated integrals would no longer evaluate to GPLs.

Another possibility is to change the variable in which we differentiate. Such a variable change $y(x)$ should have the property that it transforms all $\sqrt{x - x_i}$ to functions rational in y . Let us start with the system of the two one-loop MIs. Here we only have one letter, for which the corresponding residue has half-integer eigenvalues: $x = 1/4$. Choosing

$$y = \frac{\sqrt{1 - 4x} - 1}{\sqrt{1 - 4x} + 1} \quad \leftrightarrow \quad x = -\frac{y}{(y - 1)^2} \quad (6.46)$$

renders all ϵ -independent parts of the eigenvalues of the system integer. The pair-production threshold in y is at $y = -1$ and for $s \rightarrow \infty$ y approaches 0. As a consequence the set of letters of the one-loop system is now given by $y_i = \{0, 1, -1\}$ and a transformation to a canonical basis can be found using EPSILON. Note, that this variable change increases the numbers of letters, e.g. $x_i \in \{0, 1/4\}$ is mapped onto $y_i = \{0, 1, -1\}$.

The variable change in Eq. (6.46) also is sufficient to rationalize the system of DEs for I_1 through I_{14} . In addition to the letters appearing in the one-loop case, $x_3 = 1$ is mapped onto $y_4 = r_1$ and $y_5 = r_2$. Furthermore, x_4 and x_5 are mapped onto the roots of the polynomial $y^4 - 3y^3 + 5y^2 - 3y + 1$. The two MIs I_{15} and I_{16} require special care. In the original variable x not only the residue at $1/4$ but also the residues at $-1/3$ and 1 in the homogeneous part of the DE of I_{15} have half-integer eigenvalues. We were not able to find a variable change rationalizing all three square roots at once, even by applying the algorithm of [138]. Instead, we keep the variable y and factor out ϵ in the homogeneous part of the DE of I_{15} by a non-rational basis change. As a consequence the inhomogeneous part contains the root $\sqrt{y^4 - 6y^3 + 7y^2 - 6y + 1}$. The homogeneous part of the DE of I_{16} does not contain half-integer eigenvalues other than at $1/4$ thus, no special care is needed. However, the inhomogeneous part proportional to I_{15} also contains the aforementioned square root.

In the contributions to the Higgs boson pair-production cross-section studied in this chapter, iterated integrals involving the aforementioned square root only enter the cross-section starting from $\mathcal{O}(\epsilon)$ and thus do not contribute at NNLO.

One more comment regarding the change of variables is in order. Instead of partial fractioning the polynomials $P_2 = y^2 - y + 1$ and $P_4 = y^4 - 3y^3 + 5y^2 - 3y + 1$, which would give rise to simple poles at $r_{1/2}$ and the roots of P_4 , we instead define the integration kernels

$$f(r^{(n)}; y) = \frac{\partial_y^n P_2}{P_2}, \quad \text{and} \quad f(s^{(k)}; y) = \frac{\partial_y^k P_4}{P_4}. \quad (6.47)$$

By partial fractioning the above integration kernels, iterated integrals involving them can be re-written to linear combinations of GPLs:

$$\begin{aligned} G(\dots, r^{(n)}, \dots; y) &= \sum_{i=1}^2 c_i^{(n)} G(\dots, r_i, \dots; y), \\ G(\dots, s^{(k)}, \dots; y) &= \sum_{i=1}^4 c_i^{(k)} G(\dots, s_i, \dots; y). \end{aligned} \quad (6.48)$$

In the following we give an explicit example:

Example 11

Iterated integrals In the case of $r^{(n)}$ the constants $c_i^{(n)}$ are given by

$$c_1^{(1)} = c_2^{(1)} = 1 \quad \text{and} \quad c_1^{(2)} = -c_2^{(2)} = -\frac{2i}{\sqrt{3}}.$$

As a consequence, we can write the iterated integrals $G(0, r^{(1)}, 1; y)$ and $G(r^{(2)}, r^{(1)}; y)$ as

$$\begin{aligned} G(0, r^{(1)}, 1; y) &= G(0, r_1, 1; y) + G(0, r_2, 1; y) \\ G(r^{(2)}, r^{(1)}; y) &= G(r^{(2)}, r_1; y) + G(r^{(2)}, r_2; y) \\ &= \frac{2i}{\sqrt{3}} (G(r_2, r_1; y) - G(r_1, r_1; y) + G(r_2, r_2; y) - G(r_1, r_2; y)) \end{aligned}$$

While all iterated integrals involving the letters $\{0, 1, -1, r^{(n)}, s^{(k)}\}$ are real-valued for $-1 \leq y < 0$, the individual GPLs on the right-hand side of Eq. (6.48) are not.

FIXING THE BOUNDARY CONDITIONS Finally, we need to fix the boundary conditions $\vec{\mathcal{J}}(y_0)$. To this end, we choose $y_0 = -1$, corresponding to $\delta = 0$. Studying the poles of the inverse of the transformation matrix between the original basis \vec{I} and $\vec{\mathcal{J}}$ allows us to determine which of the original integrals is required to which order in δ . This is due to the fact, that expanding the canonical MIs around $y \approx -1$ leaves us with

$$\mathcal{J}_i(y) \approx (y + 1)^{n_i \epsilon} \sum_{j=0} \epsilon^j \vec{c}_{ij} + \mathcal{O}(y + 1), \quad (6.49)$$

where the n_i are integers and the c_{ij} , possibly complex, numbers. When transforming the expansions of the original MIs for $\delta \approx 0$ to the canonical basis by

$$\vec{\mathcal{J}} = \tilde{T}^{-1} \vec{I}, \quad (6.50)$$

only contributions of the form in Eq. (6.49) are relevant. As a consequence, the highest pole in $(y+1)$ in the i th column of \tilde{T}^{-1} determines to which power in δ I_i is needed. In the case at hand, the highest pole in $(y+1)$ is 5 and is present in the first two columns. Thus, the $\delta^{\frac{5}{2}}$ contributions of I_1 and I_2 given in Eq. (6.35) are required, but no higher order terms of them. Furthermore, the δ expansions of I_3 through I_{16} are not needed, since the respective columns are either finite, such as in the case of MIs I_7 through I_{16} , or the poles are lower than the respective starting power, such as in the case of MIs I_3 through I_6 .

RESULTS FOR THE MIS We computed all MIs to sufficiently high order in the ϵ -expansion exactly in y . The maximum weight of the GPLs contributing to the three partonic cross-sections is 3. An exception are the integrals I_9 and I_{12} . Both integrals are required through $\mathcal{O}(\epsilon^2)$ where they contain weight-4 GPLs. However, only their difference $I_9 - I_{12}$, which only contains weight-3 GPLs, is required through $\mathcal{O}(\epsilon^2)$, whereas their sum only contributes through $\mathcal{O}(\epsilon)$. Exact expressions for the MIs can be found in Ref. [35].

To obtain expansions of the MIs around $\delta \approx 0$ the Mathematica package `PolyLogTools` [139] can be used. While this approach is sufficient for obtaining expansions up to $\delta^{21/2}$ in a moderate amount of time, obtaining more expansion terms is cumbersome. To overcome this obstacle and provide an additional cross-check of the exact solutions, in Ref. [35] a second approach for obtaining expansions up to $\delta^{219/2}$ is used. Instead of transforming the system of DEs to a canonical form, the variable is changed from x to δ and an ansatz for the MIs of the form

$$I_i = \sum_{jkl} c_{ijkl} \epsilon^j \delta^{(k+1)/2} \ln^l \delta \quad (6.51)$$

is made. Plugging this ansatz in the DEs leads to recurrence relations for the coefficients c . As boundary conditions the leading terms in the δ -expansion are required, which are computed in Sec. 6.2.1.

We are now in the position to discuss the convergence of the δ -expansion of the MIs. To this end, we consider the finite parts of the MIs I_6 and I_{10} , which are shown as a function of δ in Fig. 6.5. The exact result is evaluated using a implementation of GPLs in GINAC [140, 141] and is depicted as a solid line. The various expansion orders are shown as dashed lines.

Since for $\delta < 0.8$ the difference between the exact result and the expansions is below 1%, we focus on the higher energy region. Starting from $\delta \approx 0.8$, the expansion up to δ^{10} deviates from the exact solution by more than 1%, whereas the expansion up to

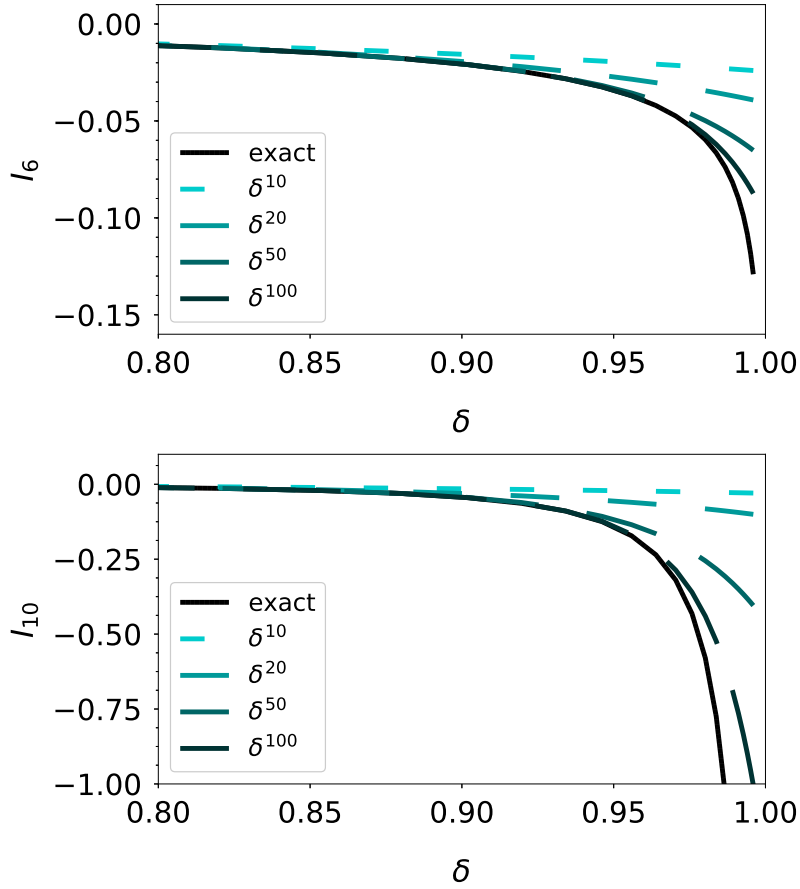


Figure 6.5: Finite parts of the MIs I_6 and I_{10} as a function of δ . The exact solution is shown as a solid line, whereas the dashed lines show the different expansion depths. Taken from [35].

δ^{20} agrees with the exact result up to $\delta \approx 0.9$. This already corresponds to $\sqrt{s} \approx 800$ GeV and thus a region where the parton distribution functions are already rather small. Increasing the expansion depth to δ^{100} is sufficient to describe the δ -dependence up to $\delta \approx 0.97$. This convergence pattern is similar for all 16 MIs and can be traced back to the fact that the DEs do not have any singular points between $y = -1$ and $y = 0$. Thus, the expansion around $y = -1$ is expected to converge well in the physical y -range.

6.3 RESULTS

We are now in the position to present results for the NNLO contributions to the total Higgs boson pair-production cross-section with both Higgs bosons coupling to different

top-quark loops. In Sec. 6.3.1 we present the leading terms in the ρ and δ expansion for the three channels and discuss their numerical impact.

6.3.1 Partonic cross-sections

In the following we present the leading terms in the δ and ρ expansion for the three partonic channels. In all three cases the leading term in the δ expansion only arises starting from $\mathcal{O}(\rho)$, showing the significance of mass-suppressed contributions directly at threshold. This is in agreement with the observations made at NLO [26]. The leading terms are given by

$$\begin{aligned}
\sigma_{gg}^{(2),n_h^3} = & \frac{a_s^4 G_F^2 m_H^2}{\pi} \left[\delta^{\frac{3}{2}} \left(-\frac{2053}{62208} + \frac{1}{27} a_1 - \frac{1}{54} a_1^2 + \frac{5}{82944} \pi^2 - \frac{25}{3456} L_{m_H^2} + \frac{1}{216} L_{m_H^2} a_1 \right. \right. \\
& + \ln \delta \left(\frac{1}{81} - \frac{1}{72} a_1 + \frac{1}{432} L_{m_H^2} \right) - \frac{1}{432} \ln^2 \delta + n_l \left(\frac{5}{46656} + \frac{1}{15552} L_{m_H^2} \right) \left. \right) \\
& + \rho \left\{ \sqrt{\delta} \left(-\frac{30587}{14929920} + \frac{7}{2880} a_1 - \frac{7}{4320} a_1^2 + \frac{7}{1327104} \pi^2 - \frac{413}{829440} L_{m_H^2} \right. \right. \\
& + \frac{7}{17280} L_{m_H^2} a_1 + \ln \delta \left(\frac{7}{8640} - \frac{7}{5760} a_1 + \frac{7}{34560} L_{m_H^2} \right) - \frac{7}{34560} \ln^2 \delta \\
& + n_l \left(\frac{7}{746496} + \frac{7}{1244160} L_{m_H^2} \right) \left. \right) + \delta^{\frac{3}{2}} \left(-\frac{32155177}{10749542400} + \frac{19}{6480} a_1 - \frac{19}{12960} a_1^2 \right. \\
& - \frac{1109}{59719680} \pi^2 + \frac{10549}{31850496} \zeta_3 - \frac{2077}{2488320} L_{m_H^2} + \frac{121}{622080} L_{M_t^2} + \frac{19}{51840} L_{m_H^2} a_1 \\
& + \ln \delta \left(\frac{283}{311040} - \frac{19}{17280} a_1 + \frac{19}{103680} L_{m_H^2} \right) - \frac{19}{103680} \ln^2 \delta \\
& \left. \left. + n_l \left(\frac{11}{11197440} + \frac{19}{3732480} L_{m_H^2} \right) \right) \right] + \mathcal{O}(\delta^{\frac{5}{2}}, \rho^2), \tag{6.52}
\end{aligned}$$

$$\begin{aligned}
\sigma_{gq}^{(2),n_h^3} = & \frac{a_s^4 G_F^2 m_H^2}{\pi} \left[\delta^{\frac{5}{2}} \left(\frac{77}{145800} - \frac{1}{1620} a_1 + \frac{1}{9720} L_{m_H^2} - \frac{1}{4860} \ln \delta \right) \right. \\
& + \rho \left\{ \delta^{\frac{3}{2}} \left(\frac{91}{1399680} - \frac{7}{77760} a_1 + \frac{7}{466560} L_{m_H^2} - \frac{7}{233280} \ln \delta \right) \right. \\
& \left. \left. + \delta^{\frac{5}{2}} \left(\frac{25}{279936} - \frac{1}{9720} a_1 + \frac{1}{58320} L_{m_H^2} - \frac{1}{29160} \ln \delta \right) \right) \right] + \mathcal{O}(\delta^{\frac{7}{2}}, \rho^2), \tag{6.53}
\end{aligned}$$

$$\sigma_{q\bar{q}}^{(2),n_h^3} = -\frac{a_s^4 G_F^2 m_H^2}{\pi} \left[\frac{64}{2525985} \delta^{\frac{11}{2}} + \rho \left\{ \frac{32}{688905} \delta^{\frac{9}{2}} + \frac{1552}{12629925} \delta^{\frac{11}{2}} \right\} \right] + \mathcal{O} \left(\delta^{\frac{13}{2}}, \rho^2 \right), \tag{6.54}$$

where $a_1 = \ln 2$, ζ_3 is the Riemann Zeta function evaluated at three, $a_s = \alpha_s^{(5)}/\pi$, $L_{m_H^2} = \ln(\mu^2/m_H^2)$, $L_{M_t^2} = \ln(\mu^2/M_t^2)$ and we set $\mu_f = \mu$. Terms through ρ^4 and $\delta^{219/2}$ for general renormalization and factorization scale can be found in Ref. [35]. We expanded the virtual corrections through δ^{18} , which is sufficient for the center-of-mass energies under consideration in the following discussion.

NUMERICAL RESULTS We are now in the position to discuss the convergence of the ρ expansion in the subset under consideration. The individual partonic channels are shown in Fig. 6.6 together with the known LO and NLO results [26] which we reproduced in the course of this computation. The gluon-gluon initiated NNLO correction follows the convergence pattern of the LO and NLO results. Above the top-quark threshold we observe no convergent behaviour, as expected. However, up to $\sqrt{s} \approx 340$ GeV the result shows a converging behaviour. The ρ^2 , ρ^3 and ρ^4 lines agree well with each other, signaling a stabilization of the LME.

In Fig. 6.7 the ratio of the higher order terms and the LO contribution in the ρ expansion is shown. Higher-order terms are sizeable, even at moderate center-of-mass energies, such as $\sqrt{s} \approx 300$ GeV. The expansion up to ρ^4 is more than 40% larger than the leading-order term in the range between 250 GeV and 340 GeV. Closer to the Higgs boson pair-production threshold, higher-order ρ terms have an even bigger impact. This is due to the ρ^0 contribution vanishing as $\delta^{3/2}$ for $\delta \rightarrow 0$, whereas the mass-suppressed terms vanish as $\delta^{1/2}$.

For the quark-gluon initial state a similar pattern is observed as for the gluon-gluon initial state. The quark-anti-quark initial state shows no sign of convergence, as at NLO. However, the contributions coming from initial states with quarks are much smaller than the pure gluon-gluon contributions.

A final comment about the size of the partial NNLO discussed in this chapter are in order. At NLO, the contributions with both Higgs bosons coupling to different top-quark loops are much smaller than the other contributions. Thus, we expect the remaining contributions, which are discussed in chapter 7, to have a bigger numerical impact.

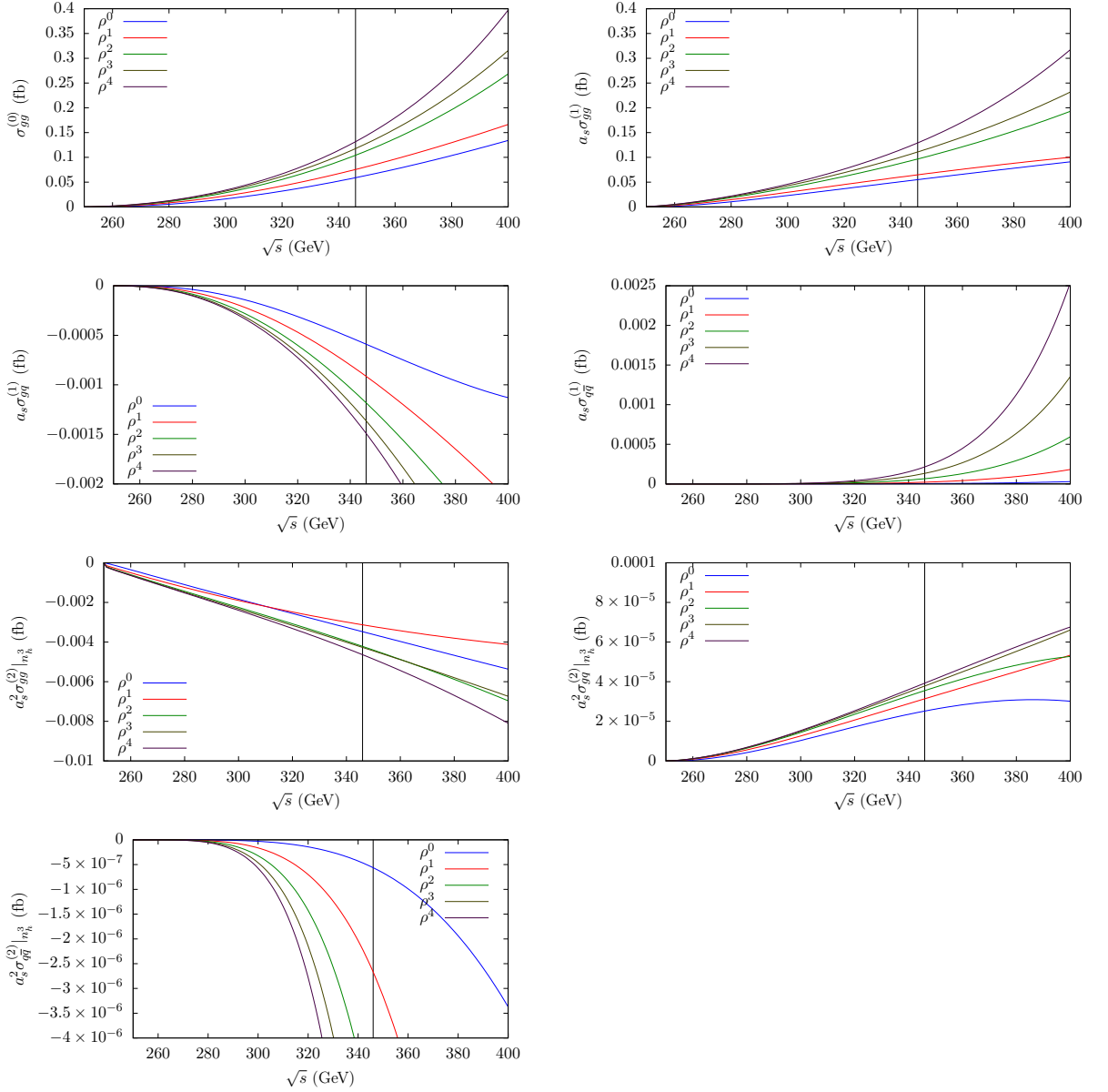


Figure 6.6: LO, NLO and NNLO partonic cross sections as a function of \sqrt{s} . The renormalization scale is $\mu = m_H$ and the vertical black line shows the top-quark pair-production threshold.

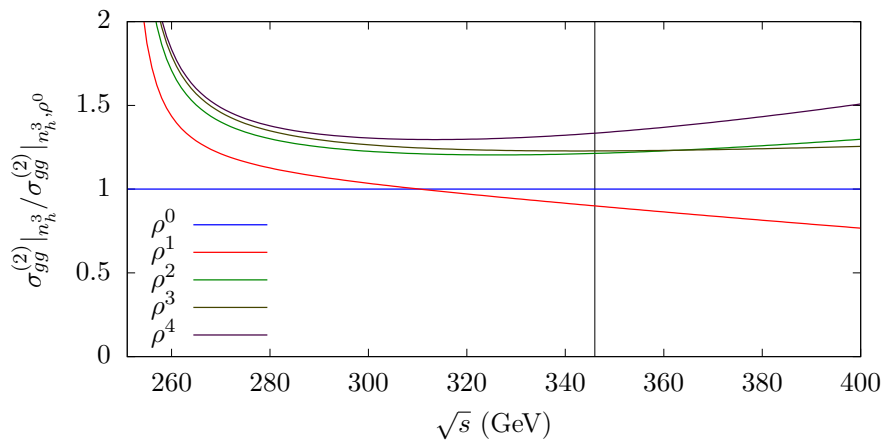


Figure 6.7: Ratio of higher-order expansions of the gluon-gluon initial state of the NNLO contribution under consideration in ρ and the LO term in the LME as a function of \sqrt{s} . The renormalization scale is $\mu = m_H$ and the vertical black line shows the top-quark pair-production threshold.

TOWARDS HIGGS BOSON PAIR PRODUCTION AT NNLO WITH FINITE TOP-QUARK-MASS EFFECTS

In this chapter we discuss the computation of the double-real radiation contribution to Higgs boson pair production in the LME at NNLO, as well as the computation of the remaining real-virtual corrections which have not been discussed in chapter 6.

In chapter 5 we laid the groundwork for the computations in this chapter by partial fractioning the linearly dependent three-loop phase-space families arising in this context and their minimization. Furthermore, most methods and concepts necessary for the computation of the contributions in this chapter are already introduced in chapter 6. As a consequence, we focus on differences w.r.t. the contributions discussed in chapter 6 in the following.

ADDITIONAL PARTONIC CHANNELS In addition to the gluon-gluon, quark-gluon and quark-anti-quark initial states at NLO and in the subset under consideration in chapter 6, two additional quark initiated partonic channels contribute. Furthermore, we also need to take into account additional ghost initial states.

Starting from NNLO also quark-quark initial states with same or different flavour quarks contribute to Higgs boson pair production. A sample diagram is shown in Fig. 7.1. There are no real-virtual corrections to the two partonic channels and both are UV finite. Their respective contribution is given by

$$\sigma_{qq}^{(2)} = \frac{a_q^2}{2s} \widetilde{\text{Disc}} \left(\mathcal{A}_{qq \rightarrow qq}^{(2)} \right), \quad (7.1)$$

$$\sigma_{qq'}^{(2)} = \frac{a_q^2}{2s} \widetilde{\text{Disc}} \left(\mathcal{A}_{qq' \rightarrow qq'}^{(2)} \right). \quad (7.2)$$

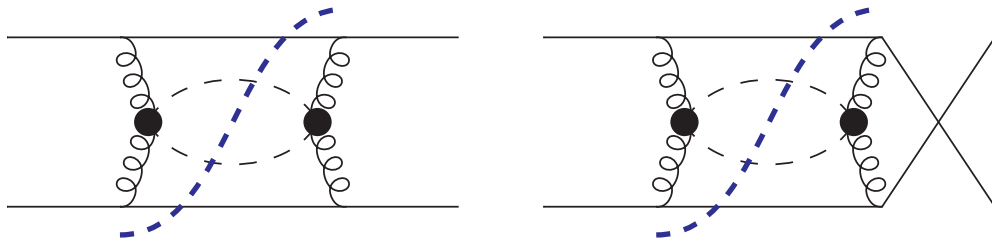


Figure 7.1: Contribution with two quarks in the initial state. In case of different-flavour quarks only the first diagram appears.

Furthermore, we need to take into account collinear counterterms for both channels which coincide and are given by

$$\begin{aligned} \sigma_{qq,\text{coll}}^{(2)} = \sigma_{qq',\text{coll}}^{(2)} &= \frac{2}{\epsilon} \left(\frac{\mu^2}{\mu_f^2} \right)^{2\epsilon} \int_{1-\delta}^1 dz P_{gq}^{(0)}(z) \sigma_{gq}^{(1)}(x/z) \\ &+ \frac{1}{\epsilon} \left(\frac{\mu^2}{\mu_f^2} \right)^{2\epsilon} \int_{1-\delta}^1 dy \int_{1-\delta}^1 dz P_{gq}^{(0)}(y) P_{gq}^{(0)}(z) \sigma_{gg}^{(0)}(x/(zy)) . \end{aligned} \quad (7.3)$$

In addition to the quark-quark contributions, new ghost contributions arise. At NNLO, also ghost-ghost and quark-ghost initial states contribute and thus we have to modify Eq. (6.7) and Eq. (6.9) to

$$\begin{aligned} \sigma_{gg}^{(2)} &= \frac{a_g^2}{2s} \left[\widetilde{\text{Disc}} \left(\mathcal{A}_{gg \rightarrow gg}^{(2)} \right) - \widetilde{\text{Disc}} \left(\mathcal{A}_{gc \rightarrow gc}^{(2)} \right) - \widetilde{\text{Disc}} \left(\mathcal{A}_{cg \rightarrow cg}^{(2)} \right) \right. \\ &\quad - \widetilde{\text{Disc}} \left(\mathcal{A}_{g\bar{c} \rightarrow g\bar{c}}^{(2)} \right) - \widetilde{\text{Disc}} \left(\mathcal{A}_{\bar{c}g \rightarrow \bar{c}g}^{(2)} \right) - \widetilde{\text{Disc}} \left(\mathcal{A}_{c\bar{c} \rightarrow c\bar{c}}^{(2)} \right) \\ &\quad \left. - \widetilde{\text{Disc}} \left(\mathcal{A}_{\bar{c}c \rightarrow \bar{c}c}^{(2)} \right) - \widetilde{\text{Disc}} \left(\mathcal{A}_{cc \rightarrow cc}^{(2)} \right) - \widetilde{\text{Disc}} \left(\mathcal{A}_{\bar{c}\bar{c} \rightarrow \bar{c}\bar{c}}^{(2)} \right) \right] \end{aligned} \quad (7.4)$$

and

$$\sigma_{qg}^{(2)} = \frac{a_g a_q}{2s} \left[\widetilde{\text{Disc}} \left(\mathcal{A}_{qg \rightarrow qg}^{(2)} \right) - \widetilde{\text{Disc}} \left(\mathcal{A}_{qc \rightarrow qc}^{(2)} \right) - \widetilde{\text{Disc}} \left(\mathcal{A}_{q\bar{c} \rightarrow q\bar{c}}^{(2)} \right) \right] , \quad (7.5)$$

respectively.

STRUCTURE OF THE CHAPTER First, in Sec. 7.1 we discuss the computation of the double-real radiation contributions. We then discuss the remaining real-virtual contributions in Sec. 7.2. Finally, in Sec. 7.3, we conclude by discussing the remaining steps required for obtaining the total, inclusive Higgs boson pair-production cross-section at NNLO including terms through $\mathcal{O}(1/M_t^8)$.

7.1 DOUBLE-REAL RADIATION

In this section we discuss the computation of the contributions due to two massless partons in the final state. We introduce two additional building blocks which arise in the double-real contributions in Sec. 7.1.1. In Sec. 7.1.2 we discuss the evaluation of the four-particle cut MIs. Finally, we present results for the qq and qq' channels, which only receive double-real radiation contributions in Sec. 7.1.3.

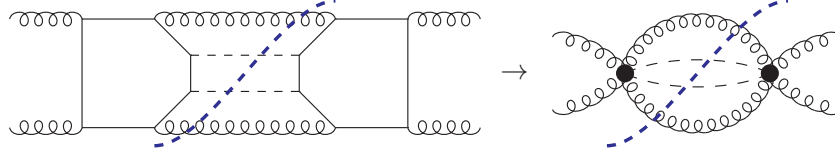


Figure 7.2: Sample contribution with four gluons coupling to the same top-quark loop. In total there are 3600 diagrams contributing to the diagram on the right side.

7.1.1 Four-gluon building blocks

Starting from NNLO diagrams with four gluons and one or two Higgs bosons coupling to the same top-quark loop, such as the one in Fig. 7.2 contribute. As a consequence, we also need to introduce building blocks with four external gluons. Following [142] we can write the four-gluon amplitude with one or two Higgs bosons as

$$\mathcal{A}_{4g-1/2H}^{\mu\nu\rho\sigma,abcd} = \sum_{ij} \rho^i c_{ij}^{abcd}(\epsilon) T_{ij}^{\mu\nu\rho\sigma}(\{q_j\}), \quad (7.6)$$

where, as in Eq. (6.11), the T_{ij} contain the dependence on the momenta of the gluons and Higgs bosons. However, the c_{ij} are tensors in colour space in case of the four-gluon building blocks. Thus, we can not separate the colour- and Lorentz-structure trivially from each other, unlike for the two- and three-gluon building blocks.

The c_{ij} can be written as linear combinations of traces over $SU(3)$ generators in the fundamental representation:

$$\begin{aligned} c_{ij}^{abcd} &= c_{ij,1} \text{Tr}(T^a T^b T^c T^d) + c_{ij,2} \text{Tr}(T^a T^b T^d T^c) + c_{ij,3} \text{Tr}(T^a T^c T^b T^d) \\ &+ c_{ij,4} \text{Tr}(T^a T^d T^c T^b) + c_{ij,5} \text{Tr}(T^a T^c T^d T^b) + c_{ij,6} \text{Tr}(T^a T^d T^b T^c) \\ &\equiv \sum_{k=1}^6 c_{ij,k} \mathcal{C}_k^{abcd}. \end{aligned} \quad (7.7)$$

Thus, we can write

$$c_{ij}^{abcd} = \sum_{k,k'=1}^6 c_{ij,k} \delta^{kk'} \mathcal{C}_k^{abcd}, \quad (7.8)$$

where δ is the Kronecker symbol.

We can now write $\mathcal{A}_{4g-1/2H}$ as

$$\mathcal{A}_{4g-1/2H}^{\mu\nu\rho\sigma,abcd} = \left(\sum_{ijk} \rho^i c_{ij,k}(\epsilon) T_{ij}^{\mu\nu\rho\sigma}(\{q_j\}) \delta_j \right) \times \left(\sum_{k'} \delta^{kk'} \mathcal{C}_k^{abcd} \right), \quad (7.9)$$

effectively separating colour- and Lorentz-structure. We can now use the second factor in Eq. (7.9) to compute the colour factors of the diagrams and the first factor for the Lorentz structure. When multiplying both structures together, we can perform the sum over k .

7.1.2 Computing the four-particle cut master integrals

In the following we discuss the computation of the four-particle cut MIs. As in chapter 6, we compute them in two ways: exactly, by finding a canonical basis, and as an expansion around $\delta \approx 0$, by making an asymptotic series ansatz. While, for phenomenological applications, the expansion around $\delta \approx 0$ is sufficient, the size and algebraic structure of the system of DEs complicate the determination of the coefficients in the series ansatz. Furthermore for the series ansatz the leading term in δ for all MIs needs to be known. However, a priori, it is unclear if all of them can indeed be computed. On the other hand, in a canonical basis typically only the leading terms of a small subset of MIs needs to be known and deeper series expansions can be obtained with less computational effort.

Thus, in the following we derive the canonical basis for all involved MIs.

MASTER INTEGRALS Using LiteRed we find that all integrals of the 14 four-particle cut integral families introduced in chapter 5 reduce to a set of 57 MIs, depicted in Figs. 7.3 and 7.4. The analytical expressions for the MIs $I_{25}^{(4)}$ to $I_{34}^{(4)}$ are the same as for the MIs $I_{35}^{(4)}$ to $I_{44}^{(4)}$. We keep them separate in the IBP reduction since they originate from the families P_6 and P_8 , as well as P_7 and P_9 ¹, respectively, which are nothing else than different cuts of the same family. The reason for keeping them separated is explained in Sec. 5.2.2. Furthermore, we did not identify any equivalent sectors of the families P_6 through P_9 with other families. As a consequence, the MIs $I_{45}^{(4)}$ and $I_{48}^{(4)}$ can be identified with $I_{27}^{(4)}$ and $I_{29}^{(4)}$, respectively.

DIFFERENTIAL EQUATIONS Due to its singular points, the system of DEs for these MIs requires a more careful treatment than the system discussed in Sec. 6.2.2. As a consequence, we use the program Libra [136] to perform manual manipulations on the system of DEs².

In contrast to Epsilon, Libra does not process systems of DEs in an automated manner. It rather provides the user with the relevant information on the system of DEs, such as its singularities and eigenvalues of the residues, and is able to construct balance transformations. The choice which eigenvalues to balance and the order in which manipulations are performed is left to the user. Thus, while it does not directly implement Lee's

¹ The families P_6 through P_9 are depicted in Fig. 5.7.

² Epsilon is only able to handle quadratic polynomials in the denominator. However, we need to deal with quartic polynomials, as will become evident later.

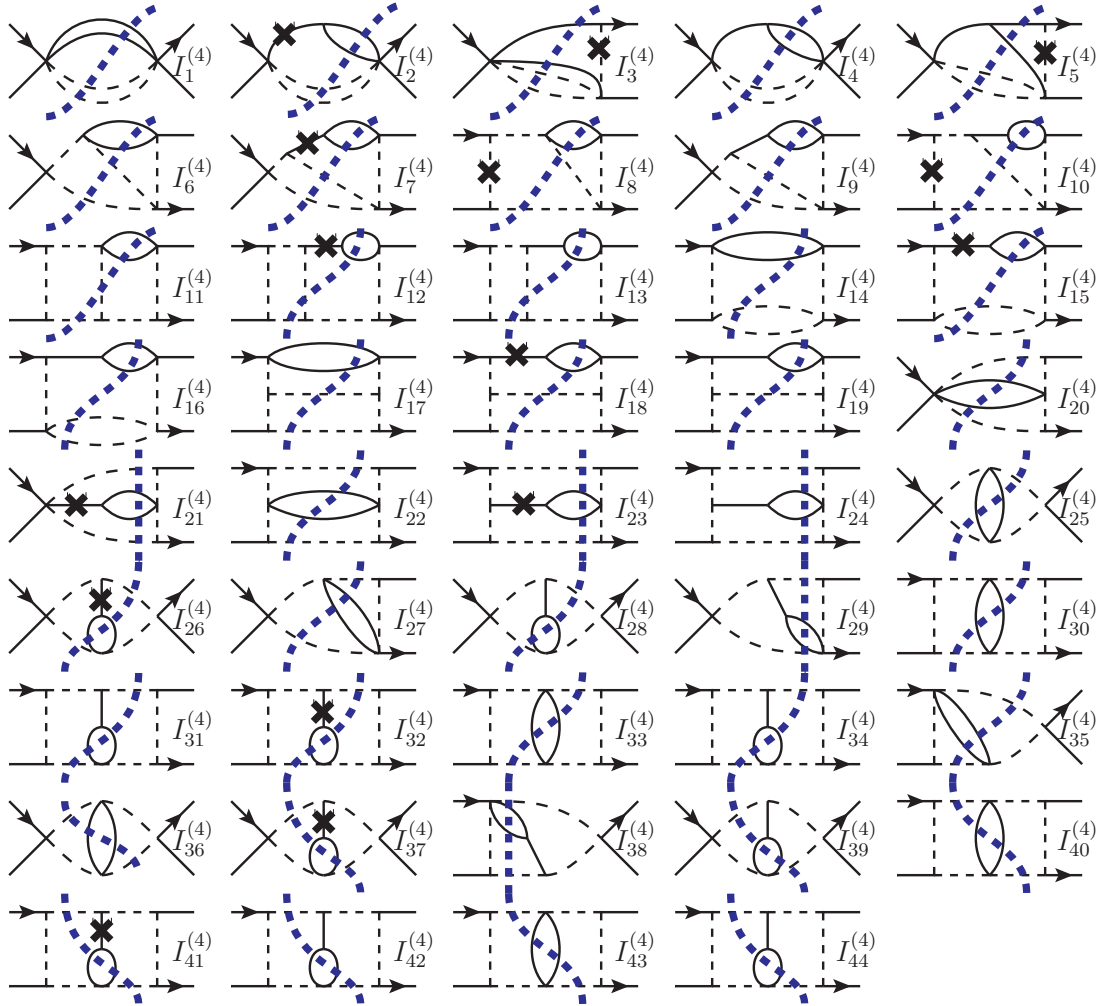


Figure 7.3: Four-particle cut master integrals contributing at NNLO. Crosses on lines denote numerators. Internal solid and dashed lines denote massless and massive particles, respectively.

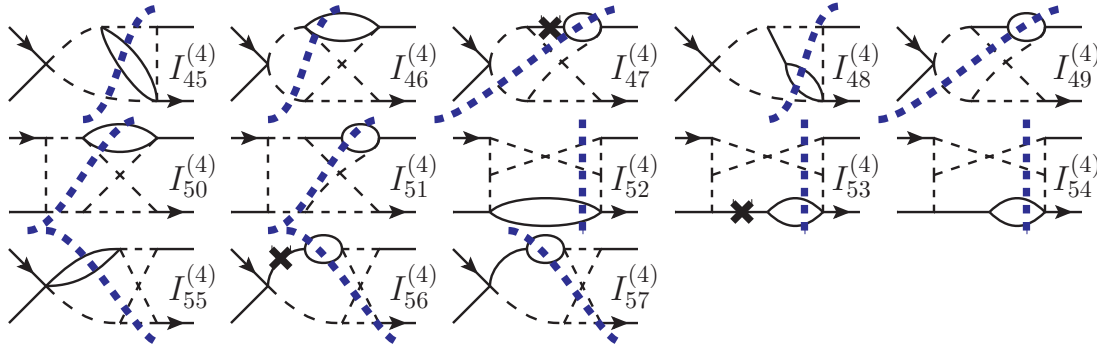


Figure 7.4: Four-particle cut master integrals contributing at NNLO. Crosses on lines denote numerators. Internal solid and dashed lines denote massless and massive particles, respectively.

algorithm, it implements all required operations. This allows us to deviate from Lee’s algorithm, which would first bring the diagonal blocks into Fuchsian form, followed by performing a variable change to render half-integer eigenvalues integer, then normalizes all eigenvalues and only then performs manipulations to the off-diagonal terms.

The rational functions in x and ϵ appearing in the off-diagonal terms have numerator and denominator degrees as large as 20 and as a consequence, algebraic manipulations of the system are rather involved. Furthermore, variable changes such as the one in 6.46 will increase the degrees of the rational functions further. Thus, we depart from the strict application of Lee’s algorithm to minimize the number of terms in off-diagonal entries. We proceed by

1. derive the system of DEs w.r.t. $x = m_H^2/s$,³
2. bring all diagonal blocks to Fuchsian form,
3. bring all off-diagonal entries to Fuchsian form,
4. reduce all eigenvalues of the residues of the diagonal blocks to $0 \pm \frac{1}{2}$,
5. bring all off-diagonal entries to Fuchsian form again.

By following these steps we arrive at a form which is close to a canonical form. The reason for having to bring the off-diagonal entries to Fuchsian form twice is, that the balance transformations required for reducing the eigenvalues of the diagonal blocks may change off-diagonal entries in a non-trivial way, introducing higher order poles again.

In the next step we investigate the poles of the system of DEs. Here, five letters appear: $x_i \in \{0, 1, -1, 1/4, -1/4\}$. Note, that the poles at $x = -1$ and $x = -1/4$ appear in the

³ In practice we set $s = 1$ and take the derivative w.r.t m_H^2 .

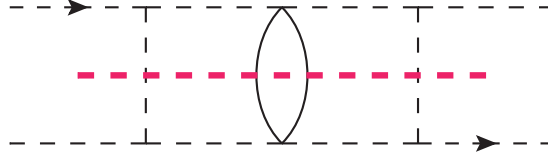


Figure 7.5: Four-particle cut master integral with the letter $x = -1/4$. The momentum $(q_1 - q_2)$ flows through the cut depicted by the red dashed line.

DEs of diagrams like the one depicted in Fig. 7.5 and correspond to the kinematic limits $s \rightarrow -m_H^2$ and $s \rightarrow -4m_H^2$, respectively. This is because the momentum $(q_1 - q_2)^2 = -s$ flows through the massive lines, instead of $(q_1 + q_2)^2 = s$, leading to the change of sign.

The eigenvalues for the residues at $x = \pm 1/4$ are half-integer and thus we need to find a variable change to make them integer. To this end, we introduce the variable t , related to x by

$$x = \frac{t^4 + 1}{8t^2}. \quad (7.10)$$

The relevant kinematic regime for Higgs boson pair production expressed in the variable t lies on the unit circle between 1 and $\exp(i\pi/4)$. In t , the three letters $x_i \in \{0, \pm 1/4\}$ take the form $t_i \in \{0, \pm 1, \pm i, \pm \exp(\pm i\pi/4)\}$. The letters $x_i \in \{1, -1\}$ are mapped onto the roots of

$$P_{4,1} = t^4 - 8t^2 + 1 \quad \text{and} \quad P_{4,-1} = t^4 + 8t^2 + 1, \quad (7.11)$$

respectively. After the variable change, only integer eigenvalues of the residues appear and we can proceed to bring the system of DEs to canonical form. We do so by applying balance transformations to normalize all eigenvalues of the residues to be proportional to ϵ .

Next, we bring the off-diagonal elements to Fuchsian form once again. Since now quartic polynomials appear in the denominators, algebraic manipulations, similar to the balance transformations, to reduce the off-diagonal elements to Fuchsian form are computationally involved. By bringing all off-diagonal elements to Fuchsian form in x first, we reduced the amount of required manipulations in t to a minimum and, as a consequence, also the computational complexity. Finally, we factor out ϵ from the system of DEs, thus arriving at a canonical form.

BOUNDARY CONDITIONS Having arrived at a canonical form, we need boundary conditions for solving the system of DE. To this end, the leading term in the δ expansion of some of the MIs need to be computed explicitly. To simplify this task, the 57 MIs were chosen such, that all numerators appearing, but the one in MIs $I_8^{(4)}$ and $I_{10}^{(4)}$, reduce to a linear combination of s and m_H^2 at LO in δ .

In [143], the four-particle phase-space was parametrized in a similar manner as the three-particle phase-space in Sec. 6.2.2. The main difference w.r.t. the three-particle phase-space is, that we now deal with two massless momenta, instead of one. As a consequence, we need to integrate over the two additional angles θ_6 and ϕ_6 . However, none of the propagators depends on the angles θ_3 and ϕ_3 , since both Higgs bosons couple to the same top-quark loop. Thus, after expanding around $\delta \approx 0$, the integration over θ_3 and ϕ_3 is trivial.

These integrals are then solved with the help of [130]⁴ and evaluate to gamma functions, as in the previous chapter. Using DEs in δ , expansions around $\delta \approx 0$ through $\mathcal{O}(\delta^{20})$ are obtained [143].

As described in Sec. 6.2.2 we can infer which of the MIs are required as boundary conditions in the limit $\delta \rightarrow 0$ for solving the system of DEs. In total, the entries of 18 MIs in the transformation matrix T contain a negative power of δ , after expanding in $\delta \approx 0$. However, the explicit computation of the LO term in δ in [143] shows that for six out of these 18 integrals, the leading power in δ is higher than the power of the pole in the inverse transformation. As a consequence, only twelve of the 57 MIs need to be known as boundary conditions for the DEs. Taking into account the choice of scalar products, only six independent angular integrals have to be performed.

ITERATED INTEGRALS To obtain exact solutions for the MIs we define the quartic polynomial

$$P_{4,0} = t^4 + 1, \quad (7.12)$$

in addition to the two polynomials in Eq. (7.11). In analogy to Eq. (6.47), we define the integration kernels

$$f(u^{(k)}; t) = \frac{\partial_t^k P_{4,0}}{P_{4,0}}, \quad f(v^{(k)}; y) = \frac{\partial_t^k P_{4,1}}{P_{4,1}} \quad \text{and} \quad f(w^{(k)}; y) = \frac{\partial_t^k P_{4,-1}}{P_{4,-1}}, \quad (7.13)$$

which appear in the iterated integrals in which the exact MIs are expressed.

As in Eq. (6.48), iterated integrals containing one or more of these kernels can be written as a sum of GPLs:

$$\begin{aligned} G(\dots, u^{(k)}, \dots; y) &= \sum_{i=1}^4 c_{i,u}^{(k)} G(\dots, u_i, \dots; y), \\ G(\dots, v^{(k)}, \dots; y) &= \sum_{i=1}^4 c_{i,v}^{(k)} G(\dots, v_i, \dots; y), \\ G(\dots, w^{(k)}, \dots; y) &= \sum_{i=1}^4 c_{i,w}^{(k)} G(\dots, w_i, \dots; y), \end{aligned} \quad (7.14)$$

⁴ During this computation a typo in Eq. (50) of [130] was discovered. The last term should read $\cos^2(\chi_2^{(1)}/2)$.

where the u_i are the roots of $P_{4,0}$, the v_i the roots of $P_{4,1}$ and the w_i the roots of $P_{4,-1}$. An explicit example for this treatment can be found in example 11. After applying Eq. (7.14) to the iterated integral under consideration, the numerical evaluation using GINAC [140, 141] is straightforward.

Since we compute the collinear counterterms as well as the double-virtual contributions in an expansion around $\delta \approx 0$, we also need to expand the MIs. However, so far, we have not been able to expand iterated integrals containing the kernels $v^{(k)}$ and $w^{(k)}$ around $\delta \approx 0$. Since most publicly available packages capable of expanding GPLs, such as PolyLogTools [139], are not able to properly handle complex polynomial roots such as the v_i and w_i .

7.1.3 Results for the quark-quark initial state

As the qq and qq' channels only receive double-real radiative corrections, we are now in the position to present results for them. We obtained results through $\mathcal{O}(\rho^4)$ and $\mathcal{O}(\delta^{27/2})$.

Only the integrals $I_1^{(4)}$ through $I_5^{(4)}$, as well as $I_{20}^{(4)}$ and $I_{21}^{(4)}$ contribute to the qq' channel. As also the second type of diagrams in Fig. 7.1 contributes to the qq channel, also integrals $I_{22}^{(4)}$ through $I_{24}^{(4)}$ contribute to it. The remaining double-real emission integrals contribute to the other channels, such as the $q\bar{q}$ channel discussed in Sec. 7.2.4.

The collinear counterterm is equal for both channels and was obtained in [144]. In the following we present the leading terms in δ and ρ for the initial-state with quarks of different flavours

$$\begin{aligned} \sigma_{qq'}^{(2)} = & \frac{a_s^4 G_F^2 m_H^2}{\pi} \left[\delta^{\frac{9}{2}} \left(\frac{5631473}{4557106575} - \frac{7748}{4822335} a_1 + \frac{4}{5103} a_1^2 - \frac{7748}{14467005} \ln \delta \right. \right. \\ & + \frac{8}{15309} a_1 \ln \delta + \frac{4}{45927} \ln^2 \delta - \frac{2}{45927} \pi^2 \left. \right) + \rho \left\{ \delta^{\frac{7}{2}} \left(\frac{493577}{15746400000} \right. \right. \\ & - \frac{3773}{87480000} a_1 + \frac{49}{1944000} a_1^2 - \frac{49}{34992000} \pi^2 - \frac{3773}{262440000} \ln \delta \\ & + \frac{49}{2916000} a_1 \ln \delta + \frac{49}{17496000} \ln^2 \delta \left. \right) + \delta^{\frac{9}{2}} \left(\frac{145608059}{195304567500} - \frac{101317}{103335750} a_1 \right. \\ & + \frac{28}{54675} a_1^2 - \frac{101317}{310007250} \ln \delta + \frac{56}{164025} a_1 \ln \delta + \frac{28}{492075} \ln^2 \delta - \frac{14}{492075} \pi^2 \left. \right) \left. \right\} \\ & + \rho^2 \left\{ \delta^{\frac{5}{2}} \left(\frac{493577}{15746400000} - \frac{3773}{87480000} a_1 + \frac{49}{1944000} a_1^2 - \frac{49}{34992000} \pi^2 \right. \right. \\ & \left. \left. - \frac{3773}{262440000} \ln \delta + \frac{49}{2916000} a_1 \ln \delta + \frac{49}{17496000} \ln^2 \delta \right) + \delta^{\frac{7}{2}} \left(\frac{344611787}{840157920000} \right. \right. \end{aligned}$$

$$\begin{aligned}
& -\frac{181147}{333396000}a_1 + \frac{1783}{6350400}a_1^2 - \frac{1783}{114307200}\pi^2 - \frac{181147}{1000188000}\ln\delta \\
& + \frac{1783}{9525600}a_1\ln\delta + \frac{1783}{57153600}\ln^2\delta \Big) + \delta^{\frac{9}{2}} \left(\frac{12635591432}{11962404759375} \right. \\
& - \frac{2268102721}{1620304560000}a_1 + \frac{314717}{428652000}a_1^2 - \frac{2268102721}{4860913680000}\ln\delta \\
& \left. + \frac{314717}{642978000}a_1\ln\delta + \frac{314717}{3857868000}\ln^2\delta - \frac{314717}{7715736000}\pi^2 \right) \Big] + \mathcal{O}(\delta^{\frac{11}{2}}, \rho^3),
\end{aligned} \tag{7.15}$$

as well as the difference between the result for equal and different flavours:

$$\sigma_{qq}^{(2)} - \sigma_{qq'}^{(2)} = -\frac{a_s^4 G_F^2 m_H^2}{\pi} \left[\frac{1}{1968300} \delta^{\frac{9}{2}} \rho + \rho^2 \left\{ \frac{7}{104976000} \delta^{\frac{7}{2}} + \frac{1627}{11573604000} \delta^{\frac{9}{2}} \right\} \right]. \tag{7.16}$$

Here $\mu_f = \mu = m_H$, $a_s = \alpha_s^{(5)}(m_H)/\pi$ and $a_1 = \ln 2$. Note, that the ρ^0 contribution of the difference starts only at $\delta^{11/2}$. The leading term in the limit $\delta \rightarrow 0$ for both channels is of $\mathcal{O}(\rho^2)$. We show subsequent terms in the LME of $\sigma_{qq}^{(2)}$, $\sigma_{qq'}^{(2)}$ and their difference $\sigma_{qq}^{(2)} - \sigma_{qq'}^{(2)}$ as a function of \sqrt{s} in Fig. 7.6. Both channels seem to slowly converge below the top-quark threshold. The ratio between the ρ^0 contribution and the subsequent terms in the LME for $\sigma_{qq}^{(2)}$ is shown in Fig. 7.7. In the lowermost plot of Fig. 7.6, we show the difference between the same- and different-flavour initial states. The difference corresponds to the second class of diagrams in Fig. 7.1, which are smaller by two orders of magnitude than the first class of diagrams.

7.2 REAL-VIRTUAL CONTRIBUTIONS

In this section we discuss the real-virtual contributions at NNLO which have not been considered in chapter 6. We need to evaluate contributions with a three-particle cut and two top-quark loops, such as the left diagram in Fig. 7.8 or three top-quark loops, such as the diagram on the right. Diagrams with three top-quark loops which all couple to a Higgs boson are discussed in chapter 6.

The loop momentum running through the massless lines in the diagram on the left can be either hard or soft. As a consequence, the LME leads to the two contributions shown in Fig. 7.9. The first contribution contains a one-loop and a two-loop tadpole integral in the hard subgraph and a two-loop phase-space integral with a three-particle cut in the co-subgraph. The two-loop phase-space integral falls into the integral families already discussed in chapter 6. In the following we call this type of contribution *hard real-virtual corrections*. We discuss their computation in Sec. 7.2.2. As second contribution

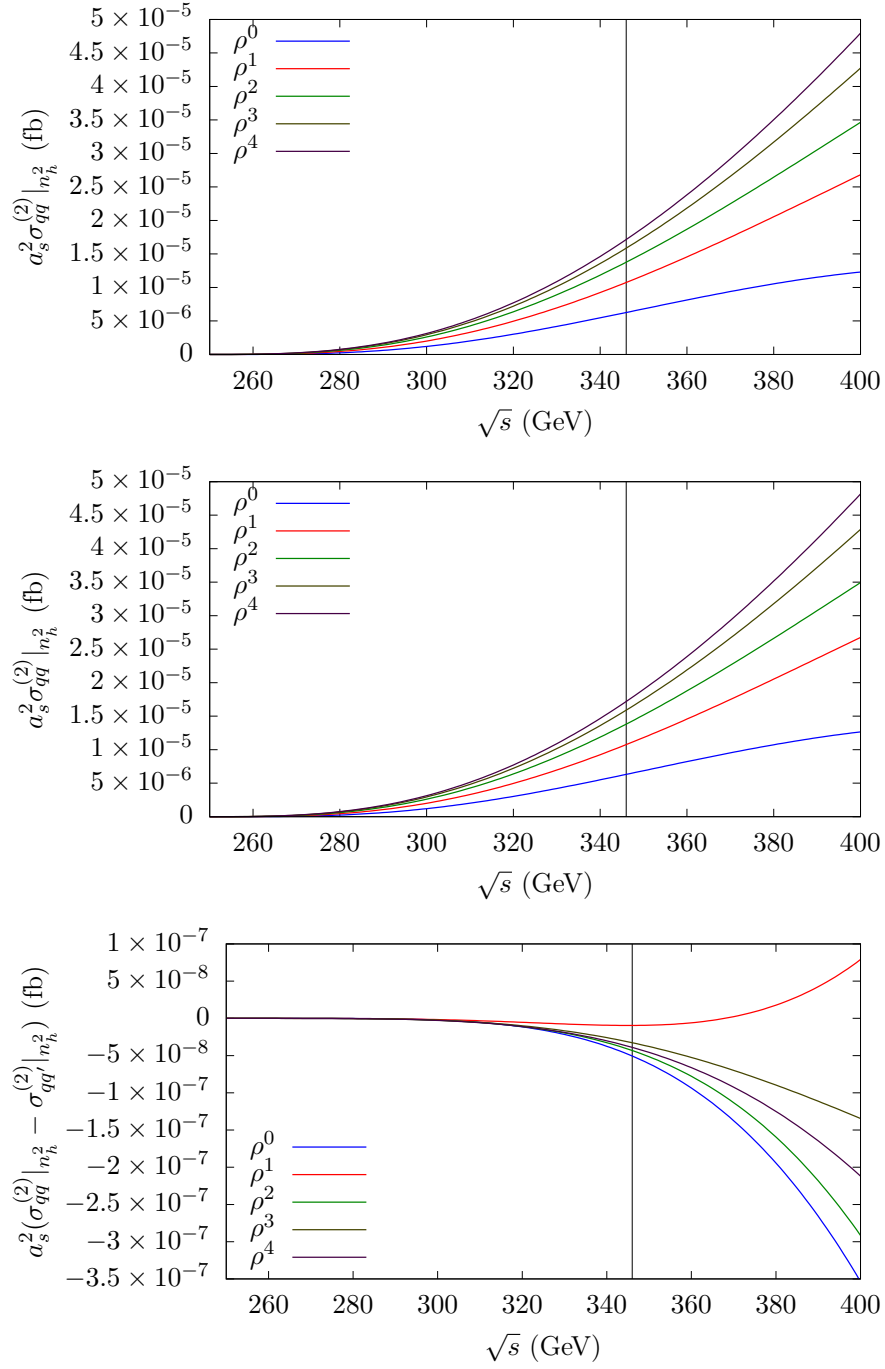


Figure 7.6: NNLO results of the two quark-quark channels as well as their difference as a function of \sqrt{s} . The renormalization scale is $\mu = m_H$ and the vertical black line shows the top-quark pair-production threshold.

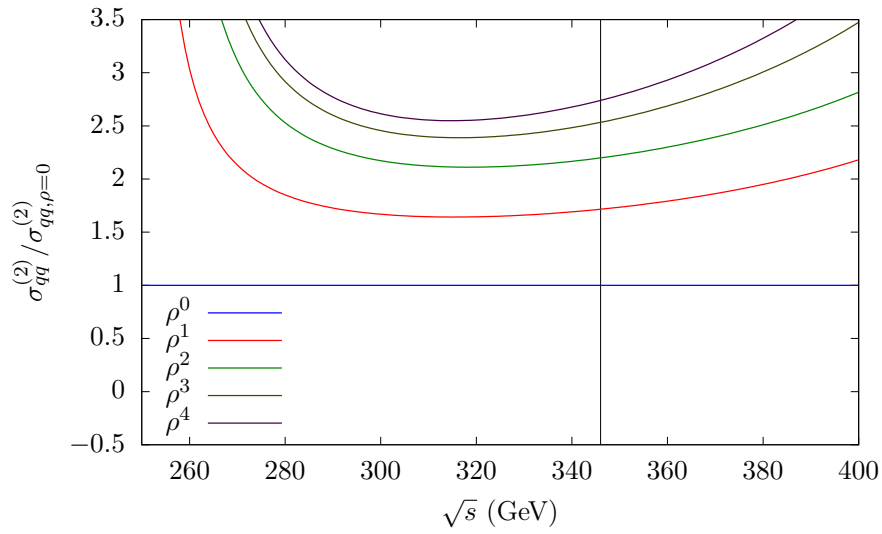


Figure 7.7: Ratio between higher-order terms in the LME and the leading term. The renormalization scale is $\mu = m_H$ and the vertical black line shows the top-quark pair-production threshold.

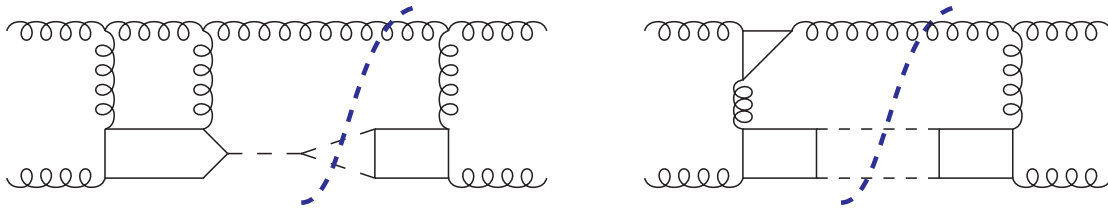


Figure 7.8: Sample real-virtual contributions under consideration in this section. The third quark loop in the diagram on the right can be either a top-quark loop or a massless quark loop.

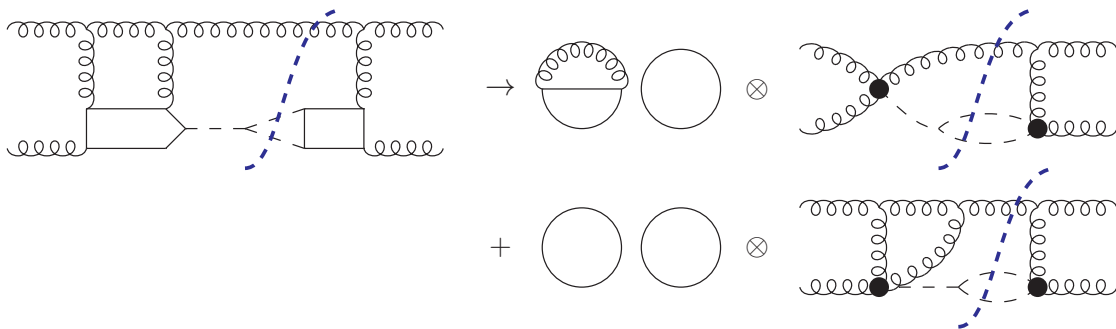


Figure 7.9: Real-virtual contribution leading to a two-loop three-particle cut phase-space integral and a three-loop three-particle cut phase-space integral.

a hard subgraph with two one-loop tadpole integrals and a three-loop integral with a three-particle cut in the co-subgraph arise. We call this contribution *soft real-virtual corrections*. Their computation, as well as the evaluation of the relevant *MI*s, is discussed in Sec. 7.2.3.

The second diagram in Fig. 7.8 has an additional quark loop. This quark loop can be either massless or a top-quark loop. In the former case, the *LME* leads to a hard subgraph with two one-loop tadpole integrals and a three-loop three-particle cut phase-space integral, whereas in the latter case, the hard subgraph contains three one-loop tadpole integrals and a two-loop phase-space integral. They are discussed in Sec. 7.2.1 and Sec. 7.2.3, respectively. In Sec. 7.2.4, we present results for the $q\bar{q}$ channel, in which all different real-virtual contributions appear.

7.2.1 Contributions with a third top-quark loop

Contributions with a third top-quark loop, that does not couple to any Higgs boson line, contribute to the gluon-gluon, quark-gluon and quark-anti-quark channels. Sample diagrams are depicted in Fig. 7.10. These diagrams yield three one-loop tadpole integrals

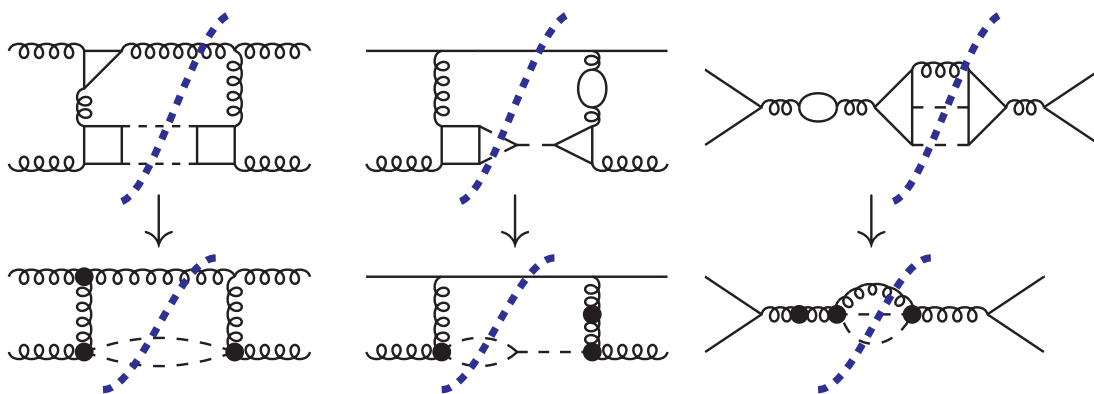


Figure 7.10: Real-virtual contributions with three closed top-quark loops that are not part of the subset discussed in chapter 6.

and a two-loop three-particle cut phase-space integral in the *LME*. The resulting two-loop phase-space integrals all fall in the families discussed in chapter 6 and reduce to the *MI*s I_1 , I_2 and I_7 .

LARGE MASS EXPANSION To compute these contributions, we need to extend the building block approach introduced in [126]. There are two possibilities to do so:

1. introduce two-gluon and three-gluon building blocks, or
2. generate diagrams with two building blocks for the top-quark loops coupling to Higgs bosons and a top-quark loop, such as the one depicted in Fig. 7.11.

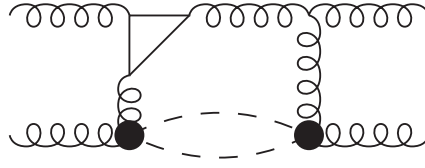


Figure 7.11: Diagram with a top-quark loop and two building blocks.

While the first approach technically would be feasible, we can not distinguish between regular gluon propagators and two-gluon building blocks when generating diagrams. To this end, we would need to introduce *dressed* gluon propagators which all correspond to two-gluon building blocks and introduce book-keeping routines to discard any products of terms stemming from the LME of two different propagators. The same holds for the three-gluon building block.

We thus choose to go with the second option and generate diagrams with two building blocks and a top-quark loop, such as the one depicted in Fig. 7.11. These diagrams can be processed by exp like when we would perform a regular LME without any building blocks. Using this approach allows us to expand the subset under consideration through $1/M_t^8$. This already has been done for the gg channel, which is the most involved one.

7.2.2 Hard real-virtual corrections

In the following, we discuss contributions involving one one-loop and one two-loop tadpole integral, such as the first term on the right side of Fig. 7.9. These contributions arise when the loop-momentum flowing through the massless lines is hard, i.e. is of the order of M_t , and lead to two-loop three-particle cut phase space integrals. As in the subset discussed in Sec. 7.2.1 the phase-space integrals reduce to I_1 , I_2 and I_7 .

Again, there are two possibilities to compute these contributions:

1. introduce two-loop building blocks, or
2. generate diagrams with one one-loop building block, as well as one top-quark loop and perform the LME with exp.

For the first approach, we need to extend the building block code to allow for two-loop building blocks. While this does not pose any major obstacles for building blocks with only gluons and Higgs bosons as external particles, diagrams such as the one depicted in Fig. 7.12 require building blocks involving external off-shell quarks. Furthermore, similar diagrams with ghosts instead of quarks need to be taken into account and thus we also need to take into account building blocks involving external ghost particles. In total, we would need to introduce eight additional building blocks: $q\bar{q}H$, $q\bar{q}HH$, $q\bar{q}gH$, $q\bar{q}gHH$, $c\bar{c}H$, $c\bar{c}HH$, $c\bar{c}gH$ and $c\bar{c}gHH$. This is because building blocks involving quarks contain a non-trivial structure of Dirac matrices and involve

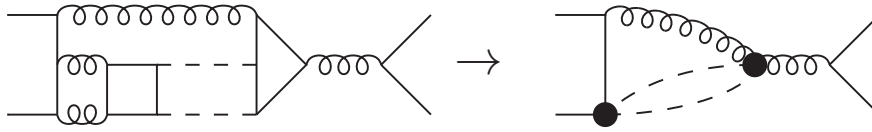


Figure 7.12: Diagram leading to a two-quark–two-Higgs boson building block.

off-shell spinors at the beginning and end of every Dirac matrix chain, which need to be taken into account correctly.

While in principle, all the above issues could be overcome, it is simpler to generate diagrams with one building block and using `exp` to perform the `LME` of the remainder. In a proof-of-principle calculation, the contribution to the $q\bar{q}$ channel has been successfully computed through $1/M_t^2$.

One comment regarding the gg channel is in order. As there are no hard real-virtual contributions involving quark- or ghost-building blocks in this channel, we could compute it using two-loop versions of the building blocks appearing in chapter 6, in case the `LME` of diagrams with one building block is computationally too demanding.

7.2.3 Soft real-virtual corrections

The final subset of real-virtual corrections has a loop-momentum that is soft, i.e. is of the order of m_H or \sqrt{s} , such as the second contribution in the second line of Fig. 7.9. These diagrams can be computed using the same building blocks as in the case of the double-real corrections and lead to three-loop three-particle cut integrals. As discussed in Sec. 5.2.2, partial fractioning and minimization of the integral families required for this subset leads to five linearly independent integral families. Using `LiteRed` we find the 17 `MI`s depicted in Fig. 7.13. In the following we discuss the computation of the `MI`s.

EVALUATION OF THE BOUNDARY CONDITIONS The 17 `MI`s are evaluated in [143], following a similar procedure as for the three-particle cut `MI`s in Sec. 6.2.1. In the following we highlight the differences w.r.t. Sec. 6.2.1.

The major difference in this calculation, as compared to the two-loop three-particle cut phase-space integrals, is given by the extra loop integration which has to be performed. Most of the loop integrals involved, such as the one appearing in `MI`s $I_5^{(3)}$ and $I_6^{(3)}$, lead to ϵ -dependent powers of polynomials in $\cos\theta_5$ and ζ , a feature not present in the calculation in Sec. 6.2.1. The more complicated loop integrals appearing in `MI`s $I_8^{(3)}$ and $I_{11}^{(3)}$ need to be evaluated using the strategy of regions [125], to obtain the leading term in the δ expansion.

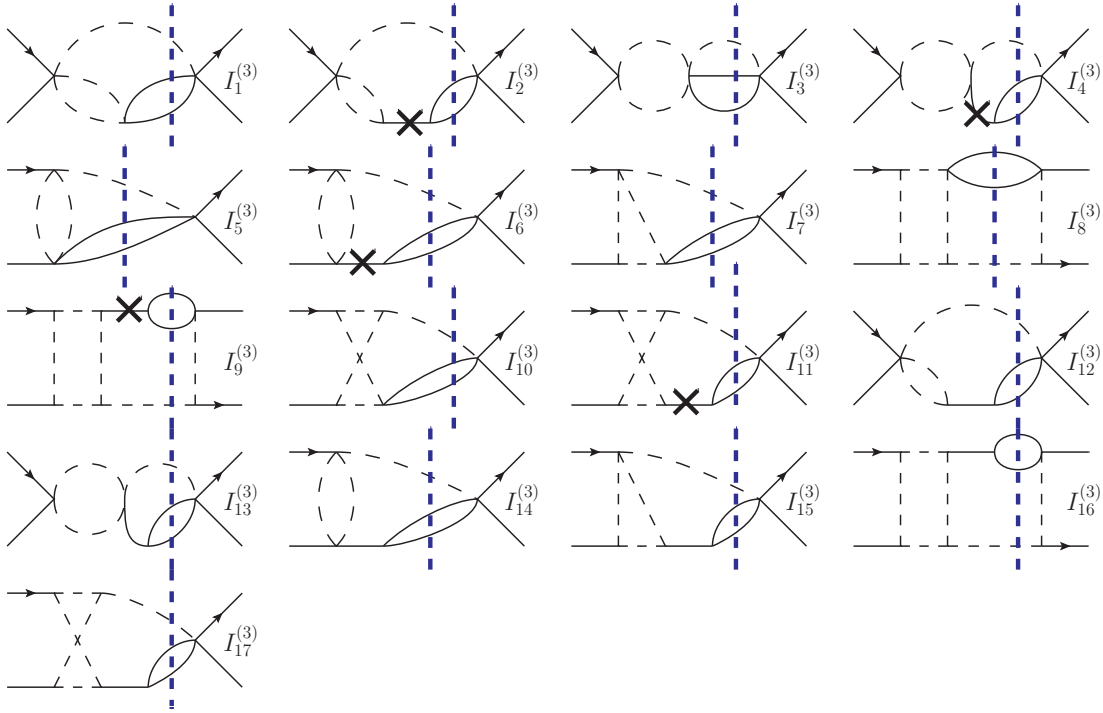


Figure 7.13: Three-loop three-particle cut **MI**s contributing at **NNLO**. Crosses denote numerators.

Furthermore, some of the loop integrals also lead to an imaginary part. One example is the loop integral appearing in **MI** $I_3^{(3)}$:

$$L_2 = \int \frac{d^D k}{(2\pi)^D} \frac{1}{k^2} \frac{1}{(k + q_1 + q_2)^2} = \frac{1}{(4\pi)^{2-\epsilon}} \frac{\Gamma(\epsilon)\Gamma^2(1-\epsilon)}{\Gamma(2-2\epsilon)} (-s)^{-\epsilon}. \quad (7.17)$$

The factor $(-s)^{-\epsilon}$ expands to $1 - \epsilon \ln(-s) + \mathcal{O}(\epsilon^2)$ and thus has a non-vanishing imaginary part. On the contrary, the partonic cross-sections are manifestly real. This apparent problem is resolved by the fact that also the complex-conjugate of $I_3^{(3)}$ contributes. As an example consider the two diagrams in Fig. 7.14. After performing Lorentz algebra, partial fractioning and minimization of the involved integrals, as well as **IBP** reduction, the sum of the two diagrams in the first row is expressed through a linear combination of the four integrals in the second row. The prefactor of $I_3^{(3)}$ and its complex conjugate $(I_3^{(3)})^*$ agree with each other. The same holds for $I_4^{(3)}$ and $(I_4^{(3)})^*$. As a consequence, only the real parts of the three-loop three-particle cut **MI**s enter. Since we already identify integrals with their complex conjugates when minimizing families, we need to take the real part of each loop integral in the boundary conditions⁵.

⁵ Greater care has to be taken when treating double-virtual corrections in the reverse unitarity approach, see e. g. [145].

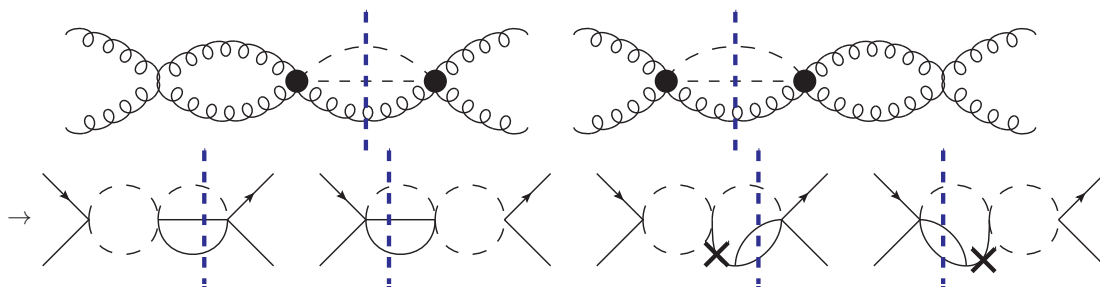


Figure 7.14: The diagrams in the top row reduce to a linear combination of the diagrams in the bottom row. The first two **MI**s are complex conjugates of one another and have the same prefactor as do the second two.

Finally, in [143] the differential equations in δ were solved by the series ansatz in Eq. (6.51).

SOLVING THE DIFFERENTIAL EQUATIONS We process the **DE**s for the 17 **MI**s following the procedure outline in Sec. 7.1.2. After bringing the system of differential equations to Fuchsian form, three letters remain in the system: $x_i \in \{0, 1, 1/4\}$. While $x = 0$ and $x = 1/4$ appear in the **DE**s for all 17 **MI**s, $x = 1$ only appears in the **DE**s for **MI**s ten through 17. As in the case of the four-particle cut and the two-loop three-particle cut **MI**s, the eigenvalues of the residue at $x = 1/4$ are half-integer. Thus, we introduce the variable z , given by

$$x = \frac{z}{(z+1)^2}. \quad (7.18)$$

Note, that the variable change in Eq. (6.46) would also have worked. However, at the time we did perform the computations in chapter 6, we did not realize that the variable change to z would have mapped the kinematical range under consideration to $z \in (0, 1]$, leading to slightly simpler expressions when dealing with **GPL**s involving the letter 0. After the variable change, we are able to bring the system of **DE**s to canonical form and express all iterated integrals by **GPL**s with the letters $z \in \{0, 1, -1, -\exp(\pm i\pi/3)\}$.

From the basis change between the original and the canonical basis we can deduce that the leading terms of the first ten **MI**s enter as boundary conditions.

The solutions obtained by solving the exact differential equations can be numerically evaluated using GINAC. In contrast to the double-real **MI**s we can expand this set of **MI**s around $\delta \approx 0$ using PolyLogTools, as the relation between δ and z is simple enough. We obtained expansions through $\mathcal{O}(\delta^{20})$ and found agreement with the results obtained by solving the differential equations in δ [143].

7.2.4 Results for the quark-anti-quark initial state

In contrast to the two channels discussed in Sec. 7.1.3, the quark-anti-quark channel also receives real-virtual contributions. The three contribution discussed in Sec. 7.2 (hard real-virtual, soft real-virtual and corrections with three top-quark loops) contribute. We renormalize the top-quark mass in the $\overline{\text{OS}}$ scheme and express the strong coupling constant in the five-flavour scheme. For $\mu_f = \mu = m_H$, the leading δ terms through $\mathcal{O}(\rho^1)$ read

$$\begin{aligned} \sigma_{q\bar{q}}^{(2)} = \frac{a_s^4 G_F^2 m_H^2}{\pi} & \left[\delta^{\frac{9}{2}} \left(\frac{5631473}{4557106575} - \frac{7748}{4822335} a_1 + \frac{4}{5103} a_1^2 - \frac{2}{45927} \pi^2 - \frac{7748}{14467005} \ln \delta \right. \right. \\ & + \frac{8}{15309} a_1 \ln \delta + \frac{4}{45927} \ln^2 \delta \left. \right) + \rho \left\{ \delta^{\frac{7}{2}} \left(\frac{565457}{1607445000} - \frac{599}{1275750} a_1 \right. \right. \\ & + \frac{1}{4050} a_1^2 - \frac{1}{72900} \pi^2 - \frac{599}{3827250} \ln \delta + \frac{1}{6075} a_1 \ln \delta + \frac{1}{36450} \ln^2 \delta \left. \right) \\ & + \delta^{\frac{5}{2}} \left(\frac{81333221}{48826141875} - \frac{16}{229635} n_l - \frac{101317}{103335750} a_1 + \frac{28}{54675} a_1^2 - \frac{14}{492075} \pi^2 \right. \\ & \left. \left. - \frac{101317}{310007250} \ln \delta + \frac{56}{164025} a_1 \ln \delta + \frac{28}{492075} \ln^2 \delta \right) \right\} + \mathcal{O}(\rho^2, \delta^{\frac{11}{2}}) \right]. \end{aligned} \quad (7.19)$$

Here $n_l = 5$ is the number of light flavours.

The result including terms up to $\delta^{29/2}$ is shown in Fig. 7.15 as a function of \sqrt{s} . The first two terms in the ρ expansion show a similar behaviour as in the case of the contributions discussed in chapter 6. However, they have a different sign and are two orders of magnitude larger.

7.3 OUTLOOK

As mentioned in the beginning of this chapter, the computations discussed here are still work in progress. In Sec. 7.3.1 we discuss the remaining steps to complete the computation of all partonic channels and the necessary steps to obtain the total Higgs boson pair-production cross-section in proton-proton collisions at the LHC. Finally, in Sec. 7.3.2 we discuss the validity of the LME and possible ways to improve our results.

7.3.1 Completing the computation

In the following we discuss the remaining steps to obtain the total Higgs boson pair-production cross-section in proton-proton collisions.

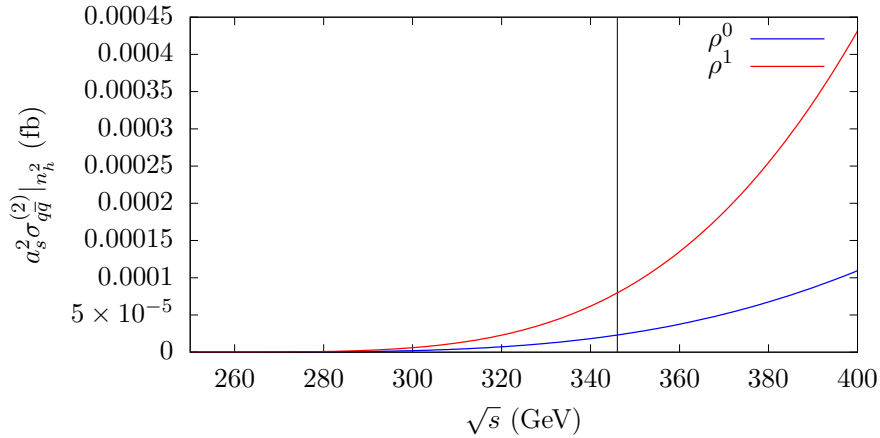


Figure 7.15: NNLO $q\bar{q}$ initial-state cross sections as a function of \sqrt{s} . The renormalization scale is $\mu = m_H$ and the vertical black line shows the top-quark pair-production threshold.

COMPLETING THE PARTONIC CHANNELS With the quark-quark and quark-anti-quark initiated partonic channels available through $\mathcal{O}(\rho^4)$ and $\mathcal{O}(\rho^1)$, respectively, the next step is to extend the computation of the quark-anti-quark channel through $\mathcal{O}(\rho^4)$. To this end, corrections leading to a two-loop tadpole integral, the hard real-virtual corrections, discussed in Sec. 7.2.2, need to be extended through $\mathcal{O}(\rho^4)$. All other contributions can be computed by the available setup and do not pose additional challenges.

However, the main task is to complete the calculation of the contributions with gluons in the initial state, i.e. the gluon-gluon and the quark-gluon channel. Here, the following contributions are already available:

- For both channels, the contributions with an additional top-quark loop, discussed in Sec. 7.2.1, are known through $\mathcal{O}(\rho^4)$.
- The expressions for the double-real and soft real-virtual contributions are available through $\mathcal{O}(\rho^1)$.
- The collinear counterterms are known [144].
- The virtual corrections to the gluon-gluon channel are also available.

Thus, for these two channels we need to extend the computation of the double-real and soft-real virtual corrections to higher powers in ρ and compute the hard real-virtual contributions. Once we are able to extend the expansion depth of the hard real-virtual contributions in the quark-anti-quark channel through $\mathcal{O}(\rho^4)$, the computational setup should, in principle, be able to also handle the quark-gluon channel without modifications. For the gluon-gluon channel further optimizations might be required.

FOUR-PARTICLE CUT MASTER INTEGRALS As described in Sec. 7.1.2, obtained a canonical form of the DEs and thus could express all double-real MIs exactly in m_H^2/s . However, as other contributions have only been obtained as an expansion around $\delta \approx 0$, we need to obtain higher-order expansion terms in δ for the four-particle cut MIs. Obtaining them by means of recurrence relations using the differential equations in δ is computationally expensive and thus we want to perform an expansion of our exact solutions. As mentioned in Sec. 7.1.2, this is a rather challenging task by itself, but preliminary studies with the Mathematica package HarmonicSums [146–148] show, that it might be feasible without the need of developing a new program to do so.

To expand the iterated integrals with HarmonicSums, we do not apply the relations in Eq. (7.14) but let HarmonicSums operate on the iterated integrals with quartic polynomials in the integration kernels. In the first step, we change to the variable $t' = t - 1$, letting HarmonicSums perform all necessary transformations of the integration kernels. In the next step we expand around $t' \approx 0$, corresponding to an expansion around $t \approx 1$ and thus $\delta \approx 0$. In the next step we would need to express the expansion in t' by δ and expand around $\delta \approx 0$ again.

The major open question regarding this procedure is the expansion depth in δ we can reach.

THE HADRONIC CROSS-SECTION Once all partonic channels are known through $\mathcal{O}(\rho^4)$, we have to obtain predictions for proton-proton collisions. To this end, we need convolute the partonic cross-sections with parton density functions f :

$$\sigma_{pp \rightarrow HH+X} = \sum_{i,j} \int dx_1 dx_2 f(x_1) f(x_2) \sigma_{ij \rightarrow HH+X}(x_1 x_2 s). \quad (7.20)$$

Here, the sum runs over all possible partonic initial-state configurations. With the results for the partonic cross-section expanded in δ the necessary numerical integrations do not pose additional challenges.

7.3.2 Beyond the large mass expansion

The results obtained in this chapter and in chapter 6 using the LME only describe the partonic cross-sections for partonic center-of-mass energies below the top-quark threshold. At higher energies, the LME diverges and we need additional methods to improve our predictions. To this end, it was found in [26] at NLO, that on the level of the total hadronic cross-section it is possible to obtain a reasonably converging behaviour by factoring out the exact LO result. Since the exact NLO result for the gluon-gluon channel is available [23–25], this analysis can be extended to NNLO.

In the following we discuss two additional ideas, which might allow for further improvements.

PADÉ APPROXIMANTS In [149] the full top-quark–mass dependence of the **NLO** form factors contributing to single-Higgs boson production and Higgs boson pair production is reconstructed from the **LME** and an expansion around the top-quark threshold of the form factors. To this end, the top-quark–mass dependence is encoded in the variable ω with

$$\frac{s}{4M_t^2} = \frac{4\omega}{(1 + \omega)^2} \quad (7.21)$$

and an Padé ansatz of the form

$$[n/m](\omega) = \frac{\sum_{i=0}^n a_i \omega^i}{1 + \sum_{i=0}^m b_i \omega^i} \quad (7.22)$$

is made. The coefficients a_i and b_i are then determined by comparing the ansatz to the **LME** and the threshold expansion.

This method has also been successfully applied to the Higgs boson–gluon form factor at **NNLO** [89] and Z-boson pair-production off-shell interference [150].

In [89] it was shown, that the knowledge of several expansion terms in the **LME** is crucial for correctly approximating the form factor. With a **LME** of similar depth available for the hadronic Higgs boson pair-production cross-section, a similar approximation can be constructed once information on the behaviour at the top-quark threshold becomes available.

TOWARDS DIFFERENTIAL DISTRIBUTIONS Another possibility to improve upon the **LME** is to combine all contributions which can be computed without an approximation in M_t together with **LME** results for those that can not. At **NNLO** such a combination was conducted in [29], where exact results through **NLO** were combined with exact results for the double-real radiation contribution, which can be obtained numerically with programs such as `Open\Loops 2` [151], and the real-virtual and purely virtual **NNLO** corrections in the limit $M_t \rightarrow \infty$. As a result, the authors of [29] were able to obtain results for differential distributions through **NNLO**.

To improve upon these predictions, **LME** results for the purely virtual and real-virtual **NNLO** corrections could be used. While the form factors for $gg \rightarrow HH$ are known through $\mathcal{O}(\rho^4)$, the real-virtual contributions are missing. As a first step towards the inclusion of higher order terms in the **LME** we thus would compute the **LME** of the form factors for $gg \rightarrow gHH$ and $gq \rightarrow qHH$ through $\mathcal{O}(\rho^4)$.

CONCLUSION

The topic of this thesis is the computation of **NNLO** corrections to Higgs boson pair production and higher-order corrections to processes involving Higgs bosons. In this section, we summarize the two parts of this thesis and the results obtained.

The first part of this thesis is devoted to the computations of three quantities, at the four-loop order, which are relevant to Higgs boson physics:

- In chapter 2 we obtain the effective coupling between two Higgs bosons and gluons. We published the result, including all decoupling constants in **QCD** at four loops, in Ref. [33]. Our result served as an important ingredient in the recent computation of the Higgs boson pair-production cross-section, in the limit $M_t \rightarrow \infty$, at **N₃LO** [31, 32].
- In chapter 3 we expand the four-loop Higgs boson–gluon vertex for $M_t \gg m_H$ through $\mathcal{O}(m_H^4/M_t^4)$ and found that the mass-suppressed terms add corrections of $\mathcal{O}(10\%)$, for the top-quark mass renormalized in the **OS** scheme, compared to the leading term. This result is the first step towards including terms suppressed by inverse powers of the top-quark mass in cross-section predictions for the production of Higgs bosons in gluon-fusion at **N₃LO**. The results obtained in this chapter are published in Ref. [34].
- Based on the computational setup established in the course of the computations of chapter 3, in chapter 4 we compute the **N₃LO QCD** corrections to the decay rate of a Higgs boson into two photons through $\mathcal{O}(m_H^4/M_t^4)$. While these contributions are small, the mass-suppressed terms are comparable to the leading term, showing the significance of the higher-order terms in the **LME** at **N₃LO** for a physical quantity. A publication of the result is in preparation [152].

In the second part, we focused on the computation of real-radiation corrections to Higgs boson pair production at **NNLO** by expanding the integrals involved for a large top-quark mass. We divided the computation into three individual pieces:

- In chapter 5 we discuss the computation of real-radiation contributions using the method of reverse unitarity. In this context linearly dependent Feynman integrals arise, which need to be partial fractioned in order to apply regular Feynman integral techniques. To this end, we developed the program **LIMIT** to partial fraction linearly dependent Feynman integral families and minimize the resulting linearly independent ones. **LIMIT** not only proved useful in this context, but was also

successfully applied to the computation of two-loop matching coefficients in non-relativistic QCD [123] and the relation between pole mass and kinetic mass at three loops [124].

- Using the techniques established in chapter 5, we compute a subset of the real-virtual contributions in chapter 6. This subset involves all diagrams with both Higgs bosons coupling to different top-quark loops. It is gauge independent and, when combined with the corresponding subset of virtual corrections, finite. At the partonic level, the corrections due to terms suppressed by inverse powers of the top-quark mass are of $\mathcal{O}(30\% - 40\%)$ compared to the leading NNLO term. We published the results in Ref. [35].
- In the final chapter, we provide results for the qq , qq' and $q\bar{q}$ channels. Furthermore, we discuss the state of the qg and gg channels. In particular we find a *canonical* basis for all MIs involved. Furthermore, we discussed possibilities to improve the knowledge of top-quark-mass dependent terms beyond the pure LME.

While the computation of the real-radiation contributions is not yet complete, the main technical challenges have been solved in the course of this thesis and the computation of the missing pieces is underway. Once all partonic channels are completed, the total inclusive cross-section for Higgs boson pair production in proton collisions can be obtained.

Part III

APPENDIX

DEFINITIONS

In this appendix we discuss several definitions used throughout this thesis. We start by introducing ghost fields in Sec. A.1 and continue with the renormalization of fields and parameters in Sec. A.2. In Sec. A.3 we introduce decoupling constants. We conclude by defining the various colour factors arising in QCD calculations in Sec. A.4 and specifying the tensor structures and projectors required in the computation of C_{HH} in Sec. A.5.

A.1 GHOSTS AND GAUGE FIXING

Deriving the gluon propagator solely based on Eq. (2.1) is not possible due to gauge invariance. To this end we choose to quantize QCD using the covariant Lorentz gauge and add an additional term to the Lagrangian density Eq. (2.1)¹:

$$\mathcal{L}^{\text{GF}} = -\frac{1}{2(1-\xi)} \left(\partial^\mu A_\mu^a \right)^2. \quad (\text{A.1})$$

The gauge parameter ξ can take arbitrary values and physical observables do not depend on it. There are two special gauge choices commonly used: $\xi = 0$, also known as *Feynman gauge* and $\xi = 1$, known as *Landau gauge*.

For abelian gauge theories, such as QED, Eq. (A.1) is enough to quantize the theory and derive Feynman rules. In the nonabelian case however, we furthermore need to introduce so-called *Faddeev-Popov ghost fields* to quantize the theory using the path-integral formalism. The ghost fields c^a are anticommuting scalar fields described by

$$\mathcal{L}^{\text{ghosts}} = (\partial^\mu \bar{c}^a) D_\mu^{ab} c^b. \quad (\text{A.2})$$

While ghosts seem to be a mere mathematical trick to quantize the theory, they also play a more physical role. Without ghosts, loop computations with internal gluons would lead to the wrong result, due to unphysical timelike and longitudinal polarizations, see e.g. the example in Ref. [153]. Ghosts exactly cancel these unphysical degrees of freedom.

A.2 RENORMALIZATION OF QCD

The fields and parameters present in Eq. (2.1) and Eq. (A.1) can not be measured directly but have to be connected to observable quantities. Furthermore, Green's functions beyond LO expressed in terms of bare quantities typically diverge in the UV regime. To this

¹ Our choice of the gauge parameter is related to the choice in Ref. [42] by $\alpha = 1 - \xi$.

end, renormalized, as well as bare fields and parameters are introduced together with renormalization constants Z , to absorb the UV divergences and obtain finite results.

The renormalization constants may not only contain UV divergences, but can also be chosen to contain finite pieces. In the widely used $\overline{\text{MS}}$ scheme [154] also finite terms of the form $\ln(4\pi)$ and γ_E , which always appear together with poles in dimensional regularization, are absorbed. In the $\overline{\text{MS}}$ scheme the bare quark, gluon and ghost fields are connected to their renormalized counterparts via [46]

$$q_f^0 = \sqrt{Z_2} q_f, \quad G_\mu^{0,a} = \sqrt{Z_3} G_\mu^a, \quad c^a = \sqrt{\tilde{Z}_3} c^a. \quad (\text{A.3})$$

The bare parameters are connected to the renormalized ones via

$$g_s^0 = \mu^\epsilon Z_{g_s} g_s, \quad m_f^0 = Z_m m_f, \quad \zeta^0 = 1 + Z_3 (\zeta - 1). \quad (\text{A.4})$$

Here μ is the so-called renormalization scale which is introduced to keep the coupling constant g_s dimensionless. As a consequence all renormalized fields and parameters depend on μ . The renormalization constants in Eq. (A.3) and Eq. (A.4) can be related to the UV divergences of two- and three-point Green's functions, by demanding cancellation of UV poles. They are known through five loops [55, 57–59, 155].

THE ON-SHELL SCHEME Another commonly used scheme for the renormalization of masses and external fields is the so-called OS scheme. In this scheme the renormalization constants for the fields and masses are chosen such that the bare propagators behave like the free propagators near the mass shell. For gluons and massless quarks using this implies that

$$Z_2^{\text{OS}} = \frac{1}{1 + \Sigma_V(0)}, \quad Z_3^{\text{OS}} = \frac{1}{1 + \Pi(0)}, \quad (\text{A.5})$$

where Σ_V is the vectorial part of the light quark self-energy and Π is the transversal part of the gluon self-energy. Since the self-energies are evaluated for $p^2 = 0$ contributions involving only massless particles vanish and thus, only contributions involving massive particles enter Z_2^{OS} and Z_3^{OS} .

For massive quarks the relation between self-energy and Z_2^{OS} is more involved and can be found e. g. in Refs. [104, 156], together with the relation for Z_m^{OS} . In contrast to the $\overline{\text{MS}}$ scheme all renormalization constants in the OS scheme contain finite parts and positive powers in ϵ . The quark mass in the $\overline{\text{MS}}$ and OS scheme can be related using the renormalization constants in the two schemes. This relation is known through four-loop order in QCD [104, 156–162]

$$\frac{m_f(\mu)}{M_f^{\text{OS}}} = \frac{Z_m}{Z_m^{\text{OS}}} = z_m(\mu). \quad (\text{A.6})$$

A.3 DECOUPLING CONSTANTS

Furthermore, in many QCD applications all scales involved are much smaller than the top-quark mass. In this case, large logarithms occur, which in the effective theory can be absorbed into parameters and fields.

Example 12 (Large logarithms)

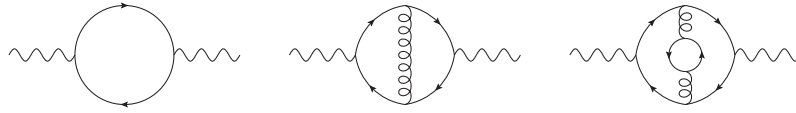
To see the effect of large scale hierarchies, consider the electromagnetic R-ratio

$$R(s) = \frac{\sigma_{e^+e^- \rightarrow \text{hadrons}}}{\sigma_{e^+e^- \rightarrow \mu^+\mu^-}}.$$

This observable is known up to $\mathcal{O}(\alpha_s^4)$ [163, 164] and plays a crucial role in the determination of α_s . Pure QCD corrections can be related to the imaginary part of the photon vacuum polarization

$$R(s) = 12\pi \text{Im}\Pi(-s - i\epsilon)$$

and thus only two-point diagrams such as the ones below contribute.



The contributions of massless quarks up to $\mathcal{O}(\alpha_s^2)$ can be easily evaluated and yield

$$\frac{R(s)}{N_c \sum_f^{n_l} Q_f^2} = 1 + \frac{\alpha_s}{\pi} + \left(\frac{\alpha_s}{\pi}\right)^2 \left[\frac{365}{24} - 11\zeta_3 + n_l \left(-\frac{11}{12} + \frac{2}{3}\zeta_3 \right) \right],$$

where the renormalization scale $\mu^2 = s$, ζ_3 is the Riemann ζ -function evaluated at 3, N_c is the number of colours, n_l is the number of massless quark flavours, and Q_f is the electric charge of the quark flavour f . If we now also consider a heavy quark with mass m_Q which is much larger than s , it only contributes through diagrams like the last one in the above figure. Its leading contribution in s/m_Q^2 is given by

$$R^{(Q)}(s) = -\frac{1}{6} N_c \sum_f^{n_l} Q_f^2 \left(\frac{\alpha_s}{\pi}\right)^2 \ln\left(\frac{s}{m_Q^2}\right).$$

For large values of m_Q , this contribution can become dominant and even spoil perturbativity if

$$\left| \frac{\alpha_s}{\pi} \ln(s/m_Q^2) \right| > 1.$$

When integrating out a heavy quark also the parameters and fields of the full and effective theories have to be related to each other. This is done by introducing the so-called decoupling constants, which in their bare form can be defined by [46]

$$\begin{aligned} G_\mu^{0,(n_l)} &= \sqrt{\zeta_3^0} G_\mu^{0,(n_f)}, \quad c^{0,(n_l)} = \sqrt{\tilde{\zeta}_3^0} c^{0,(n_f)}, \quad q_f^{0,(n_l)} = \sqrt{\zeta_2^0} q_f^{0,(n_f)}, \\ g_s^{0,(n_l)} &= \zeta_g^0 g_s^{0,(n_f)}, \quad \zeta^{0,(n_l)} = 1 + \zeta_3^0 (\zeta^{0,(n_f)} - 1), \end{aligned} \quad (\text{A.7})$$

where $n_f = n_l + 1$ and no colour indices are shown.

Replacing bare fields and parameters by renormalized ones using Eq. (A.3) and Eq. (A.4) yields for the parameters² [46]

$$\begin{aligned} \alpha_s^{(n_l)} &= \left(\frac{Z_g^{(n_f)}}{Z_g^{(n_l)}} \zeta_g^0 \right)^2 \alpha_s^{(n_f)} = \zeta_{\alpha_s} \alpha_s^{(n_f)}, \\ \zeta^{(n_l)} &= 1 + \frac{Z_3^{(n_f)}}{Z_3^{(n_l)}} \zeta_3^0 (\zeta^{(n_f)} - 1) = \zeta_3 (\zeta^{(n_f)} - 1), \end{aligned} \quad (\text{A.8})$$

where the renormalized decoupling constants depend on $\alpha_s^{(n_f)}$, $\ln(\mu^2/m_Q^2)$ and, in the case of ζ_3 , on $\zeta^{(n_f)}$. Note that in the n_l -flavour renormalization constants the parameters need to be replaced by their n_f -flavour versions using the above relations.

Example 13 (Absorbing large logarithms)

Recall the *NLO* corrections as well as *NNLO* involving massive quarks to the *R*-ratio

$$\begin{aligned} R(s) &= N_c \sum_f^{n_l} Q_f^2 \left(1 + \frac{\alpha_s^{(n_f)}}{\pi} \right), \\ R^{(Q)}(s) &= -\frac{1}{6} N_c \sum_f^{n_l} Q_f^2 \left(\frac{\alpha_s^{(n_f)}}{\pi} \right)^2 \ln \left(\frac{s}{m_Q^2} \right), \end{aligned}$$

where now the number of quark flavours $n_f = n_l + 1$ is explicit. Up to one loop the inverse of the decoupling constant of α_s is given by

$$\frac{1}{\zeta_{\alpha_s}} = 1 + \frac{1}{6} \frac{\alpha_s^{(n_l)}}{\pi} \ln \left(\frac{\mu^2}{m_Q^2} \right) + \mathcal{O}(\alpha_s^2),$$

where we replaced $\alpha_s^{(n_f)}$ by iteratively applying Eq. (A.8). Expressing $\alpha_s^{(n_f)}$ in $R(s)$ through $\alpha_s^{(n_l)}$ absorbs the large logarithm in the coupling constant.

² Similar relations hold for ζ_2 and $\tilde{\zeta}_3$.

MATCHING FOR THE DECOUPLING CONSTANTS Following the same reasoning as in the previous two subsections the bare decoupling constants for the gluon and ghost fields are given by their vacuum polarization $\Pi(p^2)$ and $\tilde{\Pi}(p^2)$ [46]

$$\zeta_3^0 = 1 + \Pi^h(0) , \quad (\text{A.9})$$

$$\tilde{\zeta}_3^0 = 1 + \tilde{\Pi}^h(0) . \quad (\text{A.10})$$

Combining Eq. (A.9) and Eq. (A.5) we obtain

$$Z_3^{\text{OS}} = \frac{1}{\zeta_3^0} . \quad (\text{A.11})$$

The bare gauge coupling decoupling constant ζ_g^0 can be extracted from the 1PI part of the gauge boson–ghost vertex $\Gamma_{\bar{c}cg}(p, q)$ by [46]

$$\tilde{\zeta}_1^0 = 1 + \Gamma_{\bar{c}cg}^h(0, 0) , \quad (\text{A.12})$$

$$\zeta_g^0 = \frac{\tilde{\zeta}_1^0}{\tilde{\zeta}_3^0 \sqrt{\zeta_3^0}} . \quad (\text{A.13})$$

A.4 COLOUR FACTORS

In this section we provide explicit expressions for the colour factors appearing in our computations. We provide expressions, both for a generic number of colours N_c and the case of QCD ($N_c = 3$). In the following we normalize

$$\text{Tr} \left(T^a T^b \right) = T_F \delta^{ab} = \frac{\delta^{ab}}{2} , \quad (\text{A.14})$$

where the T are generators in the fundamental representation.

The dimension and quadratic Casimir operator in the fundamental representation are given by

$$N_F = N_c = 3 , \quad C_F = \frac{N_c^2 - 1}{2N_c} = \frac{4}{3} , \quad (\text{A.15})$$

whereas the corresponding quantities in the adjoint representation read

$$N_A = N_c^2 - 1 = 8 , \quad C_A = N_c = 3 . \quad (\text{A.16})$$

Furthermore, the following contractions of symmetric rank-4 tensors arise at four loops:

$$\frac{d_A^{abcd} d_F^{abcd}}{N_A} = \frac{N_c(N_c^2 + 6)}{48} = \frac{45}{48} , \quad \frac{d_F^{abcd} d_F^{abcd}}{N_A} = \frac{N_c^4 - 6N_c^2 + 18}{96N_c^2} = \frac{5}{96} . \quad (\text{A.17})$$

A.5 PROJECTORS AND TENSORS STRUCTURES

Here, we provide the Lorentz tensor structures and projectors appearing in Higgs boson and Higgs boson pair-production.

In the case of single Higgs boson production, there is only one contributing tensor structure, discussed in Sec. 2.2.1. We project on this structure, by applying

$$P^{\mu\nu} = \frac{q}{D-2} \left((q_1 \cdot q_2) g^{\mu\nu} - q_1^\nu q_2^\mu - q_1^\mu q_2^\nu \right). \quad (\text{A.18})$$

In the case of Higgs boson pair-production two tensor structures arise. They can be found, e. g. in Ref. [126], and are given by

$$\begin{aligned} \mathcal{A}_1^{\mu\nu} &= g^{\mu\nu} - \frac{q_1^\nu q_2^\mu}{(q_1 \cdot q_2)}, \\ \mathcal{A}_2^{\mu\nu} &= g^{\mu\nu} + \frac{q_3^2}{q_T^2 (q_1 \cdot q_2)} q_1^\nu q_2^\mu - \frac{(q_2 \cdot q_3)}{q_T^2 (q_1 \cdot q_2)} q_1^\nu q_3^\mu - \frac{(q_1 \cdot q_3)}{q_T^2 (q_1 \cdot q_2)} q_3^\nu q_2^\mu + \frac{2}{q_T^2} q_3^\mu q_3^\nu, \end{aligned} \quad (\text{A.19})$$

where $q_T^2 = 2(q_1 \cdot q_3)(q_2 \cdot q_3)/(q_1 \cdot q_2) - q_3^2$. Note, that the first tensor structure is the same, as in the case of single Higgs boson production. However, the projector can not be re-used, as it is not orthogonal to the second structure.

As a consequence, we need two new projectors, given by

$$\begin{aligned} P_1^{\mu\nu} &= \frac{1}{2(D-3)} \left(g^{\mu\nu} - \left[(1-\epsilon) - \frac{q_3^2}{q_T^2} \epsilon \right] \frac{q_1^\nu q_2^\mu}{(q_1 \cdot q_2)} \right. \\ &\quad \left. - \frac{2\epsilon}{q_T^2 (q_1 \cdot q_2)} [(q_2 \cdot q_3) q_1^\nu q_3^\mu + (q_1 \cdot q_3) q_2^\mu q_3^\nu] + \frac{2\epsilon}{q_T^2} q_3^\mu q_3^\nu \right), \\ P_2^{\mu\nu} &= \frac{1}{2(D-3)} \left(g^{\mu\nu} - \left[\epsilon - (1-\epsilon) \frac{q_3^2}{q_T^2} \right] \frac{q_1^\nu q_2^\mu}{(q_1 \cdot q_2)} \right. \\ &\quad \left. - \frac{2(1-\epsilon)}{q_T^2 (q_1 \cdot q_2)} [(q_2 \cdot q_3) q_1^\nu q_3^\mu + (q_1 \cdot q_3) q_2^\mu q_3^\nu] + \frac{2(1-\epsilon)}{q_T^2} q_3^\mu q_3^\nu \right). \end{aligned} \quad (\text{A.20})$$

In the calculation of C_{HH} , we only need $P_1^{\mu\nu}$ as the form-factor of $\mathcal{A}_2^{\mu\nu}$ vanishes in the limit $m_t \rightarrow \infty$. Still, we need $P_1^{\mu\nu}$ and have to keep the three external momenta different from each other and zero, to avoid mixing with unphysical operators.

A.6 GONCHAROV POLYLOGARITHMS

The phase-space MIs discussed in chapters 6 and 7 can be expressed in terms of so-called GPLs [165]. They can be defined recursively as

$$G(a_1, \dots, a_n; x) = \int_0^x \frac{dy}{y - a_1} G(a_2, \dots, a_n; y), \quad (\text{A.21})$$

with $G(x) = 1$. The a_i are called *letters* and the set of letters $\vec{a} = \{a_1, \dots, a_n\}$ is called a *word*. In case the rightmost letter is zero, special care has to be taken. To this end one generally defines

$$G(0; x) = \log(x) . \tag{A.22}$$

The product of two **GPLs** of the same argument with the words \vec{a} and \vec{b} can be written as a sum of **GPLs**:

$$G(\vec{a}; x)G(\vec{b}; x) = \sum_{\vec{c}=\vec{a}\sqcup\vec{b}} G(\vec{c}; x) . \tag{A.23}$$

The sum runs over all shuffles of the letters in \vec{a} and \vec{b} . In the following we give an explicit example of this property:

Example 14 (Shuffle algebra)

The shuffle of two words keeps the order of the letters in each individual word unchanged. In the case of two words with length two, the above sum becomes:

$$\begin{aligned} G(a, b; x)G(c, d; x) &= G(a, b, c, d; x) + G(a, c, b, d; x) + G(a, c, d, b; x) \\ &\quad + G(c, a, b, d; x) + G(c, a, d, b; x) + G(c, d, a, b; x) . \end{aligned}$$

Further properties of **GPLs** are reviewed in Ref. [139].

LARGE MASS EXPANSION

Throughout this thesis we apply the large mass expansion (LME)¹ to various problems in Higgs boson physics. Here, we want to briefly describe the method.

The expansion of a Feynman diagram Γ in the large mass M takes the form

$$\Gamma(M, \{q\}, \{m\}) \stackrel{M \rightarrow \infty}{\approx} \sum_{\gamma} \Gamma/\gamma(\{q\}, \{m\}) \otimes \mathcal{T}_{\{q_{\gamma}\}, \{m_{\gamma}\}} \gamma(M, \{q_{\gamma}\}, \{m_{\gamma}\}), \quad (\text{B.1})$$

where $\{q\}$ and $\{m\}$ denote the sets of small momenta and masses, respectively. The sum goes over all sub-graphs γ of Γ with the following properties:

1. γ contains all lines carrying the large mass M ,
2. γ is **1PI** in its connected parts after contracting all lines carrying the large mass.

The operator $\mathcal{T}_{\{q_{\gamma}\}, \{m_{\gamma}\}}$ denotes a Taylor expansion in the small momenta and masses appearing in the respective subgraphs, before loop-integration is carried out. The set $\{q_{\gamma}\}$ also contains the loop momenta that are external to the subgraph. The notation $\Gamma/\gamma \otimes \mathcal{T}\gamma$ means that we first Taylor-expand γ in the small parameters and then re-insert the Taylor-expansion into the diagram Γ where the lines in γ are contracted. The subgraphs γ are generally referred to as *hard subgraphs*, whereas the Γ/γ are called *co-subgraphs*.

This procedure allows us to systematically perform an expansion in a large mass at the level of Feynman diagrams. Thus, we reduce the involved integrals by one scale already before performing **IBP** reduction.

Sample applications of the procedure are shown in Figs. 2.2 and 3.1.

¹ This method is also known as the *hard mass procedure* in the literature.

ADDITIONAL RESULTS

In this section we present additional results that have been obtained in the course of the computations of Ref. [33], but have not been presented there. In Sec. C.1, we present the effective coupling of a Higgs boson to light quarks. In Sec. C.2 and Sec. C.3 we provide additional terms in the ϵ expansion of C_H and the OS renormalization constant of gluons, respectively.

C.1 EFFECTIVE COUPLING OF A HIGGS BOSON TO QUARKS

The discussion of chapter 2 and Sec. A.3 can be extended to account for the leading effects of the masses of light quarks. To this end, we introduce the quark mass decoupling constant ζ_m , relating quark masses in the n_f and n_l flavour theories:

$$m_f^{(n_l)} = \zeta_m m_f^{(n_f)}. \quad (\text{C.1})$$

Four-loop results for ζ_m have been obtained for general N_c in Ref. [166] and in terms of $SU(N)$ colour factors in Ref. [33].

At LO in the light-quark mass, the effective coupling of the Higgs boson to light quarks can be written as

$$\mathcal{L}_O \supset -C_2^0 \frac{H}{v} \sum_f m_f^0 \bar{q}_f^0 q_f^0, \quad (\text{C.2})$$

where the sum runs over all light quark flavours, the m_f^0 are the bare quark masses and the q_f^0 the bare quark fields.

In Ref. [46] a low-energy theorem connecting the effective coupling constant C_2 to ζ_m was derived:

$$C_2 = 1 + m_f^2 \frac{\partial}{\partial m_f^2} \log \zeta_m. \quad (\text{C.3})$$

The effective coupling C_2 can be written as

$$C_2 = 1 + T_F \sum_{i=1} \left(\frac{\alpha_s^{(n_f)}(\mu)}{\pi} \right)^i C_2^{(i)}, \quad (\text{C.4})$$

where the coefficients $C_2^{(i)}$ are given by

$$C_2^{(1)} = 0$$

$$\begin{aligned}
C_2^{(2)} &= \frac{5}{12} C_F, \\
C_2^{(3)} &= C_F^2 \left(\frac{13}{32} - \frac{3}{2} \zeta_3 \right) + C_F C_A \left(-\frac{5}{32} + \frac{3}{2} \zeta_3 \right) + \frac{31}{54} C_F T_F + \frac{53}{72} n_l C_F T_F, \\
C_2^{(4)} &= C_F^3 \left(-\frac{217}{384} - \frac{169}{128} \zeta_3 + \frac{15}{4} \zeta_5 \right) + C_F^2 T_F \left(-\frac{87}{32} + 8a_4 + \frac{1}{3} a_1^4 - 2a_1^2 \zeta_2 + \frac{595}{128} \zeta_3 - \frac{25}{4} \zeta_4 \right) \\
&\quad + C_F^2 C_A \left(\frac{3529}{384} - 22a_4 - \frac{11}{12} a_1^4 + \frac{11}{2} a_1^2 \zeta_2 - \frac{8913}{512} \zeta_3 + \frac{275}{16} \zeta_4 - \frac{5}{8} \zeta_5 \right) \\
&\quad + C_F C_A^2 \left(-\frac{233903}{124416} + 11a_4 + \frac{11}{24} a_1^4 - \frac{11}{4} a_1^2 \zeta_2 + \frac{119723}{9216} \zeta_3 - \frac{407}{32} \zeta_4 - \frac{25}{8} \zeta_5 \right) \\
&\quad + C_F C_A T_F \left(\frac{39259}{10368} - 4a_4 - \frac{1}{6} a_1^4 + a_1^2 \zeta_2 - \frac{4343}{768} \zeta_3 + \frac{37}{8} \zeta_4 \right) + C_F T_F^2 \left(-\frac{359}{972} + \frac{2}{3} \zeta_3 \right) \\
&\quad + \frac{d_F^{abcd} d_F^{abcd}}{T_F N_F} \left(-\frac{1}{2} + \frac{15}{4} \zeta_3 \right) + n_l C_F^2 T_F \left(-\frac{319}{96} + 8a_4 + \frac{1}{3} a_1^4 - 2a_1^2 \zeta_2 + \frac{97}{16} \zeta_3 - 7\zeta_4 \right) \\
&\quad + n_l C_F C_A T_F \left(\frac{5155}{15552} - 4a_4 - \frac{1}{6} a_1^4 + a_1^2 \zeta_2 - \frac{997}{288} \zeta_3 + \frac{43}{8} \zeta_4 \right) + \frac{143}{324} n_l C_F T_F^2 \\
&\quad + n_l^2 C_F T_F \left(\frac{3401}{3888} - \frac{7}{9} \zeta_3 \right), \tag{C.5}
\end{aligned}$$

Here, $\mu = m_t$, n_l is the number of light quark flavours, ζ is the Riemann ζ -function Eq. (2.35) and $a_n = \text{Li}_n(1/2)$.

The four-loop term $C_2^{(4)}$ in terms of $SU(N)$ colour factors has not been presented in the literature so far.

C.2 EFFECTIVE COUPLING OF A HIGGS BOSON TO GLUONS

To construct the EFT expression of the Higgs boson–gluon form factor in chapter 3 we require the one-, two- and three-loop contributions to the effective Higgs boson–gluon coupling C_H to higher orders in ϵ . In particular, we require terms up to ϵ^{8-2l} for the l -loop contribution. We write

$$C_H = -\frac{2}{3} T_F \sum_{i=1} \left(\frac{\alpha_s^{(n_l)}(\mu)}{\pi} \right)^i C_H^{(i)}, \tag{C.6}$$

where the coefficients $C_H^{(i)}$ are given by

$$\begin{aligned}
C_H^{(1)} &= 1 + l_{mt} \epsilon + \left(\frac{1}{2} \zeta_2 + \frac{1}{2} l_{mt}^2 \right) \epsilon^2 + \left(-\frac{1}{3} \zeta_3 + \frac{1}{2} \zeta_2 l_{mt} + \frac{1}{6} l_{mt}^3 \right) \epsilon^3 \\
&\quad + \left(\frac{1}{4} \zeta_4 + \frac{1}{8} \zeta_2^2 - \frac{1}{3} \zeta_3 l_{mt} + \frac{1}{4} \zeta_2 l_{mt}^2 + \frac{1}{24} l_{mt}^4 \right) \epsilon^4
\end{aligned}$$

$$\begin{aligned}
& + \left(-\frac{1}{5}\zeta_5 - \frac{1}{6}\zeta_2\zeta_3 + \frac{1}{4}\zeta_4 l_{mt} + \frac{1}{8}\zeta_2^2 l_{mt} - \frac{1}{6}\zeta_3 l_{mt}^2 + \frac{1}{12}\zeta_2 l_{mt}^3 + \frac{1}{120}l_{mt}^5 \right) \epsilon^5 \\
& + \left(\frac{1}{6}\zeta_6 + \frac{1}{18}\zeta_3^2 + \frac{1}{8}\zeta_2\zeta_4 + \frac{1}{48}\zeta_2^3 - \frac{1}{5}\zeta_5 l_{mt} - \frac{1}{6}\zeta_2\zeta_3 l_{mt} + \frac{1}{8}\zeta_4 l_{mt}^2 \right. \\
& \left. + \frac{1}{16}\zeta_2^2 l_{mt}^2 - \frac{1}{18}\zeta_3 l_{mt}^3 + \frac{1}{48}\zeta_2 l_{mt}^4 + \frac{1}{720}l_{mt}^6 \right) \epsilon^6, \\
C_H^{(2)} = & C_A \left[\frac{5}{4} + \left(-\frac{4}{3} + \frac{5}{2}l_{mt} \right) \epsilon + \left(\frac{43}{18} + \frac{5}{4}\zeta_2 - \frac{8}{3}l_{mt} + \frac{5}{2}l_{mt}^2 \right) \epsilon^2 \right. \\
& + \left(-\frac{523}{108} - \frac{5}{6}\zeta_3 - \frac{4}{3}\zeta_2 + \frac{43}{9}l_{mt} + \frac{5}{2}\zeta_2 l_{mt} - \frac{8}{3}l_{mt}^2 + \frac{5}{3}l_{mt}^3 \right) \epsilon^3 \\
& + \left(\frac{6223}{648} + \frac{35}{16}\zeta_4 + \frac{8}{9}\zeta_3 + \frac{43}{18}\zeta_2 - \frac{523}{54}l_{mt} - \frac{5}{3}\zeta_3 l_{mt} - \frac{8}{3}\zeta_2 l_{mt} \right. \\
& \left. + \frac{43}{9}l_{mt}^2 + \frac{5}{2}\zeta_2 l_{mt}^2 - \frac{16}{9}l_{mt}^3 + \frac{5}{6}l_{mt}^4 \right) \epsilon^4 \left. \right] \\
& + C_F \left[-\frac{3}{4} + \left(\frac{13}{8} - 3l_{mt} \right) \epsilon + \left(-\frac{35}{16} - \frac{3}{2}\zeta_2 + \frac{13}{4}l_{mt} - \frac{15}{4}l_{mt}^2 \right) \epsilon^2 \right. \\
& + \left(\frac{157}{32} + \frac{13}{8}\zeta_2 + \zeta_3 - \frac{35}{8}l_{mt} - \frac{15}{4}\zeta_2 l_{mt} + \frac{13}{4}l_{mt}^2 - \frac{11}{4}l_{mt}^3 \right) \epsilon^3 \\
& + \left(-\frac{611}{64} - \frac{57}{16}\zeta_4 - \frac{13}{12}\zeta_3 - \frac{35}{16}\zeta_2 + \frac{3}{16}\zeta_2^2 + \frac{157}{16}l_{mt} + \frac{5}{2}\zeta_3 l_{mt} + \frac{13}{4}\zeta_2 l_{mt} \right. \\
& \left. - \frac{35}{8}l_{mt}^2 - \frac{33}{8}\zeta_2 l_{mt}^2 + \frac{13}{6}l_{mt}^3 - \frac{23}{16}l_{mt}^4 \right) \epsilon^4 \left. \right], \\
C_H^{(3)} = & C_A^2 \left[\frac{1063}{576} + \frac{7}{16}l_{mt} + \left(-\frac{26473}{6912} + \frac{15}{512}\zeta_3 + \frac{7}{32}\zeta_2 + \frac{2485}{576}l_{mt} + \frac{139}{96}l_{mt}^2 \right) \epsilon \right. \\
& + \left(\frac{99697}{6912} + \frac{5061}{512}\zeta_4 - \frac{9265}{1024}\zeta_3 + \frac{2485}{1152}\zeta_2 - \frac{789}{32}a_4 - \frac{64283}{6912}l_{mt} + \frac{45}{512}\zeta_3 l_{mt} \right. \\
& \left. + \frac{139}{96}\zeta_2 l_{mt} + \frac{6047}{1152}l_{mt}^2 + \frac{67}{32}l_{mt}^3 + \frac{789}{128}a_1^2 \zeta_2 - \frac{263}{256}a_1^4 \right) \epsilon^2 \left. \right] \\
& + C_A C_F \left[-\frac{25}{12} - \frac{11}{16}l_{mt} + \left(-\frac{10847}{1152} + \frac{3819}{256}\zeta_3 - \frac{11}{32}\zeta_2 - \frac{337}{32}l_{mt} - \frac{77}{32}l_{mt}^2 \right) \epsilon \right.
\end{aligned}$$

$$\begin{aligned}
& + \left(-\frac{2161}{216} - \frac{24615}{256}\zeta_4 + \frac{95455}{1536}\zeta_3 - \frac{337}{64}\zeta_2 + \frac{1143}{16}a_4 - \frac{10081}{384}l_{mt} + \frac{11457}{256}\zeta_3l_{mt} \right. \\
& \left. - \frac{77}{32}\zeta_2l_{mt} - \frac{3661}{192}l_{mt}^2 - \frac{341}{96}l_{mt}^3 - \frac{1143}{64}a_1^2\zeta_2 + \frac{381}{128}a_1^4 \right) \epsilon^2 \Big] \\
& + C_F^2 \left[\frac{27}{32} + \left(\frac{19}{32} - \frac{285}{64}\zeta_3 + \frac{219}{32}l_{mt} \right) \epsilon + \left(-\frac{1715}{192} + \frac{2433}{64}\zeta_4 - \frac{409}{64}\zeta_3 + \frac{219}{64}\zeta_2 \right. \right. \\
& \left. \left. - \frac{177}{4}a_4 - \frac{99}{32}l_{mt} - \frac{855}{64}\zeta_3l_{mt} + \frac{1011}{64}l_{mt}^2 + \frac{177}{16}a_1^2\zeta_2 - \frac{59}{32}a_1^4 \right) \epsilon^2 \right] \\
& + C_A T_F \left[-\frac{5}{96} + \left(-\frac{1423}{1728} + \frac{63}{128}\zeta_3 - \frac{5}{32}l_{mt} \right) \epsilon + \left(\frac{9533}{10368} - \frac{893}{256}\zeta_4 + \frac{1799}{768}\zeta_3 \right. \right. \\
& \left. \left. - \frac{5}{64}\zeta_2 - \frac{5}{128}\zeta_2^2 + \frac{27}{8}a_4 - \frac{1423}{576}l_{mt} + \frac{189}{128}\zeta_3l_{mt} - \frac{15}{64}l_{mt}^2 - \frac{27}{32}a_1^2\zeta_2 + \frac{9}{64}a_1^4 \right) \epsilon^2 \right] \\
& + C_F T_F \left[-\frac{1}{12} + \left(-\frac{101}{288} + \frac{63}{64}\zeta_3 + \frac{1}{6}l_{mt} - \frac{1}{4}l_{mt}^2 \right) \epsilon + \left(-\frac{1817}{432} - \frac{459}{64}\zeta_4 + \frac{665}{128}\zeta_3 \right. \right. \\
& \left. \left. + \frac{1}{12}\zeta_2 + \frac{27}{4}a_4 - \frac{101}{96}l_{mt} + \frac{189}{64}\zeta_3l_{mt} - \frac{1}{4}\zeta_2l_{mt} + \frac{11}{24}l_{mt}^2 - \frac{1}{2}l_{mt}^3 - \frac{27}{16}a_1^2\zeta_2 + \frac{9}{32}a_1^4 \right) \epsilon^2 \right] \\
& + n_l C_A T_F \left[-\frac{47}{144} + \left(-\frac{341}{864} - \frac{77}{144}l_{mt} - \frac{5}{24}l_{mt}^2 \right) \epsilon + \left(\frac{1193}{576} - \frac{5}{3}\zeta_3 \right. \right. \\
& \left. \left. - \frac{77}{288}\zeta_2 - \frac{1711}{864}l_{mt} - \frac{5}{24}\zeta_2l_{mt} - \frac{103}{288}l_{mt}^2 - \frac{5}{12}l_{mt}^3 \right) \epsilon^2 \right] \\
& + n_l C_F T_F \left[-\frac{5}{16} + \frac{1}{2}l_{mt} + \left(\frac{761}{288} + \frac{1}{4}\zeta_2 - \frac{17}{16}l_{mt} + \frac{11}{8}l_{mt}^2 \right) \epsilon + \left(-\frac{19861}{1728} + \frac{29}{6}\zeta_3 \right. \right. \\
& \left. \left. - \frac{17}{32}\zeta_2 + \frac{277}{32}l_{mt} + \frac{11}{8}\zeta_2l_{mt} - \frac{185}{96}l_{mt}^2 + \frac{11}{6}l_{mt}^3 \right) \epsilon^2 \right], \\
C_H^{(4)} & = C_A^3 \left[\frac{110041}{41472} - \frac{1577}{3072}\zeta_3 + \frac{1993}{1152}l_{mt} + \frac{77}{192}l_{mt}^2 \right] + C_A^2 C_F \left[-\frac{105763}{6912} + \frac{5105}{512}\zeta_3 \right. \\
& \left. - \frac{1289}{288}l_{mt} - \frac{121}{192}l_{mt}^2 \right] + C_A C_F^2 \left[\frac{3491}{384} - \frac{407}{128}\zeta_3 + \frac{165}{64}l_{mt} \right] - \frac{471}{128}C_F^3 + C_A^2 T_F \left[-\frac{1081}{3456} \right. \\
& \left. + \frac{1}{384}\zeta_3 - \frac{55}{576}l_{mt} \right] + n_l C_A^2 T_F \left[-\frac{12421}{10368} - \frac{151}{256}\zeta_3 - \frac{55}{288}l_{mt} - \frac{7}{48}l_{mt}^2 \right]
\end{aligned}$$

$$\begin{aligned}
& + C_A C_F T_F \left[\frac{4537}{1728} - \frac{115}{64} \zeta_3 - \frac{11}{72} l_{mt} \right] + n_l C_A C_F T_F \left[\frac{9605}{2592} - \frac{1145}{384} \zeta_3 + \frac{55}{36} l_{mt} + \frac{11}{16} l_{mt}^2 \right] \\
& + C_F^2 T_F \left[-\frac{5}{12} + \frac{13}{32} \zeta_3 \right] + n_l C_F^2 T_F \left[-\frac{73}{288} + \frac{127}{96} \zeta_3 - \frac{11}{8} l_{mt} \right] + C_A T_F^2 \left[\frac{2}{27} - \frac{7}{64} \zeta_3 \right] \\
& + n_l C_A T_F^2 \left[\frac{7}{216} - \frac{7}{64} \zeta_3 + \frac{5}{144} l_{mt} \right] + n_l^2 C_A T_F^2 \left[-\frac{161}{2592} + \frac{5}{144} l_{mt} \right] \\
& + C_F T_F^2 \left[\frac{113}{432} - \frac{7}{32} \zeta_3 \right] + n_l C_F T_F^2 \left[-\frac{29}{144} - \frac{7}{32} \zeta_3 + \frac{1}{18} l_{mt} \right] + n_l^2 C_F T_F^2 \left[-\frac{677}{1296} \right. \\
& \left. + \frac{1}{18} l_{mt} - \frac{1}{6} l_{mt}^2 \right] + \frac{d^{abcd} d_F^{abcd}}{T_F N_A} \left[-\frac{2}{3} + \frac{13}{2} \zeta_3 \right] + \frac{d_F^{abcd} d_F^{abcd}}{T_F N_A} \left[\frac{11}{12} - 2\zeta_3 \right] \\
& + n_l \frac{d_A^{abcd} d_F^{abcd}}{T_F N_A} \left[\frac{11}{6} - 4\zeta_3 \right]. \tag{C.7}
\end{aligned}$$

Here n_l is the number of light quark flavours, ζ is the Riemann ζ -function Eq. (2.35), $a_n = \text{Li}_n(1/2)$ and $l_{mt} = \ln(\mu^2/m_t^2(\mu^2))$, where m_t is the top-quark mass renormalized in the $\overline{\text{MS}}$ scheme.

C.3 ON-SHELL RENORMALIZATION OF GLUONS

In chapters 2 and 3 we need the gluon wave-function renormalization constant in the OS scheme, including higher orders in the ϵ expansion. It is connected to the inverse of the bare gluon decoupling constant, as discussed in Sec. A.3. Analogously to the gluon case in Eq. (A.11). As in the case of C_H in Sec. C.2, we require the l -loop contribution up to ϵ^{8-2l} . We write the renormalization constant as

$$Z_3^{\text{OS}} = 1 + T_F \sum_i \left(\frac{\alpha_s^{(n_f)}(\mu)}{\pi} \right)^i z_3^{(i)}. \tag{C.8}$$

The coefficients $z_3^{(i)}$ are given by

$$\begin{aligned}
z_3^{(1)} = & -\frac{4}{3\epsilon} - \frac{4}{3} l_{mt} + \left(-\frac{2}{3} l_{mt}^2 - \frac{1}{9} \pi^2 \right) \epsilon + \left(\frac{4}{9} \zeta_3 - \frac{2}{9} l_{mt}^3 - \frac{1}{9} \pi^2 l_{mt} \right) \epsilon^2 \\
& + \left(\frac{4}{9} l_{mt} \zeta_3 - \frac{1}{18} l_{mt}^4 - \frac{1}{18} \pi^2 l_{mt}^2 - \frac{1}{120} \pi^4 \right) \epsilon^3 + \left(\frac{4}{15} \zeta_5 + \frac{2}{9} l_{mt}^2 \zeta_3 - \frac{1}{90} l_{mt}^5 + \frac{1}{27} \pi^2 \zeta_3 \right. \\
& \left. - \frac{1}{54} \pi^2 l_{mt}^3 - \frac{1}{120} \pi^4 l_{mt} \right) \epsilon^4 + \left(-\frac{2}{27} \zeta_3^2 + \frac{4}{15} l_{mt} \zeta_5 + \frac{2}{27} l_{mt}^3 \zeta_3 - \frac{1}{540} l_{mt}^6 + \frac{1}{27} \pi^2 l_{mt} \zeta_3 \right) \epsilon^5
\end{aligned}$$

$$\begin{aligned}
& -\frac{1}{216}\pi^2 l_{mt}^4 - \frac{1}{240}\pi^4 l_{mt}^2 - \frac{61}{90720}\pi^6 \Big) \epsilon^5 + \left(\frac{4}{21}\zeta_7 - \frac{2}{27}l_{mt}\zeta_3^2 + \frac{2}{15}l_{mt}^2\zeta_5 + \frac{1}{54}l_{mt}^4\zeta_3 \right. \\
& \left. - \frac{1}{3780}l_{mt}^7 + \frac{1}{45}\pi^2\zeta_5 + \frac{1}{54}\pi^2 l_{mt}^2\zeta_3 - \frac{1}{1080}\pi^2 l_{mt}^5 + \frac{1}{360}\pi^4\zeta_3 - \frac{1}{720}\pi^4 l_{mt}^3 - \frac{61}{90720}\pi^6 l_{mt} \right) \epsilon^6, \\
z_3^{(2)} = & C_A \left[\frac{35}{9\epsilon^2} + \left(-\frac{5}{2} + \frac{26}{9}l_{mt} \right) \frac{1}{\epsilon} + \frac{13}{12} - 5l_{mt} + \frac{4}{9}l_{mt}^2 + \frac{13}{54}\pi^2 + \left(-\frac{169}{72} - \frac{26}{27}\zeta_3 \right. \right. \\
& \left. \left. + \frac{13}{6}l_{mt} - 5l_{mt}^2 - \frac{14}{27}l_{mt}^3 - \frac{5}{12}\pi^2 + \frac{2}{27}\pi^2 l_{mt} \right) \epsilon + \left(\frac{1765}{432} + \frac{5}{3}\zeta_3 - \frac{169}{36}l_{mt} - \frac{8}{27}l_{mt}\zeta_3 \right. \right. \\
& \left. \left. + \frac{13}{6}l_{mt}^2 - \frac{10}{3}l_{mt}^3 - \frac{25}{54}l_{mt}^4 + \frac{13}{72}\pi^2 - \frac{5}{6}\pi^2 l_{mt} - \frac{7}{54}\pi^2 l_{mt}^2 + \frac{1}{90}\pi^4 \right) \epsilon^2 + \left(-\frac{22801}{2592} \right. \\
& \left. - \frac{26}{45}\zeta_5 - \frac{13}{18}\zeta_3 + \frac{1765}{216}l_{mt} + \frac{10}{3}l_{mt}\zeta_3 - \frac{169}{36}l_{mt}^2 + \frac{14}{27}l_{mt}^2\zeta_3 + \frac{13}{9}l_{mt}^3 - \frac{5}{3}l_{mt}^4 - \frac{61}{270}l_{mt}^5 \right. \\
& \left. - \frac{169}{432}\pi^2 - \frac{2}{81}\pi^2\zeta_3 + \frac{13}{36}\pi^2 l_{mt} - \frac{5}{6}\pi^2 l_{mt}^2 - \frac{25}{162}\pi^2 l_{mt}^3 - \frac{7}{144}\pi^4 - \frac{1}{120}\pi^4 l_{mt} \right) \epsilon^3 \\
& + \left(\frac{261709}{15552} + \zeta_5 + \frac{169}{108}\zeta_3 + \frac{4}{81}\zeta_3^2 - \frac{22801}{1296}l_{mt} - \frac{8}{45}l_{mt}\zeta_5 - \frac{13}{9}l_{mt}\zeta_3 + \frac{1765}{216}l_{mt}^2 \right. \\
& \left. + \frac{10}{3}l_{mt}^2\zeta_3 - \frac{169}{54}l_{mt}^3 + \frac{50}{81}l_{mt}^3\zeta_3 + \frac{13}{18}l_{mt}^4 - \frac{2}{3}l_{mt}^5 - \frac{133}{1620}l_{mt}^6 + \frac{1765}{2592}\pi^2 + \frac{5}{18}\pi^2\zeta_3 \right. \\
& \left. - \frac{169}{216}\pi^2 l_{mt} + \frac{7}{81}\pi^2 l_{mt}\zeta_3 + \frac{13}{36}\pi^2 l_{mt}^2 - \frac{5}{9}\pi^2 l_{mt}^3 - \frac{61}{648}\pi^2 l_{mt}^4 + \frac{91}{4320}\pi^4 - \frac{7}{72}\pi^4 l_{mt} \right. \\
& \left. - \frac{17}{720}\pi^4 l_{mt}^2 + \frac{113}{272160}\pi^6 \right) \epsilon^4 \Big] + C_F \left[-\frac{2}{\epsilon} + -\frac{13}{3} + 4l_{mt} + \left(\frac{35}{6} - \frac{26}{3}l_{mt} + 8l_{mt}^2 \right. \right. \\
& \left. \left. + \frac{1}{3}\pi^2 \right) \epsilon + \left(-\frac{157}{12} - \frac{4}{3}\zeta_3 + \frac{35}{3}l_{mt} - \frac{26}{3}l_{mt}^2 + \frac{20}{3}l_{mt}^3 - \frac{13}{18}\pi^2 + \frac{4}{3}\pi^2 l_{mt} \right) \epsilon^2 \right. \\
& \left. + \left(\frac{611}{24} + \frac{26}{9}\zeta_3 - \frac{157}{6}l_{mt} - \frac{16}{3}l_{mt}\zeta_3 + \frac{35}{3}l_{mt}^2 - \frac{52}{9}l_{mt}^3 + \frac{11}{3}l_{mt}^4 + \frac{35}{36}\pi^2 - \frac{13}{9}\pi^2 l_{mt} \right. \right. \\
& \left. \left. + \frac{5}{3}\pi^2 l_{mt}^2 + \frac{1}{15}\pi^4 \right) \epsilon^3 + \left(-\frac{2461}{48} - \frac{4}{5}\zeta_5 - \frac{35}{9}\zeta_3 + \frac{611}{12}l_{mt} + \frac{52}{9}l_{mt}\zeta_3 - \frac{157}{6}l_{mt}^2 \right. \right. \\
& \left. \left. - \frac{20}{3}l_{mt}^2\zeta_3 + \frac{70}{9}l_{mt}^3 - \frac{26}{9}l_{mt}^4 + \frac{23}{15}l_{mt}^5 - \frac{157}{72}\pi^2 - \frac{4}{9}\pi^2\zeta_3 + \frac{35}{18}\pi^2 l_{mt} - \frac{13}{9}\pi^2 l_{mt}^2 \right. \right. \\
& \left. \left. + \frac{11}{9}\pi^2 l_{mt}^3 - \frac{91}{1080}\pi^4 + \frac{11}{60}\pi^4 l_{mt} \right) \epsilon^4 \Big] + T_F \left[\frac{16}{9\epsilon} l_{mt} + \left(\frac{8}{3}l_{mt}^2 + \frac{4}{27}\pi^2 \right) + \left(-\frac{16}{27}\zeta_3 \right. \right.
\end{aligned}$$

$$\begin{aligned}
& + \frac{56}{27} l_{mt}^3 + \frac{4}{9} \pi^2 l_{mt} \Big) \epsilon + \left(-\frac{16}{9} l_{mt} \zeta_3 + \frac{10}{9} l_{mt}^4 + \frac{14}{27} \pi^2 l_{mt}^2 + \frac{19}{810} \pi^4 \right) \epsilon^2 + \left(-\frac{16}{45} \zeta_5 \right. \\
& - \frac{56}{27} l_{mt}^2 \zeta_3 + \frac{62}{135} l_{mt}^5 - \frac{4}{27} \pi^2 \zeta_3 + \frac{10}{27} \pi^2 l_{mt}^3 + \frac{47}{810} \pi^4 l_{mt} \Big) \epsilon^3 + \left(\frac{8}{27} \zeta_3^2 - \frac{16}{15} l_{mt} \zeta_5 \right. \\
& \left. - \frac{40}{27} l_{mt}^3 \zeta_3 + \frac{7}{45} l_{mt}^6 - \frac{28}{81} \pi^2 l_{mt} \zeta_3 + \frac{31}{162} \pi^2 l_{mt}^4 + \frac{103}{1620} \pi^4 l_{mt}^2 + \frac{187}{68040} \pi^6 \right) \epsilon^4 \Big] \\
& + n_l T_F \left[-\frac{16}{9\epsilon^2} - \frac{16}{9\epsilon} l_{mt} + \left(-\frac{8}{9} l_{mt}^2 - \frac{4}{27} \pi^2 \right) + \left(\frac{16}{27} \zeta_3 - \frac{8}{27} l_{mt}^3 - \frac{4}{27} \pi^2 l_{mt} \right) \epsilon \right. \\
& + \left(\frac{16}{27} l_{mt} \zeta_3 - \frac{2}{27} l_{mt}^4 - \frac{2}{27} \pi^2 l_{mt}^2 - \frac{1}{90} \pi^4 \right) \epsilon^2 + \left(\frac{16}{45} \zeta_5 + \frac{8}{27} l_{mt}^2 \zeta_3 - \frac{2}{135} l_{mt}^5 \right. \\
& + \frac{4}{81} \pi^2 \zeta_3 - \frac{2}{81} \pi^2 l_{mt}^3 - \frac{1}{90} \pi^4 l_{mt} \Big) \epsilon^3 + \left(-\frac{8}{81} \zeta_3^2 + \frac{16}{45} l_{mt} \zeta_5 + \frac{8}{81} l_{mt}^3 \zeta_3 - \frac{1}{405} l_{mt}^6 \right. \\
& \left. + \frac{4}{81} \pi^2 l_{mt} \zeta_3 - \frac{1}{162} \pi^2 l_{mt}^4 - \frac{1}{180} \pi^4 l_{mt}^2 - \frac{61}{68040} \pi^6 \right) \epsilon^4 \Big] , \\
z_3^{(3)} = & C_A^2 \left[\left(-\frac{695}{54} - \frac{1}{6} \zeta \right) \frac{1}{\epsilon^3} + \left(\frac{2015}{108} - \frac{545}{54} l_{mt} + \left\{ \frac{7}{12} - \frac{1}{2} l_{mt} \right\} \zeta \right) \frac{1}{\epsilon^2} + \left(-\frac{4897}{216} \right. \right. \\
& \left. + 6\zeta_3 + \frac{811}{36} l_{mt} - \frac{491}{108} l_{mt}^2 - \frac{545}{648} \pi^2 + \left\{ -\frac{137}{72} + \frac{7}{4} l_{mt} - \frac{3}{4} l_{mt}^2 - \frac{1}{24} \pi^2 \right\} \zeta \right) \frac{1}{\epsilon} \\
& + \frac{109723}{3888} + \frac{18425}{648} \zeta_3 + 64a_4 - \frac{4325}{72} l_{mt} + 18l_{mt} \zeta_3 + \frac{569}{72} l_{mt}^2 - \frac{1121}{324} l_{mt}^3 + \frac{811}{432} \pi^2 \\
& - \frac{491}{648} \pi^2 l_{mt} - \frac{53}{90} \pi^4 - \frac{8}{3} a_1^2 \pi^2 + \frac{8}{3} a_1^4 + \left\{ \frac{3577}{432} - \frac{7}{6} \zeta_3 - \frac{137}{24} l_{mt} + \frac{21}{8} l_{mt}^2 - \frac{3}{4} l_{mt}^3 \right. \\
& \left. + \frac{7}{48} \pi^2 - \frac{1}{8} \pi^2 l_{mt} \right\} \zeta + \left(-\frac{4097371}{23328} - 370\zeta_5 + \frac{6239}{48} \zeta_3 + 384a_5 + \frac{1222}{3} a_4 \right. \\
& + \frac{87415}{1296} l_{mt} + \frac{50699}{648} l_{mt} \zeta_3 + 192l_{mt} a_4 - \frac{11831}{144} l_{mt}^2 + 27l_{mt}^2 \zeta_3 - \frac{1477}{216} l_{mt}^3 \\
& - \frac{4595}{1296} l_{mt}^4 - \frac{4325}{864} \pi^2 + \frac{3}{2} \pi^2 \zeta_3 + \frac{569}{432} \pi^2 l_{mt} - \frac{1121}{1296} \pi^2 l_{mt}^2 - \frac{9077}{2880} \pi^4 - \frac{53}{30} \pi^4 l_{mt} \\
& + \frac{68}{15} a_1 \pi^4 - \frac{611}{36} a_1^2 \pi^2 - 8a_1^2 \pi^2 l_{mt} + \frac{16}{3} a_1^3 \pi^2 + \frac{611}{36} a_1^4 + 8a_1^4 l_{mt} - \frac{16}{5} a_1^5 \\
& \left. + \left\{ -\frac{80285}{2592} + \frac{49}{12} \zeta_3 + \frac{3577}{144} l_{mt} - \frac{7}{2} l_{mt} \zeta_3 - \frac{137}{16} l_{mt}^2 + \frac{21}{8} l_{mt}^3 - \frac{9}{16} l_{mt}^4 - \frac{137}{288} \pi^2 \right. \right.
\end{aligned}$$

$$\begin{aligned}
& + \frac{7}{16} \pi^2 l_{mt} - \frac{3}{16} \pi^2 l_{mt}^2 + \frac{173}{2880} \pi^4 \left. \vphantom{\frac{7}{16}} \right\} \zeta \Big) \epsilon + \left(\frac{8289707}{15552} + 960s_6 - \frac{1118449}{432} \zeta_5 \right. \\
& + \frac{120769}{864} \zeta_3 - 426\zeta_3^2 + 2304a_6 + 2444a_5 + \frac{9293}{9} a_4 - \frac{3864391}{7776} l_{mt} - 1110l_{mt}\zeta_5 \\
& + \frac{175909}{432} l_{mt}\zeta_3 + 1152l_{mt}a_5 + 1222l_{mt}a_4 + \frac{24181}{288} l_{mt}^2 + \frac{150689}{1296} l_{mt}^2 \zeta_3 + 288l_{mt}^2 a_4 \\
& - \frac{33205}{432} l_{mt}^3 + 27l_{mt}^3 \zeta_3 - \frac{10255}{864} l_{mt}^4 - \frac{3637}{1296} l_{mt}^5 + \frac{87415}{15552} \pi^2 + \frac{50699}{7776} \pi^2 \zeta_3 + 16\pi^2 a_4 \\
& - \frac{11831}{864} \pi^2 l_{mt} + \frac{9}{2} \pi^2 l_{mt} \zeta_3 - \frac{1477}{864} \pi^2 l_{mt}^2 - \frac{4595}{3888} \pi^2 l_{mt}^3 - \frac{591899}{51840} \pi^4 - \frac{80989}{8640} \pi^4 l_{mt} \\
& - \frac{53}{20} \pi^4 l_{mt}^2 - \frac{3803}{2520} \pi^6 + \frac{10387}{360} a_1 \pi^4 + \frac{68}{5} a_1 \pi^4 l_{mt} - \frac{9293}{216} a_1^2 \pi^2 - \frac{611}{12} a_1^2 \pi^2 l_{mt} \\
& - 12a_1^2 \pi^2 l_{mt}^2 - \frac{214}{15} a_1^2 \pi^4 + \frac{611}{18} a_1^3 \pi^2 + 16a_1^3 \pi^2 l_{mt} + \frac{9293}{216} a_1^4 + \frac{611}{12} a_1^4 l_{mt} + 12a_1^4 l_{mt}^2 \\
& - \frac{22}{3} a_1^4 \pi^2 - \frac{611}{30} a_1^5 - \frac{48}{5} a_1^5 l_{mt} + \frac{16}{5} a_1^6 + \left\{ \frac{1985017}{15552} - \frac{239}{10} \zeta_5 - \frac{959}{72} \zeta_3 - \frac{80285}{864} l_{mt} \right. \\
& + \frac{49}{4} l_{mt} \zeta_3 + \frac{3577}{96} l_{mt}^2 - \frac{21}{4} l_{mt}^2 \zeta_3 - \frac{137}{16} l_{mt}^3 + \frac{63}{32} l_{mt}^4 - \frac{27}{80} l_{mt}^5 + \frac{3577}{1728} \pi^2 - \frac{7}{24} \pi^2 \zeta_3 \\
& \left. - \frac{137}{96} \pi^2 l_{mt} + \frac{21}{32} \pi^2 l_{mt}^2 - \frac{3}{16} \pi^2 l_{mt}^3 - \frac{1211}{5760} \pi^4 + \frac{173}{960} \pi^4 l_{mt} \right\} \zeta \Big) \epsilon^2 \Big] \\
& + C_A C_F \left[\frac{70}{9\epsilon^2} + \left(\frac{251}{27} - 8\zeta_3 - \frac{26}{3} l_{mt} \right) \frac{1}{\epsilon} + \frac{8221}{81} - \frac{1957}{12} \zeta_3 - 128a_4 + \frac{623}{9} l_{mt} \right. \\
& - 24l_{mt}\zeta_3 - l_{mt}^2 - \frac{13}{18} \pi^2 + \frac{44}{45} \pi^4 + \frac{16}{3} a_1^2 \pi^2 - \frac{16}{3} a_1^4 + \left(-\frac{47857}{972} + 812\zeta_5 - \frac{38045}{72} \zeta_3 \right. \\
& - 768a_5 - 972a_4 + \frac{9025}{27} l_{mt} - \frac{1957}{4} l_{mt}\zeta_3 - 384l_{mt}a_4 + \frac{2225}{18} l_{mt}^2 - 36l_{mt}^2 \zeta_3 + \frac{65}{3} l_{mt}^3 \\
& + \frac{623}{108} \pi^2 - 2\pi^2 \zeta_3 - \frac{1}{6} \pi^2 l_{mt} + \frac{301}{24} \pi^4 + \frac{44}{15} \pi^4 l_{mt} - \frac{136}{15} a_1 \pi^4 + \frac{81}{2} a_1^2 \pi^2 + 16a_1^2 \pi^2 l_{mt} \\
& \left. - \frac{32}{3} a_1^3 \pi^2 - \frac{81}{2} a_1^4 - 16a_1^4 l_{mt} + \frac{32}{5} a_1^5 \right) \epsilon + \left(\frac{4272319}{2916} - 1920s_6 + \frac{34593}{8} \zeta_5 - \frac{558581}{432} \zeta_3 \right. \\
& + 864\zeta_3^2 - 4608a_6 - 5832a_5 - 2546a_4 - \frac{69817}{324} l_{mt} + 2436l_{mt}\zeta_5 - \frac{38237}{24} l_{mt}\zeta_3 \\
& - 2304l_{mt}a_5 - 2916l_{mt}a_4 + \frac{3187}{6} l_{mt}^2 - \frac{5871}{8} l_{mt}^2 \zeta_3 - 576l_{mt}^2 a_4 + \frac{2333}{18} l_{mt}^3 - 36l_{mt}^3 \zeta_3 \\
& + \frac{125}{4} l_{mt}^4 + \frac{9025}{324} \pi^2 - \frac{1957}{48} \pi^2 \zeta_3 - 32\pi^2 a_4 + \frac{2225}{108} \pi^2 l_{mt} - 6\pi^2 l_{mt} \zeta_3 + \frac{65}{12} \pi^2 l_{mt}^2 \\
& \left. + \frac{10267}{270} \pi^4 + \frac{301}{8} \pi^4 l_{mt} + \frac{22}{5} \pi^4 l_{mt}^2 + \frac{169}{63} \pi^6 - \frac{1377}{20} a_1 \pi^4 - \frac{136}{5} a_1 \pi^4 l_{mt} + \frac{1273}{12} a_1^2 \pi^2 \right.
\end{aligned}$$

$$\begin{aligned}
& + \frac{243}{2} a_1^2 \pi^2 l_{mt} + 24 a_1^2 \pi^2 l_{mt}^2 + \frac{428}{15} a_1^2 \pi^4 - 81 a_1^3 \pi^2 - 32 a_1^3 \pi^2 l_{mt} - \frac{1273}{12} a_1^4 - \frac{243}{2} a_1^4 l_{mt} \\
& - 24 a_1^4 l_{mt}^2 + \frac{44}{3} a_1^4 \pi^2 + \frac{243}{5} a_1^5 + \frac{96}{5} a_1^5 l_{mt} - \frac{32}{5} a_1^6 \left. \varepsilon^2 \right] \\
& + C_F^2 \left[\frac{2}{3\varepsilon} - \frac{194}{9} + \frac{95}{3} \zeta_3 - 18 l_{mt} + \left(\frac{2345}{27} + \frac{409}{9} \zeta_3 + \frac{944}{3} a_4 - \frac{38}{3} l_{mt} + 95 l_{mt} \zeta_3 \right. \right. \\
& - 73 l_{mt}^2 - \frac{3}{2} \pi^2 - \frac{811}{270} \pi^4 - \frac{118}{9} a_1^2 \pi^2 + \frac{118}{9} a_1^4 \left. \varepsilon + \left(\frac{32663}{162} - \frac{10681}{6} \zeta_5 - \frac{10126}{27} \zeta_3 \right. \right. \\
& + 1888 a_5 + \frac{8656}{9} a_4 + \frac{1715}{9} l_{mt} + \frac{409}{3} l_{mt} \zeta_3 + 944 l_{mt} a_4 + 33 l_{mt}^2 + \frac{285}{2} l_{mt}^2 \zeta_3 - \frac{337}{3} l_{mt}^3 \\
& - \frac{19}{18} \pi^2 + \frac{95}{12} \pi^2 \zeta_3 - \frac{73}{6} \pi^2 l_{mt} - \frac{5357}{810} \pi^4 - \frac{811}{90} \pi^4 l_{mt} + \frac{1003}{45} a_1 \pi^4 - \frac{1082}{27} a_1^2 \pi^2 \\
& \left. \left. - \frac{118}{3} a_1^2 \pi^2 l_{mt} + \frac{236}{9} a_1^3 \pi^2 + \frac{1082}{27} a_1^4 + \frac{118}{3} a_1^4 l_{mt} - \frac{236}{15} a_1^5 \right) \varepsilon^2 \right] \\
& + C_A T_F \left[\frac{4}{9\varepsilon^3} + \left(-\frac{50}{27} - \frac{244}{27} l_{mt} \right) \frac{1}{\varepsilon^2} + \left(\frac{37}{27} + 10 l_{mt} - \frac{98}{9} l_{mt}^2 - \frac{61}{81} \pi^2 \right) \frac{1}{\varepsilon} + \frac{6361}{486} \right. \\
& - \frac{2095}{162} \zeta_3 + \frac{11}{9} l_{mt} + \frac{235}{9} l_{mt}^2 - \frac{386}{81} l_{mt}^3 + \frac{5}{6} \pi^2 - \frac{49}{27} \pi^2 l_{mt} + \left(\frac{1775}{2916} - \frac{5911}{108} \zeta_3 - \frac{328}{3} a_4 \right. \\
& + \frac{7375}{162} l_{mt} - \frac{2191}{54} l_{mt} \zeta_3 - \frac{19}{18} l_{mt}^2 + \frac{865}{27} l_{mt}^3 + \frac{31}{54} l_{mt}^4 + \frac{11}{108} \pi^2 + \frac{235}{54} \pi^2 l_{mt} - \frac{193}{162} \pi^2 l_{mt}^2 \\
& + \frac{11567}{9720} \pi^4 + \frac{41}{9} a_1^2 \pi^2 - \frac{41}{9} a_1^4 \left. \varepsilon + \left(\frac{283811}{5832} + \frac{286951}{540} \zeta_5 - \frac{18575}{216} \zeta_3 - 656 a_5 \right. \right. \\
& - \frac{3172}{9} a_4 - \frac{8815}{972} l_{mt} - \frac{18533}{108} l_{mt} \zeta_3 - 328 l_{mt} a_4 + \frac{8051}{108} l_{mt}^2 - \frac{21703}{324} l_{mt}^2 \zeta_3 - \frac{161}{54} l_{mt}^3 \\
& + \frac{2875}{108} l_{mt}^4 + \frac{1799}{810} l_{mt}^5 + \frac{7375}{1944} \pi^2 - \frac{2191}{648} \pi^2 \zeta_3 - \frac{19}{108} \pi^2 l_{mt} + \frac{865}{108} \pi^2 l_{mt}^2 + \frac{31}{162} \pi^2 l_{mt}^3 \\
& + \frac{9439}{2160} \pi^4 + \frac{7217}{1944} \pi^4 l_{mt} - \frac{697}{90} a_1 \pi^4 + \frac{793}{54} a_1^2 \pi^2 + \frac{41}{3} a_1^2 \pi^2 l_{mt} - \frac{82}{9} a_1^3 \pi^2 - \frac{793}{54} a_1^4 \\
& \left. \left. - \frac{41}{3} a_1^4 l_{mt} + \frac{82}{15} a_1^5 \right) \varepsilon^2 \right] + n_l C_A T_F \left[\frac{304}{27\varepsilon^3} + \left(-\frac{280}{27} + \frac{280}{27} l_{mt} \right) \frac{1}{\varepsilon^2} + \left(\frac{280}{27} - \frac{140}{9} l_{mt} \right. \right. \\
& + \frac{140}{27} l_{mt}^2 + \frac{70}{81} \pi^2 \left. \varepsilon - \frac{4724}{243} + \frac{296}{81} \zeta_3 + \frac{254}{9} l_{mt} - \frac{110}{9} l_{mt}^2 + \frac{212}{81} l_{mt}^3 - \frac{35}{27} \pi^2 \right. \\
& \left. \left. + \frac{70}{81} \pi^2 l_{mt} + \left(\frac{68242}{729} + \frac{100}{9} \zeta_3 - \frac{4217}{81} l_{mt} + \frac{1448}{81} l_{mt} \zeta_3 + \frac{355}{9} l_{mt}^2 - \frac{170}{27} l_{mt}^3 + \frac{143}{81} l_{mt}^4 \right. \right. \right.
\end{aligned}$$

$$\begin{aligned}
& + \frac{127}{54} \pi^2 - \frac{55}{27} \pi^2 l_{mt} + \frac{53}{81} \pi^2 l_{mt}^2 - \frac{157}{540} \pi^4 \Big) \epsilon + \left(-\frac{23791}{81} + \frac{3400}{27} \zeta_5 + \frac{454}{9} \zeta_3 \right. \\
& + \frac{131189}{486} l_{mt} + \frac{700}{27} l_{mt} \zeta_3 - \frac{431}{6} l_{mt}^2 + \frac{2380}{81} l_{mt}^2 \zeta_3 + \frac{1013}{27} l_{mt}^3 - \frac{115}{54} l_{mt}^4 + \frac{97}{81} l_{mt}^5 - \frac{4217}{972} \pi^2 \\
& \left. + \frac{362}{243} \pi^2 \zeta_3 + \frac{355}{54} \pi^2 l_{mt} - \frac{85}{54} \pi^2 l_{mt}^2 + \frac{143}{243} \pi^2 l_{mt}^3 - \frac{275}{648} \pi^4 - \frac{59}{60} \pi^4 l_{mt} \right) \epsilon^2 \Big] \\
& + C_F T_F \left[-\frac{8}{9\epsilon^2} + \left(\frac{200}{27} - \frac{8}{3} l_{mt} \right) \frac{1}{\epsilon} - \frac{218}{81} - 7\zeta_3 + \frac{224}{9} l_{mt} - \frac{68}{3} l_{mt}^2 - \frac{2}{9} \pi^2 \right. \\
& + \left(\frac{10094}{243} - \frac{649}{18} \zeta_3 - 48a_4 - \frac{638}{27} l_{mt} - 21l_{mt} \zeta_3 + \frac{400}{9} l_{mt}^2 - \frac{124}{3} l_{mt}^3 + \frac{56}{27} \pi^2 - \frac{34}{9} \pi^2 l_{mt} \right. \\
& \left. + \frac{17}{30} \pi^4 + 2a_1^2 \pi^2 - 2a_1^4 \right) \epsilon + \left(\frac{40295}{1458} + \frac{465}{2} \zeta_5 - \frac{18865}{108} \zeta_3 - 288a_5 - \frac{760}{3} a_4 + \frac{12920}{81} l_{mt} \right. \\
& - \frac{1723}{18} l_{mt} \zeta_3 - 144l_{mt} a_4 - 51l_{mt}^2 - \frac{63}{2} l_{mt}^2 \zeta_3 + \frac{152}{3} l_{mt}^3 - \frac{377}{9} l_{mt}^4 - \frac{319}{162} \pi^2 - \frac{7}{4} \pi^2 \zeta_3 \\
& + \frac{200}{27} \pi^2 l_{mt} - \frac{31}{3} \pi^2 l_{mt}^2 + \frac{763}{270} \pi^4 + \frac{17}{10} \pi^4 l_{mt} - \frac{17}{5} a_1 \pi^4 + \frac{95}{9} a_1^2 \pi^2 + 6a_1^2 \pi^2 l_{mt} - 4a_1^3 \pi^2 \\
& \left. - \frac{95}{9} a_1^4 - 6a_1^4 l_{mt} + \frac{12}{5} a_1^5 \right) \epsilon^2 \Big] + n_l C_F T_F \left[-\frac{64}{9\epsilon^2} - \frac{68}{27\epsilon} - \frac{682}{81} - \frac{44}{9} l_{mt} + \frac{8}{3} l_{mt}^2 \right. \\
& + \left(\frac{14209}{243} - \frac{320}{9} \zeta_3 - \frac{1102}{27} l_{mt} - \frac{2}{9} l_{mt}^2 - \frac{16}{9} l_{mt}^3 - \frac{11}{27} \pi^2 + \frac{4}{9} \pi^2 l_{mt} \right) \epsilon \\
& + \left(-\frac{446333}{1458} + \frac{1036}{27} \zeta_3 + \frac{17035}{81} l_{mt} - \frac{976}{9} l_{mt} \zeta_3 - \frac{691}{9} l_{mt}^2 + 6l_{mt}^3 - \frac{46}{9} l_{mt}^4 - \frac{551}{162} \pi^2 \right. \\
& \left. - \frac{1}{27} \pi^2 l_{mt} - \frac{4}{9} \pi^2 l_{mt}^2 + \frac{97}{54} \pi^4 \right) \epsilon^2 \Big] \\
& + T_F^2 \left[-\frac{64}{27\epsilon} l_{mt}^2 - \frac{128}{27} l_{mt}^3 - \frac{32}{81} \pi^2 l_{mt} + \left(\frac{128}{81} l_{mt} \zeta_3 - \frac{400}{81} l_{mt}^4 - \frac{32}{27} \pi^2 l_{mt}^2 - \frac{4}{243} \pi^4 \right) \epsilon \right. \\
& + \left(\frac{128}{27} l_{mt}^2 \zeta_3 - \frac{32}{9} l_{mt}^5 + \frac{32}{243} \pi^2 \zeta_3 - \frac{400}{243} \pi^2 l_{mt}^3 - \frac{136}{1215} \pi^4 l_{mt} \right) \epsilon^2 \Big] + n_l T_F^2 \left[\frac{128}{27\epsilon^2} l_{mt} \right. \\
& + \left(\frac{64}{9} l_{mt}^2 + \frac{32}{81} \pi^2 \right) \frac{1}{\epsilon} - \frac{128}{81} \zeta_3 + \frac{448}{81} l_{mt}^3 + \frac{32}{27} \pi^2 l_{mt} + \left(-\frac{128}{27} l_{mt} \zeta_3 + \frac{80}{27} l_{mt}^4 \right. \\
& \left. + \frac{112}{81} \pi^2 l_{mt}^2 + \frac{76}{1215} \pi^4 \right) \epsilon + \left(-\frac{128}{135} \zeta_5 - \frac{448}{81} l_{mt}^2 \zeta_3 + \frac{496}{405} l_{mt}^5 - \frac{32}{81} \pi^2 \zeta_3 + \frac{80}{81} \pi^2 l_{mt}^3 \right) \epsilon
\end{aligned}$$

$$\begin{aligned}
& + \frac{188}{1215} \pi^4 l_{mt} \left) \epsilon^2 \right] + n_l^2 T_F^2 \left[-\frac{64}{27\epsilon^3} - \frac{64}{27\epsilon^2} l_{mt} + \left(-\frac{32}{27} l_{mt}^2 - \frac{16}{81} \pi^2 \right) \frac{1}{\epsilon} + \frac{64}{81} \zeta_3 \right. \\
& - \frac{32}{81} l_{mt}^3 - \frac{16}{81} \pi^2 l_{mt} + \left(\frac{64}{81} l_{mt} \zeta_3 - \frac{8}{81} l_{mt}^4 - \frac{8}{81} \pi^2 l_{mt}^2 - \frac{2}{135} \pi^4 \right) \epsilon + \left(\frac{64}{135} \zeta_5 \right. \\
& \left. \left. + \frac{32}{81} l_{mt}^2 \zeta_3 - \frac{8}{405} l_{mt}^5 + \frac{16}{243} \pi^2 \zeta_3 - \frac{8}{243} \pi^2 l_{mt}^3 - \frac{2}{135} \pi^4 l_{mt} \right) \epsilon^2 \right], \\
z_3^{(4)} = & C_A^3 \left[\left(\frac{57905}{1296} + \frac{139}{144} \zeta - \frac{1}{12} \zeta^2 \right) \frac{1}{\epsilon^4} + \left(-\frac{14653}{144} + \frac{11945}{324} l_{mt} + \left\{ -\frac{571}{144} + \frac{20}{9} l_{mt} \right\} \zeta \right. \right. \\
& \left. \left. + \left\{ \frac{1}{3} - \frac{1}{4} l_{mt} \right\} \zeta^2 \right) \frac{1}{\epsilon^3} + \left(\frac{782453}{5184} - \frac{153}{8} \zeta_3 - \frac{12169}{108} l_{mt} + \frac{2885}{162} l_{mt}^2 + \frac{11945}{3888} \pi^2 \right. \right. \\
& \left. \left. + \left\{ \frac{15361}{1728} + \frac{59}{24} \zeta_3 - \frac{81}{8} l_{mt} + \frac{143}{72} l_{mt}^2 + \frac{5}{27} \pi^2 \right\} \zeta + \left\{ -\frac{337}{288} - \frac{1}{48} \zeta_3 + \frac{25}{24} l_{mt} - \frac{3}{8} l_{mt}^2 \right. \right. \\
& \left. \left. - \frac{1}{48} \pi^2 \right\} \zeta^2 \right) \frac{1}{\epsilon^2} + \left(-\frac{387227}{1728} - \frac{55}{2} \zeta_5 + \frac{108545}{1944} \zeta_3 - 32a_4 + \frac{10751}{48} l_{mt} - \frac{21}{2} l_{mt} \zeta_3 \right. \\
& \left. - \frac{269}{4} l_{mt}^2 + \frac{1618}{243} l_{mt}^3 - \frac{12169}{1296} \pi^2 + \frac{2885}{972} \pi^2 l_{mt} + \frac{37}{1440} \pi^4 + \frac{4}{3} a_1^2 \pi^2 - \frac{4}{3} a_1^4 \right. \\
& \left. + \left\{ -\frac{134743}{5184} + \frac{691}{108} \zeta_3 + 32a_4 + \frac{1213}{72} l_{mt} + \frac{59}{6} l_{mt} \zeta_3 - \frac{559}{48} l_{mt}^2 + \frac{41}{216} l_{mt}^3 - \frac{27}{32} \pi^2 \right. \right. \\
& \left. \left. + \frac{143}{432} \pi^2 l_{mt} - \frac{437}{1440} \pi^4 - \frac{4}{3} a_1^2 \pi^2 + \frac{4}{3} a_1^4 \right\} \zeta + \left\{ \frac{17605}{3456} - \frac{1}{2} \zeta_3 - \frac{179}{48} l_{mt} \right. \right. \\
& \left. \left. - \frac{1}{12} l_{mt} \zeta_3 + \frac{79}{48} l_{mt}^2 - \frac{3}{8} l_{mt}^3 + \frac{25}{288} \pi^2 - \frac{1}{16} \pi^2 l_{mt} - \frac{1}{2880} \pi^4 \right\} \zeta^2 \right) \frac{1}{\epsilon} + \frac{476476793}{3919104} \\
& + \frac{425347}{504} \zeta_5 + \frac{72710737}{30240} \zeta_3 - \frac{20992}{63} a_5 + \frac{301576}{63} a_4 - \frac{2128963}{3888} l_{mt} - 110 l_{mt} \zeta_5 \\
& + \frac{1038425}{1944} l_{mt} \zeta_3 + 576 l_{mt} a_4 + \frac{13531}{648} l_{mt}^2 + 78 l_{mt}^2 \zeta_3 - \frac{18103}{324} l_{mt}^3 - \frac{770}{243} l_{mt}^4 \\
& + \frac{10751}{576} \pi^2 - \frac{7}{8} \pi^2 \zeta_3 - \frac{269}{24} \pi^2 l_{mt} + \frac{809}{486} \pi^2 l_{mt}^2 - \frac{9516539}{181440} \pi^4 - \frac{51}{8} \pi^4 l_{mt} - \frac{1}{756} \pi^6 \\
& + \frac{13547}{2835} a_1 \pi^4 - \frac{37697}{189} a_1^2 \pi^2 - 24 a_1^2 \pi^2 l_{mt} - \frac{2624}{567} a_1^3 \pi^2 + \frac{37697}{189} a_1^4 + 24 a_1^4 l_{mt} + \frac{2624}{945} a_1^5 \\
& + \left\{ \frac{901513}{62208} - \frac{3041}{12} \zeta_5 + \frac{1793}{72} \zeta_3 + 256 a_5 + 80 a_4 - \frac{19481}{864} l_{mt} + \frac{1525}{108} l_{mt} \zeta_3 + 128 l_{mt} a_4 \right. \\
& \left. + \frac{1621}{288} l_{mt}^2 + \frac{59}{3} l_{mt}^2 \zeta_3 - \frac{997}{144} l_{mt}^3 - \frac{1429}{864} l_{mt}^4 + \frac{1213}{864} \pi^2 + \frac{59}{72} \pi^2 \zeta_3 - \frac{559}{288} \pi^2 l_{mt} \right.
\end{aligned}$$

$$\begin{aligned}
& + \frac{41}{864} \pi^2 l_{mt}^2 - \frac{4501}{5760} \pi^4 - \frac{437}{360} \pi^4 l_{mt} + \frac{151}{45} a_1 \pi^4 - \frac{10}{3} a_1^2 \pi^2 - \frac{16}{3} a_1^2 \pi^2 l_{mt} + \frac{32}{9} a_1^3 \pi^2 \\
& + \frac{10}{3} a_1^4 + \frac{16}{3} a_1^4 l_{mt} - \frac{32}{15} a_1^5 \left. \right\} \zeta + \left[-\frac{236161}{10368} - \frac{7}{48} \zeta_5 + \frac{803}{288} \zeta_3 + \frac{1169}{72} l_{mt} - \frac{17}{12} l_{mt} \zeta_3 \right. \\
& - \frac{193}{32} l_{mt}^2 - \frac{1}{6} l_{mt}^2 \zeta_3 + \frac{253}{144} l_{mt}^3 - \frac{9}{32} l_{mt}^4 - \frac{179}{576} \pi^2 - \frac{1}{144} \pi^2 \zeta_3 + \frac{79}{288} \pi^2 l_{mt} - \frac{3}{32} \pi^2 l_{mt}^2 \\
& \left. + \frac{181}{5760} \pi^4 - \frac{1}{720} \pi^4 l_{mt} \right\} \zeta^2 \Big] \\
& + C_A^2 C_F \left[\left(-\frac{695}{24} - \frac{3}{8} \zeta \right) \frac{1}{\epsilon^3} + \left(-5 + 25 \zeta_3 + \frac{545}{18} l_{mt} + \left\{ \frac{15}{8} - 3 \zeta_3 + \frac{3}{2} l_{mt} \right\} \zeta \right) \frac{1}{\epsilon^2} \right. \\
& + \left(-\frac{157057}{2592} - 30 \zeta_5 + \frac{1513}{8} \zeta_3 + 64 a_4 - \frac{10349}{54} l_{mt} + 12 l_{mt} \zeta_3 + \frac{241}{6} l_{mt}^2 + \frac{545}{216} \pi^2 \right. \\
& - \frac{5}{36} \pi^4 - \frac{8}{3} a_1^2 \pi^2 + \frac{8}{3} a_1^4 + \left. \left\{ \frac{519}{32} - \frac{43}{2} \zeta_3 - 64 a_4 - 3 l_{mt} - 12 l_{mt} \zeta_3 + \frac{15}{2} l_{mt}^2 + \frac{1}{8} \pi^2 \right. \right. \\
& \left. \left. + \frac{91}{180} \pi^4 + \frac{8}{3} a_1^2 \pi^2 - \frac{8}{3} a_1^4 \right\} \zeta \right) \frac{1}{\epsilon} + \frac{175778221}{204120} - \frac{937892}{315} \zeta_5 - \frac{418199}{140} \zeta_3 + 105 \zeta_3^2 \\
& + \frac{785152}{315} a_5 - \frac{300008}{105} a_4 + \frac{1023661}{648} l_{mt} - 120 l_{mt} \zeta_5 - \frac{13745}{12} l_{mt} \zeta_3 - 1152 l_{mt} a_4 - \frac{685}{36} l_{mt}^2 \\
& - 108 l_{mt}^2 \zeta_3 + \frac{3815}{54} l_{mt}^3 - \frac{10349}{648} \pi^2 + \pi^2 \zeta_3 + \frac{241}{36} \pi^2 l_{mt} + \frac{393553}{12600} \pi^4 + \frac{51}{5} \pi^4 l_{mt} + \frac{74}{189} \pi^6 \\
& + \frac{163822}{14175} a_1 \pi^4 + \frac{37501}{315} a_1^2 \pi^2 + 48 a_1^2 \pi^2 l_{mt} + \frac{98144}{2835} a_1^3 \pi^2 - \frac{37501}{315} a_1^4 - 48 a_1^4 l_{mt} - \frac{98144}{4725} a_1^5 \\
& + \left\{ -\frac{14639}{96} + 556 \zeta_5 + \frac{57}{4} \zeta_3 - 512 a_5 - 160 a_4 + \frac{793}{8} l_{mt} - 86 l_{mt} \zeta_3 - 256 l_{mt} a_4 - \frac{87}{4} l_{mt}^2 \right. \\
& - 24 l_{mt}^2 \zeta_3 + \frac{29}{2} l_{mt}^3 - \frac{1}{4} \pi^2 - \pi^2 \zeta_3 + \frac{5}{4} \pi^2 l_{mt} + \frac{175}{72} \pi^4 + \frac{91}{45} \pi^4 l_{mt} - \frac{302}{45} a_1 \pi^4 + \frac{20}{3} a_1^2 \pi^2 \\
& \left. + \frac{32}{3} a_1^2 \pi^2 l_{mt} - \frac{64}{9} a_1^3 \pi^2 - \frac{20}{3} a_1^4 - \frac{32}{3} a_1^4 l_{mt} + \frac{64}{15} a_1^5 \right\} \zeta \Big] \\
& + C_A C_F^2 \left[-\frac{35}{12 \epsilon^2} + \left(-\frac{253}{72} + 60 \zeta_5 - \frac{575}{6} \zeta_3 + 39 l_{mt} \right) \frac{1}{\epsilon} - \frac{8006087}{7560} + \frac{719650}{63} \zeta_5 \right. \\
& - \frac{6955451}{630} \zeta_3 - 348 \zeta_3^2 - \frac{559616}{63} a_5 - \frac{1281520}{63} a_4 - \frac{5201}{6} l_{mt} + 240 l_{mt} \zeta_5 + 109 l_{mt} \zeta_3 \\
& - \frac{49}{3} l_{mt}^2 + \frac{13}{4} \pi^2 + \frac{633511}{2835} \pi^4 - \frac{26}{189} \pi^6 - \frac{51232}{567} a_1 \pi^4 + \frac{160190}{189} a_1^2 \pi^2 \\
& \left. - \frac{69952}{567} a_1^3 \pi^2 - \frac{160190}{189} a_1^4 + \frac{69952}{945} a_1^5 \right]
\end{aligned}$$

$$\begin{aligned}
& + C_F^3 \left[\frac{23}{2\epsilon} + \frac{37441}{135} - \frac{27432}{5} \zeta_5 + \frac{30196}{5} \zeta_3 + \frac{65536}{15} a_5 + \frac{491264}{45} a_4 \right. \\
& + 314 l_{mt} - \frac{232004}{2025} \pi^4 + \frac{27136}{675} a_1 \pi^4 - \frac{61408}{135} a_1^2 \pi^2 + \frac{8192}{135} a_1^3 \pi^2 + \frac{61408}{135} a_1^4 - \frac{8192}{225} a_1^5 \left. \right] \\
& + \frac{d^{abcd} d_F^{abcd}}{T_F N_A} \left[\left(\frac{128}{9} - 30 \zeta_5 - \frac{344}{3} \zeta_3 \right) \frac{1}{\epsilon} + \frac{52936}{945} - \frac{2184661}{105} \zeta_5 + \frac{1173344}{315} \zeta_3 - 6 \zeta_3^2 \right. \\
& + \frac{1918976}{105} a_5 + \frac{913408}{105} a_4 + \frac{512}{9} l_{mt} - 120 l_{mt} \zeta_5 - \frac{1376}{3} l_{mt} \zeta_3 - \frac{361478}{4725} \pi^4 + \frac{11}{63} \pi^6 \\
& + \left. \frac{794576}{4725} a_1 \pi^4 - \frac{114176}{315} a_1^2 \pi^2 + \frac{239872}{945} a_1^3 \pi^2 + \frac{114176}{315} a_1^4 - \frac{239872}{1575} a_1^5 \right] \\
& + C_A^2 T_F \left[\left(-\frac{199}{54} + \frac{1}{9} \zeta \right) \frac{1}{\epsilon^4} + \left(\frac{2675}{162} + \frac{1130}{27} l_{mt} + \left\{ -\frac{7}{18} + \frac{8}{9} l_{mt} \right\} \zeta \right) \frac{1}{\epsilon^3} \right. \\
& + \left(-\frac{10301}{648} - 2 \zeta_3 - \frac{6608}{81} l_{mt} + \frac{1472}{27} l_{mt}^2 + \frac{565}{162} \pi^2 + \left\{ \frac{29}{12} - \frac{28}{9} l_{mt} + \frac{22}{9} l_{mt}^2 \right. \right. \\
& + \left. \left. \frac{2}{27} \pi^2 \right\} \zeta \right) \frac{1}{\epsilon^2} + \left(-\frac{223097}{5832} - \frac{13937}{324} \zeta_3 - \frac{256}{3} a_4 + \frac{23963}{162} l_{mt} - 32 l_{mt} \zeta_3 - \frac{12433}{81} l_{mt}^2 \right. \\
& + \frac{3172}{81} l_{mt}^3 - \frac{1652}{243} \pi^2 + \frac{736}{81} \pi^2 l_{mt} + \frac{239}{270} \pi^4 + \frac{32}{9} a_1^2 \pi^2 - \frac{32}{9} a_1^4 + \left\{ -\frac{5317}{648} - \frac{110}{27} \zeta_3 \right. \\
& + \left. \frac{398}{27} l_{mt} - \frac{77}{9} l_{mt}^2 + \frac{106}{27} l_{mt}^3 - \frac{7}{27} \pi^2 + \frac{11}{27} \pi^2 l_{mt} \right\} \zeta \left. \right) \frac{1}{\epsilon} + \frac{8534362439}{28576800} + \frac{818}{9} \zeta_5 \\
& - \frac{1755468433}{1190700} \zeta_3 - 512 a_5 - \frac{312896}{105} a_4 - \frac{214925}{1458} l_{mt} - \frac{34546}{81} l_{mt} \zeta_3 - \frac{1792}{3} l_{mt} a_4 \\
& + \frac{4453}{9} l_{mt}^2 - 100 l_{mt}^2 \zeta_3 - \frac{24895}{243} l_{mt}^3 + \frac{2411}{81} l_{mt}^4 + \frac{23963}{1944} \pi^2 - \frac{8}{3} \pi^2 \zeta_3 - \frac{12433}{486} \pi^2 l_{mt} \\
& + \frac{793}{81} \pi^2 l_{mt}^2 + \frac{11210597}{340200} \pi^4 + \frac{796}{135} \pi^4 l_{mt} - \frac{272}{45} a_1 \pi^4 + \frac{39112}{315} a_1^2 \pi^2 + \frac{224}{9} a_1^2 \pi^2 l_{mt} \\
& - \frac{64}{9} a_1^3 \pi^2 - \frac{39112}{315} a_1^4 - \frac{224}{9} a_1^4 l_{mt} + \frac{64}{15} a_1^5 + \left\{ \frac{42683}{1296} - \frac{224}{27} \zeta_3 - \frac{128}{3} a_4 - \frac{4447}{81} l_{mt} \right. \\
& - \frac{356}{27} l_{mt} \zeta_3 + \frac{2003}{54} l_{mt}^2 - \frac{371}{27} l_{mt}^3 + \frac{239}{54} l_{mt}^4 + \frac{199}{162} \pi^2 - \frac{77}{54} \pi^2 l_{mt} + \frac{53}{54} \pi^2 l_{mt}^2 \\
& + \left. \frac{577}{1080} \pi^4 + \frac{16}{9} a_1^2 \pi^2 - \frac{16}{9} a_1^4 \right\} \zeta \left. \right] + n_l C_A^2 T_F \left[\left(-\frac{1534}{27} - \frac{2}{9} \zeta \right) \frac{1}{\epsilon^4} + \left(\frac{920}{9} \right. \right. \\
& - \left. \frac{1396}{27} l_{mt} + \left\{ \frac{7}{9} - \frac{4}{9} l_{mt} \right\} \zeta \right) \frac{1}{\epsilon^3} + \left(-\frac{10901}{81} + 12 \zeta_3 + \frac{3436}{27} l_{mt} - \frac{698}{27} l_{mt}^2 \right.
\end{aligned}$$

$$\begin{aligned}
& -\frac{349}{81}\pi^2 + \left\{ -\frac{13}{54} + \frac{14}{9}l_{mt} - \frac{2}{9}l_{mt}^2 - \frac{1}{27}\pi^2 \right\} \zeta \bigg) \frac{1}{\epsilon^2} + \left(\frac{52487}{324} - \frac{889}{162}\zeta_3 - \frac{6151}{27}l_{mt} \right. \\
& + 24l_{mt}\zeta_3 + \frac{250}{3}l_{mt}^2 - \frac{734}{81}l_{mt}^3 + \frac{859}{81}\pi^2 - \frac{349}{81}\pi^2 l_{mt} + \frac{1}{5}\pi^4 + \left\{ -\frac{2179}{324} + \frac{136}{27}\zeta_3 \right. \\
& + \left. \frac{37}{9}l_{mt} + \frac{7}{9}l_{mt}^2 + \frac{10}{27}l_{mt}^3 + \frac{7}{54}\pi^2 - \frac{1}{27}\pi^2 l_{mt} \right\} \zeta \bigg) \frac{1}{\epsilon} - \frac{4083139}{17496} + \frac{4024}{9}\zeta_5 + \frac{8521}{54}\zeta_3 \\
& - 512a_5 - \frac{3320}{9}a_4 + \frac{143747}{486}l_{mt} - \frac{15217}{162}l_{mt}\zeta_3 - 256l_{mt}a_4 - \frac{17527}{162}l_{mt}^2 + 12l_{mt}^2\zeta_3 \\
& + \frac{3718}{81}l_{mt}^3 + \frac{299}{162}l_{mt}^4 - \frac{6151}{324}\pi^2 + 2\pi^2\zeta_3 + \frac{125}{9}\pi^2 l_{mt} - \frac{367}{162}\pi^2 l_{mt}^2 + \frac{11077}{3240}\pi^4 \\
& + \frac{142}{45}\pi^4 l_{mt} - \frac{392}{45}a_1\pi^4 + \frac{415}{27}a_1^2\pi^2 + \frac{32}{3}a_1^2\pi^2 l_{mt} - \frac{64}{9}a_1^3\pi^2 - \frac{415}{27}a_1^4 - \frac{32}{3}a_1^4 l_{mt} \\
& + \frac{64}{15}a_1^5 + \left\{ \frac{168263}{1944} - \frac{476}{27}\zeta_3 - \frac{2645}{54}l_{mt} + \frac{628}{27}l_{mt}\zeta_3 + \frac{95}{6}l_{mt}^2 - \frac{35}{27}l_{mt}^3 + \frac{47}{54}l_{mt}^4 + \frac{37}{108}\pi^2 \right. \\
& + \left. \frac{7}{54}\pi^2 l_{mt} + \frac{5}{54}\pi^2 l_{mt}^2 - \frac{121}{360}\pi^4 \right\} \zeta \bigg] \\
& + C_A C_F T_F \left[\frac{194}{27\epsilon^3} + \left(-\frac{4109}{81} + \frac{8}{3}\zeta_3 + \frac{296}{27}l_{mt} \right) \frac{1}{\epsilon^2} + \left(-\frac{24173}{243} + \frac{4771}{18}\zeta_3 + \frac{512}{3}a_4 \right. \right. \\
& - \left. \frac{14564}{81}l_{mt} + \frac{128}{3}l_{mt}\zeta_3 + \frac{2116}{27}l_{mt}^2 + \frac{74}{81}\pi^2 - \frac{194}{135}\pi^4 - \frac{64}{9}a_1^2\pi^2 + \frac{64}{9}a_1^4 \right) \frac{1}{\epsilon} \\
& + \frac{293361767}{1786050} - 632\zeta_5 + \frac{284760583}{99225}\zeta_3 + 1024a_5 + \frac{1625488}{315}a_4 - \frac{213830}{243}l_{mt} \\
& + \frac{13568}{9}l_{mt}\zeta_3 + \frac{3584}{3}l_{mt}a_4 - \frac{47998}{81}l_{mt}^2 + \frac{400}{3}l_{mt}^2\zeta_3 + \frac{4060}{81}l_{mt}^3 - \frac{3641}{243}\pi^2 + \frac{32}{9}\pi^2\zeta_3 \\
& + \frac{1058}{81}\pi^2 l_{mt} - \frac{1755167}{28350}\pi^4 - \frac{1304}{135}\pi^4 l_{mt} + \frac{544}{45}a_1\pi^4 - \frac{203186}{945}a_1^2\pi^2 - \frac{448}{9}a_1^2\pi^2 l_{mt} \\
& + \left. \frac{128}{9}a_1^3\pi^2 + \frac{203186}{945}a_1^4 + \frac{448}{9}a_1^4 l_{mt} - \frac{128}{15}a_1^5 \right] + n_l C_A C_F T_F \left[\frac{152}{3\epsilon^3} + \left(-\frac{520}{27} - 16\zeta_3 \right) \frac{1}{\epsilon^2} \right. \\
& + \left(\frac{27227}{243} - \frac{689}{9}\zeta_3 + \frac{2840}{27}l_{mt} - 32l_{mt}\zeta_3 - \frac{76}{3}l_{mt}^2 - \frac{4}{15}\pi^4 \right) \frac{1}{\epsilon} + \frac{135499}{486} - 1256\zeta_5 \\
& + \frac{10673}{27}\zeta_3 + 1024a_5 + \frac{7888}{9}a_4 - \frac{62908}{243}l_{mt} + \frac{1963}{9}l_{mt}\zeta_3 + 512l_{mt}a_4 + \frac{4282}{27}l_{mt}^2 \\
& - 16l_{mt}^2\zeta_3 - \frac{356}{9}l_{mt}^3 + \frac{710}{81}\pi^2 - \frac{8}{3}\pi^2\zeta_3 - \frac{38}{9}\pi^2 l_{mt} - \frac{5494}{405}\pi^4 - \frac{224}{45}\pi^4 l_{mt} + \frac{784}{45}a_1\pi^4 \\
& - \left. \frac{986}{27}a_1^2\pi^2 - \frac{64}{3}a_1^2\pi^2 l_{mt} + \frac{128}{9}a_1^3\pi^2 + \frac{986}{27}a_1^4 + \frac{64}{3}a_1^4 l_{mt} - \frac{128}{15}a_1^5 \right]
\end{aligned}$$

$$\begin{aligned}
 & + C_F^2 T_F \left[-\frac{14}{9\epsilon^2} + \left(\frac{1348}{27} - \frac{556}{9}\zeta_3 + \frac{136}{9}l_{mt} \right) \frac{1}{\epsilon} + \frac{1821397}{4050} + \frac{1929484}{675}\zeta_3 + \frac{68288}{15}a_4 \right. \\
 & \left. + \frac{2032}{27}l_{mt} - \frac{2212}{9}l_{mt}\zeta_3 + \frac{1592}{9}l_{mt}^2 + \frac{34}{27}\pi^2 - \frac{36946}{675}\pi^4 - \frac{8536}{45}a_1^2\pi^2 + \frac{8536}{45}a_1^4 \right] \\
 & + n_l C_F^2 T_F \left[-\frac{16}{3\epsilon^2} + \left(-\frac{568}{27} + \frac{28}{9}\zeta_3 - \frac{16}{3}l_{mt} \right) \frac{1}{\epsilon} + \frac{10054}{81} - \frac{6184}{27}\zeta_3 - \frac{832}{3}a_4 \right. \\
 & \left. - \frac{808}{27}l_{mt} + \frac{124}{9}l_{mt}\zeta_3 - \frac{16}{3}l_{mt}^2 - \frac{4}{9}\pi^2 + \frac{428}{135}\pi^4 + \frac{104}{9}a_1^2\pi^2 - \frac{104}{9}a_1^4 \right] \\
 & + \frac{d_F^{abcd} d_F^{abcd}}{T_F N_A} \left[\left(-\frac{176}{9} + \frac{128}{3}\zeta_3 \right) \frac{1}{\epsilon} + \left(-\frac{38576}{315} + \frac{320}{3}\zeta_5 + \frac{54232}{35}\zeta_3 + \frac{9344}{3}a_4 \right. \right. \\
 & \left. \left. - \frac{704}{9}l_{mt} + \frac{512}{3}l_{mt}\zeta_3 - \frac{4378}{135}\pi^4 - \frac{1168}{9}a_1^2\pi^2 + \frac{1168}{9}a_1^4 \right) \right] + n_l \frac{d_F^{abcd} d_F^{abcd}}{T_F N_A} \left[\left(-\frac{352}{9} \right. \right. \\
 & \left. \left. + \frac{256}{3}\zeta_3 \right) \frac{1}{\epsilon} - \frac{3296}{27} + \frac{640}{3}\zeta_5 - \frac{4192}{9}\zeta_3 - \frac{1408}{9}l_{mt} + \frac{1024}{3}l_{mt}\zeta_3 + \frac{64}{45}\pi^4 \right] \\
 & + C_A T_F^2 \left[\frac{8}{27\epsilon^4} + \left(-\frac{100}{81} - \frac{16}{27}l_{mt} \right) \frac{1}{\epsilon^3} + \left(\frac{82}{81} + \frac{200}{81}l_{mt} + \frac{152}{9}l_{mt}^2 - \frac{4}{81}\pi^2 \right) \frac{1}{\epsilon^2} \right. \\
 & + \left(-\frac{8615}{729} + \frac{1594}{81}\zeta_3 - \frac{748}{81}l_{mt} - \frac{2180}{81}l_{mt}^2 + \frac{2296}{81}l_{mt}^3 + \frac{50}{243}\pi^2 + \frac{76}{27}\pi^2 l_{mt} \right) \frac{1}{\epsilon} \\
 & - \frac{2318791}{153090} + \frac{411311}{8505}\zeta_3 + \frac{1312}{9}a_4 - \frac{72626}{729}l_{mt} + \frac{1174}{9}l_{mt}\zeta_3 - \frac{670}{27}l_{mt}^2 - \frac{20060}{243}l_{mt}^3 \\
 & \left. + \frac{542}{27}l_{mt}^4 - \frac{187}{243}\pi^2 - \frac{1090}{243}\pi^2 l_{mt} + \frac{574}{81}\pi^2 l_{mt}^2 - \frac{3973}{2430}\pi^4 - \frac{164}{27}a_1^2\pi^2 + \frac{164}{27}a_1^4 \right] \\
 & + n_l C_A T_F^2 \left[\frac{40}{27\epsilon^4} + \left(-\frac{500}{81} - \frac{368}{9}l_{mt} \right) \frac{1}{\epsilon^3} + \left(-\frac{118}{81} + \frac{3880}{81}l_{mt} - \frac{1576}{27}l_{mt}^2 - \frac{92}{27}\pi^2 \right) \frac{1}{\epsilon^2} \right. \\
 & + \left(\frac{28073}{729} - \frac{158}{27}\zeta_3 - \frac{5540}{81}l_{mt} + \frac{8660}{81}l_{mt}^2 - \frac{1192}{27}l_{mt}^3 + \frac{970}{243}\pi^2 - \frac{788}{81}\pi^2 l_{mt} \right) \frac{1}{\epsilon} \\
 & - \frac{127543}{1458} - \frac{11179}{243}\zeta_3 - \frac{32}{3}a_4 + \frac{130814}{729}l_{mt} - \frac{298}{81}l_{mt}\zeta_3 - \frac{5494}{27}l_{mt}^2 + \frac{28220}{243}l_{mt}^3 \\
 & \left. - \frac{2170}{81}l_{mt}^4 - \frac{1385}{243}\pi^2 + \frac{4330}{243}\pi^2 l_{mt} - \frac{298}{27}\pi^2 l_{mt}^2 - \frac{2017}{2430}\pi^4 + \frac{4}{9}a_1^2\pi^2 - \frac{4}{9}a_1^4 \right] \\
 & + n_l^2 C_A T_F^2 \left[\frac{632}{27\epsilon^4} + \left(-\frac{220}{9} + \frac{608}{27}l_{mt} \right) \frac{1}{\epsilon^3} + \left(\frac{1670}{81} - \frac{880}{27}l_{mt} + \frac{304}{27}l_{mt}^2 + \frac{152}{81}\pi^2 \right) \frac{1}{\epsilon^2} \right.
 \end{aligned}$$

$$\begin{aligned}
& + \left(-\frac{565}{81} - \frac{1040}{81}\zeta_3 + \frac{896}{27}l_{mt} - \frac{200}{9}l_{mt}^2 + \frac{304}{81}l_{mt}^3 - \frac{220}{81}\pi^2 + \frac{152}{81}\pi^2 l_{mt} \right) \frac{1}{\epsilon} \\
& - \frac{444263}{4374} + \frac{680}{27}\zeta_3 + \frac{12116}{243}l_{mt} - \frac{4640}{81}l_{mt}\zeta_3 + \frac{488}{81}l_{mt}^2 - \frac{760}{81}l_{mt}^3 + \frac{4}{81}l_{mt}^4 + \frac{224}{81}\pi^2 \\
& - \left. \frac{100}{27}\pi^2 l_{mt} + \frac{76}{81}\pi^2 l_{mt}^2 + \frac{103}{135}\pi^4 \right] \\
& + C_F T_F^2 \left[-\frac{16}{27\epsilon^3} + \left(\frac{88}{81} + \frac{32}{27}l_{mt} \right) \frac{1}{\epsilon^2} + \left(-\frac{1340}{243} + \frac{28}{3}\zeta_3 - \frac{1616}{81}l_{mt} + \frac{400}{27}l_{mt}^2 \right. \right. \\
& + \left. \left. \frac{8}{81}\pi^2 \right) \frac{1}{\epsilon} - \frac{680462}{8505} + \frac{265442}{2835}\zeta_3 + 64a_4 - \frac{6104}{243}l_{mt} + \frac{196}{3}l_{mt}\zeta_3 - \frac{6088}{81}l_{mt}^2 + \frac{5776}{81}l_{mt}^3 \right. \\
& - \left. \frac{404}{243}\pi^2 + \frac{200}{81}\pi^2 l_{mt} - \frac{34}{45}\pi^4 - \frac{8}{3}a_1^2\pi^2 + \frac{8}{3}a_1^4 \right] + n_l C_F T_F^2 \left[-\frac{80}{27\epsilon^3} + \left(\frac{1688}{81} \right. \right. \\
& + \left. \left. \frac{160}{27}l_{mt} \right) \frac{1}{\epsilon^2} + \left(\frac{2780}{243} - \frac{28}{3}\zeta_3 + \frac{4112}{81}l_{mt} - \frac{688}{27}l_{mt}^2 + \frac{40}{81}\pi^2 \right) \frac{1}{\epsilon} - \frac{3754}{81} + \frac{3386}{81}\zeta_3 \right. \\
& - \left. \frac{64}{3}a_4 + \frac{15200}{243}l_{mt} - \frac{28}{3}l_{mt}\zeta_3 + \frac{5416}{81}l_{mt}^2 - \frac{3664}{81}l_{mt}^3 + \frac{1028}{243}\pi^2 - \frac{344}{81}\pi^2 l_{mt} + \frac{4}{135}\pi^4 \right. \\
& + \left. \frac{8}{9}a_1^2\pi^2 - \frac{8}{9}a_1^4 \right] + n_l^2 C_F T_F^2 \left[-\frac{16}{\epsilon^3} + \left(\frac{56}{27} - \frac{64}{9}l_{mt} \right) \frac{1}{\epsilon^2} + \left(-\frac{1804}{243} - \frac{16}{27}\pi^2 \right) \frac{1}{\epsilon} \right. \\
& - \left. \frac{5458}{729} + \frac{160}{9}\zeta_3 - \frac{2392}{243}l_{mt} + \frac{16}{27}l_{mt}^2 + \frac{32}{27}l_{mt}^3 \right] \\
& + T_F^3 \left[\frac{256}{81\epsilon}l_{mt}^3 + \frac{640}{81}l_{mt}^4 + \frac{64}{81}\pi^2 l_{mt}^2 \right] + n_l T_F^3 \left[-\frac{256}{27\epsilon^2}l_{mt}^2 + \left(-\frac{512}{27}l_{mt}^3 - \frac{128}{81}\pi^2 l_{mt} \right) \frac{1}{\epsilon} \right. \\
& + \left. \frac{512}{81}l_{mt}\zeta_3 - \frac{1600}{81}l_{mt}^4 - \frac{128}{27}\pi^2 l_{mt}^2 - \frac{16}{243}\pi^4 \right] + n_l^2 T_F^3 \left[\frac{256}{27\epsilon^3}l_{mt} + \left(\frac{128}{9}l_{mt}^2 + \frac{64}{81}\pi^2 \right) \frac{1}{\epsilon^2} \right. \\
& + \left. \left(-\frac{256}{81}\zeta_3 + \frac{896}{81}l_{mt}^3 + \frac{64}{27}\pi^2 l_{mt} \right) \frac{1}{\epsilon} - \frac{256}{27}l_{mt}\zeta_3 + \frac{160}{27}l_{mt}^4 + \frac{224}{81}\pi^2 l_{mt}^2 + \frac{152}{1215}\pi^4 \right] \\
& + n_l^3 T_F^3 \left[-\frac{256}{81\epsilon^4} - \frac{256}{81\epsilon^3}l_{mt} + \left(-\frac{128}{81}l_{mt}^2 - \frac{64}{243}\pi^2 \right) \frac{1}{\epsilon^2} + \frac{256}{243}\zeta_3 - \frac{128}{243}l_{mt}^3 \right. \\
& - \left. \frac{64}{243}\pi^2 l_{mt} \right) \frac{1}{\epsilon} + \frac{256}{243}l_{mt}\zeta_3 - \frac{32}{243}l_{mt}^4 - \frac{32}{243}\pi^2 l_{mt}^2 - \frac{8}{405}\pi^4 \left. \right]. \tag{C.9}
\end{aligned}$$

Here n_l is the number of light quark flavours, ζ is the Riemann ζ -function Eq. (2.35), $a_n = \text{Li}_n(1/2)$ and $l_{mt} = \ln(\mu^2/m_t^2(\mu^2))$, where m_t is the top-quark mass renormalized in the $\overline{\text{MS}}$ scheme. Furthermore s_6 is given by [75]

$$s_6 = \sum_{m=1}^{\infty} \sum_{k=1}^m \frac{(-1)^{m+k}}{m^5 k} \approx 0.987. \quad (\text{C.10})$$

BIBLIOGRAPHY

- [1] Georges Aad et al. "Observation of a new particle in the search for the Standard Model Higgs boson with the ATLAS detector at the LHC." In: *Phys. Lett. B* 716 (2012), pp. 1–29. DOI: [10.1016/j.physletb.2012.08.020](https://doi.org/10.1016/j.physletb.2012.08.020). arXiv: [1207.7214](https://arxiv.org/abs/1207.7214) [hep-ex].
- [2] Serguei Chatrchyan et al. "Observation of a New Boson at a Mass of 125 GeV with the CMS Experiment at the LHC." In: *Phys. Lett. B* 716 (2012), pp. 30–61. DOI: [10.1016/j.physletb.2012.08.021](https://doi.org/10.1016/j.physletb.2012.08.021). arXiv: [1207.7235](https://arxiv.org/abs/1207.7235) [hep-ex].
- [3] R.P. Feynman and Murray Gell-Mann. "Theory of Fermi interaction." In: *Phys. Rev.* 109 (1958). Ed. by L.M. Brown, pp. 193–198. DOI: [10.1103/PhysRev.109.193](https://doi.org/10.1103/PhysRev.109.193).
- [4] S.L. Glashow. "Partial Symmetries of Weak Interactions." In: *Nucl. Phys.* 22 (1961), pp. 579–588. DOI: [10.1016/0029-5582\(61\)90469-2](https://doi.org/10.1016/0029-5582(61)90469-2).
- [5] Murray Gell-Mann. "Symmetries of baryons and mesons." In: *Phys. Rev.* 125 (1962), pp. 1067–1084. DOI: [10.1103/PhysRev.125.1067](https://doi.org/10.1103/PhysRev.125.1067).
- [6] Jeffrey Goldstone, Abdus Salam, and Steven Weinberg. "Broken Symmetries." In: *Phys. Rev.* 127 (1962), pp. 965–970. DOI: [10.1103/PhysRev.127.965](https://doi.org/10.1103/PhysRev.127.965).
- [7] Peter W. Higgs. "Broken symmetries, massless particles and gauge fields." In: *Phys. Lett.* 12 (1964), pp. 132–133. DOI: [10.1016/0031-9163\(64\)91136-9](https://doi.org/10.1016/0031-9163(64)91136-9).
- [8] F. Englert and R. Brout. "Broken Symmetry and the Mass of Gauge Vector Mesons." In: *Phys. Rev. Lett.* 13 (1964). Ed. by J.C. Taylor, pp. 321–323. DOI: [10.1103/PhysRevLett.13.321](https://doi.org/10.1103/PhysRevLett.13.321).
- [9] Peter W. Higgs. "Broken Symmetries and the Masses of Gauge Bosons." In: *Phys. Rev. Lett.* 13 (1964). Ed. by J.C. Taylor, pp. 508–509. DOI: [10.1103/PhysRevLett.13.508](https://doi.org/10.1103/PhysRevLett.13.508).
- [10] G.S. Guralnik, C.R. Hagen, and T.W.B. Kibble. "Global Conservation Laws and Massless Particles." In: *Phys. Rev. Lett.* 13 (1964). Ed. by J.C. Taylor, pp. 585–587. DOI: [10.1103/PhysRevLett.13.585](https://doi.org/10.1103/PhysRevLett.13.585).
- [11] Peter W. Higgs. "Spontaneous Symmetry Breakdown without Massless Bosons." In: *Phys. Rev.* 145 (1966), pp. 1156–1163. DOI: [10.1103/PhysRev.145.1156](https://doi.org/10.1103/PhysRev.145.1156).
- [12] Steven Weinberg. "A Model of Leptons." In: *Phys. Rev. Lett.* 19 (1967), pp. 1264–1266. DOI: [10.1103/PhysRevLett.19.1264](https://doi.org/10.1103/PhysRevLett.19.1264).
- [13] Abdus Salam. "Weak and Electromagnetic Interactions." In: *Conf. Proc. C* 680519 (1968), pp. 367–377. DOI: [10.1142/9789812795915_0034](https://doi.org/10.1142/9789812795915_0034).

- [14] H. Fritzsche, Murray Gell-Mann, and H. Leutwyler. "Advantages of the Color Octet Gluon Picture." In: *Phys. Lett. B* 47 (1973), pp. 365–368. DOI: [10.1016/0370-2693\(73\)90625-4](https://doi.org/10.1016/0370-2693(73)90625-4).
- [15] Albert M Sirunyan et al. "Evidence for Higgs boson decay to a pair of muons." In: (Sept. 2020). arXiv: [2009.04363 \[hep-ex\]](https://arxiv.org/abs/2009.04363).
- [16] Gudrun Heinrich. "Collider Physics at the Precision Frontier." In: (Sept. 2020). arXiv: [2009.00516 \[hep-ph\]](https://arxiv.org/abs/2009.00516).
- [17] Charalampos Anastasiou, Claude Duhr, Falko Dulat, Franz Herzog, and Bernhard Mistlberger. "Higgs Boson Gluon-Fusion Production in QCD at Three Loops." In: *Phys. Rev. Lett.* 114 (2015), p. 212001. DOI: [10.1103/PhysRevLett.114.212001](https://doi.org/10.1103/PhysRevLett.114.212001). arXiv: [1503.06056 \[hep-ph\]](https://arxiv.org/abs/1503.06056).
- [18] Bernhard Mistlberger. "Higgs boson production at hadron colliders at N³LO in QCD." In: *JHEP* 05 (2018), p. 028. DOI: [10.1007/JHEP05\(2018\)028](https://doi.org/10.1007/JHEP05(2018)028). arXiv: [1802.00833 \[hep-ph\]](https://arxiv.org/abs/1802.00833).
- [19] Albert M Sirunyan et al. "Combined measurements of Higgs boson couplings in proton–proton collisions at $\sqrt{s} = 13$ TeV." In: *Eur. Phys. J. C* 79.5 (2019), p. 421. DOI: [10.1140/epjc/s10052-019-6909-y](https://doi.org/10.1140/epjc/s10052-019-6909-y). arXiv: [1809.10733 \[hep-ex\]](https://arxiv.org/abs/1809.10733).
- [20] J. Alison et al. "Higgs Boson Pair Production at Colliders: Status and Perspectives." In: *Double Higgs Production at Colliders*. Ed. by B. Di Micco, M. Gouzevitch, J. Mazzitelli, and C. Vernieri. Sept. 2019. arXiv: [1910.00012 \[hep-ph\]](https://arxiv.org/abs/1910.00012).
- [21] Georges Aad et al. "Combination of searches for Higgs boson pairs in pp collisions at $\sqrt{s} = 13$ TeV with the ATLAS detector." In: *Phys. Lett. B* 800 (2020), p. 135103. DOI: [10.1016/j.physletb.2019.135103](https://doi.org/10.1016/j.physletb.2019.135103). arXiv: [1906.02025 \[hep-ex\]](https://arxiv.org/abs/1906.02025).
- [22] A. Abada et al. "FCC-hh: The Hadron Collider: Future Circular Collider Conceptual Design Report Volume 3." In: *Eur. Phys. J. ST* 228.4 (2019), pp. 755–1107. DOI: [10.1140/epjst/e2019-900087-0](https://doi.org/10.1140/epjst/e2019-900087-0).
- [23] S. Borowka, N. Greiner, G. Heinrich, S.P. Jones, M. Kerner, J. Schlenk, U. Schubert, and T. Zirke. "Higgs Boson Pair Production in Gluon Fusion at Next-to-Leading Order with Full Top-Quark Mass Dependence." In: *Phys. Rev. Lett.* 117.1 (2016). [Erratum: *Phys.Rev.Lett.* 117, 079901 (2016)], p. 012001. DOI: [10.1103/PhysRevLett.117.079901](https://doi.org/10.1103/PhysRevLett.117.079901). arXiv: [1604.06447 \[hep-ph\]](https://arxiv.org/abs/1604.06447).
- [24] S. Borowka, N. Greiner, G. Heinrich, S.P. Jones, M. Kerner, J. Schlenk, and T. Zirke. "Full top quark mass dependence in Higgs boson pair production at NLO." In: *JHEP* 10 (2016), p. 107. DOI: [10.1007/JHEP10\(2016\)107](https://doi.org/10.1007/JHEP10(2016)107). arXiv: [1608.04798 \[hep-ph\]](https://arxiv.org/abs/1608.04798).

- [25] J. Baglio, F. Campanario, S. Glaus, M. Mühlleitner, J. Ronca, M. Spira, and J. Streicher. “Higgs-Pair Production via Gluon Fusion at Hadron Colliders: NLO QCD Corrections.” In: *JHEP* 04 (2020), p. 181. DOI: [10.1007/JHEP04\(2020\)181](https://doi.org/10.1007/JHEP04(2020)181). arXiv: [2003.03227](https://arxiv.org/abs/2003.03227) [hep-ph].
- [26] Jonathan Grigo, Jens Hoff, Kirill Melnikov, and Matthias Steinhauser. “On the Higgs boson pair production at the LHC.” In: *Nucl. Phys. B* 875 (2013), pp. 1–17. DOI: [10.1016/j.nuclphysb.2013.06.024](https://doi.org/10.1016/j.nuclphysb.2013.06.024). arXiv: [1305.7340](https://arxiv.org/abs/1305.7340) [hep-ph].
- [27] F. Maltoni, E. Vryonidou, and M. Zaro. “Top-quark mass effects in double and triple Higgs production in gluon-gluon fusion at NLO.” In: *JHEP* 11 (2014), p. 079. DOI: [10.1007/JHEP11\(2014\)079](https://doi.org/10.1007/JHEP11(2014)079). arXiv: [1408.6542](https://arxiv.org/abs/1408.6542) [hep-ph].
- [28] Jonathan Grigo, Jens Hoff, and Matthias Steinhauser. “Higgs boson pair production: top quark mass effects at NLO and NNLO.” In: *Nucl. Phys. B* 900 (2015), pp. 412–430. DOI: [10.1016/j.nuclphysb.2015.09.012](https://doi.org/10.1016/j.nuclphysb.2015.09.012). arXiv: [1508.00909](https://arxiv.org/abs/1508.00909) [hep-ph].
- [29] Massimiliano Grazzini, Gudrun Heinrich, Stephen Jones, Stefan Kallweit, Matthias Kerner, Jonas M. Lindert, and Javier Mazzitelli. “Higgs boson pair production at NNLO with top quark mass effects.” In: *JHEP* 05 (2018), p. 059. DOI: [10.1007/JHEP05\(2018\)059](https://doi.org/10.1007/JHEP05(2018)059). arXiv: [1803.02463](https://arxiv.org/abs/1803.02463) [hep-ph].
- [30] Daniel de Florian and Javier Mazzitelli. “Higgs Boson Pair Production at Next-to-Next-to-Leading Order in QCD.” In: *Phys. Rev. Lett.* 111 (2013), p. 201801. DOI: [10.1103/PhysRevLett.111.201801](https://doi.org/10.1103/PhysRevLett.111.201801). arXiv: [1309.6594](https://arxiv.org/abs/1309.6594) [hep-ph].
- [31] Long-Bin Chen, Hai Tao Li, Hua-Sheng Shao, and Jian Wang. “Higgs boson pair production via gluon fusion at N³LO in QCD.” In: *Phys. Lett. B* 803 (2020), p. 135292. DOI: [10.1016/j.physletb.2020.135292](https://doi.org/10.1016/j.physletb.2020.135292). arXiv: [1909.06808](https://arxiv.org/abs/1909.06808) [hep-ph].
- [32] Long-Bin Chen, Hai Tao Li, Hua-Sheng Shao, and Jian Wang. “The gluon-fusion production of Higgs boson pair: N³LO QCD corrections and top-quark mass effects.” In: *JHEP* 03 (2020), p. 072. DOI: [10.1007/JHEP03\(2020\)072](https://doi.org/10.1007/JHEP03(2020)072). arXiv: [1912.13001](https://arxiv.org/abs/1912.13001) [hep-ph].
- [33] Marvin Gerlach, Florian Herren, and Matthias Steinhauser. “Wilson coefficients for Higgs boson production and decoupling relations to $\mathcal{O}(\alpha_s^4)$.” In: *JHEP* 11 (2018), p. 141. DOI: [10.1007/JHEP11\(2018\)141](https://doi.org/10.1007/JHEP11(2018)141). arXiv: [1809.06787](https://arxiv.org/abs/1809.06787) [hep-ph].
- [34] Joshua Davies, Florian Herren, and Matthias Steinhauser. “Top Quark Mass Effects in Higgs Boson Production at Four-Loop Order: Virtual Corrections.” In: *Phys. Rev. Lett.* 124.11 (2020), p. 112002. DOI: [10.1103/PhysRevLett.124.112002](https://doi.org/10.1103/PhysRevLett.124.112002). arXiv: [1911.10214](https://arxiv.org/abs/1911.10214) [hep-ph].
- [35] Joshua Davies, Florian Herren, Go Mishima, and Matthias Steinhauser. “Real-virtual corrections to Higgs boson pair production at NNLO: three closed top quark loops.” In: *JHEP* 05 (2019), p. 157. DOI: [10.1007/JHEP05\(2019\)157](https://doi.org/10.1007/JHEP05(2019)157). arXiv: [1904.11998](https://arxiv.org/abs/1904.11998) [hep-ph].

- [36] Joshua Davies, Florian Herren, Colin Poole, Matthias Steinhauser, and Anders Eller Thomsen. “Gauge Coupling β Functions to Four-Loop Order in the Standard Model.” In: *Phys. Rev. Lett.* 124.7 (2020), p. 071803. DOI: [10.1103/PhysRevLett.124.071803](https://doi.org/10.1103/PhysRevLett.124.071803). arXiv: [1912.07624](https://arxiv.org/abs/1912.07624) [hep-ph].
- [37] A.V. Bednyakov and A.F. Pikelner. “Four-loop strong coupling beta-function in the Standard Model.” In: *Phys. Lett. B* 762 (2016), pp. 151–156. DOI: [10.1016/j.physletb.2016.09.007](https://doi.org/10.1016/j.physletb.2016.09.007). arXiv: [1508.02680](https://arxiv.org/abs/1508.02680) [hep-ph].
- [38] M.F. Zoller. “Top-Yukawa effects on the β -function of the strong coupling in the SM at four-loop level.” In: *JHEP* 02 (2016), p. 095. DOI: [10.1007/JHEP02\(2016\)095](https://doi.org/10.1007/JHEP02(2016)095). arXiv: [1508.03624](https://arxiv.org/abs/1508.03624) [hep-ph].
- [39] Colin Poole and Anders Eller Thomsen. “Constraints on 3- and 4-loop β -functions in a general four-dimensional Quantum Field Theory.” In: *JHEP* 09 (2019), p. 055. DOI: [10.1007/JHEP09\(2019\)055](https://doi.org/10.1007/JHEP09(2019)055). arXiv: [1906.04625](https://arxiv.org/abs/1906.04625) [hep-th].
- [40] P.A. Zyla et al. “Review of Particle Physics.” In: *PTEP* 2020.8 (2020), p. 083C01. DOI: [10.1093/ptep/ptaa104](https://doi.org/10.1093/ptep/ptaa104).
- [41] Takeo Inami, Takahiro Kubota, and Yasuhiro Okada. “Effective Gauge Theory and the Effect of Heavy Quarks in Higgs Boson Decays.” In: *Z. Phys. C* 18 (1983), pp. 69–80. DOI: [10.1007/BF01571710](https://doi.org/10.1007/BF01571710).
- [42] T. Muta. *Foundations of quantum chromodynamics. Second edition*. Vol. 57. 1998.
- [43] V.P. Spiridonov. “Anomalous Dimension of $G_{\mu\nu}^2$ and β Function.” In: (Jan. 1984).
- [44] A. Djouadi, M. Spira, and P.M. Zerwas. “Production of Higgs bosons in proton colliders: QCD corrections.” In: *Phys. Lett. B* 264 (1991), pp. 440–446. DOI: [10.1016/0370-2693\(91\)90375-Z](https://doi.org/10.1016/0370-2693(91)90375-Z).
- [45] K.G. Chetyrkin, Bernd A. Kniehl, and M. Steinhauser. “Hadronic Higgs decay to order α_s^4 .” In: *Phys. Rev. Lett.* 79 (1997), pp. 353–356. DOI: [10.1103/PhysRevLett.79.353](https://doi.org/10.1103/PhysRevLett.79.353). arXiv: [hep-ph/9705240](https://arxiv.org/abs/hep-ph/9705240).
- [46] K.G. Chetyrkin, Bernd A. Kniehl, and M. Steinhauser. “Decoupling relations to $\mathcal{O}(\alpha_s^3)$ and their connection to low-energy theorems.” In: *Nucl. Phys. B* 510 (1998), pp. 61–87. DOI: [10.1016/S0550-3213\(97\)00649-4](https://doi.org/10.1016/S0550-3213(97)00649-4). arXiv: [hep-ph/9708255](https://arxiv.org/abs/hep-ph/9708255).
- [47] Y. Schroder and M. Steinhauser. “Four-loop decoupling relations for the strong coupling.” In: *JHEP* 01 (2006), p. 051. DOI: [10.1088/1126-6708/2006/01/051](https://doi.org/10.1088/1126-6708/2006/01/051). arXiv: [hep-ph/0512058](https://arxiv.org/abs/hep-ph/0512058).
- [48] K.G. Chetyrkin, Johann H. Kuhn, and Christian Sturm. “QCD decoupling at four loops.” In: *Nucl. Phys. B* 744 (2006), pp. 121–135. DOI: [10.1016/j.nuclphysb.2006.03.020](https://doi.org/10.1016/j.nuclphysb.2006.03.020). arXiv: [hep-ph/0512060](https://arxiv.org/abs/hep-ph/0512060).
- [49] Konstantin Chetyrkin, Pavel Baikov, and Johann Kühn. “The β -function of Quantum Chromodynamics and the effective Higgs-gluon-gluon coupling in five-loop order.” In: *PoS LL2016* (2016), p. 010. DOI: [10.22323/1.260.0010](https://doi.org/10.22323/1.260.0010).

- [50] Jonathan Grigo, Kirill Melnikov, and Matthias Steinhauser. “Virtual corrections to Higgs boson pair production in the large top quark mass limit.” In: *Nucl. Phys. B* 888 (2014), pp. 17–29. DOI: [10.1016/j.nuclphysb.2014.09.003](https://doi.org/10.1016/j.nuclphysb.2014.09.003). arXiv: [1408.2422](https://arxiv.org/abs/1408.2422) [hep-ph].
- [51] Michael Spira. “Effective Multi-Higgs Couplings to Gluons.” In: *JHEP* 10 (2016), p. 026. DOI: [10.1007/JHEP10\(2016\)026](https://doi.org/10.1007/JHEP10(2016)026). arXiv: [1607.05548](https://arxiv.org/abs/1607.05548) [hep-ph].
- [52] P.A. Baikov, K.G. Chetyrkin, and J.H. Kühn. “Five-Loop Running of the QCD coupling constant.” In: *Phys. Rev. Lett.* 118.8 (2017), p. 082002. DOI: [10.1103/PhysRevLett.118.082002](https://doi.org/10.1103/PhysRevLett.118.082002). arXiv: [1606.08659](https://arxiv.org/abs/1606.08659) [hep-ph].
- [53] Thomas Luthe, Andreas Maier, Peter Marquard, and York Schröder. “Towards the five-loop Beta function for a general gauge group.” In: *JHEP* 07 (2016), p. 127. DOI: [10.1007/JHEP07\(2016\)127](https://doi.org/10.1007/JHEP07(2016)127). arXiv: [1606.08662](https://arxiv.org/abs/1606.08662) [hep-ph].
- [54] F. Herzog, B. Ruijl, T. Ueda, J.A.M. Vermaseren, and A. Vogt. “The five-loop beta function of Yang-Mills theory with fermions.” In: *JHEP* 02 (2017), p. 090. DOI: [10.1007/JHEP02\(2017\)090](https://doi.org/10.1007/JHEP02(2017)090). arXiv: [1701.01404](https://arxiv.org/abs/1701.01404) [hep-ph].
- [55] Thomas Luthe, Andreas Maier, Peter Marquard, and York Schroder. “The five-loop Beta function for a general gauge group and anomalous dimensions beyond Feynman gauge.” In: *JHEP* 10 (2017), p. 166. DOI: [10.1007/JHEP10\(2017\)166](https://doi.org/10.1007/JHEP10(2017)166). arXiv: [1709.07718](https://arxiv.org/abs/1709.07718) [hep-ph].
- [56] Vladimir A. Smirnov. *Analytic tools for Feynman integrals*. Vol. 250. 2012. DOI: [10.1007/978-3-642-34886-0](https://doi.org/10.1007/978-3-642-34886-0).
- [57] P.A. Baikov, K.G. Chetyrkin, and J.H. Kühn. “Quark Mass and Field Anomalous Dimensions to $\mathcal{O}(\alpha_s^5)$.” In: *JHEP* 10 (2014), p. 076. DOI: [10.1007/JHEP10\(2014\)076](https://doi.org/10.1007/JHEP10(2014)076). arXiv: [1402.6611](https://arxiv.org/abs/1402.6611) [hep-ph].
- [58] Thomas Luthe, Andreas Maier, Peter Marquard, and York Schröder. “Five-loop quark mass and field anomalous dimensions for a general gauge group.” In: *JHEP* 01 (2017), p. 081. DOI: [10.1007/JHEP01\(2017\)081](https://doi.org/10.1007/JHEP01(2017)081). arXiv: [1612.05512](https://arxiv.org/abs/1612.05512) [hep-ph].
- [59] P.A. Baikov, K.G. Chetyrkin, and J.H. Kühn. “Five-loop fermion anomalous dimension for a general gauge group from four-loop massless propagators.” In: *JHEP* 04 (2017), p. 119. DOI: [10.1007/JHEP04\(2017\)119](https://doi.org/10.1007/JHEP04(2017)119). arXiv: [1702.01458](https://arxiv.org/abs/1702.01458) [hep-ph].
- [60] Max F. Zoller. “On the renormalization of operator products: the scalar gluonic case.” In: *JHEP* 04 (2016), p. 165. DOI: [10.1007/JHEP04\(2016\)165](https://doi.org/10.1007/JHEP04(2016)165). arXiv: [1601.08094](https://arxiv.org/abs/1601.08094) [hep-ph].
- [61] Paulo Nogueira. “Automatic Feynman graph generation.” In: *J. Comput. Phys.* 105 (1993), pp. 279–289. DOI: [10.1006/jcph.1993.1074](https://doi.org/10.1006/jcph.1993.1074).

- [62] R. Harlander, T. Seidensticker, and M. Steinhauser. “Complete corrections of Order α_s^2 to the decay of the Z boson into bottom quarks.” In: *Phys. Lett. B* 426 (1998), pp. 125–132. DOI: [10.1016/S0370-2693\(98\)00220-2](https://doi.org/10.1016/S0370-2693(98)00220-2). arXiv: [hep-ph/9712228](https://arxiv.org/abs/hep-ph/9712228).
- [63] T. Seidensticker. “Automatic application of successive asymptotic expansions of Feynman diagrams.” In: *6th International Workshop on New Computing Techniques in Physics Research: Software Engineering, Artificial Intelligence Neural Nets, Genetic Algorithms, Symbolic Algebra, Automatic Calculation*. May 1999. arXiv: [hep-ph/9905298](https://arxiv.org/abs/hep-ph/9905298).
- [64] Ben Ruijl, Takahiro Ueda, and Jos Vermaseren. “FORM version 4.2.” In: (July 2017). arXiv: [1707.06453 \[hep-ph\]](https://arxiv.org/abs/1707.06453).
- [65] T. van Ritbergen, A.N. Schellekens, and J.A.M. Vermaseren. “Group theory factors for Feynman diagrams.” In: *Int. J. Mod. Phys. A* 14 (1999), pp. 41–96. DOI: [10.1142/S0217751X99000038](https://doi.org/10.1142/S0217751X99000038). arXiv: [hep-ph/9802376](https://arxiv.org/abs/hep-ph/9802376).
- [66] K.G. Chetyrkin and F.V. Tkachov. “Integration by Parts: The Algorithm to Calculate beta Functions in 4 Loops.” In: *Nucl. Phys. B* 192 (1981), pp. 159–204. DOI: [10.1016/0550-3213\(81\)90199-1](https://doi.org/10.1016/0550-3213(81)90199-1).
- [67] F.V. Tkachov. “A Theorem on Analytical Calculability of Four Loop Renormalization Group Functions.” In: *Phys. Lett. B* 100 (1981), pp. 65–68. DOI: [10.1016/0370-2693\(81\)90288-4](https://doi.org/10.1016/0370-2693(81)90288-4).
- [68] Matthias Steinhauser. “MATAD: A Program package for the computation of MAssive TADpoles.” In: *Comput. Phys. Commun.* 134 (2001), pp. 335–364. DOI: [10.1016/S0010-4655\(00\)00204-6](https://doi.org/10.1016/S0010-4655(00)00204-6). arXiv: [hep-ph/0009029](https://arxiv.org/abs/hep-ph/0009029).
- [69] S. Laporta. “High precision calculation of multiloop Feynman integrals by difference equations.” In: *Int. J. Mod. Phys. A* 15 (2000), pp. 5087–5159. DOI: [10.1016/S0217-751X\(00\)00215-7](https://doi.org/10.1016/S0217-751X(00)00215-7). arXiv: [hep-ph/0102033](https://arxiv.org/abs/hep-ph/0102033).
- [70] Alexander V. Smirnov. “FIRE5: a C++ implementation of Feynman Integral REDuction.” In: *Comput. Phys. Commun.* 189 (2015), pp. 182–191. DOI: [10.1016/j.cpc.2014.11.024](https://doi.org/10.1016/j.cpc.2014.11.024). arXiv: [1408.2372 \[hep-ph\]](https://arxiv.org/abs/1408.2372).
- [71] R.N. Lee. “Presenting LiteRed: a tool for the Loop InTEgrals REDuction.” In: (Dec. 2012). arXiv: [1212.2685 \[hep-ph\]](https://arxiv.org/abs/1212.2685).
- [72] Roman N. Lee. “LiteRed 1.4: a powerful tool for reduction of multiloop integrals.” In: *J. Phys. Conf. Ser.* 523 (2014). Ed. by Jianxiong Wang, p. 012059. DOI: [10.1088/1742-6596/523/1/012059](https://doi.org/10.1088/1742-6596/523/1/012059). arXiv: [1310.1145 \[hep-ph\]](https://arxiv.org/abs/1310.1145).
- [73] Y. Schroder and A. Vuorinen. “High-precision epsilon expansions of single-mass-scale four-loop vacuum bubbles.” In: *JHEP* 06 (2005), p. 051. DOI: [10.1088/1126-6708/2005/06/051](https://doi.org/10.1088/1126-6708/2005/06/051). arXiv: [hep-ph/0503209](https://arxiv.org/abs/hep-ph/0503209).

- [74] K.G. Chetyrkin, M. Faisst, Christian Sturm, and M. Tentyukov. “epsilon-finite basis of master integrals for the integration-by-parts method.” In: *Nucl. Phys. B* 742 (2006), pp. 208–229. DOI: [10.1016/j.nuclphysb.2006.02.030](https://doi.org/10.1016/j.nuclphysb.2006.02.030). arXiv: [hep-ph/0601165](https://arxiv.org/abs/hep-ph/0601165).
- [75] R.N. Lee and I.S. Terekhov. “Application of the DRA method to the calculation of the four-loop QED-type tadpoles.” In: *JHEP* 01 (2011), p. 068. DOI: [10.1007/JHEP01\(2011\)068](https://doi.org/10.1007/JHEP01(2011)068). arXiv: [1010.6117 \[hep-ph\]](https://arxiv.org/abs/1010.6117).
- [76] Roman N Lee. Private communication.
- [77] Marvin Gerlach. “Matching in QCD and NRQCD.” MA thesis. KIT, Karlsruhe, 2019.
- [78] Robert Harlander and Philipp Kant. “Higgs production and decay: Analytic results at next-to-leading order QCD.” In: *JHEP* 12 (2005), p. 015. DOI: [10.1088/1126-6708/2005/12/015](https://doi.org/10.1088/1126-6708/2005/12/015). arXiv: [hep-ph/0509189](https://arxiv.org/abs/hep-ph/0509189).
- [79] Charalampos Anastasiou, Stefan Beerli, Stefan Bucherer, Alejandro Daleo, and Zoltan Kunszt. “Two-loop amplitudes and master integrals for the production of a Higgs boson via a massive quark and a scalar-quark loop.” In: *JHEP* 01 (2007), p. 082. DOI: [10.1088/1126-6708/2007/01/082](https://doi.org/10.1088/1126-6708/2007/01/082). arXiv: [hep-ph/0611236](https://arxiv.org/abs/hep-ph/0611236).
- [80] U. Aglietti, R. Bonciani, G. Degrossi, and A. Vicini. “Analytic Results for Virtual QCD Corrections to Higgs Production and Decay.” In: *JHEP* 01 (2007), p. 021. DOI: [10.1088/1126-6708/2007/01/021](https://doi.org/10.1088/1126-6708/2007/01/021). arXiv: [hep-ph/0611266](https://arxiv.org/abs/hep-ph/0611266).
- [81] Mario Prausa and Johann Usovitsch. “The analytic leading color contribution to the Higgs-gluon form factor in QCD at NNLO.” In: (Aug. 2020). arXiv: [2008.11641 \[hep-ph\]](https://arxiv.org/abs/2008.11641).
- [82] Robert V. Harlander, Mario Prausa, and Johann Usovitsch. “The light-fermion contribution to the exact Higgs-gluon form factor in QCD.” In: *JHEP* 10 (2019), p. 148. DOI: [10.1007/JHEP10\(2019\)148](https://doi.org/10.1007/JHEP10(2019)148). arXiv: [1907.06957 \[hep-ph\]](https://arxiv.org/abs/1907.06957).
- [83] Alexey Pak, Mikhail Rogal, and Matthias Steinhauser. “Virtual three-loop corrections to Higgs boson production in gluon fusion for finite top quark mass.” In: *Phys. Lett. B* 679 (2009), pp. 473–477. DOI: [10.1016/j.physletb.2009.08.016](https://doi.org/10.1016/j.physletb.2009.08.016). arXiv: [0907.2998 \[hep-ph\]](https://arxiv.org/abs/0907.2998).
- [84] Robert V. Harlander and Kemal J. Ozeren. “Top mass effects in Higgs production at next-to-next-to-leading order QCD: Virtual corrections.” In: *Phys. Lett. B* 679 (2009), pp. 467–472. DOI: [10.1016/j.physletb.2009.08.012](https://doi.org/10.1016/j.physletb.2009.08.012). arXiv: [0907.2997 \[hep-ph\]](https://arxiv.org/abs/0907.2997).
- [85] Alexey Pak, Mikhail Rogal, and Matthias Steinhauser. “Finite top quark mass effects in NNLO Higgs boson production at LHC.” In: *JHEP* 02 (2010), p. 025. DOI: [10.1007/JHEP02\(2010\)025](https://doi.org/10.1007/JHEP02(2010)025). arXiv: [0911.4662 \[hep-ph\]](https://arxiv.org/abs/0911.4662).

- [86] Robert V. Harlander and Kemal J. Ozeren. “Finite top mass effects for hadronic Higgs production at next-to-next-to-leading order.” In: *JHEP* 11 (2009), p. 088. DOI: [10.1088/1126-6708/2009/11/088](https://doi.org/10.1088/1126-6708/2009/11/088). arXiv: [0909.3420](https://arxiv.org/abs/0909.3420) [hep-ph].
- [87] Robert V. Harlander, Hendrik Mantler, Simone Marzani, and Kemal J. Ozeren. “Higgs production in gluon fusion at next-to-next-to-leading order QCD for finite top mass.” In: *Eur. Phys. J. C* 66 (2010), pp. 359–372. DOI: [10.1140/epjc/s10052-010-1258-x](https://doi.org/10.1140/epjc/s10052-010-1258-x). arXiv: [0912.2104](https://arxiv.org/abs/0912.2104) [hep-ph].
- [88] Joshua Davies and Matthias Steinhauser. “Three-loop form factors for Higgs boson pair production in the large top mass limit.” In: *JHEP* 10 (2019), p. 166. DOI: [10.1007/JHEP10\(2019\)166](https://doi.org/10.1007/JHEP10(2019)166). arXiv: [1909.01361](https://arxiv.org/abs/1909.01361) [hep-ph].
- [89] Joshua Davies, Ramona Gröber, Andreas Maier, Thomas Rauh, and Matthias Steinhauser. “Top quark mass dependence of the Higgs boson-gluon form factor at three loops.” In: *Phys. Rev. D* 100.3 (2019), p. 034017. DOI: [10.1103/PhysRevD.100.034017](https://doi.org/10.1103/PhysRevD.100.034017). arXiv: [1906.00982](https://arxiv.org/abs/1906.00982) [hep-ph].
- [90] Micha L. Czakon and Marco Niggetiedt. “Exact quark-mass dependence of the Higgs-gluon form factor at three loops in QCD.” In: *JHEP* 05 (2020), p. 149. DOI: [10.1007/JHEP05\(2020\)149](https://doi.org/10.1007/JHEP05(2020)149). arXiv: [2001.03008](https://arxiv.org/abs/2001.03008) [hep-ph].
- [91] K.G. Chetyrkin. “A closed analytical formula for two loop massive tadpoles with arbitrary tensor numerators.” In: *3rd International Workshop on Software Engineering, Artificial Intelligence and Expert systems for High-energy and Nuclear Physics*. 1993, pp. 559–563. arXiv: [hep-ph/0212040](https://arxiv.org/abs/hep-ph/0212040).
- [92] Thomas Luthe. Private communication.
- [93] P.A. Baikov, K.G. Chetyrkin, A.V. Smirnov, V.A. Smirnov, and M. Steinhauser. “Quark and gluon form factors to three loops.” In: *Phys. Rev. Lett.* 102 (2009), p. 212002. DOI: [10.1103/PhysRevLett.102.212002](https://doi.org/10.1103/PhysRevLett.102.212002). arXiv: [0902.3519](https://arxiv.org/abs/0902.3519) [hep-ph].
- [94] G. Heinrich, T. Huber, D.A. Kosower, and V.A. Smirnov. “Nine-Propagator Master Integrals for Massless Three-Loop Form Factors.” In: *Phys. Lett. B* 678 (2009), pp. 359–366. DOI: [10.1016/j.physletb.2009.06.038](https://doi.org/10.1016/j.physletb.2009.06.038). arXiv: [0902.3512](https://arxiv.org/abs/0902.3512) [hep-ph].
- [95] T. Gehrmann, E.W.N. Glover, T. Huber, N. Ikizlerli, and C. Studerus. “Calculation of the quark and gluon form factors to three loops in QCD.” In: *JHEP* 06 (2010), p. 094. DOI: [10.1007/JHEP06\(2010\)094](https://doi.org/10.1007/JHEP06(2010)094). arXiv: [1004.3653](https://arxiv.org/abs/1004.3653) [hep-ph].
- [96] R.N. Lee and V.A. Smirnov. “Analytic Epsilon Expansions of Master Integrals Corresponding to Massless Three-Loop Form Factors and Three-Loop $g-2$ up to Four-Loop Transcendentality Weight.” In: *JHEP* 02 (2011), p. 102. DOI: [10.1007/JHEP02\(2011\)102](https://doi.org/10.1007/JHEP02(2011)102). arXiv: [1010.1334](https://arxiv.org/abs/1010.1334) [hep-ph].

- [97] T. Gehrmann, E.W.N. Glover, T. Huber, N. Iqbal, and C. Studerus. “The quark and gluon form factors to three loops in QCD through to $O(\epsilon^2)$.” In: *JHEP* 11 (2010), p. 102. DOI: [10.1007/JHEP11\(2010\)102](https://doi.org/10.1007/JHEP11(2010)102). arXiv: [1010.4478](https://arxiv.org/abs/1010.4478) [hep-ph].
- [98] D.R. Yennie, Steven C. Frautschi, and H. Suura. “The infrared divergence phenomena and high-energy processes.” In: *Annals Phys.* 13 (1961), pp. 379–452. DOI: [10.1016/0003-4916\(61\)90151-8](https://doi.org/10.1016/0003-4916(61)90151-8).
- [99] J.G.M. Gatheral. “Exponentiation of Eikonal Cross-sections in Nonabelian Gauge Theories.” In: *Phys. Lett. B* 133 (1983), pp. 90–94. DOI: [10.1016/0370-2693\(83\)90112-0](https://doi.org/10.1016/0370-2693(83)90112-0).
- [100] J. Frenkel and J.C. Taylor. “NONABELIAN EIKONAL EXPONENTIATION.” In: *Nucl. Phys. B* 246 (1984), pp. 231–245. DOI: [10.1016/0550-3213\(84\)90294-3](https://doi.org/10.1016/0550-3213(84)90294-3).
- [101] Thomas Becher and Matthias Neubert. “Infrared singularities of scattering amplitudes in perturbative QCD.” In: *Phys. Rev. Lett.* 102 (2009). [Erratum: *Phys.Rev.Lett.* 111, 199905 (2013)], p. 162001. DOI: [10.1103/PhysRevLett.102.162001](https://doi.org/10.1103/PhysRevLett.102.162001). arXiv: [0901.0722](https://arxiv.org/abs/0901.0722) [hep-ph].
- [102] Thomas Becher and Matthias Neubert. “On the Structure of Infrared Singularities of Gauge-Theory Amplitudes.” In: *JHEP* 06 (2009). [Erratum: *JHEP* 11, 024 (2013)], p. 081. DOI: [10.1088/1126-6708/2009/06/081](https://doi.org/10.1088/1126-6708/2009/06/081). arXiv: [0903.1126](https://arxiv.org/abs/0903.1126) [hep-ph].
- [103] S. Moch, J.A.M. Vermaseren, and A. Vogt. “The Quark form-factor at higher orders.” In: *JHEP* 08 (2005), p. 049. DOI: [10.1088/1126-6708/2005/08/049](https://doi.org/10.1088/1126-6708/2005/08/049). arXiv: [hep-ph/0507039](https://arxiv.org/abs/hep-ph/0507039).
- [104] Peter Marquard, Alexander V. Smirnov, Vladimir A. Smirnov, Matthias Steinhauser, and David Wellmann. “ $\overline{\text{MS}}$ -on-shell quark mass relation up to four loops in QCD and a general $SU(N)$ gauge group.” In: *Phys. Rev. D* 94.7 (2016), p. 074025. DOI: [10.1103/PhysRevD.94.074025](https://doi.org/10.1103/PhysRevD.94.074025). arXiv: [1606.06754](https://arxiv.org/abs/1606.06754) [hep-ph].
- [105] Florian Herren and Matthias Steinhauser. “Version 3 of RunDec and CRunDec.” In: *Comput. Phys. Commun.* 224 (2018), pp. 333–345. DOI: [10.1016/j.cpc.2017.11.014](https://doi.org/10.1016/j.cpc.2017.11.014). arXiv: [1703.03751](https://arxiv.org/abs/1703.03751) [hep-ph].
- [106] Albert M Sirunyan et al. “A measurement of the Higgs boson mass in the diphoton decay channel.” In: *Phys. Lett. B* 805 (2020), p. 135425. DOI: [10.1016/j.physletb.2020.135425](https://doi.org/10.1016/j.physletb.2020.135425). arXiv: [2002.06398](https://arxiv.org/abs/2002.06398) [hep-ex].
- [107] A. Djouadi, M. Spira, and P.M. Zerwas. “Two photon decay widths of Higgs particles.” In: *Phys. Lett. B* 311 (1993), pp. 255–260. DOI: [10.1016/0370-2693\(93\)90564-X](https://doi.org/10.1016/0370-2693(93)90564-X). arXiv: [hep-ph/9305335](https://arxiv.org/abs/hep-ph/9305335).
- [108] J. Fleischer, O.V. Tarasov, and V.O. Tarasov. “Analytical result for the two loop QCD correction to the decay $H \rightarrow 2 \gamma$.” In: *Phys. Lett. B* 584 (2004), pp. 294–297. DOI: [10.1016/j.physletb.2004.01.063](https://doi.org/10.1016/j.physletb.2004.01.063). arXiv: [hep-ph/0401090](https://arxiv.org/abs/hep-ph/0401090).

- [109] Matthias Steinhauser. “Corrections of $O(\alpha - s^2)$ to the decay of an intermediate mass Higgs boson into two photons.” In: *Ringberg Workshop: The Higgs Puzzle - What can We Learn from LEP2, LHC, NLC, and FMC?* Dec. 1996, pp. 177–185. arXiv: [hep-ph/9612395](#).
- [110] P. Maierhöfer and P. Marquard. “Complete three-loop QCD corrections to the decay $H \rightarrow \gamma\gamma$.” In: *Phys. Lett. B* 721 (2013), pp. 131–135. DOI: [10.1016/j.physletb.2013.02.040](#). arXiv: [1212.6233 \[hep-ph\]](#).
- [111] Marco Niggetiedt. “Exact quark-mass dependence of the Higgs-photon form factor at three loops in QCD.” In: (Sept. 2020). arXiv: [2009.10556 \[hep-ph\]](#).
- [112] Frank Fugel, Bernd A. Kniehl, and Matthias Steinhauser. “Two loop electroweak correction of $O(G(F)M(t)^2)$ to the Higgs-boson decay into photons.” In: *Nucl. Phys. B* 702 (2004), pp. 333–345. DOI: [10.1016/j.nuclphysb.2004.09.018](#). arXiv: [hep-ph/0405232](#).
- [113] Giuseppe Degrandi and Fabio Maltoni. “Two-loop electroweak corrections to the Higgs-boson decay $H \rightarrow \gamma\gamma$.” In: *Nucl. Phys. B* 724 (2005), pp. 183–196. DOI: [10.1016/j.nuclphysb.2005.06.027](#). arXiv: [hep-ph/0504137](#).
- [114] Giampiero Passarino, Christian Sturm, and Sandro Uccirati. “Complete Two-Loop Corrections to $H \rightarrow \gamma\gamma$.” In: *Phys. Lett. B* 655 (2007), pp. 298–306. DOI: [10.1016/j.physletb.2007.09.002](#). arXiv: [0707.1401 \[hep-ph\]](#).
- [115] Stefano Actis, Giampiero Passarino, Christian Sturm, and Sandro Uccirati. “NNLO Computational Techniques: The Cases $H \rightarrow \gamma\gamma$ and $H \rightarrow gg$.” In: *Nucl. Phys. B* 811 (2009), pp. 182–273. DOI: [10.1016/j.nuclphysb.2008.11.024](#). arXiv: [0809.3667 \[hep-ph\]](#).
- [116] F.J. Dyson. “Divergence of perturbation theory in quantum electrodynamics.” In: *Phys. Rev.* 85 (1952), pp. 631–632. DOI: [10.1103/PhysRev.85.631](#).
- [117] W.H. Furry. “A Symmetry Theorem in the Positron Theory.” In: *Phys. Rev.* 51 (1937), pp. 125–129. DOI: [10.1103/PhysRev.51.125](#).
- [118] Christian Sturm. “Higher order QCD results for the fermionic contributions of the Higgs-boson decay into two photons and the decoupling function for the $\overline{\text{MS}}$ renormalized fine-structure constant.” In: *Eur. Phys. J. C* 74.8 (2014), p. 2978. DOI: [10.1140/epjc/s10052-014-2978-0](#). arXiv: [1404.3433 \[hep-ph\]](#).
- [119] Charalampos Anastasiou and Kirill Melnikov. “Higgs boson production at hadron colliders in NNLO QCD.” In: *Nucl. Phys. B* 646 (2002), pp. 220–256. DOI: [10.1016/S0550-3213\(02\)00837-4](#). arXiv: [hep-ph/0207004](#).

- [120] Alexey Pak. “The Toolbox of modern multi-loop calculations: novel analytic and semi-analytic techniques.” In: *J. Phys. Conf. Ser.* 368 (2012). Ed. by Liliana Teodorescu, David Britton, Nigel Glover, Gudrun Heinrich, Jerome Lauret, Axel Naumann, Thomas Speer, and Pedro Teixeira-Dias, p. 012049. DOI: [10.1088/1742-6596/368/1/012049](https://doi.org/10.1088/1742-6596/368/1/012049). arXiv: [1111.0868](https://arxiv.org/abs/1111.0868) [hep-ph].
- [121] Jens Simon Hoff. “Methods for multiloop calculations and Higgs boson production at the LHC.” PhD thesis. KIT, Karlsruhe, 2015. DOI: [10.5445/IR/1000047447](https://doi.org/10.5445/IR/1000047447).
- [122] Roman N. Lee and Andrei A. Pomeransky. “Critical points and number of master integrals.” In: *JHEP* 11 (2013), p. 165. DOI: [10.1007/JHEP11\(2013\)165](https://doi.org/10.1007/JHEP11(2013)165). arXiv: [1308.6676](https://arxiv.org/abs/1308.6676) [hep-ph].
- [123] Marvin Gerlach, Go Mishima, and Matthias Steinhauser. “Matching coefficients in nonrelativistic QCD to two-loop accuracy.” In: *Phys. Rev. D* 100.5 (2019), p. 054016. DOI: [10.1103/PhysRevD.100.054016](https://doi.org/10.1103/PhysRevD.100.054016). arXiv: [1907.08227](https://arxiv.org/abs/1907.08227) [hep-ph].
- [124] Matteo Fael, Kay Schönwald, and Matthias Steinhauser. “The Kinetic Heavy Quark Mass to Three Loops.” In: *Phys. Rev. Lett.* 125.5 (2020), p. 052003. DOI: [10.1103/PhysRevLett.125.052003](https://doi.org/10.1103/PhysRevLett.125.052003). arXiv: [2005.06487](https://arxiv.org/abs/2005.06487) [hep-ph].
- [125] M. Beneke and Vladimir A. Smirnov. “Asymptotic expansion of Feynman integrals near threshold.” In: *Nucl. Phys. B* 522 (1998), pp. 321–344. DOI: [10.1016/S0550-3213\(98\)00138-2](https://doi.org/10.1016/S0550-3213(98)00138-2). arXiv: [hep-ph/9711391](https://arxiv.org/abs/hep-ph/9711391).
- [126] Jonathan Grigo. “Korrekturen höherer Ordnung zur Produktion von Higgs-Boson-Paaren.” PhD thesis. KIT, Karlsruhe, 2015. DOI: [10.5445/IR/1000048688](https://doi.org/10.5445/IR/1000048688).
- [127] V. Ravindran, J. Smith, and W. L. van Neerven. “NNLO corrections to the total cross-section for Higgs boson production in hadron hadron collisions.” In: *Nucl. Phys. B* 665 (2003), pp. 325–366. DOI: [10.1016/S0550-3213\(03\)00457-7](https://doi.org/10.1016/S0550-3213(03)00457-7). arXiv: [hep-ph/0302135](https://arxiv.org/abs/hep-ph/0302135).
- [128] S. Moch, J.A.M. Vermaseren, and A. Vogt. “The Three loop splitting functions in QCD: The Nonsinglet case.” In: *Nucl. Phys. B* 688 (2004), pp. 101–134. DOI: [10.1016/j.nuclphysb.2004.03.030](https://doi.org/10.1016/j.nuclphysb.2004.03.030). arXiv: [hep-ph/0403192](https://arxiv.org/abs/hep-ph/0403192).
- [129] A. Vogt, S. Moch, and J.A.M. Vermaseren. “The Three-loop splitting functions in QCD: The Singlet case.” In: *Nucl. Phys. B* 691 (2004), pp. 129–181. DOI: [10.1016/j.nuclphysb.2004.04.024](https://doi.org/10.1016/j.nuclphysb.2004.04.024). arXiv: [hep-ph/0404111](https://arxiv.org/abs/hep-ph/0404111).
- [130] Gabor Somogyi. “Angular integrals in d dimensions.” In: *J. Math. Phys.* 52 (2011), p. 083501. DOI: [10.1063/1.3615515](https://doi.org/10.1063/1.3615515). arXiv: [1101.3557](https://arxiv.org/abs/1101.3557) [hep-ph].
- [131] A.V. Kotikov. “Differential equations method: New technique for massive Feynman diagrams calculation.” In: *Phys. Lett. B* 254 (1991), pp. 158–164. DOI: [10.1016/0370-2693\(91\)90413-K](https://doi.org/10.1016/0370-2693(91)90413-K).

- [132] A.V. Kotikov. “Differential equations method: The Calculation of vertex type Feynman diagrams.” In: *Phys. Lett. B* 259 (1991), pp. 314–322. DOI: [10.1016/0370-2693\(91\)90834-D](https://doi.org/10.1016/0370-2693(91)90834-D).
- [133] A.V. Kotikov. “Differential equation method: The Calculation of N point Feynman diagrams.” In: *Phys. Lett. B* 267 (1991). [Erratum: *Phys.Lett.B* 295, 409–409 (1992)], pp. 123–127. DOI: [10.1016/0370-2693\(91\)90536-Y](https://doi.org/10.1016/0370-2693(91)90536-Y).
- [134] Johannes M. Henn. “Multiloop integrals in dimensional regularization made simple.” In: *Phys. Rev. Lett.* 110 (2013), p. 251601. DOI: [10.1103/PhysRevLett.110.251601](https://doi.org/10.1103/PhysRevLett.110.251601). arXiv: [1304.1806](https://arxiv.org/abs/1304.1806) [hep-th].
- [135] Roman N. Lee. “Reducing differential equations for multiloop master integrals.” In: *JHEP* 04 (2015), p. 108. DOI: [10.1007/JHEP04\(2015\)108](https://doi.org/10.1007/JHEP04(2015)108). arXiv: [1411.0911](https://arxiv.org/abs/1411.0911) [hep-ph].
- [136] Roman N Lee. *Libra, a tool for reducing differential systems to ϵ -form*. Private communication.
- [137] Mario Prausa. “epsilon: A tool to find a canonical basis of master integrals.” In: *Comput. Phys. Commun.* 219 (2017), pp. 361–376. DOI: [10.1016/j.cpc.2017.05.026](https://doi.org/10.1016/j.cpc.2017.05.026). arXiv: [1701.00725](https://arxiv.org/abs/1701.00725) [hep-ph].
- [138] Marco Besier, Duco Van Straten, and Stefan Weinzierl. “Rationalizing roots: an algorithmic approach.” In: *Commun. Num. Theor. Phys.* 13 (2019), pp. 253–297. DOI: [10.4310/CNTP.2019.v13.n2.a1](https://doi.org/10.4310/CNTP.2019.v13.n2.a1). arXiv: [1809.10983](https://arxiv.org/abs/1809.10983) [hep-th].
- [139] Claude Duhr and Falko Dulat. “PolyLogTools —polylogs for the masses.” In: *JHEP* 08 (2019), p. 135. DOI: [10.1007/JHEP08\(2019\)135](https://doi.org/10.1007/JHEP08(2019)135). arXiv: [1904.07279](https://arxiv.org/abs/1904.07279) [hep-th].
- [140] Christian W. Bauer, Alexander Frink, and Richard Kreckel. “Introduction to the GiNaC framework for symbolic computation within the C++ programming language.” In: *J. Symb. Comput.* 33 (2002), pp. 1–12. DOI: [10.1006/jscs.2001.0494](https://doi.org/10.1006/jscs.2001.0494). arXiv: [cs/0004015](https://arxiv.org/abs/cs/0004015).
- [141] Jens Vollinga and Stefan Weinzierl. “Numerical evaluation of multiple polylogarithms.” In: *Comput. Phys. Commun.* 167 (2005), p. 177. DOI: [10.1016/j.cpc.2004.12.009](https://doi.org/10.1016/j.cpc.2004.12.009). arXiv: [hep-ph/0410259](https://arxiv.org/abs/hep-ph/0410259).
- [142] Joshua Davies, Florian Herren, Go Mishima, and Matthias Steinhauser. “NNLO real corrections to $gg \rightarrow HH$ in the large- m_t limit.” In: *PoS RADCOR2019* (2019), p. 022. DOI: [10.22323/1.375.0022](https://doi.org/10.22323/1.375.0022). arXiv: [1912.01646](https://arxiv.org/abs/1912.01646) [hep-ph].
- [143] Go Mishima. *Three- and four-particle cut master integrals at threshold*. Internal note.
- [144] Go Mishima and Matthias Steinhauser. *Collinear counterterms for Higgs boson pair-production*. Internal note.

- [145] Alexey Pak, Mikhail Rogal, and Matthias Steinhauser. “Production of scalar and pseudo-scalar Higgs bosons to next-to-next-to-leading order at hadron colliders.” In: *JHEP* 09 (2011), p. 088. DOI: [10.1007/JHEP09\(2011\)088](https://doi.org/10.1007/JHEP09(2011)088). arXiv: [1107.3391](https://arxiv.org/abs/1107.3391) [hep-ph].
- [146] Jakob Ablinger. “A Computer Algebra Toolbox for Harmonic Sums Related to Particle Physics.” MA thesis. Linz U., 2009. arXiv: [1011.1176](https://arxiv.org/abs/1011.1176) [math-ph].
- [147] Jakob Ablinger. “Computer Algebra Algorithms for Special Functions in Particle Physics.” PhD thesis. Linz U., Apr. 2012. arXiv: [1305.0687](https://arxiv.org/abs/1305.0687) [math-ph].
- [148] Jakob Ablinger. “The package HarmonicSums: Computer Algebra and Analytic aspects of Nested Sums.” In: *PoS LL2014* (2014). Ed. by Martina Mende, p. 019. DOI: [10.22323/1.211.0019](https://doi.org/10.22323/1.211.0019). arXiv: [1407.6180](https://arxiv.org/abs/1407.6180) [cs.SC].
- [149] Ramona Gröber, Andreas Maier, and Thomas Rauh. “Reconstruction of top-quark mass effects in Higgs pair production and other gluon-fusion processes.” In: *JHEP* 03 (2018), p. 020. DOI: [10.1007/JHEP03\(2018\)020](https://doi.org/10.1007/JHEP03(2018)020). arXiv: [1709.07799](https://arxiv.org/abs/1709.07799) [hep-ph].
- [150] Ramona Gröber, Andreas Maier, and Thomas Rauh. “Top quark mass effects in $gg \rightarrow ZZ$ at two loops and off-shell Higgs boson interference.” In: *Phys. Rev. D* 100.11 (2019), p. 114013. DOI: [10.1103/PhysRevD.100.114013](https://doi.org/10.1103/PhysRevD.100.114013). arXiv: [1908.04061](https://arxiv.org/abs/1908.04061) [hep-ph].
- [151] Federico Buccioni, Jean-Nicolas Lang, Jonas M. Lindert, Philipp Maierhöfer, Stefano Pozzorini, Hantian Zhang, and Max F. Zoller. “OpenLoops 2.” In: *Eur. Phys. J. C* 79.10 (2019), p. 866. DOI: [10.1140/epjc/s10052-019-7306-2](https://doi.org/10.1140/epjc/s10052-019-7306-2). arXiv: [1907.13071](https://arxiv.org/abs/1907.13071) [hep-ph].
- [152] Joshua Davies, Florian Herren, and Matthias Steinhauser. *Four-loop corrections to Higgs boson decay into photons*. in preparation.
- [153] Michael E. Peskin and Daniel V. Schroeder. *An Introduction to quantum field theory*. Reading, USA: Addison-Wesley, 1995. ISBN: 978-0-201-50397-5.
- [154] William A. Bardeen, A.J. Buras, D.W. Duke, and T. Muta. “Deep Inelastic Scattering Beyond the Leading Order in Asymptotically Free Gauge Theories.” In: *Phys. Rev. D* 18 (1978), p. 3998. DOI: [10.1103/PhysRevD.18.3998](https://doi.org/10.1103/PhysRevD.18.3998).
- [155] K.G. Chetyrkin, G. Falcioni, F. Herzog, and J.A.M. Vermaseren. “Five-loop renormalisation of QCD in covariant gauges.” In: *JHEP* 10 (2017). [Addendum: *JHEP* 12, 006 (2017)], p. 179. DOI: [10.1007/JHEP10\(2017\)179](https://doi.org/10.1007/JHEP10(2017)179). arXiv: [1709.08541](https://arxiv.org/abs/1709.08541) [hep-ph].
- [156] Peter Marquard, Alexander V. Smirnov, Vladimir A. Smirnov, and Matthias Steinhauser. “Quark Mass Relations to Four-Loop Order in Perturbative QCD.” In: *Phys. Rev. Lett.* 114.14 (2015), p. 142002. DOI: [10.1103/PhysRevLett.114.142002](https://doi.org/10.1103/PhysRevLett.114.142002). arXiv: [1502.01030](https://arxiv.org/abs/1502.01030) [hep-ph].
- [157] R. Tarrach. “The Pole Mass in Perturbative QCD.” In: *Nucl. Phys. B* 183 (1981), pp. 384–396. DOI: [10.1016/0550-3213\(81\)90140-1](https://doi.org/10.1016/0550-3213(81)90140-1).

- [158] N. Gray, David J. Broadhurst, W. Grafe, and K. Schilcher. “Three Loop Relation of Quark (Modified) M_s and Pole Masses.” In: *Z. Phys. C* 48 (1990), pp. 673–680. DOI: [10.1007/BF01614703](https://doi.org/10.1007/BF01614703).
- [159] K.G. Chetyrkin and M. Steinhauser. “Short distance mass of a heavy quark at order α_s^3 .” In: *Phys. Rev. Lett.* 83 (1999), pp. 4001–4004. DOI: [10.1103/PhysRevLett.83.4001](https://doi.org/10.1103/PhysRevLett.83.4001). arXiv: [hep-ph/9907509](https://arxiv.org/abs/hep-ph/9907509).
- [160] K.G. Chetyrkin and M. Steinhauser. “The Relation between the \overline{MS} -bar and the on-shell quark mass at order $\alpha(s)^3$.” In: *Nucl. Phys. B* 573 (2000), pp. 617–651. DOI: [10.1016/S0550-3213\(99\)00784-1](https://doi.org/10.1016/S0550-3213(99)00784-1). arXiv: [hep-ph/9911434](https://arxiv.org/abs/hep-ph/9911434).
- [161] Kirill Melnikov and Timo van Ritbergen. “The Three loop relation between the \overline{MS} -bar and the pole quark masses.” In: *Phys. Lett. B* 482 (2000), pp. 99–108. DOI: [10.1016/S0370-2693\(00\)00507-4](https://doi.org/10.1016/S0370-2693(00)00507-4). arXiv: [hep-ph/9912391](https://arxiv.org/abs/hep-ph/9912391).
- [162] P. Marquard, L. Mihaila, J.H. Piclum, and M. Steinhauser. “Relation between the pole and the minimally subtracted mass in dimensional regularization and dimensional reduction to three-loop order.” In: *Nucl. Phys. B* 773 (2007), pp. 1–18. DOI: [10.1016/j.nuclphysb.2007.03.010](https://doi.org/10.1016/j.nuclphysb.2007.03.010). arXiv: [hep-ph/0702185](https://arxiv.org/abs/hep-ph/0702185).
- [163] P.A. Baikov, K.G. Chetyrkin, and Johann H. Kuhn. “Order $\alpha^4(s)$ QCD Corrections to Z and tau Decays.” In: *Phys. Rev. Lett.* 101 (2008), p. 012002. DOI: [10.1103/PhysRevLett.101.012002](https://doi.org/10.1103/PhysRevLett.101.012002). arXiv: [0801.1821 \[hep-ph\]](https://arxiv.org/abs/0801.1821).
- [164] F. Herzog, B. Ruijl, T. Ueda, J.A.M. Vermaseren, and A. Vogt. “On Higgs decays to hadrons and the R-ratio at N^4 LO.” In: *JHEP* 08 (2017), p. 113. DOI: [10.1007/JHEP08\(2017\)113](https://doi.org/10.1007/JHEP08(2017)113). arXiv: [1707.01044 \[hep-ph\]](https://arxiv.org/abs/1707.01044).
- [165] Alexander B. Goncharov. “Multiple polylogarithms, cyclotomy and modular complexes.” In: *Math. Res. Lett.* 5 (1998), pp. 497–516. DOI: [10.4310/MRL.1998.v5.n4.a7](https://doi.org/10.4310/MRL.1998.v5.n4.a7). arXiv: [1105.2076 \[math.AG\]](https://arxiv.org/abs/1105.2076).
- [166] Tao Liu and Matthias Steinhauser. “Decoupling of heavy quarks at four loops and effective Higgs-fermion coupling.” In: *Phys. Lett. B* 746 (2015), pp. 330–334. DOI: [10.1016/j.physletb.2015.05.023](https://doi.org/10.1016/j.physletb.2015.05.023). arXiv: [1502.04719 \[hep-ph\]](https://arxiv.org/abs/1502.04719).
- [167] D. Binosi and L. Theussl. “JaxoDraw: A Graphical user interface for drawing Feynman diagrams.” In: *Comput. Phys. Commun.* 161 (2004), pp. 76–86. DOI: [10.1016/j.cpc.2004.05.001](https://doi.org/10.1016/j.cpc.2004.05.001). arXiv: [hep-ph/0309015](https://arxiv.org/abs/hep-ph/0309015).

ACKNOWLEDGMENTS

First of all I want to thank Prof. Dr. Matthias Steinhauser for offering me the chance to perform the almost three years of fruitful research that culminated in this thesis. He gave me the possibility to work on various topics, ranging from Higgs boson pair production to the computation of higher-order beta functions, and provided me with continuous support, advice and feedback on this thesis.

I also want to thank Prof. Dr. Kirill Melnikov for agreeing to be the second reviewer of this thesis. During my time at the TTP I learned a lot about physics from his lectures and questions.

During the past three years I worked together with many great people, who I want to thank: Joshua Davies, Thomas Deppisch, Marvin Gerlach, Go Mishima, Colin Poole and Anders Eller Thomsen. I had a great time working with all of you and am really looking forward to continue to collaborate in future projects.

I want to thank Joshua Davies, Max Delto, Go Mishima, Kay Schönwald and Raynette van Tonder for reading parts of this thesis and providing valuable feedback on it.

Furthermore, I want to thank past and present members of the TTP:

- Konstantin Asteriadis, Max Delto and Ulises Saldaña-Salazar for the great time I had in our enclave 12/15 in ITP territory,
- Arnd Behring, Thomas Deppisch, Marvin Gerlach and Kay Schönwald for all the enlightening discussions while waiting for the coffee machine,
- Konstantin Asteriadis, Martin Gabelmann, David Wellmann and Mustafa Tabet for keeping the cluster up and running,
- Marvin Gerlach and Martin Lang for keeping the coffee flowing

and last but not least Martina Schorn for taking care of all the paperwork that needed to be done, making my life here much easier.

I want to thank my family for encouraging me to think more carefully about my choice of studies and their continuous support throughout them.

Finally I want to thank Raynette for always encouraging and supporting me, especially throughout these past months of finishing this work.

COLOPHON

All Feynman diagrams in this document were drawn using Jaxodraw [167].

This document was typeset using the typographical look-and-feel `classicthesis` developed by André Miede and Ivo Pletikosić. The style was inspired by Robert Bringhurst's seminal book on typography "*The Elements of Typographic Style*". `classicthesis` is available for both \LaTeX and \LyX :

<https://bitbucket.org/amiede/classicthesis/>

Happy users of `classicthesis` usually send a real postcard to the author, a collection of postcards received so far is featured here:

<http://postcards.miede.de/>

Thank you very much for your feedback and contribution.

Final Version as of November 2, 2020 (`classicthesis` v4.6).